
Pulsed Free Space Photonic Vector Network Analyzers



TECHNISCHE
UNIVERSITÄT
DARMSTADT

Terahertz Devices and Systems
Institute of Microwave Engineering and Photonics
Department of Electrical Engineering and Information Technology
Technical University of Darmstadt
Darmstadt, Germany

To obtain the academic degree Doktoringenieur (Dr.-Ing.)

Approved dissertation by

Fahd Rushd Faridi

First Reviewer: Dr. rer. nat. Sascha Preu
Second Reviewer: Dr. Zachary Taylor

Darmstadt 2023

Pulsed Free Space Photonic Vector Network Analyzers Gepulster Photonischer Vektornetzwerkanalysator im Freistrahlbetrieb

Zur Erlangung des akademischen Grades Doktor-Ingenieur (Dr.-Ing.)
Genehmigte Dissertation von **Fahd Rushd Faridi**

Erstreferent: Dr. rer. nat. Sascha Preu
Koreferent: Dr. Zachary Taylor

Tag der Einreichung: 29.11.2022
Tag der Prüfung: 17.02.2023

Technische Universität Darmstadt
Darmstadt 2023

2. überarbeitete Auflage

Bitte zitieren Sie dieses Dokument als:

URN: urn:nbn:de:tuda-tuprints-287815

URL: <https://tuprints.ulb.tu-darmstadt.de/id/eprint/28781>

Dieses Dokument wird bereitgestellt von tuprints,
E-Publishing-Service der TU Darmstadt
<http://tuprints.ulb.tu-darmstadt.de>
tuprints@ulb.tu-darmstadt.de



Die Veröffentlichung steht unter folgender Creative Commons Lizenz:
Namensnennung 4.0 International (CC BY 4.0)
<https://creativecommons.org/licenses/by/4.0/>

This work is licensed under a Creative Commons License:
Attribution 4.0 International (CC BY 4.0)
<https://creativecommons.org/licenses/by/4.0/>

To my family...

ABSTRACT

Terahertz (THz) radiation (0.1–10 THz) has demonstrated great significance in a wide range of interdisciplinary applications due to its unique properties such as the capacity to penetrate optically opaque materials without ionizing effect, superior spatial resolution as compared to the microwave domain for imaging or ability to identify a vast array of molecules using THz fingerprinting. Advancements in generation and detection techniques, as well as the necessities of application-driven research and industry, have created a substantial demand for THz-range devices and components. However, progress in the development of THz components is hampered by a lack of efficient and affordable characterization systems, resulting in limited development in THz science and technology.

Vector Network Analyzers (VNAs) are highly sophisticated well-established characterization instruments in the microwave bands, which are now employed in the lower end of the THz spectrum (up to 1.5 THz) using frequency extender modules. These modules are extremely expensive, and due to the implementation of hollow metallic waveguides for their configuration, they are narrowband, requiring at least six modules to achieve a frequency coverage of 0.2–1.5 THz. Moreover, they are susceptible to problems like material losses, manufacturing and alignment tolerances etc., making them less than ideal for fast, broadband investigation. The main objective of this thesis is to design a robust but cost-effective characterization system based on a photonic method that can characterize THz components up to several THz in a single configuration.

To achieve this, we design architectures for the Photonic Vector Network Analyzer (PVNA) concept, incorporating ErAs:In(Al)GaAs-based photoconductive sources and ErAs:InGaAs-based photoconductive receivers, driven with a femtosecond pulsed laser operating at 1550 nm. The broadband photonic devices replace narrowband electronic ones in order to record the Scattering (S)-parameters in a free space configuration. Corresponding calibration and data evaluation methods are also developed. Then the PVNAs are configured, and their capabilities are validated by characterizing various THz components, including a THz isolator, a Distributed Bragg Reflector, a Split-Ring Resonator array and a Crossed-Dipole Resonator (CDR) array, in terms of their S -parameters. The PVNAs are also implemented to determine the complex refractive index or dielectric permittivity and physical thickness of several materials in the THz range. Finally, we develop an ErAs:In(Al)GaAs-based THz transceiver and implement it in a PVNA configuration, resulting in a more compact setup that is useful for industrial applications. The feasibility of such systems is also verified by characterizing several THz components.

The configured systems achieve a bandwidth of more than 2.5 THz, exceeding the maximum attainable frequency of the commercial Electronic Vector Network Analyzer (EVNA) extender modules. For the 1.1-1.5 THz band, the dynamic range of 47-35 dB (Equivalent Noise Bandwidth (ENBW) = 9.196 Hz) achieved with the PVNA is comparable to the dynamic range of 45-25 dB (ENBW = 10 Hz) of the EVNA. Both amplitude and phase of the S -parameters,

determined by the configured PVNAs, are compared with simulations or theoretical models and showed excellent agreement. The PVNA could discern multi-peak and narrow resonance characteristics despite its lower spectral resolution ($\sim 3\text{-}7$ GHz) compared to the EVNA. By accurately determining the S -parameters of multiple THz components, the transceiver-based PVNA also demonstrated its exceptional competence.

With huge bandwidth and simpler calibration techniques, the PVNA provides a potential solution to bridge the existing technological gap in THz-range characterization systems and offers a solid platform for THz component development, paving the way for more widespread application of THz technologies in research and industry.

ZUSAMMENFASSUNG

Terahertz (THz)-Strahlung (0,1–10 THz) hat aufgrund ihrer einzigartigen Eigenschaften große Bedeutung für ein breites Spektrum interdisziplinärer Anwendungen erlangt. Dazu zählen die Fähigkeit, optisch undurchsichtige Materialien ohne ionisierende Wirkung zu durchdringen, eine bessere räumliche Auflösung als Mikrowellenstrahlung für die Bildgebung und die Fähigkeit, verschiedenste Moleküle mit Hilfe von THz-Fingerabdrücken zu identifizieren. Fortschritte bei Quellen und Detektoren beschleunigt durch die Erfordernisse der anwendungsorientierten Forschung und Industrie haben zu einer erheblichen Nachfrage nach Geräten und Komponenten im THz-Bereich geführt. Der Fortschritt bei der Entwicklung von THz-Komponenten wird jedoch durch einen Mangel an effizienten und erschwinglichen Messgeräten behindert, was zu einer begrenzten Entwicklung von Terahertz-Technologien führt.

Vektorielle Netzwerkanalysatoren (VNAs) sind hochentwickelte und etablierte Charakterisierungsinstrumente für den Mikrowellenbereich, die nun auch im unteren Bereich des THz-Spektrums (bis zu 1,5 THz) unter Verwendung von Frequenzerweiterungsmodulen eingesetzt werden. Diese Module sind extrem teuer und aufgrund der Verwendung von Hohlleitern schmalbandig, so dass mindestens sechs Module erforderlich sind, um eine Frequenzabdeckung von 0,2 bis 1,5 THz zu erreichen. Außerdem sind die Bänder und insbesondere deren Tausch anfällig für Fertigungs- und Ausrichtungstoleranzen, was sie für schnelle Untersuchungen mit großer Frequenzabdeckung nicht gerade ideal macht. Das Hauptziel dieser Arbeit ist es, ein robustes, aber kostengünstiges Messgerät auf der Grundlage einer photonischen Methode zu entwickeln, das THz-Komponenten bis zu mehreren THz mit Hilfe eines einzigen Systems charakterisieren kann.

Um dies zu erreichen, haben wir Architekturen für photonische vektorielle Netzwerkanalysatoren (PVNA) entwickelt, die ErAs:In(Al)GaAs photoleitende Quellen und ErAs:InGaAs photoleitende Empfänger enthalten, welche mit einem gepulsten Femtosekundenlaser bei 1550 nm betrieben werden. Diese breitbandigen Komponenten ersetzen die schmalbandigen elektronischen Komponenten. Passende Kalibrierungs- und Datenauswertungsmethoden wurden ebenfalls entwickelt. Anschließend werden die PVNAs konfiguriert und ihre Fähigkeiten durch die Charakterisierung verschiedener THz-Komponenten wie einem THz-Isolator, einem Bragg-Reflektor, ein Ringresonator-Array und ein gekreuztes Dipolresonator-Array im Hinblick auf ihre Streuparameter (S-Parameter) validiert. Die PVNAs wurden auch zur Bestimmung des komplexen Brechungsindex oder der Dielektrizitätskonstante und der physikalischen Dicke verschiedener Materialien im THz-Bereich eingesetzt. Abschließend entwickelten wir einen ErAs:In(Al)GaAs-basierten THz-Transceiver und implementierten ihn in einer PVNA-Konfiguration. Dies führt zu einem kompakteren Aufbau, der für industrielle Anwendungen nützlich ist. Die Funktionalität solcher Systeme wurde auch durch die Charakterisierung verschiedener THz-Komponenten verifiziert.

Die Systeme erreichten eine Bandbreite von mehr als 2,5 THz (bis zu 3 THz für den 2-Port PVNA) und übertrafen damit die maximal erreichbare Frequenz der kommerziellen elektronischen vektoriiellen Netzwerkanalysatoren (EVNA)-Erweiterungsmodule. Der Dynamikbereich von 47-35 dB (Äquivalente Rauschbandbreite (ENBW) = 9.196 Hz) der mit dem PVNA für das 1,1-1,5 THz-Band erreicht wird, ist vergleichbar mit dem Dynamikbereich von 45-25 dB (ENBW = 10 Hz) des EVNA. Sowohl Amplitude als auch Phase der von den PVNAs ermittelten S-Parameter wurden mit Simulationen oder theoretischen Modellen verglichen und zeigten eine ausgezeichnete Übereinstimmung. Der PVNA konnte trotz seiner im Vergleich zu den EVNAs geringen Spektralaufösung ($\sim 3-7$ GHz) sowohl schmale Resonanzcharakteristiken, als auch solche mit mehreren Linien erkennen. Durch die genaue Bestimmung der S-Parameter mehrerer THz-Komponenten bewies der Transceiver-basierte PVNA auch sein außergewöhnliches Können.

Mit seiner großen Bandbreite und den einfacheren Kalibrierungsmethoden stellt der PVNA eine potenzielle Lösung für die bestehende technologische Lücke bei den Charakterisierungssystemen für den THz-Bereich dar und bietet eine solide Plattform für die Entwicklung von THz-Komponenten, die den Weg für eine breitere Anwendung von THz-Technologien in Forschung und Industrie ebnet.

CONTENTS

CHAPTER 1 – INTRODUCTION	1
1.1 Motivation and State of the Art	3
1.2 Research Objectives and Overview	6
CHAPTER 2 – STATE-OF-THE-ART CHARACTERIZATION SYSTEMS IN THZ RANGE	9
2.1 Electronic Characterization System: The VNA	9
2.1.1 Network Analysis Basics and Scattering Parameters	9
2.1.2 System Architecture of a VNA	12
2.1.3 THz VNA Architecture	13
2.1.4 Measurement Errors	15
2.1.5 Calibration	16
2.1.6 State-of-the-Art THz VNA	18
2.2 Photonic Characterization Systems	20
2.2.1 THz Generation by Photomixing	20
2.2.2 THz Pulse Detection by Photoconductors	24
2.2.3 Terahertz Time Domain Spectrometer	27
2.2.4 State-of-the-Art THz-TDS Systems	33
2.2.5 Conclusion	35
CHAPTER 3 – PHOTONIC VNA: SYSTEM ARCHITECTURE, CALIBRATION AND DATA EVALUATION	37
3.1 System Architecture	37
3.1.1 Optical Component: Ultrafast Laser	37
3.1.2 Transmitters and Detectors: Pulsed Photoconductive THz Emitters and Detectors	38
3.1.3 Test Set: Wire Grid Polarizer-based Directional Coupler	39
3.1.4 Post-Detection Electronics	42
3.2 Calibration Standards and Calibration Process	42
3.3 Data Evaluation	46
3.3.1 Time-Domain Data Processing	46
3.3.2 Algorithm for Material Characterization	48
3.4 Conclusion	52
CHAPTER 4 – 1.5 PORT VECTOR SPECTROMETER	53
4.1 Experimental Setup	54
4.2 System Attributes	55

4.3	Applications	57
4.3.1	Material Parameter Extraction	57
4.3.2	Device Characterization	59
4.4	Conclusion	65
CHAPTER 5 – TWO-PORT PHOTONIC VECTOR NETWORK ANALYZER		67
5.1	Experimental Setup	67
5.2	System Characteristics	69
5.2.1	Definition of Measurement Parameters	69
5.2.2	Cross-talk Measurement	71
5.2.3	System Bandwidth and Dynamic Range	72
5.3	Applications	73
5.3.1	Metamaterial Characterization	73
5.3.2	Characterization of a Distributed Bragg-Reflector	77
5.3.3	Material Permittivity and Thickness Extraction	78
5.4	Comparison with Continuous Wave PVNA	80
5.5	Comparison with Electronic VNA	83
5.6	Conclusion	85
CHAPTER 6 – TERAHERTZ TRANSCEIVERS AND TRANSCEIVER-BASED PVNA		87
6.1	Development of the Transceiver	88
6.1.1	Material Properties	88
6.1.2	Fabrication Process	89
6.1.3	Packaging	92
6.2	Transceiver-based One-Port PVNA	93
6.2.1	Experimental setup	93
6.2.2	System Characteristics	94
6.2.3	Applications	95
6.3	Conclusion	96
CHAPTER 7 – SUMMARY AND OUTLOOK		99
7.1	Limitations and Outlook	101
APPENDIX A – DATA ACQUISITION GUI		103
APPENDIX B – MATLAB CODE FOR MATERIAL CHARACTERIZATION ALGORITHM		105
APPENDIX C – MATERIAL CHARACTERIZATION SOFTWARE		115
REFERENCES		117
LIST OF FIGURES		143

LIST OF PUBLICATIONS

147

ACRONYMS

150

CHAPTER 1

Introduction

Terahertz (THz) radiation, conventionally referred to as the sub-millimeter or far-infrared radiation for most of the 20th century, corresponds to the region of the electromagnetic spectrum that lies between the microwave and the infrared bands, with a frequency range of 0.1–10 THz (1 THz = 10^{12} Hz). For a long time, this frequency range has remained underdeveloped compared to the neighboring frequencies due to a lack of powerful, room-temperature-operated, compact sources and detectors. However, over the past few decades, THz research and technology have seen a dramatic shift, evolving from an underdeveloped field to one that now encompasses both fundamental science and commercial implementation. Such progress is driven not only by the evolution of THz generation and detection techniques but also by the demands of a wide range of applications.

Although historically, THz radiation was mainly utilized for astronomy and spectroscopy, after the development of laser-based Terahertz Time-Domain Spectroscopy (THz-TDS) in the 1980s and 1990s [1–4], its applications expanded rapidly. Today a wide range of THz systems and applications have been developed across a broad range of sectors.

The demand for ultra-high data rate wireless communication has been driven by the proliferation of wireless devices and bandwidth-intensive internet applications. By 2023, according to the estimate of Cisco visual networking index report [5], 5G will generate three times as much traffic as 4G, and by 2030, the volume of wireless traffic is predicted to equal or even surpass that of wired services [5]. Consequently, high-precision wireless services will require a peak data rate beyond 100 Gb/s and, in due course, 1 Tb/s [5]. The THz spectrum is a potential alternative for future uses in information and communication technology due to its broad spectrum, which corresponds to high data rate (Shannon-Hartley theorem [6]). Optoelectronic THz communications have greatly accelerated the 6G research, enabling the realization of 100 Gb/s and higher data rates [7]. In 2008, IEEE 802.15 established the THz Interest Group, which led to the development of the first 300 GHz wireless communication standard, IEEE Std.802.15.3d-2017 [5]. With the 2019 World Radio-communication Conferences allowing the identification of frequency bands in the range of 275-450 GHz for use by land-mobile and fixed services applications, standardization of the low-frequency window of the THz band for future wireless communications is a real possibility [8].

THz radiation does not ionize molecules because of its low energy in the millielectronvolt range (~ 4.1 meV at 1 THz [9]). It provides a huge benefit in medical imaging compared to X-

rays, which can cause biological molecules to break down. In addition, the THz energy spectrum encompasses the characteristic energies of biomolecular collective movements such as vibration, rotation, and libration, as well as the low energy of hydrogen bonds, which are prevalent in water-based biomedical samples [10]. Utilizing these qualities, THz radiation has been used to investigate water [11, 12], numerous biological molecules such as nucleic acid [13, 14], amino acids [15], carbohydrates [16, 17], proteins [18] etc., and perform and conduct exhalation and flatus gas spectroscopy to detect Asthma, lung and colon cancers [10]. Using THz sensors and cutting-edge metamaterial technology, researchers have been able to examine a minuscule amount of biological molecules, which has led to advances in the diagnosis of diabetes and other blood or breathing-based medical conditions [10]. THz radiation imaging of cancer is another promising application. THz radiation is particularly well-suited for superficial imaging of soft tissues, where the vast majority of malignancies begin [19]. Researchers have studied diagnostic imaging for several types of cancers, including skin [20], oral [21], gastric [22], and brain [23] cancer. Cheon *et al.*, in search of a cancer-specific fingerprint, discovered a resonant characteristic at 1.65 THz that is believed to originate from methylation DNA and may act as a biomarker for all types of cancer [24]. Demethylation of cancerous DNA aids in the recovery of gene expression, the induction of cell apoptosis, and the diminution of tumor growth [25]. Demethylation utilizing the resonant absorption of high-power THz radiation may generate a comparable effect, hence boosting the efficiency of cancer treatments [26].

Using molecular rotations induced features in the THz range (THz fingerprint), which constitute a material's unique and distinct signature, it is possible to identify various substances [27], even if they are concealed by paper, wood, clothing, or other plastic packaging materials [28]. This method is used to identify explosives such as (2,4,6)-trinitrotoluene (TNT), cyclotetramethylene tetranitramine (HMX), pentaerythritol tetranitrate (PETN), cyclo-1,3,5-trimethylene (RDX), as well as narcotics such as cocaine, crack cocaine, MDMA (commonly known as ecstasy), heroin, amphetamine, carbamazepine, etc. [28]. THz radiation can image concealed weapons during security screening of the human body since it can penetrate clothes and has a higher resolution than microwave radiation without having an ionizing effect [29]. After the successful implementation of SafeView millimeter wave array radar system from Pacific Northwest National Laboratory (PNNL) in airports for body security screening [30], several organizations are now focusing on THz radar security screening systems. Among these are PNNL's subsequently updated L-3 with 350 GHz THz array radar [31], the 670 GHz security screening system of Jet Propulsion Laboratory (JPL) [32], the 3D THz security imaging system of National University of Defense Technology (NUDT), China [33], and the walk-through radar imaging system of Rohde & Schwarz [34].

In recent years, THz non-destructive testing has gained prominence in the industrial setting, particularly in the manufacturing industry, for quality control [35, 36]. THz waves are superior to ultrasonic, X-ray, and infrared testing methods primarily because they are non-contact, non-ionizing, and can propagate through optically opaque materials such as paint coating, fabrics, polymers etc, as well as through air inclusions. THz radiation enables the inspection and identification of flaws in small devices such as integrated circuits [37], structural flaws in concrete [38], contamination and delamination between layers of high-density polyethylene [39], corrosion and damage in copper cables [40], small protrusions in steel [41], etc. In addition, the high sensitivity of THz waves to water and other polar liquids is used to measure moisture content and monitor water intrusion in a variety of construction materials and goods [42] and to detect water vapor in pressurized gas pipelines [43]. THz radiation has also shown promise

for in-line quality monitoring of multilayer paint coatings in the automobile sector [44, 45]. Numerous other disciplines of research, including earth and space science [46–48], fundamental science [49–52], food and agriculture [53], etc., gain significant advantages from THz-based applications.

1.1 Motivation and State of the Art

The demand for efficient THz devices and components has increased at an unprecedented rate due to the wide range of applications in cross-disciplinary sectors. Demand continues to rise as these innovations become more widespread in industry. A standardized characterization system that guarantees the proper operation of the developed devices and components is detrimental to keeping up with this demand. The characterization instruments are crucial at various phases of development and deployment, for instance, in the research and development stage, a system is characterized by validating design simulations and testing specifications of individual components (i.e., amplifiers, filters, antennas, cables, mixers etc.) to ensure that the system as a whole functions as intended. Then, in the manufacturing process, a characterization instrument is utilized to guarantee that all items are consistent with the customer criteria prior to shipment. Furthermore, characterization instruments are also employed in the field for operational system troubleshooting and verification of specifications.

The Spectrum Analyzer (SA) and the Vector Network Analyzer (VNA) are the two main characterization systems available for device development and characterization at the lower end of the THz spectrum, where it overlaps with the millimeter wave and microwave bands. An SA determines the frequency, power, distortion, harmonics, bandwidth, and other spectral aspects of an incoming signal. In contrast, a VNA characterizes and measures the response of a device or network to determine how it operates inside the Radio Frequency (RF) circuit for which it is designed. This thesis focuses on realization of a THz-VNA using a photonic approach.

The function of a VNA is to determine the frequency-domain amplitude and phase of an electromagnetic signal that is reflected, transmitted or scattered by a Device Under Test (DUT). Typically, frequency coverage is attained by sweeping the frequency over the whole band while capturing well-established characteristics, such as frequency-dependent Scattering (S)-parameters. The S -parameters fundamentally represent the transmission and reflection coefficients which describe how the incident signal interacts with the DUT. A calibration process eradicates the systematic error of the measurement and cancels the influence of the system components. The calibrated S -parameters are either employed to create a physically sensible equivalent circuit or compared to the simulation-predicted theoretical performance. This enables the understanding of how various components impact the performance of the device, therefore providing useful information about potential design flaws and facilitating the improvement of the device layout and components. Measurements of S -parameters also help researchers test and characterize new sensor technologies [54, 55], quantify the transmission of electromagnetic waves through antennas and propagation media [56–58], and assess the electromagnetic characteristics of novel materials [59–61].

The VNA is the most sophisticated, high-precision system available to date for device characterization in the microwave, millimeter wave and lower end of the THz range. Although 110 GHz VNAs are commercially available [62], contemporary VNAs primarily operate at frequencies between 40-65 GHz [63, 64]. To a large extent, this is owing to the fact that, at frequencies exceeding 100 GHz, the electronic components, such as oscillators and amplifiers

of the VNA, become inefficient and prohibitively costly. Frequency extender modules [65] are therefore implemented to characterize networks or devices operating above f_m ($\approx 40\text{-}65$ GHz) of the VNA. These extenders use Schottky diode-based frequency doublers and triplers in a hollow core metallic waveguide design to achieve a frequency $f = N \times f_m$. These components are employed on both the transmitter (for up-conversion) and receiver (for down-conversion) sides of the configuration. The hollow metallic waveguides are utilized to reject out-of-band noise and simultaneously enable the incorporation of the planar Schottky diodes with transitions to microstrip waveguides or similar.

The bandwidth of the frequency-extended system is constrained due to the hollow metallic waveguides, which feature cut-offs at both low and high frequencies caused by waveguide cut-off and commencement of multimodal behavior, respectively. This limits their tuning range to less than 50% of the center frequency. For instance, a WR3.4 waveguide extender with a 265 GHz center frequency can only be swept between 200 and 330 GHz. Consequently, a broad frequency range analysis necessitates the exchange of the entire extender setup, accompanied by alignment and rigorous calibration steps. A frequency sweep from 110 GHz to 1.5 THz requires a minimum of eight extenders [65], possibly more, to guarantee the overlap of the individual bands. Therefore, the exchange, realignment and recalibration process must be repeated several times. This drastically complicates and lengthens the measurement process. In addition, the system becomes progressively more expensive as additional extensions are added.

Losses due to surface roughness and restrictions owing to manufacturing tolerances in hollow metallic waveguides already cause problems in the microwave range, and these issues become even more pronounced in the THz range. The physical dimensions of the components decrease when the operating frequency of a standard rectangular waveguide approaches THz frequencies, and micromachining waveguides and directional couplers at these minuscule dimensions become increasingly challenging [66]. Measurement uncertainty is also prompted by other factors, such as the repeatability of the waveguide flange connections [67, 68], the impact of flexures on Local Oscillator (LO) signal cables [68, 69], and so on. Additionally, as the dimensions of the Ground-Source-Ground (GSG) probes get smaller to meet the necessary standards, the probe tips become more fragile and more susceptible to losses and inadequacies from misalignment.

The tiny dimensions of metal waveguides and the misalignment of waveguide flanges both contribute to the repeatability and stability issues of the calibration process [70]. At THz frequencies, the calibration equipment also requires to be very small. In the 0.75–1.1 THz range, for instance, metal shims (thin sheets of metal with $\lambda_{THz}/4$ thickness, in which the waveguide aperture is constructed) need to have a thickness of around 100 μm in order to actuate the *line* standard [71]. Such thin metal shims are exceedingly brittle, making them difficult to fabricate and handle and are susceptible to deterioration over time [69]. Also, their precision is restricted by the exact mechanical tolerances that impact THz waveguide flanges. Occasionally this leads to the implementation of less-than-ideal calibration techniques with a finite scaling constraint eventually leading to fragility issues with higher frequencies. Fabrication tolerances also limit the use of alternative calibration methods that entail well-known calibration standards and preclude the establishment of traceability to the International System of Units (SI) for S -parameter measurements [71, 72].

The conversion efficiency of Schottky diodes drops at higher THz frequencies f_{THz} due to their RC roll-off. This is especially apparent above ~ 400 GHz when the efficiency declines according to a power law at least as steep as f_{THz}^{-2} .

The majority of VNAs currently employ horn antennas to couple out to free space for accessing bands over a few 100 GHz [73–75]. In this regard, there is essentially no benefit over a photonic system that immediately emits a free space THz beam.

The lack of efficient characterization tools in the THz range impedes development by complicating and lengthening the optimization and engineering processes. Furthermore, the high cost of the characterization instrument means that the developed systems remain pricey, which slows down the process of widespread industrial adoption. This compels the engineers to rely solely on simulations to define the overall device performance, preventing them from gaining any insight into the role of individual components. THz technology is now transitioning from laboratory research to commercial applications. An efficient and cost-effective characterization system is essential not only for this transition but also for the future engineering of THz devices and components with vast bandwidth and power.

The maximum frequency that the commercially available frequency-extension modules of VNA can reach is 1.5 THz [65]. Due to the aforementioned challenges with manufacturing tolerances, increased scattering by surface roughness of hollow metallic waveguides, etc., it is difficult to upscale the existing technology. Substituting electrical systems with photonic systems is a promising alternative to tackle these problems and achieve a broad frequency coverage. THz sources and receivers based on a photonic approach have seen huge improvements over the course of the past decade, making them an ideal choice for Photonic Vector Network Analyzer (PVNA) concept implementations. A standard technique for generating and detecting THz radiation with a broad bandwidth is photoconductor-based devices driven by an ultrafast laser, which can be implemented to configure systems reaching up to 6.5 THz [76,77] or, recently, 10 THz [78].

In pulsed operation, a photoconductive device consists of a highly resistive semiconductor with two metallic contacts separated by a photoconductive gap. An ultrafast (\sim fs) laser pulse with photon energy greater than the bandgap of the semiconductor illuminates the gap, generating free carriers, which alters the conductance of the photoconductor at the same time scale. By applying a DC bias, the free carriers are accelerated, which gives rise to a photocurrent with THz components that emerges from the fs-scale turn on of the current. The time-domain profile of this photocurrent is a narrow pulse with a sub-picosecond scale duration; this corresponds to a broad THz spectrum with numerous frequency components. Consequently, pulsed THz radiation is emitted as a result of this photocurrent driving the antenna. At the receiving end, another photoconductive antenna receives the THz field and induces an electric field in the active region between the antenna arms. A laser pulse with a fixed time delay modulates the conductivity of the receiver in a manner similar to the source. This causes a mixing process with a DC component proportional to the received THz field strength convoluted with the optical pulse. Scanning the time delay between the arrival of the THz signal and the optical pulse allows the entire THz waveform to be resolved [79–81].

Pulsed photoconductors are often implemented for the configuration of THz-TDS systems that explore the optical characteristics of materials or components across a broad frequency range [82–87]. A THz-TDS system is typically set up in transmission or reflection geometry. It captures the amplitude and phase information of the THz field transmitted through or reflected by the sample, providing the transmission or reflection coefficients analogous to the S_{21} and S_{11} parameters of the DUT or Material Under Test (MUT).

To date, several studies have been published demonstrating THz-TDS systems for extracting one or two vector S -parameters of devices or materials. In 2015, Ramer *et al.* reported a THz-

TDS-based VNA and used it to measure S_{21} parameter of several H band (220-330 GHz) amplifiers and a W band (75-110 GHz) amplifier [88,89]. In this case, the THz signal is coupled using input and output rectangular waveguides with horn antennas, which are incorporated in the packaged DUT. Bieker *et al.* deployed a similar setup to realize a one-port VNA with electro-optic detection [90] by employing wire-bonds for connection to the DUT [91]. These systems are not entirely free space, therefore, are limited by the narrow bandwidth of the metallic waveguides. Cui *et al.* presented a proof of concept for the configuration of a one-port quasi-optical VNA in reference [92], demonstrating that it is possible to build a photonic-based VNA employing quasi-optical components for beam guiding. Mueh *et al.* reported on the calibration process for THz-TDS systems to measure S -parameters and verified the technique by determining S_{21} and S_{11} parameters of a known Sapphire wafer [93]. This system is incapable of determining the complete set of S -parameters in a single measurement step and, therefore, requires reversing the sample and repeated measurements in order to ascertain the comprehensive characteristics of the sample. This causes an increase in measurement time and uncertainty owing to potential changes in setup between consecutive measurement steps.

1.2 Research Objectives and Overview

The main objective of the thesis is to develop a powerful yet affordable characterization system capable of characterizing THz components up to several THz in a single setup based on a photonic approach to create a solid basis for THz component engineering. The system should have the following attributes:

- Telecom wavelength compatibility and the ability to operate at room temperature
- A dynamic range comparable to that of electronic systems
- A bandwidth of several THz (ideally ~ 4 THz) in a single setup without the requirement of multiple exchanges, alignment and calibration steps for broadband investigation
- Simple calibration routine and
- The capability to measure a complete set of S -parameters simultaneously.

The thesis is composed of three parts. The first part, comprised of Chapters 2 and 3, covers existing characterization systems in the THz range, and presents system design and data evaluation methods for constructing broadband PVNAs, respectively. In the second part, which consists of Chapters 4 and 5, these characterization systems are configured and implemented for a variety of applications in order to demonstrate their capability. Chapter 6 represents the third part, which pursues miniaturizing the characterization systems for on-chip integration and industrial implementation. The following outline constitutes the framework of the thesis.

Chapter 2 reviews the prevalent electrical and photonic characterization systems for broadband THz-range analysis. We start with the basics of network analysis using S -parameters and then discuss the system architecture of typical and frequency-extended VNAs, which is the standard systems for characterization in the electronic domain. This is followed by common measurement errors of the THz VNA and the conventional calibration procedures used to correct them. The fundamentals of THz generation and detection using the photomixing technique are presented. Since the main scope of the thesis is photonic systems under pulsed operation,

we focus on THz-TDS, a widely used photonic characterization system in the THz range. This part addresses standard THz-TDS configurations, their operating principle, system parameters, error sources, and the calibration procedure. In addition, we evaluate state-of-the-art photonic systems against commercially accessible VNAs.

Chapter 3 presents the system architecture, calibration and data evaluation techniques for proposed PVNAs. The system architecture covers the technologies and components that enable the photonic characterization tools to be realized. Time-domain measurements are conducted for pulsed PVNAs, as opposed to the frequency-domain measurements used for Electronic Vector Network Analyzers (E VNAs). This results in a deviation from standard calibration and data assessment practices, which are discussed in detail later in the chapter.

Chapter 4 discusses a 1.5 port Vector Spectrometer (VSM), a multiport photonic characterization system that can simultaneously characterize both transmission and reflection coefficients of a device or material. This chapter delves further into the system's features and two main applications: characterization of a nonreciprocal device and determination of optical properties, including refractive index, absorption coefficient, and thickness of several materials.

Chapter 5 covers a two-port PVNA that extracts a complete set of S -parameters from the devices or materials being tested. The system characteristics are investigated, and the performance of the system is verified by characterizing several THz components. The derived S -parameters are also utilized to calculate the complex permittivity and thickness of several materials. In addition, the pulsed two-port PVNA is compared to its Continuous Wave (CW) and electronic counterparts in terms of system characteristics and observed S -parameters of test components.

With the aim of making the above mentioned photonic systems more compact, we developed a transceiver containing both transmitter and receiver modules integrated into the same chip. The fabrication method, design, and packaging of these devices are detailed in Chapter 6. The transceiver is also deployed in a one-port PVNA configuration, and several THz components are characterized to evaluate its performance in setting up photonic characterization systems.

Chapter 7 concludes with a summary of the main findings of the thesis and a discussion of future work that may be done to enhance THz characterization systems further.

State-of-the-Art Characterization Systems in THz Range

For the design and development of electrical and photonic devices and components, it is necessary to comprehend how a device and its constituent parts interact with incoming signals. This information is obtained by describing the device in terms of well-established characteristic parameters, like Scattering (S)-parameters and comparing them to a simulation or an equivalent circuit. Through this review, engineers can assess the performance of various components and identify areas for improvement, which subsequently helps them to identify design flaws and develop devices with close-to-ideal response. The characterization of different elements, as well as the complex system in the THz range, can be carried out by an electronic approach that utilizes the local oscillator of a Radio Frequency (RF) Vector Network Analyzer (VNA), and a chain of frequency multipliers to upconvert the RF signal to the THz range where it interacts with the Device Under Test (DUT) and then down-convert it back to the RF signal on the receiver side. Alternatively, a photonic approach can be implemented that uses laser signals that contain a THz beat note or even a broad THz spectral width as local oscillators and photomixers that down-convert the optical signal to the THz range. In this chapter, we discuss the available characterization tools in the electronic and photonic domains for investigating devices and components operating in the THz range.

2.1 Electronic Characterization System: The VNA

2.1.1 Network Analysis Basics and Scattering Parameters

In RF engineering, Network Analyzers (NAs) are widely implemented to execute accurate and efficient analysis of circuits or networks such as filters, amplifiers and even complex modules. It is used in research and development for verification of component designs and specifications, in manufacturing lines for quality control and in field operations to verify and troubleshoot deployed systems. Some of the applications of NAs include detecting invisible material de-

fects [94, 95], perform antenna measurements in Radar systems [96, 97], determine material permittivity [98] etc.

A sinusoidal test signal generated from the analyzer is applied to the DUT, and then the DUT response is recorded. A scalar network analyzer measures the amplitude difference between the stimulus and response waves, whereas the vector network analyzer measures both amplitude and phase difference. Vector measurement consisting of both amplitude and phase information, despite of more complex implementation, is preferred due to several advantages:

- Total systematic error compensation (Vector error correction) is feasible [99].
- Can be transformed into the time domain for interpolation and data processing.
- Fully characterizes a linear network and ensures distortion-free transmission.
- Can be implemented to design efficient matching networks, which requires measuring the complex impedance.
- Accurately allows to verify models in Computer-Aided Engineering (CAE) circuit simulation.

A VNA can be used to characterize one, two- or multi-port networks in terms of so-called wave quantities. A one port network is depicted in Figure 2.1(a), where a is the amplitude of the incident wave that propagates from the VNA to the DUT, and b is the amplitude of the reflected wave traveling in the opposite direction from DUT to the VNA. The power traveling to the one-port network is given by $|a|^2$, and the power it reflects by $|b|^2$. The field reflection coefficient is the ratio of the reflected wave to the incident wave and is given by,

$$\Gamma = \frac{b}{a} = \rho \exp(j\phi_r) = \frac{Z_L - Z_0}{Z_L + Z_0} \quad (2.1)$$

where Z_L = load impedance, Z_0 = feeder characteristic impedance and $\rho = |\Gamma|$. For instance, when a transmission line terminated by a lumped element with an impedance corresponding to the characteristic impedance ($Z_L = Z_0$), all energy is transferred to the load ($b = 0$ and $\rho = 0$), and when the load impedance is a short or open circuit ($Z_0 = 0$ or ∞), it results in all the energy being reflected ($\rho = 1$).

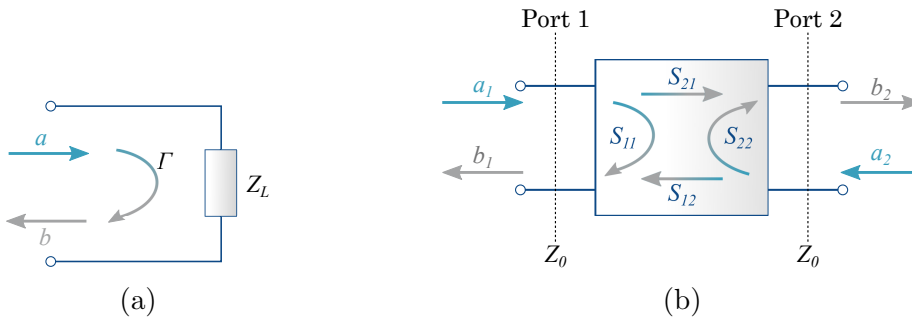


Figure 2.1: (a) A one-port network with incident and reflected wave. (b) A two-port network with all S -parameters.

In a two-port network, in addition to reflections at both ports, transmission measurements in the forward and reverse directions are also possible. S -parameters are usually the preferred choice for characterizing a network or DUT [100–102]. They describe how the incident energy from a port is scattered by the network and exits through the other or the same port. A two-port VNA has four complex and frequency-dependent S -parameters, as illustrated in Figure 2.1(b).

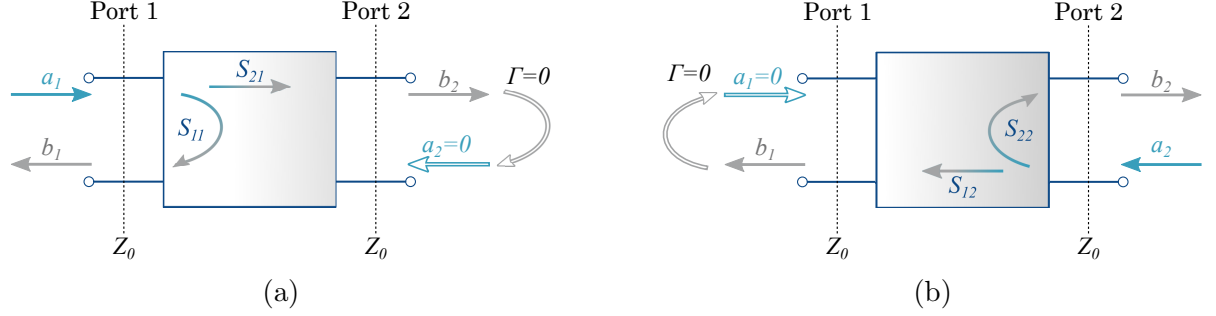


Figure 2.2: S -parameter measurement for (a) forward and (b) backward propagations.

For the forward measurement, as shown in Figure 2.2(a), the internal source of the network analyzer excites an incident wave on port 1, namely a_1 . Now b_1 and b_2 , the outgoing waves from the DUT, can be measured, which allows for the determination of S_{11} and S_{21} , provided that a reflection-free termination $\Gamma = 0$ (match) is used on port 2. This also means that there is no incoming signal from port 2, i.e. $a_2 = 0$.

$$S_{21} = \frac{b_2}{a_1} \quad S_{11} = \frac{b_1}{a_1} \quad (2.2)$$

For backward measurement (Figure 2.2(b)), port 2 is excited with an incident wave a_2 , and a match ($\Gamma = 0$) is used on port 1, resulting in no input signal from port 1 ($a_1 = 0$).

$$S_{12} = \frac{b_1}{a_2} \quad S_{22} = \frac{b_2}{a_2} \quad (2.3)$$

Here, S_{11} and S_{22} are equal to the reflection coefficients Γ for the respective ports, and S_{21} and S_{12} are the forward and reverse transmission coefficients, respectively. It is crucial to use the appropriate characteristic impedances to terminate each port of the DUT, which prevents undesired reflections and ensures that the DUT is only excited by one incident wave. In practice, both incident waves are non-zero ($a_1 \neq 0$ and $a_2 \neq 0$), and in that case, it can be considered as a superposition of the two measurement situations ($a_1 = 0, a_2 \neq 0$ and $a_1 \neq 0, a_2 = 0$). Then the characteristics of a network can be expressed by a series of linear equations as

$$b_1 = S_{11}a_1 + S_{12}a_2 \quad b_2 = S_{21}a_1 + S_{22}a_2 \quad (2.4)$$

The S parameters can be grouped and written in a matrix format to obtain the wave quantities as

$$\begin{bmatrix} b_1 \\ b_2 \end{bmatrix} = \begin{bmatrix} S_{11} & S_{12} \\ S_{21} & S_{22} \end{bmatrix} \begin{bmatrix} a_1 \\ a_2 \end{bmatrix} \quad (2.5)$$

The S -matrix is a linear model of the DUT, where its diagonal elements (S_{11} and S_{22}) represent the reflection coefficients of each port and the remaining elements (S_{21} and S_{12}) characterize all possible signal transmission paths between the ports. Since S -parameters are typically functions of frequency, the set of linear equations must be solved one frequency at a time. A discussion of the general properties of the S -matrix can be found in Reference [103].

The S -parameters are intrinsic characteristics of the DUT, independent of the measurement instrumentation and not reliant on the incident power employed in the measurement (linearity condition). A number of additional parameters can be calculated from the S -parameters of a DUT. For example, the time domain S -parameters can be extracted by inverse Fourier transform [104] or the propagation delay of the DUT can be determined by plotting the transmission phase against frequency [105]. S -parameters are frequently used to derive material permittivity [59, 60].

2.1.2 System Architecture of a VNA

To provide a general overview, a simplified block diagram of a typical VNA is illustrated in Figure 2.3. The figure demonstrates the fundamental building blocks of the VNA, which include signal source, test set, receivers, processor and display. Although far more complex, any VNA nonetheless comprises these fundamental components. In this section, we review the works presented in the References [99] and [106].

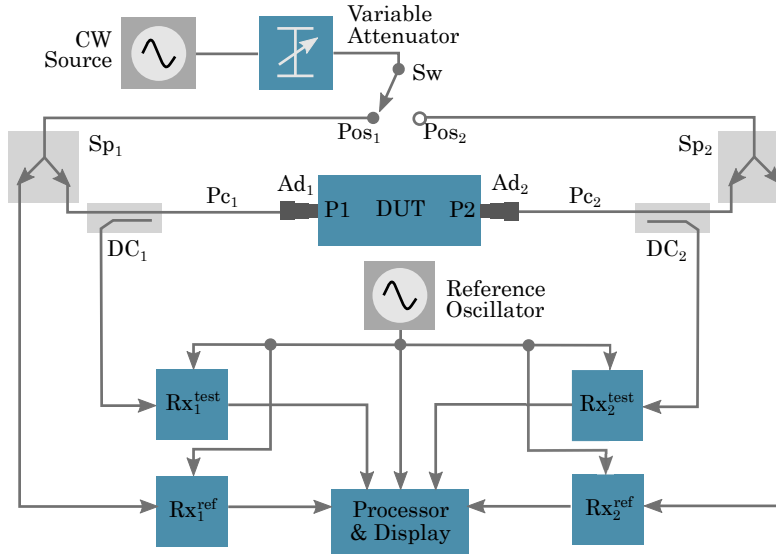


Figure 2.3: Block diagram of a typical VNA architecture. Recreated and adapted from [106].

A VNA typically uses a built-in Continuous Wave (CW) signal source to provide the RF signal to the DUT. The source switch controls which test port the signal will travel through. In the case of high-performance VNAs, two built-in sources are used, which are advantageous for applications such as mixer tests [107] or amplifier intermodulation tests [108]. In the mixer test, one of the sources provides the RF signal and the other functions as a local oscillator (LO).

The test sets distinguish between the incident reference signal and the emerging transmitted or reflected (test) signals and guide them towards the specific port and the receiver, respectively. The test sets are also used to extract a sample of the incident wave and direct it to the receivers via the reference channel, which is essential for the phase reference. Generally, directional couplers or two resistor power dividers are implemented as test sets in VNAs [99].

The VNA consists of two separate receivers – one for the measurement or test channel and the other for the reference channel. The received test and reference signals form the basis of the S -parameter measurement. The processor and display block corrects the system errors of the raw measurement data received from the receiver unit and processes them to display the results in a variety of formats, including Smith chart, Cartesian format, and real and imaginary values. This VNA unit serves as the human-machine interface, providing control, usability, and user-friendly displays, which are essential features of contemporary test instruments.

Figure 2.3 illustrates the fundamental operating principle of a standard VNA. The switch Sw is at position Pos_1 , implying that the test signal generated from the variable frequency source is guided towards port 1 ($P1$) of the DUT at a specific power determined by the variable attenuator. Splitter Sp_1 splits the signal into two paths. One path (reference channel) feeds the reference signal to the reference receiver. In contrast, the other path (test channel) guides the test signal towards $P1$ of the DUT through a directional coupler DC_1 connected using the external connection adapter Ad_1 and the precision cable Pc_1 . DC_1 distinguishes the signal reflected from $P1$ and sends it to test receiver Rx_1^{test} . The signal transmitted through the DUT emerges from port 2 ($P2$) and is then guided by the other directional coupler DC_2 towards the second test receiver Rx_2^{test} . The receivers share a common reference oscillator and can measure both amplitude and phase information due to the reference signal provided by means of the reference channel. All the detected complex signals are fed to the processing unit for mathematical processing to calculate and present S_{21} and S_{11} parameters. Similarly, setting the Sw to position 2, S_{12} and S_{22} parameters are calculated.

2.1.3 THz VNA Architecture

State-of-the-art VNAs predominantly operate up to 40-67 GHz [63, 64]. This is mainly because electronic components, including oscillators and amplifiers implemented in the VNA, become inefficient and expensive above 100 GHz. For the characterization of networks or devices in the THz range frequency extender modules are implemented [65], which contain Schottky diodes based frequency multipliers, similar to those described in [109]. Also, ports consisting mainly of coaxial cables and connectors in low frequencies are replaced by rectangular metallic waveguides above 100 GHz, where established standards for waveguide sizes and interconnecting flange specifications are available [110]. Detailed reviews about waveguide dimensions and flange designs for THz frequencies can be found in References [67, 111, 112]. Depending on the requirements of the DUT, the VNAs can also be implemented in a free-space configuration where the signal is launched into the air with the help of horn antennas. The free-space measurement technique is prevalent for dielectric property investigation due to its non-contact, non-destructive and broadband properties [59, 113–115]. The ports are defined electrically and physically in VNA application environment to provide the measurement reference planes.

Figure 2.4 depicts the frequency extender configuration employed to generate and detect THz signals in addition to the RF or Electronic Vector Network Analyzer (EVNA). The working principle described here is the revision of the reference [116]. The EVNA generates two signals:

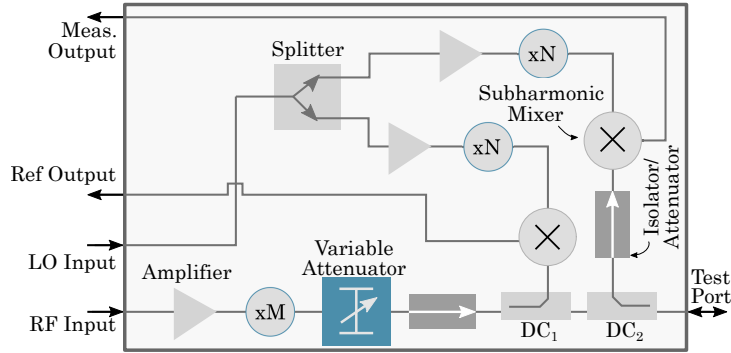


Figure 2.4: Frequency extender configuration to perform THz measurements with RF VNA. Adapted from [116].

the RF signal, which is fed to the RF input of the extender module, and the local oscillator (LO), which is fed to the LO input. A slight frequency offset is introduced between the RF and LO signals to generate an intermediate frequency (IF) signal (heterodyne concept), which the VNA then measures. Both the RF and LO signals are amplified and then up-converted to higher frequencies by a series of full waveguide band frequency multipliers. A couple of directional couplers DC_1 and DC_2 are used to separate and guide the signal power. DC_1 samples the incident (reference) signal, whereas DC_2 samples the signal emerging from the test port (test signal). The test signal can either be the signal transmitted by this module and reflected from the DUT, which forms the basis for the S_{11} parameter calculation, or the signal that is transmitted by another module and has propagated through the DUT, which forms the basis for the calculation of S_{21} parameter.

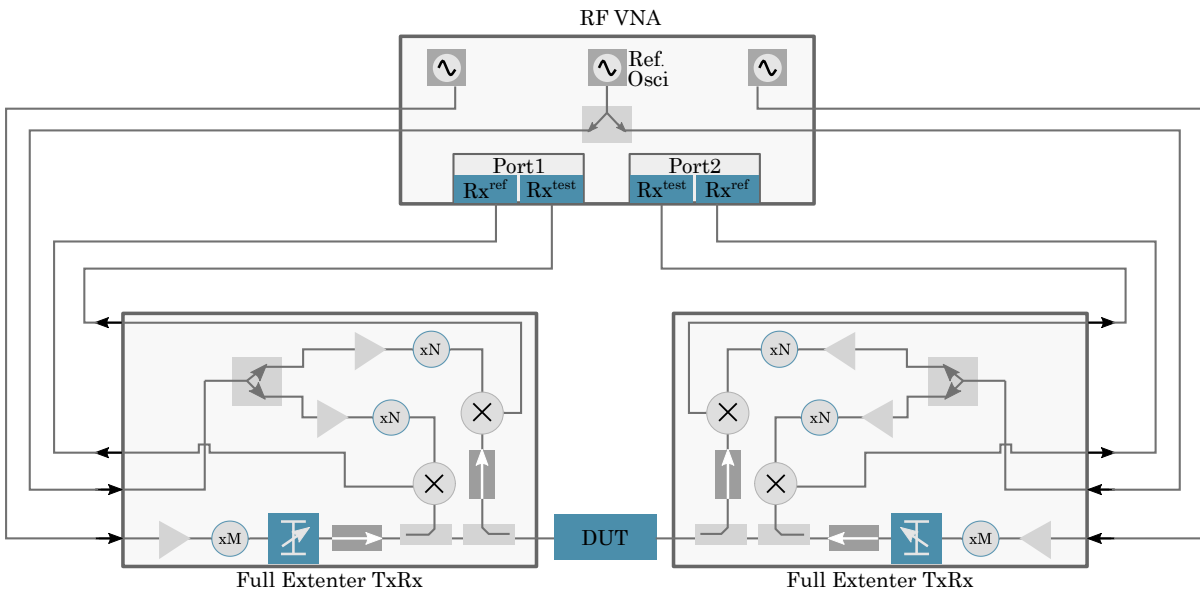


Figure 2.5: Block diagram of THz measurement setup of THz VNA demonstrating the connection of EVNA with frequency extenders [65].

The reference and the test signals must be down-converted to IF before feeding it to the EVNA, where their magnitude and the phase can be directly sampled (digitized) as the phase relationship between the signals is retained in frequency translation. This is achieved by two subharmonic mixers, which permit a lower LO frequency [116, 117]. Details on subharmonic mixers for THz detection are described in [118, 119] and the advantages of heterodyne detection and their application in the THz range can be found in [120–122]. Figure 2.5 depicts a two-port VNA configuration with frequency extenders for the characterization of a DUT in the THz range.

2.1.4 Measurement Errors

The typical VNA architecture described above inherently introduces errors that can be divided into three categories - systematic, random, and drift errors [123]. Among these, random and drift errors are non-repeatable and, therefore, very difficult to be quantified and eradicated. The random and drift error sources include variations due to noise, frequency and temperature drift, and other physical changes that may take place in the setup between the calibration and the measurement. In contrast, systematic error sources such as measurement signal path loss, internal reflections, different port impedances, phase shifts, imbalance in the directional couplers etc., are repeatable and can be measured. However, only if each of these sources of error continues to be linear, it is possible to aggregate them into a reduced set of systematic errors that are relatively simple to eliminate using a calibration technique.

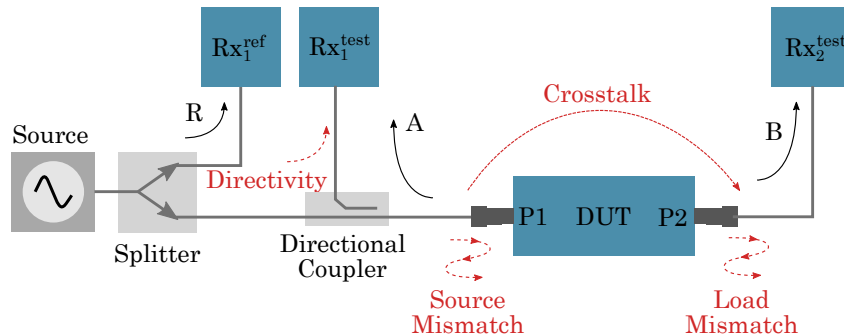


Figure 2.6: Systematic measurement errors. Reflection tracking is calculated by A/R and transmission tracking by B/R . Adapted from [124].

Figure 2.6 depicts significant sources of systematic errors for a VNA, which are described below [124, 125]:

Directivity is a property of the directional coupler and is defined as the ratio of signal through the coupled path to the signal coupled through the uncoupled path. The error originates from the fraction of the source signal that never reaches the DUT.

Cross-talk (Isolation) is a measure of internal signal leakage around the signal path that may be present in the system.

Source match is the return loss of a driving port due to multiple internal reflections between the source and the DUT.

Load match describes the return loss of a terminating port.

Reflection Tracking refers to the frequency response of a reflect measurement, including loss behaviors resulting from the couplers, transmission lines, converters, and other components. From Figure 2.6, reflection tracking is calculated by A/R .

Transmission Tracking describes the frequency response for the transmission paths. From Figure 2.6, transmission tracking is calculated by B/R . Various error models based on the above-mentioned error terms have been developed for one- and two-port VNAs to standardize the calibration process, which can also be used in the THz range [126].

2.1.5 Calibration

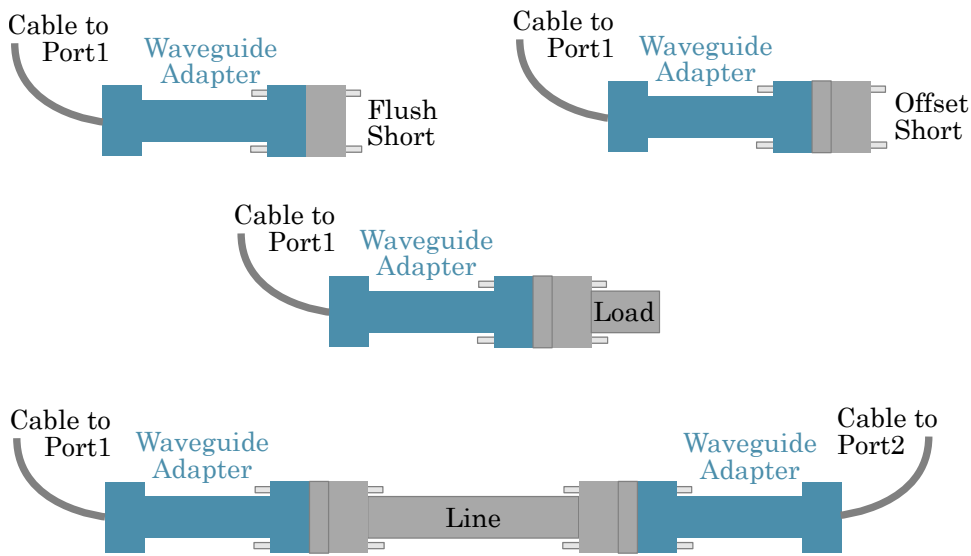


Figure 2.7: Calibration standards. Adapted from [106].

Various calibration techniques have been developed for error minimization in EVNA measurements, which require transmission, reflection and isolation tests. Generally the calibration procedure entails comparing established standards with measured results of the instrument to evaluate and remove systematic errors associated with the test setup [127]. The one port standards include *short*, *open*, *load* and *sliding load*. In addition to those, two-port calibration includes the *line* or a *reciprocal network* standard [128]. The graphical representation of these standards, except for the *reciprocal network*, is depicted in Figure 2.7. For *reciprocal network*, the reciprocity condition of $S_{21} = S_{12}$, must be satisfied. During calibration, the *reciprocal network* can be employed as an unknown *through* [128]. This section reviews some of the well-established calibration procedures for a two-port VNA [128].

The ‘*Short-Open-Load-Through*’ (SOLT) [129] calibration technique utilizes three one port standards (*short*, *open*, *load*) on both test ports and a *through* (direct connection) standard that identifies transmission error coefficients. Due to the radiation effects at the open end of the waveguide, an *offset short* with an offset length of $\lambda/4$ is used instead of the *open* standard in waveguide systems. The standards of this particular technique are redundant as one of the *load* standards determines the reference impedance of the whole. However, the accuracy of this

method which is heavily reliant on the accurate definition of standards, can be improved by upgrading calibration standard models [130, 131] or utilizing standards already characterized by a reference calibration [132].

A more accurate and suitable waveguide configuration is the ‘*Through-Reflect-Line*’ (TRL) technique [133], which involves a *line*, one port *reflect* of unknown reflection and a *through*. The *line* standard is realized by implementing a $\lambda_m/4$ long waveguide line, where λ_m is the center wavelength of the waveguide band, resulting in a phase change across the whole band. The *through* standard is attained by directly connecting the reference planes to form a zero transmission loss and delay path. The advantage of this technique stems from the fact that for this method, only *through* calibration standard requires prior knowledge of the waveguide property, and this standard can be easily actualized in a genderless interconnection environment like rectangular waveguides. The bandwidth of the *line* standard, which is realized by a short waveguide section, is somewhat restricted in the TRL method since the signal phase difference between the line and through standards must obtain a value of $m\pi$, where m is an integer. This is particularly problematic in the THz range as the waveguide length for *line* standard required at 1 THz is $\sim 100 \mu\text{m}$ [117, 134]. However, TRL calibration can still be implemented in mm-wave and sub-THz range where the waveguide line lengths greater than 1 mm is feasible. The waveguide dimensions required for different *line* standards for the sub-THz band in a TRL technique are discussed in [134].

‘*Line-Reflect-Line*’ (LRL) [135] is used to circumvent the shortcomings of the TRL technique in the THz band by substituting a second *line* for the *through* standard. This technique does not require the phase shift between two lines to be precisely $m\pi$, allowing the implementation of longer line lengths [136]. Similar to the TRL technique, the electrical properties (delay and loss) of the first *line* standard in the LRL method must be known accurately.

The selection of calibration techniques is less straightforward for frequencies close to 1 THz and beyond. The very short length ($\sim 100 \mu\text{m}$ at 1 THz) of *line* standard manifests practical problems such as manufacturing, alignment and strain tolerances in the TRL method, while the LRL technique is also not very favorable due to its requirement of prior information on the *line* properties. For these reasons, some manufacturers still provide the SOLT calibration scheme till 1.1 THz [65]. TRL still is the more accurate method, and by accepting a reduction in the useful bandwidth of the *line* standard, TRL calibration in the 0.75 – 1.1 THz range is feasible [71, 134]. In addition to these techniques, multiline methods are also effectively implemented [137, 138]. Further in-depth analyses of the performance of several VNA calibration approaches at THz frequencies are discussed in References [139] and [140]. Moreover, VNA measurements around and above 1 THz are susceptible to additional complications mostly linked to the decreasing physical size of the waveguides used to implement the measuring ports. Among them, repeatability of the waveguide interfaces introduces a significant random error, which is the dominant factor of inaccuracy in measurements [141–143].

For the scope of this thesis, calibration of THz VNAs in free space configuration is particularly vital. In such configurations, horn antennas are usually implemented to transmit and receive the THz signal in free space. In general, self-calibration procedures are advantageous for this type of setup [144]. Among the techniques discussed before, TRL [145] and ‘*Through-Reflect-Match*’ (TRM) [146] are the most common calibration methods that are implemented in free space investigation. In this case, the *reflect* standard is realized with a metal plate, and the *match* standard requires an absorber. There are certain drawbacks to TRL and TRM: TRL requires precise positioning of the antenna to achieve defined separations with the Ma-

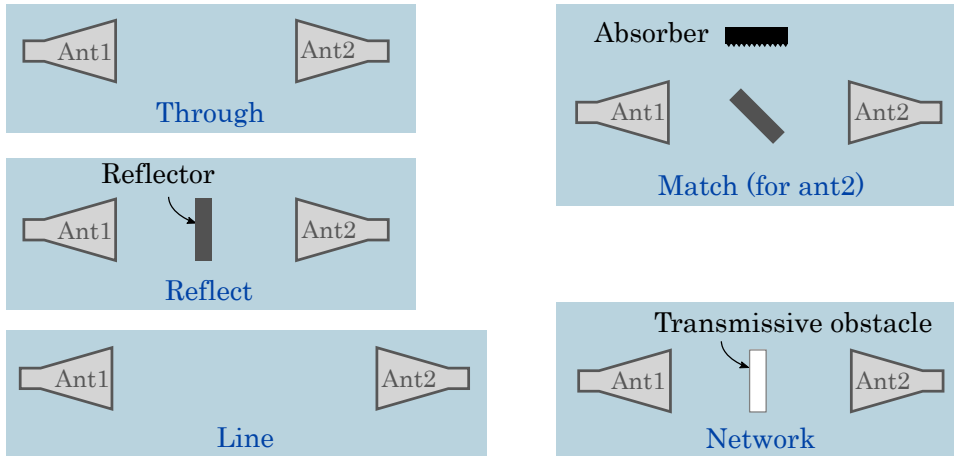


Figure 2.8: Calibration standards for free space VNA configuration. Antenna 1 (Ant1) is connected to port 1 and Antenna 2 (Ant2) is connected to port 2 of the VNA.

terial Under Test (MUT) for the *line* standard, and TRM requires a well-matched broadband absorber. These limitations can be addressed by implementing ‘*Line-Network-Network*’ (LNN) (transmissive) [147] and ‘*Line-Reflect-Reflect*’ (LRR) [148] (reflective) methods. An obstacle network must be positioned in three consecutive positions to perform the LNN construction. While a transmissive obstacle is necessary for LNN, LRR requires a non-transmissive or weakly transmissive obstruction. Rolfes *et al.* describe these methods and propose different variations for improved accuracy in [144].

Another free space calibration technique is ‘*Gated-Reflect-Line*’ (GRL) [149], which in contrast to other popular methods, only requires two standards. It is realized by time-gated (*gated*) measurements of an empty fixture (*line*) and a metal plate (*reflect*).

‘*Through-Line-Network*’ (TLN) [150] is an additional calibration technique very similar to TRL, only in this case, instead of the *reflect* standard, it uses a symmetrical and *reciprocal network* as the third standard. A variation of this technique is the ‘*Through-Through-Network*’ (TTN) [151, 152] method, which eradicates the limitation of the *line* standard by using a neighboring frequency point to achieve variation in the geometrical length. A slight frequency shift alters the electrical length comparable with the change in the mechanical length under the assumption that the measurement setup exhibits a flat frequency response [152]. Various other free space VNA calibration techniques are also reported recently, including ‘*Short-Open-Load-Reciprocal*’ (SOLR) [153], Standard Load [154] etc.

2.1.6 State-of-the-Art THz VNA

The first VNA operating in the THz range was reported in 1990. Goy *et al.* described in [155, 156] a Schottky diode-based THz generator and detector that uses a Gunn oscillator for frequency multiplication. This was later patented and commercialized by AB millimeter LTD. This sub-THz VNA could function in the 8-180 GHz range without requiring frequency extenders. However, one and two Gunn oscillators were employed for the 180-500 GHz and 500-800 GHz bands. For more than two decades, millimeter wave VNAs operating up to 352 GHz [157] have been available commercially, which use ‘millimeter-wave extender heads’ in

conjunction with the EVNA. This extender module comprises harmonic multipliers for generation and sub-harmonic mixers for down-converting the reference and test signals. Nowadays, commercial VNAs, by implementing frequency multipliers, can reach up to 1.5 THz [65, 158]. The development of frequency multipliers and associated components for frequency extension modules is an active field of study, with frequency multiplier chains generating in the 1.7-1.9 THz range has yet been demonstrated [159]. However, at higher THz frequencies manufacturing tolerances and higher loss due to surface roughness associated with the metallic structures makes this development process extremely challenging.

Waveguide Band	Frequency Coverage (GHz)	Dynamic Range (BW = 10 Hz, dB)	
		Typical	Minimum
WR3.4	220-330	115	105
WM-710 (WR2.8)	260-400	100	80
WM-570 (WR2.2)	330-500	110	100
WM-380 (WR1.5)	500-750	100	80
WM-380 (WR1.5) Mini	500-750	110	95
WM-250 (WR1.0)	750-1100	65	45
WM-250 (WR1.0) Mini	750-1100	95	75
WM-164 (WR0.65)	1100-1500	60	40

Table 2.1: Specifications of EVNA extenders from Virginia Diodes, Inc. [65].

Table 2.1 details the frequency extenders required to cover the range from 110 GHz to 1.5 THz with their corresponding Dynamic Range (DNR). The commercial VNAs extenders can attain a maximum peak DNR of ~ 120 dB for lower frequencies (110 – 220 GHz) [65], which declines drastically to 60 dB for the 1.1-1.5 THz band. This is owing to the fact that, as frequency increases, the manufacturing and alignment tolerances of the hollow metallic waveguides become more prominent, and the conversion efficiency of Schottky diodes decreases due to RC roll-off.

With the development in the field of THz radiation, the demand for broadband characterization tools covering larger frequency spans of 1 THz or more is increasing. To achieve that with the available VNAs, multiple modules have to be implemented. This not only increases measurement efforts due to multiple realignment and calibration steps but also the system cost goes up immensely. Depending on application requirements, most VNAs already operate in free space for accessing bands above a few 100 GHz by using horn antennas [73], having essentially

no advantage over a photonic system that immediately emits in free space. Furthermore, the photonic systems have made significant advancements in reaching comparable DNR to commercial EVNAs [77, 78, 160, 161], especially at higher THz frequencies. All these advantages make photonic systems the potential solution for bandwidth limitations of EVNAs.

2.2 Photonic Characterization Systems

Developing a broadband Photonic Vector Network Analyzer (PVNA) is highly dependent on efficient generation and detection techniques in the THz range. Recent advancements in this field have resulted in THz sources and receivers capable of building systems with comprehensive frequency coverage and high DNR. The photonic approach for THz generation mainly consists of using either CW or femtosecond pulsed lasers as the source of the optical signal, which is then down-converted to THz signal by means of nonlinear frequency conversion in a $\chi^{(2)}$ -active nonlinear crystal (optical rectification) [162–164], photomixing concept [161, 165, 166] or recently, using spintronic devices [167–170]. Popular detection methods use photoconductive [171–173] and electro-optic detectors [174–176]. For the scope of the thesis, we limit our discussion only to the photomixing technique with a focus on photoconductive antennas for THz generation and detection under pulsed operation. Pulsed photoconductor-based systems are particularly advantageous as they can be implemented at room temperature in a table-top environment and are capable of generating and detecting broadband THz signals with high peak DNR. For pulsed operation, 6.5 THz bandwidth with ~ 110 dB peak DNR (1000 sample average, 1 min measurement time) have been demonstrated [76, 161]. Due to these advantages, pulsed photoconductors are preferred in many applications and well-suited for broadband photonic VNAs.

2.2.1 THz Generation by Photomixing

The THz generation principle based on the photomixing technique is a review of References [177] and [178].

CW Operation

To generate a CW THz signal, two lasers with powers P_1 and P_2 and frequencies $\nu_{1,2} = \bar{\nu} \pm \frac{\nu_{THz}}{2}$ are used to excite the semiconductor. The laser must have sufficient photon energy to generate photoinduced free carriers in the substrate, meaning $h\nu_{1,2} > E_G$, where E_G is the band gap energy of the semiconductor and h is the Planck constant. Heterodyne mixing of two separate lasers with $E_{1,0} \sim \sqrt{P_1}$ and $E_{2,0} \sim \sqrt{P_2}$ electric field strengths takes place in the photomixer resulting in an optical field strength of

$$\vec{E}(t) = \vec{E}_1(t) + \vec{E}_2(t) = \vec{E}_{1,0} e^{i(\bar{\omega} + \frac{\omega_{THz}}{2})t} + \vec{E}_{2,0} e^{i(\bar{\omega} - \frac{\omega_{THz}}{2})t - i\phi} \quad (2.6)$$

where $\omega_i = 2\pi\nu_i$ and ϕ are the angular frequencies and relative phase. The optical intensity is given by

$$I_L(t) \sim \left| \vec{E}(t) \right|^2 = E_{1,0}^2 + E_{2,0}^2 + 2 \left| \vec{E}_{1,0} \cdot \vec{E}_{2,0} \right| \cos(\omega_{THz}t + \phi) \quad (2.7)$$

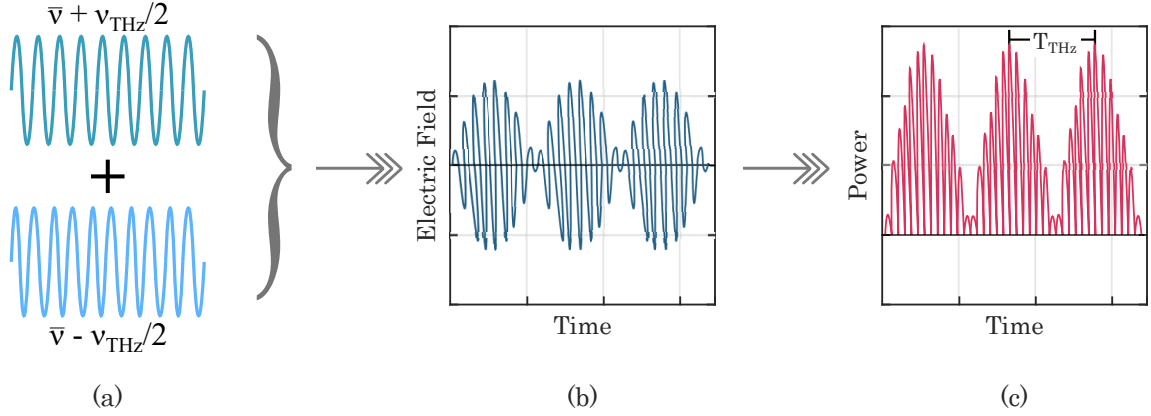


Figure 2.9: Photomixing process. (a) Heterodyne mixing of two lasers, (b) resulting electric field and (c) resulting power modulation with a beat node at the difference frequency.

and in terms of power

$$P_L(t) = P_1 + P_2 + 2\sqrt{P_1 P_2} \cos(\beta) \cdot \cos(\omega_{\text{THz}} t + \phi) \quad (2.8)$$

where, β denotes the angle between the polarizations of the electric fields. An ideal semiconductor situated between electrodes, absorbs all the incident light without any loss and forms electron-hole pairs. Photocurrent is generated by applying a DC bias via the electrodes that separates the electron-hole pair. The photocurrent is expressed as

$$I_{ph}^{id}(t) = \frac{eP_L(t)}{h\nu} = \frac{e(P_1 + P_2)}{h\nu} + 2\frac{e\sqrt{P_1 P_2}}{h\nu} \cos \beta \cdot \cos(\omega_{\text{THz}} t + \phi) \quad (2.9)$$

$I_{ph}^{id}(t)$ has an AC component $I_{\text{THz}}^{id}(t) = 2\frac{e\sqrt{P_1 P_2}}{h\nu} \cos \beta \cdot \cos(\omega_{\text{THz}} t + \phi)$ and a DC component $I_{\text{DC}}^{id}(t) = \frac{e(P_1 + P_2)}{h\nu}$. For the condition when the two lasers have identical power and polarization, meaning $P_1 = P_2 = P_L = P_{\text{tot}}/2$ and $\beta = 0$, the AC term is maximized and becomes $I_{\text{THz}}^{id}(t) = \frac{e\sqrt{P_{\text{tot}}}}{h\nu} = I_{\text{DC}}^{id} = I^{id}$, where $P_{\text{tot}} = 2P_L$ is the total laser power. In that case, the Equation 2.9 yields

$$I_{Ph}^{id}(t) = I^{id} [1 + \cos(\omega_{\text{THz}} t + \phi)]. \quad (2.10)$$

An antenna fabricated on the semiconductor converts this AC current to THz power,

$$P_{\text{THz}}^{id} = \frac{1}{2} R_A (I_{\text{THz}}^{id})^2 = \frac{1}{2} R_A \left(\frac{eP_{\text{tot}}}{h\nu} \right)^2 \quad (2.11)$$

where R_A is the radiation resistance of the antenna. Equation 2.11 represents an ideal case.

In summary, the heterodyne mixing of two individual lasers (with frequencies separated by the THz frequency) takes place in a photomixer resulting in difference-frequency modulation of the photocurrent that drives an antenna to emit the THz radiation into free space. In a photoconductive mixer, the semiconductor in the electrode gap absorbs the heterodyned laser beams, resulting in the formation of electron-hole pairs which are separated by an external DC bias that generates the photocurrent. Depending on the electrode gap and the semiconductor break-down field strength, the bias level ranges within a few volts to ~ 100 V.

Pulsed Operation

Under pulsed operation several laser frequencies are mixed to form a laser pulse in contrast to two frequencies of the CW operation. The laser pulse can be expressed as

$$\vec{E}_L(t) = \sum_j^n \vec{E}_j \exp[i(\omega_j t + \phi_j)] \quad (2.12)$$

where $\omega_j = 2\pi\nu_j$ and ϕ_j represent the angular frequencies and phases of the optical E-field E_j of the modes of the pulsed laser. A typical mode-locked fs laser usually has the following features: a) the frequency components must be equally spaced, meaning $\nu_j - \nu_{j-1} = R_p$ (R_p is the repetition rate of the laser) and b) the phase should have a fixed (linear) relationship, that is $\phi_j - \phi_{j-1} = \text{constant}$. The fixed-phase-relationship is achieved by the Mode-locking technique allowing to generate extremely short (almost) Fourier-limited laser pulses, typically in the femtosecond range. While the actual spectral distribution can be quite complex, we for now assume a simpler case of a Gaussian intensity distribution in order to calculate the shape of the emerging THz field. So, assuming \vec{E}_j show a Gaussian distribution, the temporal shape of the laser pulse field strength can be expressed as

$$\vec{E}_L(t) = \vec{A}(t) \exp(i\omega_L t) \quad (2.13)$$

where $\vec{A}(t)$ and ω_L are the complex envelope and the central frequency of the laser pulse, respectively. The Gaussian pulse is Fourier transform-limited for a linear phase relationship, with an envelope of

$$\vec{A}(t) = \vec{A}_0 \exp\left(\frac{-t^2}{\tau^2}\right) \quad (2.14)$$

where τ is the e^{-2} width of the pulse in time domain. The intensity ($I_L(t)$) is given by the square of the field strength

$$I_L(t) \propto |\vec{E}_L(t)|^2 = I_L^0 \exp\left(\frac{-2t^2}{\tau^2}\right) \quad (2.15)$$

$I_L^0 \sim |\vec{A}_0|^2$ corresponds to the peak intensity. The intensity also has a Gaussian profile with τ the e^{-2} width and $\sqrt{2\ln 2}\tau$ the Full Width at Half Maximum (FWHM). Now the Fourier transform of Equation 2.13 gives us the spectral components of the pulse

$$V(\nu) = \int_{-\infty}^{\infty} E_L(t) \exp(-i2\pi\nu t) dt = |V(\nu)| \exp[i\psi(\nu)] \quad (2.16)$$

where ψ is the spectral phase. For a Gaussian pulse the spectral intensity is given by

$$I_L(\nu) = |V(\nu)|^2 \propto \exp[-2\pi^2\tau^2(\nu - \nu_L)^2] \quad (2.17)$$

with a spectral e^{-2} width of $\sigma = \frac{\sqrt{2}}{\pi\tau}$. The temporal and spectral profile of the laser pulse along with time domain intensity profile is depicted in Figure 2.10.

From Equation 2.9 and 2.15 we can calculate the generated photocurrent for the ideal case

$$I_{Ph}^{id}(t) = \frac{eP_L(t)}{h\nu} = I_{Ph}^{peak} \exp\left(\frac{-2t^2}{\tau^2}\right). \quad (2.18)$$

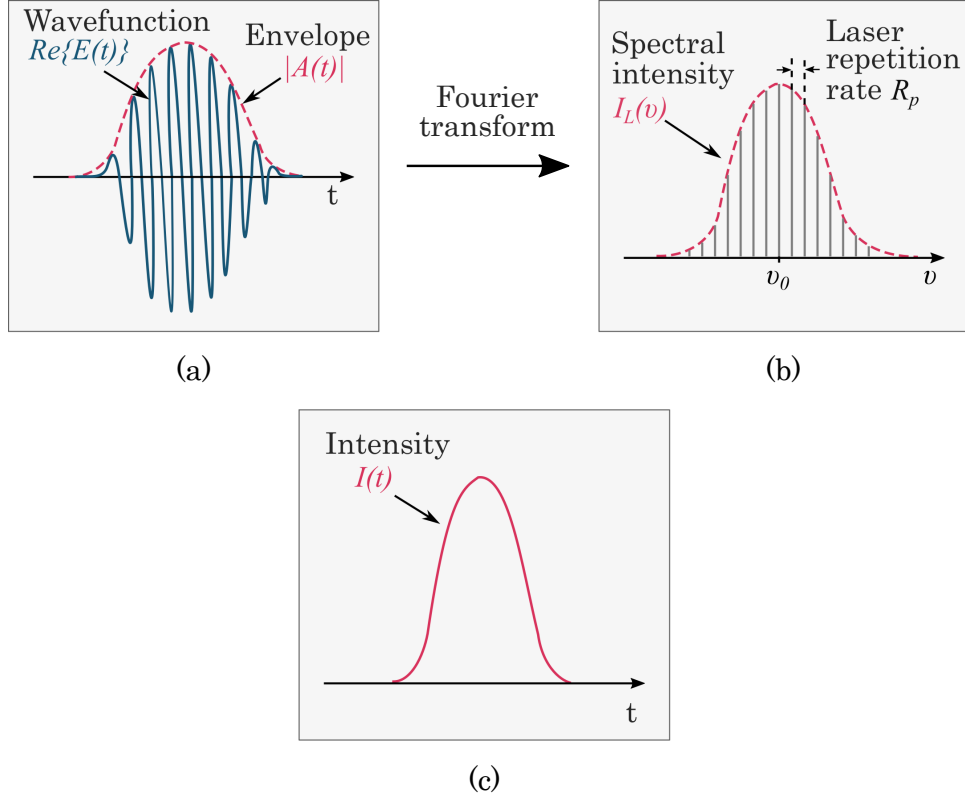


Figure 2.10: (a) Temporal profile, (b) spectral profile and (c) time-domain intensity of a femtosecond laser pulse. Reproduced and adapted from [178].

According to this equation, under ideal circumstances, the resulting photocurrent is Gaussian because the carriers respond to the envelope of the laser pulse.

The emitted THz field is proportional to the first time derivative of the photocurrent

$$E_{THz}(t) \sim \frac{\partial I_{Ph}(t)}{\partial t}. \quad (2.19)$$

The frequency spectrum of the transmitted signal is the Fourier transform of the THz field

$$E_{THz}(\omega) \sim \mathcal{F} \left[\frac{\partial I_{Ph}(t)}{\partial t} \right] = i\omega I_{Ph}(\omega) \quad (2.20)$$

where $I_{Ph}(\omega)$ is the spectrum of the photocurrent.

The equations derived for CW and pulsed operation of photomixers are only valid for an ideal case and do not consider the reflection at the semiconductor surface, intrinsic response of the photoconductive material and RC roll-off losses. To include the material response, a convolution approach is reported in Reference [79] for THz generation. Due to reflections and finite absorption in the material, not all of the incident laser power is converted to electron-hole pairs. The external quantum efficiency

$$\eta_{ext} = (1 - R)[1 - \exp(-\alpha d_i)] \quad (2.21)$$

takes these losses into account, where R is the reflection coefficient and α is the absorption coefficient of the material. As a result the total photocurrent becomes $I_{Ph}(t) = \eta_{ext} I_{Ph}^{id}(t)$. By using an anti-reflection coating and sufficiently thick absorbing layers $\eta_{ext} \sim 1$ can be reached.

At higher frequencies, further factors reduce the AC photocurrent, namely lifetime and RC roll-off. Only a portion of the electron-hole pairs produced by photons in the photoconductors contribute to the photocurrent. The other electron-hole pairs recombine before reaching the electrodes. Due to recombination, the number of available charge carriers diminishes exponentially over time. The average photocurrent over the transit time τ_{tr} can be calculated from Equation 2.10 as follows [79]

$$I_{Ph}^{id}(t) = \frac{1}{\tau_{rec}} \int_0^\infty I^{id} [1 + \cos(\omega_{THz}t + \phi)] \exp\left(\frac{-t}{\tau_{rec}}\right) dt = I^{id} \frac{\tau_{rec}}{\tau_{tr}} \left[1 + \frac{\sin(\omega_{THz}t + \phi)}{\sqrt{1 + (\omega_{THz}\tau_{rec})^2}} \right] \quad (2.22)$$

where τ_{rec} is the recombination time and the factor $\tau_{rec}/\tau_{tr} \ll 1$ is photoconductive gain g , which has an equal impact on both the DC and THz photocurrents. The lifetime (power) roll-off can be expressed as [177]

$$\eta_{lt}(\omega) = \frac{1}{1 + (\omega_{THz}\tau_{rec})^2} \quad (2.23)$$

At frequencies $\omega_{THz} \gg 1/\tau_{rec}$ the power rolls off as ν_{THz}^2 .

A finite device capacitance in combination with the antenna radiation resistance, as well as additional parallel and series resistances attributed to the active area of the semiconductor and the interconnects, respectively, causes the RC roll-off, leading to a further power roll-off of [165]

$$\eta_{RC}(\nu_{THz}) = \frac{1}{1 + (2\pi R_A C_p \nu_{THz})^2} \quad (2.24)$$

where C_p is capacitance of the device. The overall THz emitted power now can be expressed as

$$P_{THz}(\omega) = \frac{1}{2} R_A \eta_{ext}^2 g \eta_{lt}(\omega) \eta_{RC}(\omega) (I_{THz}^{id})^2 \quad (2.25)$$

More detailed description of the THz generation using photomixing technique can be found in References [79, 177].

2.2.2 THz Pulse Detection by Photoconductors

The theory presented in this section is a revision of References [178] and [179]. A photoconductive detector consists of a semiconductor with high-dark resistance and two metallic contacts, separated by a gap, deposited on it. An ultrafast laser pulse and the incoming THz signal are focused concurrently on the active region situated between the electrode gap. The laser pulse absorbed by the semiconductor generates electron-hole pair, which increases its conductivity. The electric field of the THz pulse acts as a transient bias field. The synchronous incidence results in a convolution of both, giving rise to a low frequency, i.e. rectified current, which is then read out by external electronics. The whole THz waveform can be mapped out by varying the delay between the arrival of the THz signal and the optical pulse. Photoconductive detectors can work in integrating, direct, or intermediate sampling modes, depending on the characteristics of the semiconductor [179, 180].

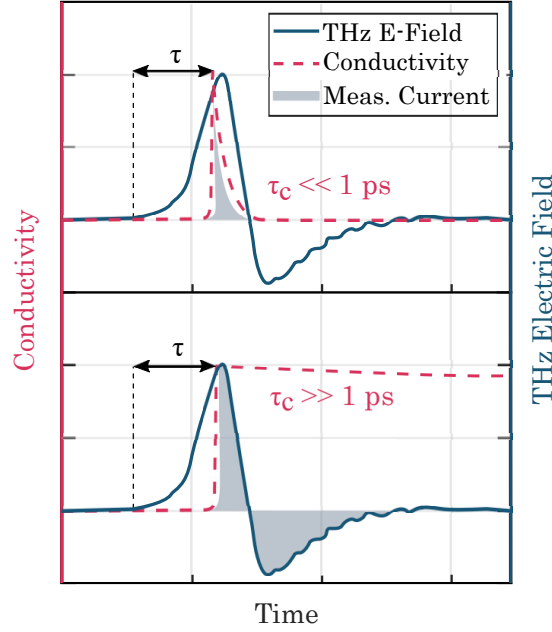


Figure 2.11: Current response for a transient overlap between THz and laser pulses. Top: For a short carrier lifetime ($\tau_c \ll 1$ ps) material. Bottom: For a long carrier lifetime ($\tau_c \gg 1$ ps) material. Reproduced and adapted from [179].

Direct sampling detectors comprise highly-resistive semiconductors that exhibit a very short carrier lifetime, meaning generated carriers are trapped very quickly, therefore, showing an increase in conductivity only as long as the laser pulse illuminates it. As a result, the measured photocurrent samples only the point when both the optical and THz signal coincide temporally, which is depicted in Figure 2.11 (top). This means at that point, the measured photocurrent is proportional to the THz electric field strength. It is therefore, feasible to quantify the electric field of the THz pulse E_{THz} as a function of time t , by delaying the laser pulse by τ relative to the THz transient. Assuming that the spike in the conductivity generated by the optical pulse is much shorter than any features of the THz wave, the measured photocurrent $I(\tau)$ can be expressed as

$$I(\tau) \propto E_{THz}(t = \tau). \quad (2.26)$$

Integrating detection takes place in semiconductors with a carrier lifetime longer than the duration of the incoming THz pulse. As a result, the photoconductor remains photoexcited much longer than the duration of the THz transient, and the measured photocurrent I_{Ph}^{det} is given by the convolution of the THz electric field and material conductivity [179, 181, 182]

$$I_{Ph}^{det}(\tau) \propto \int_{-\infty}^{+\infty} E_{THz}(t)\sigma(t - \tau)dt. \quad (2.27)$$

If the time-resolved conductivity of the material ($\sigma(t)$) is known, the original THz field can be extracted by deconvoluting Equation 2.27. $\sigma(t)$ frequently has a monoexponential decay and is expressed as

$$\sigma(t) = \sigma_0 e^{\frac{-t}{\tau_{rec}}} + \sigma_{dark} \quad (2.28)$$

where σ_0 refers to the peak conductivity exactly after excitation and τ_{rec} represents the charge-carrier lifetime of the material. The very low dark conductivity σ_{dark} is neglected in the following for simplicity. $\sigma(t)$ can also be described in terms of mobility μ and the carrier concentration of the material n by $\sigma(t) = e\mu(t)n(t)$. The conductivity of the semiconductor can be assumed to rise like a step function. In that case, Equation 2.27 becomes

$$I_{Ph}^{det}(\tau) \propto \int_{\tau}^{\infty} E_{THz}(t) dt \quad (2.29)$$

and THz electric field ($E_{THz}(t)$) can be recovered by differentiating the detected photocurrent ($I_{Ph}(\tau)$) with respect to τ . Equation 2.29 signifies that a short carrier lifetime is not a prerequisite for a wide-band photoconductive detector. To achieve a wide bandwidth the rise time in the photoconductivity must be short, which is mainly dependent on the duration of the laser pulse rather than the material properties [179]. However, for long carrier-lifetime materials the signal-to-noise ratio is affected as integration over the noise is performed when the sample is still conductive. Therefore, low noise photoconductive detectors usually feature a carrier lifetime below at least 0.5 ps. In practice, the photoconductive detector can act both i.e. as a direct detector below 200 GHz and as an integrating detector at 2 THz and above.

For the case when prior knowledge of the time-resolved photoconductivity of the material ($\sigma(t)$) is available, the THz electric field can be calculated from the measured photocurrent ($I_{Ph}^{det}(\tau)$) by numerical methods. A fast deconvolution method to achieve this is described in [179]. Equation 2.27 can be rewritten as

$$I(\tau) = \beta \int_{-\infty}^{+\infty} E_{THz}(t) \Phi(t - \tau) dt \quad (2.30)$$

where β is a constant dependent on the Fresnel transmission coefficient, the wavelength of the laser beam, laser power [179] as well as the device geometry, whereas, $\Phi(t)$ is the normalized time dependent conductivity expressed as $\Phi(t) = \theta(t)e^{-t/\tau_{rec}}$, with $\theta(t)$ representing a step function. Fourier transform of Equation 2.30 returns

$$I(\omega) = \beta E_{THz}(\omega) \Phi(\omega) \quad (2.31)$$

The inverse Fourier transform of Equation 2.31 yields the time domain THz electric field

$$E_{THz}(t) = \frac{1}{\beta} \mathcal{F}^{-1} \left[\frac{I(\omega)}{\Phi(\omega)} \right] = \frac{1}{\beta} \mathcal{F}^{-1} \left[I(\omega) \left(\frac{1}{\tau_c} + i\omega \right) \right] \quad (2.32)$$

In the above derivation, the assumption of Φ as a step function is only valid for a δ -function like laser pulse and infinite trapping and recombination lifetime. In reality, Φ has a more complicated shape, necessitating a more sophisticated approach [179]. Still, this deconvolution approach is fast and provides a good approximation for photoconductive response correction.

Although a few photonic characterization tools in the THz range are commercially available, they use either CW (e.g. frequency domain spectrometer) [8, 183, 184] or pulsed lasers for generating and detecting THz signals. However, for the scope of the thesis, we limit our discussion to pulsed systems, namely, the Terahertz Time Domain Spectrometer. These spectrometers are the most popular and widely used systems for material characterization [83, 185] and imaging [82, 87] because of their attributes, including high DNR > 100 dB, bandwidth > 6 THz, availability of amplitude and phase data, and its ability to perform non-contact, non-invasive and non-destructive inspection. Also for these reasons, the Terahertz Time-Domain Spectroscopy (THz-TDS) system is a reasonable choice as the backbone of developing photonic VNAs.

2.2.3 Terahertz Time Domain Spectrometer

Similar to an RF VNA, the THz-TDS systems use coherent detection to measure the field amplitude and phase of an electromagnetic wave and provide a straightforward method of determining the attenuation and phase shift associated with the interaction of THz waves with the device or material under test. In contrast to a VNA, which does frequency sweeping and records data at each frequency point, a pulsed THz-TDS captures broadband THz signal in the time domain.

Architecture and Operation

The system architecture of a THz-TDS mainly consists of an ultrafast laser, a transmitter, a receiver and post-detection electronics. A simple schematic of a THz-TDS system is depicted in Figure 2.12. To perform coherent detection, THz-TDS employs a closed-loop pump-probe approach where the pump and probe beams are obtained from the same laser, and the detector samples the temporal overlap of the THz and probe pulses. This guarantees that the system has a high signal-to-noise ratio and a high DNR [118].

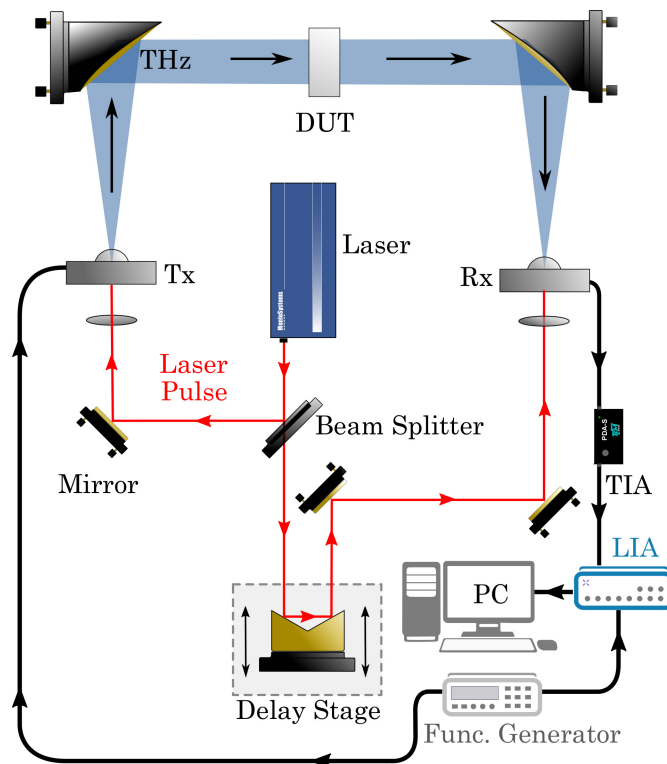


Figure 2.12: System architecture of a typical THz-TDS setup. LIA = Lock-in Amplifier, TIA = Transimpedance Amplifier.

In a pulsed THz-TDS system, the source and the detector are driven by an ultrafast laser with a pulse duration in the ~ 100 fs range. The laser beam is split into pump and probe beam paths that activate the transmitter and receiver, respectively. The pump beam modulates the

conductance of the source photoconductor, and an applied bias generates a photocurrent with a THz component, which is then radiated by an antenna. The antenna on the receiver side receives the THz field that biases the photoconductor while the probe beam modulates its conductance. This results in a mixing process containing a DC component proportional to the convolution of the incoming THz field and the optical signal [79, 179], which is subsequently read out by the post-detection electronics. The complete THz pulse is extracted by varying the relative delay between the THz and optical pulses. This generation and detection process was described in detail in the Sections 2.2.1 and 2.2.2.

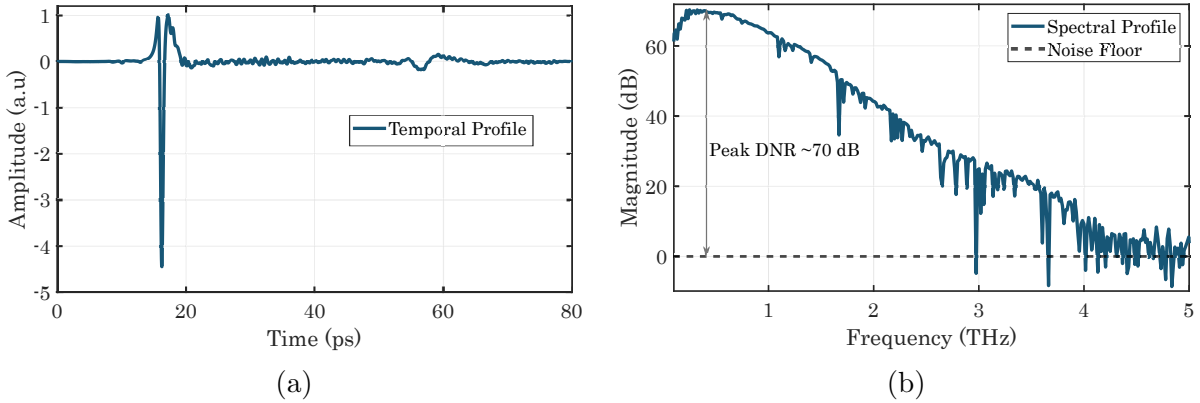


Figure 2.13: (a) Temporal and (b) spectral profile of a THz pulse.

The relative delay between the THz and laser pulses is scanned by implementing a mechanical delay line. The emitted THz field is guided, collimated and focused using quasi-optical elements, including parabolic mirrors and TPX lenses. Post-detection electronics typically include a Trans-Impedance Amplifier (TIA) that amplifies and converts the current to voltage, followed by an Analogue to Digital Converter (ADC) or a Lock-In Amplifier (LIA) for read-out. Figure 2.13 depicts an exemplary case of a received THz pulse in the time domain, and its spectral profile obtained by Fourier transform, for a typical commercial THz-TDS system. Almost all the pulsed THz-TDS systems that employ photoconductors to generate and detect THz signals show similar temporal and spectral profiles.

The absolute value of the generated THz power has no direct influence on the measurement and must be consistent during the measurement procedure. The THz-TDS primarily evaluates the difference in amplitude and phase of a THz field yielded by the studied sample compared to a reference THz wave. Typical THz-TDS systems are configured in transmission mode, which measures the transmission coefficient of the DUT or MUT. In this case, the transmission coefficient is determined by the ratio of the THz field transmitted through the sample (test) to the field propagated through an empty setup (reference), as illustrated in Figure 2.14. The transmission coefficient $t(\omega)$ is analogous to the S_{21} parameter and is given by

$$t(\omega) = S_{21}(\omega) = \frac{E_t^{DUT}(\omega)}{E_t^{ref}(\omega)}, \quad (2.33)$$

where $E_t^{DUT}(\omega)$ is the THz wave transmitted through the sample and $E_t^{ref}(\omega)$ is the reference THz wave propagated through an empty setup.

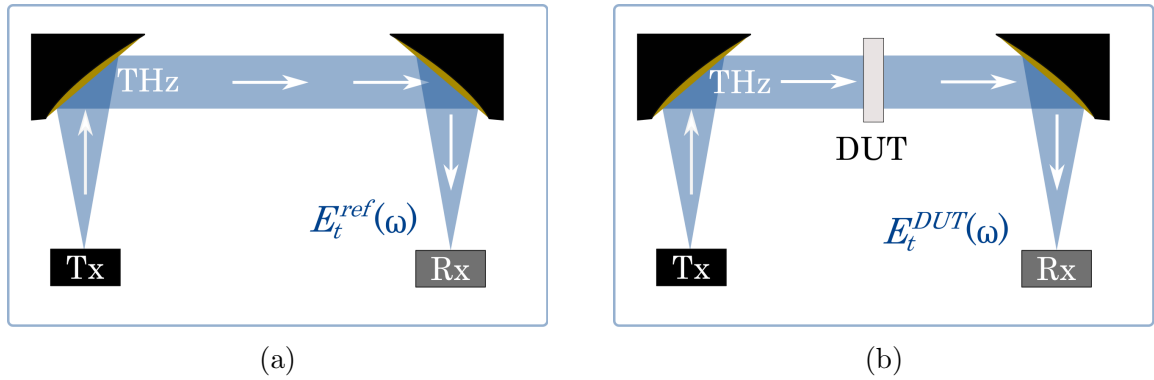


Figure 2.14: Transmission geometry THz-TDS setup for (a) reference and (b) test measurements.

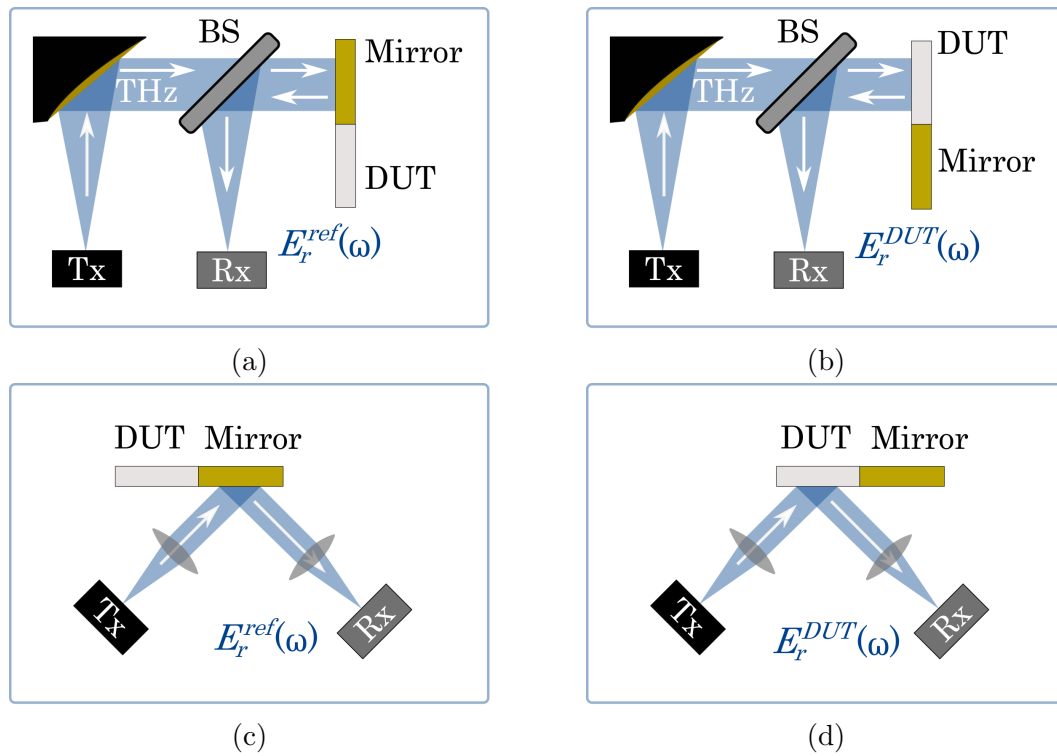


Figure 2.15: (a) Reference and (b) test measurement setup for perpendicular incidence reflection THz-TDS. (c) Reference and (d) test measurement setup for oblique incidence reflection THz-TDS. Tx = Transmitter, Rx = Receiver, BS = Beam Splitter.

For specific experiments such as the characterization of opaque materials in the THz range [186] or imaging [187], THz-TDS is implemented in reflection geometry, to measure the reflection coefficients of the inspected samples. This approach is less accurate than the transmission geometry due to the comparatively smaller phase change of the reflected signals [188] and misplacement errors associated with the relative position of the reference plane and the sample plane [189]. However, for the aforementioned applications, it is advantageous to use reflection

data since, in those cases, the samples are either not transmissive (e.g., opaque materials) or only weakly transmissive (e.g., highly absorptive materials). Moreover, the reflection coefficient or S_{11} parameter cannot be extracted in transmission geometry. The reflection geometry can be implemented for a perpendicular incidence where the reflected signal is separated from the incoming signal path using a beam splitter (as shown in Figures 2.15a and 2.15b) [108], or by placing the sample at an angle (as shown in Figure 2.15c and 2.15d) [190]. The configuration with perpendicular incidence is subjected to power loss due to the beam splitter. In contrast, the arrangement with oblique incidence is susceptible to misalignment of the THz wave when the reference element and the sample are exchanged. Nevertheless, both systems are employed based on the application requirements. For example, incidence at an angle is preferred in coating thickness measurement applications [190, 191]. In order to measure the reference signal in reflection mode, a metal plate is usually inserted in the THz path, and the reflected signal is recorded ($E_r^{ref}(\omega)$). This metal plate represents a physical plane that determines the reference phase. Then the metal reflector is replaced by the DUT or MUT, ensuring that it exactly matches the reference plane of the reflector, and subsequently, the THz field reflected from the sample $E_r^{DUT}(\omega)$ is measured. The reflection coefficient is given by

$$r(\omega) = S_{11}(\omega) = \frac{E_r^{DUT}(\omega)}{E_r^{ref}(\omega)} \quad (2.34)$$

System Specifications

The fundamental operational specifications of a THz-TDS system are its spectral bandwidth, frequency resolution, and DNR. The accuracy and resolution of measured transmission and reflection coefficients, along with properties derived from them such as refractive index, absorption coefficient etc., are highly dependent on these parameters.

DNR is defined as the ratio of the amplitude at a given frequency to the noise floor. A typical value of DNR denotes the capability of the system, where large DNR allows for investigating strongly absorbing materials, and lower DNR restricts the accuracy and amplitude response of these measurements. Figure 2.13(b) demonstrates the spectral profile of a THz pulse recorded using a commercial THz-TDS system in transmission geometry with a peak DNR of ~ 70 dB at around 500 GHz and a DNR of about 20 dB at 3 THz. As a result, measurements made at frequencies below 3 THz are trustworthy. Despite the fact that there is signal over 3 THz, it is common practice to choose reliable data with at least 20 dB of DNR for subsequent processing.

The DNR describes only the amplitude of the measured data and provides no information about the phase. The phase data, similar to the amplitude, is susceptible to noise. However, amplitude and phase measurements have different noise sources, namely, power fluctuations and temporal inaccuracy. The phase noise of a measurement can be quantified by repeating it several times. The standard deviation of these iterations provides a reasonable estimate of the phase noise [86].

The frequency resolution is the frequency interval of the spectral data and is reliant on the DNR. The frequency interval is given by $c_0/2l$, where c_0 is the speed of light in vacuum and l is the delay length. For a system with no noise and an infinite delay, the maximum resolution of a pulsed system will be equal to the repetition rate of the pump laser [117]. In the presence of noise, however, the attainable resolution degrades significantly. As the signal's amplitude and DNR decrease with increasing delay from the main pulse, the signal can no longer be distinguished from noise. From then on, increasing the delay will not yield any further

information, thus limiting the maximum sensible delay. According to research on the noise dependency of frequency resolution, a typical system can achieve a maximum feasible spectral resolution in the order of 1 GHz [192]. Nevertheless, a sub-GHz resolution is achievable in systems employing the mechanical delay-stage-free Asynchronous Optical Sampling (ASOPS) technique [193].

The scan speed of the THz-TDS system is another crucial component, particularly when used in combination with a lock-in amplifier. The lock-in amplifier reduces the random noise by averaging the signal over a period determined by the time constant. The THz signal, however, is continuously changing as the delay stage moves to sample various time points of the signal. It is crucial to select the combination of lock-in time constant and scanning speed such that it takes an equivalent time of at least 3 to 5 time constants to pass for the delay stage to move the distance corresponding to the sharpest feature in the THz pulse [86]. Too fast scan speed results in reduced magnitude and change in the temporal pulse shape, which in turn reduces the frequency bandwidth and DNR at higher frequencies of the spectral data [86].

Eliminating random noise sources is key to proper operation of a THz-TDS. Mechanical noise sources include vibrations, air currents along beam pathways, air particles, and thermal deformations. Variations in pump laser intensity between pulses can also cause amplitude noise [117]. The study conducted on different THz-TDS systems by Hübbers *et al.* confirmed that amplitude noise is proportional to absolute amplitude, and even when all electrical and mechanical noise sources are minimized, the residual amplitude noise is around 1% of the signal intensity [118]. Other investigations evaluated laser amplitude changes, beam aiming deflections, and detector noise as noise sources, but determined that their contributions to the measured noise level were negligible [102, 118, 194].

Error Sources

Numerous causes of randomness impacting THz-TDS signals have thus far been identified, such as laser intensity variation [195–197], optical and electrical noise [198, 199], delay line jitter [200], registration error [201], etc. In general, mathematical treatment for these noise sources is available [83, 202]. Along with the signal’s inherent randomness, flaws in the physical setup (e.g., sample alignment) and extraction procedure (e.g., false phase unwrapping) also contribute to the error in the predicted attributes.

Figure 2.16 presents significant causes of error originating from THz-TDS measurement and the parameter extraction procedure [203]. The sample signal incorporates Fabry-Pérot reflections in addition to noise, and if they are not appropriately treated, they might result in systematic errors. The variation caused by the amplitude error from multiple measurements propagates through the parameter extraction, Fourier transform, and deconvolution steps, resulting in the variance in magnitude and phase of the estimated transfer function. The extraction of parameters sometimes necessitates knowledge of the sample thickness, sample alignment, and refractive index of the surrounding medium, all of which are subject to ambiguity. All of these variations aggregate at the output and contribute to the uncertainty in the retrieved properties of the DUT or MUT. It is vital to highlight that amplitude variance is a significant source of measurement uncertainty. Further analysis of sources of errors is detailed in [203].

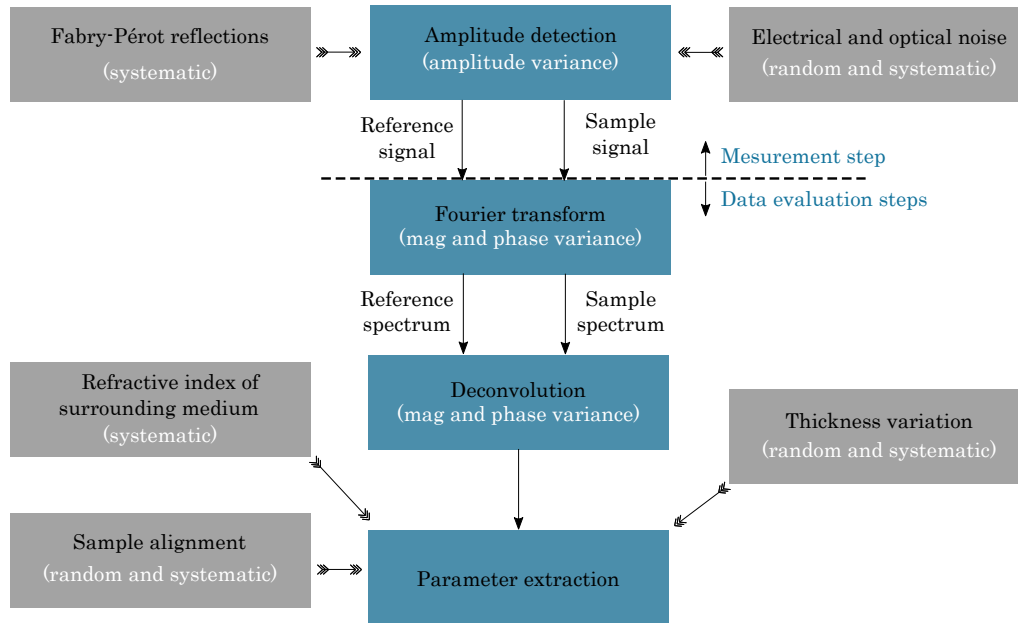


Figure 2.16: Error sources of THz-TDS measurement and error types (grey). Blue rectangles denote the parameter extraction procedure steps. Adapted from [203].

System Calibration

Correct spectral information is one of the key aspects of calibration for THz-TDS devices. It is obvious that accurate frequency scale calibration is necessary for the detection and characterization of spectral characteristics including absorption lines, resonance peaks, and other features. The delay data of the time-domain scan are used to determine the phase information, which is then converted to frequency domain using the Fourier transform. The accuracy of the phase data and the parameters obtained from it, such as the refractive index, are also ensured by calibrating the frequency scale.

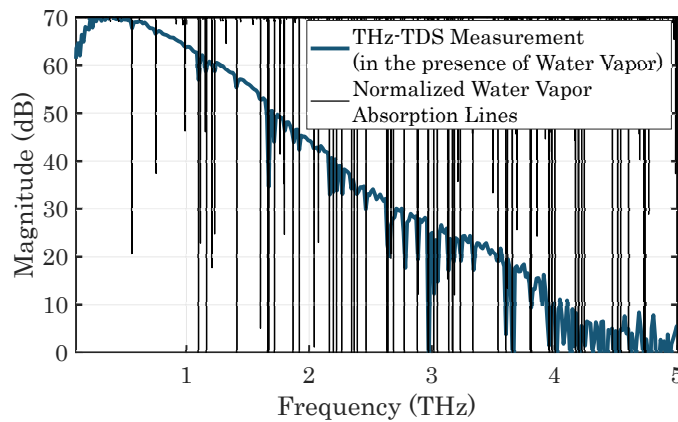


Figure 2.17: Frequency calibration using water vapor absorption lines

Numerous gases feature narrow linewidth rotational transitions at terahertz frequencies, making them excellent choices for frequency calibration. Readily available water vapor with well-known strong and narrow absorption lines [204, 205] (Figure 2.17), or absorption gas cells containing CO , N_2O , etc. with a linear molecular structure whose absorption spectrum consists of a regular comb of lines with a characteristic amplitude envelope [206], are utilized for this purpose. However, relative amplitudes of the water vapor lines vary with air pressure and humidity [207], and gas cells are comparatively bulky, cumbersome, and in most cases, toxic (e.g. CO). An etalon, which produces resonance peaks at regular frequency intervals (free spectral range (FSR)) over the whole operation band of the THz-TDS, is therefore preferred. The most straightforward approach to frequency calibration using an etalon entails recording the frequencies of the maxima and minima in the transmission spectrum and comparing them with their expected value determined by $FSR = c_0/2n_e d_e$, where n_e and d_e are the refractive index and thickness of the etalon material, respectively. It is, therefore, possible to display the discrepancy between the measured and calculated frequencies for each maximum and minimum as a function of the expected frequency, indicating any systematic frequency inaccuracies as well as noise and digitization problems. This can be accomplished using a high-finesse air-gap etalon [208, 209] or a low-finesse etalon consisting of a high-resistivity silicon wafer [210]. A method for in-line calibration of a THz-TDS system employing both a gas cell and an etalon was developed by Deng *et al.* [211].

2.2.4 State-of-the-Art THz-TDS Systems

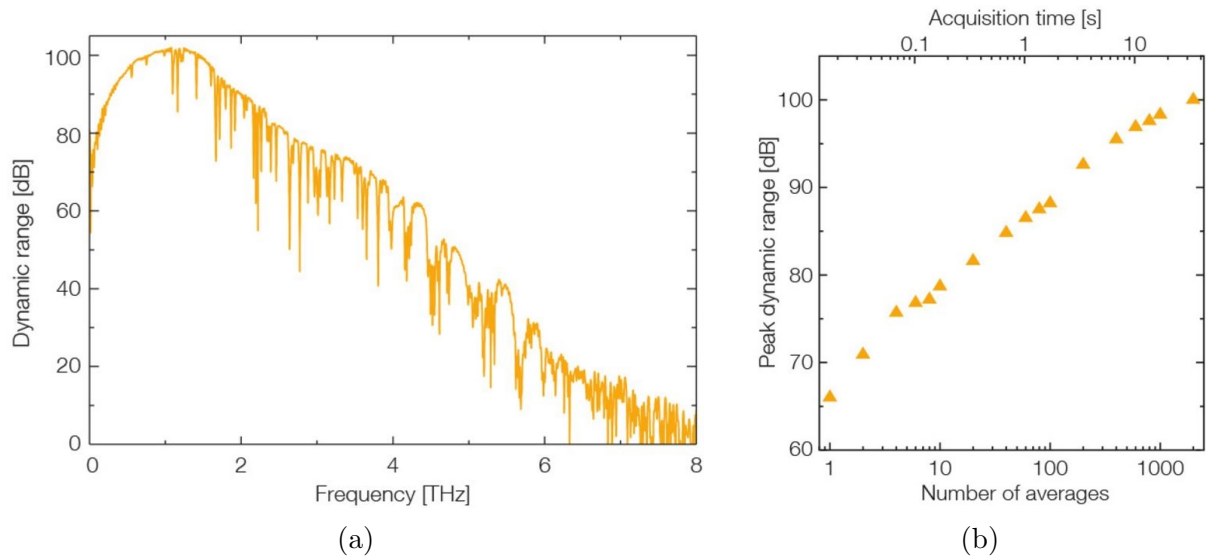


Figure 2.18: State-of-the-art commercial THz-TDS measurement (Toptica Photonics /Fraunhofer HHI, Berlin). (a) THz spectrum (b) Peak DNR versus number of averaged time traces and total acquisition time [212].

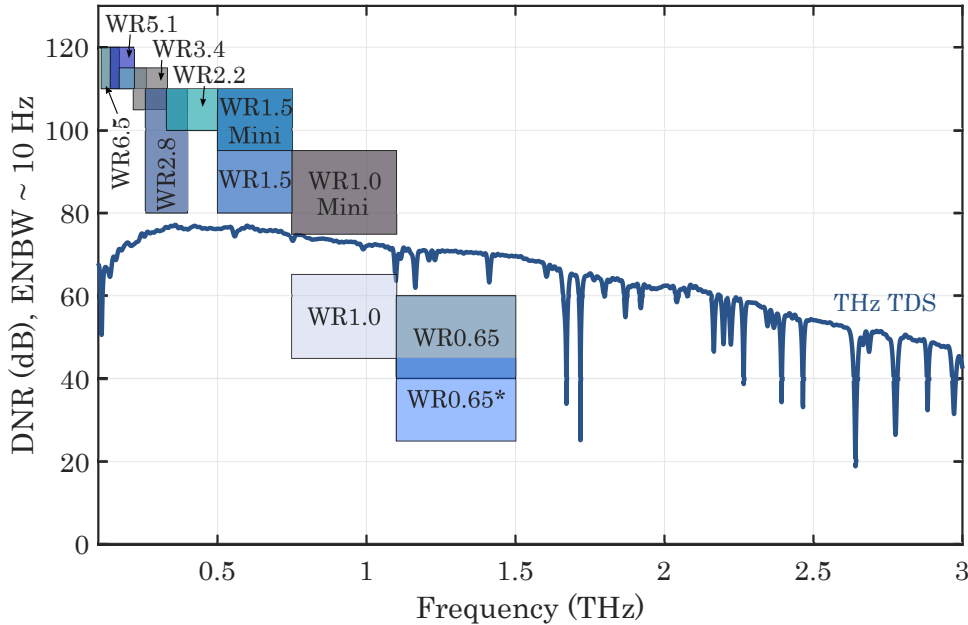


Figure 2.19: DNR of VNA extenders from Virginia Diodes Inc. [65] and state-of-the-art THz-TDS measurement [161]. *For two-port configuration.

THz systems based on pulsed photoconductors have advanced significantly in the past decade. Commercially available pulsed THz-TDS systems (Toptica Photonics/Fraunhofer HHI), in a typical transmission setting, already reach more than 6 THz bandwidth with 100 dB peak DNR (averaged over ~ 2000 scans with ~ 30 s acquisition time) (Figure 2.18) [212]. This system employs fiber-coupled InGaAs/InP photoconductive antennas to generate and detect THz pulses, which are driven by an ultrafast laser centered on 1550 nm with a ~ 90 fs pulse duration at a repetition rate of 100 MHz (TeraFlash Pro) [212]. With a similar laser, Nandi *et al.* reported a bandwidth of 6.5 THz with ~ 110 dB maximum DNR (averaged over 1000 scans with 1 min measurement time) using an ErAs:In(Al)GaAs photoconductive transmitter and an ErAs:InGaAs based photoconductive detector [76]. Kohlhaas *et al.* from Fraunhofer HHI, Berlin, also demonstrated a similar outcome using InGaAs:Rh-based photoconductors [77]. Until recently, they presented a THz-TDS measurement with III-V photoconductive membranes on Silicon to attain ~ 10 THz bandwidth with ~ 100 dB peak DNR [78].

Modern photonic systems possess an adequate DNR to compete with electrical systems, particularly beyond 1 THz. Figure 2.19 compares the DNR of the frequency extenders from Virginia Diodes, Inc. [65], where the source and receiver have been directly connected, to that of a state-of-the-art free space ErAs:InGaAs based transmission geometry THz-TDS [161]. For a fair comparison, the THz-TDS data is modified to have a similar Equivalent Noise Bandwidth (ENBW) of ~ 10 Hz as the VNA data. At frequencies below 500 GHz, the VNA performs significantly better than the THz-TDS, with 50 to 20 dB higher DNR. Even though a deficit of 50 dB in DNR at 200 GHz in the photonic system is rather large, the remaining DNR of roughly 70 dB is still suitable for most experiments. The DNR of the photonic system peaks at around 500 GHz. In this range, the WR2.2 and WR1.5 extenders show a typical DNR of around 100 dB. The DNR of the photonic system is ~ 20 dB lower than that of the electronic VNAs at this stage, as the Schottky multipliers of the VNA still only exhibit negligible roll-off.

At higher frequencies, the difference in DNR between the systems becomes smaller due to the conversion efficiency roll-off of the Schottky-diode-based multiplier chain, increased losses of hollow core metallic waveguides, and low alignment tolerances within electronic systems. The photonic system yields roughly 70 dB DNR at 1 THz, whereas conventional extender chains achieve similar values for WR1.0 mini (95-75 dB) and lower values for WR1.0 (40-60 dB) [65]. Beyond 1.1 THz, the photonic system outperforms the electronic one, indicating that a competitive pulsed PVNA system covering frequencies over 1 THz should be feasible. Provided that a smaller DNR can be accepted in the experiment, an extension towards ~ 6 THz is even achievable. Most notably, there would be no requirement for swapping bands compared to the electronic VNA, where a minimum of six bands are required to span the frequency range from 220 GHz to 1.5 THz. As a result, broadband measurements are greatly simplified by the photonic approach, as the system only has to be calibrated once, and realignment is not necessary (as it would be when switching bands).

2.2.5 Conclusion

To the knowledge of the author, the highest frequency extension for VNAs currently available on the market is 1.5 THz [65]. Due to the fabrication tolerances and increased scattering by surface roughness of hollow metallic waveguides, upscaling existing technology is challenging. THz-TDS systems can determine S_{21} and S_{11} parameters when implemented in transmission and reflection geometry, respectively. Therefore, a complete two-port PVNA can be configured by adding a few components to an existing free space photonic system. This will be demonstrated in the next chapter, along with data evaluation and calibration techniques which for time-domain measurements require an entirely new methodology.

Photonic VNA: System Architecture, Calibration and Data Evaluation

Electronic Vector Network Analyzers (EVNAs) are typically set up in a two-port configuration that facilitates recording a complete set of Scattering(S) parameters (S_{21} , S_{11} , S_{12} , S_{22}) of a Device Under Test (DUT). In contrast, Terahertz Time-Domain Spectroscopy (THz-TDS) systems are usually configured in either transmission or reflection geometry enabling only S_{21} or S_{11} parameter extraction. For a complete characterization, the DUT must be physically reversed and moved between different setups. In this thesis, we enhance the capability of the existing THz-TDS systems by first building a setup similar to a two-port single path configuration of a Vector Network Analyzer (VNA), which is capable of measuring both S_{21} and S_{11} parameters simultaneously. We refer to this system as a 1.5 port Vector Spectrometer (VSM). Then it is upgraded to a two-port Photonic Vector Network Analyzer (PVNA) by incorporating a few components. In this chapter, we describe the various components of these systems and propose novel calibration and data assessment approaches.

3.1 System Architecture

The PVNA setup essentially consists of a laser, transmitters and receivers, test sets and post-detection electronics. Figure 3.1 depicts the simple block diagrams of a 1.5 port VSM and a two-port PVNA configuration. In this section, we discuss the specifications of each component that is used to realize these systems.

3.1.1 Optical Component: Ultrafast Laser

To optically modulate the conductance of both transmitters and receivers in a pump-probe configuration, an ultrafast laser is used. A modified Menlo C-fiber laser system [213] operating at a center wavelength of around 1560 nm with 90 fs pulse duration and a repetition rate of 100 MHz is implemented to realize the VSM and the PVNA. It features two fiber ports – one

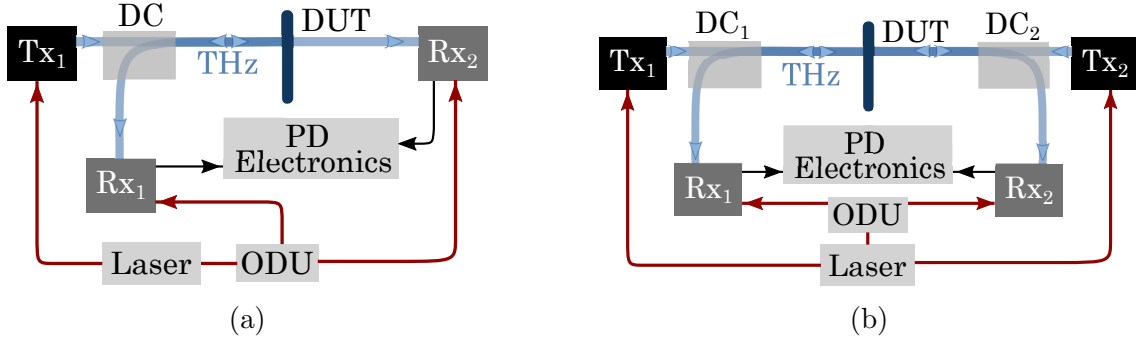


Figure 3.1: Simple block diagrams of (a) a 1.5 port VSM and (b) a two-port PVNA. Tx = Transmitter, Rx = Receiver, DC = Directional coupler, ODU = Optical delay unit, PD = Post-detection.

emits 45 mW of power, and the other emits a power of around 16 mW. It also consists of a free-space port that is phase-locked to the fiber ports, featuring a maximum of 350 mW of optical power.

3.1.2 Transmitters and Detectors: Pulsed Photoconductive THz Emitters and Detectors

The transmitters and the receivers are actualized by ErAs:In(Al)GaAs and ErAs:InGaAs based photoconductors, respectively. The emitter material is grown by molecular beam epitaxy at standard growth temperatures of InGaAs (490 °C) and contains $90 \times [15 \text{ nm InGaAs} \mid 1.5 \text{ nm C:InAlAs} \mid \delta_C 0.8 \text{ ML ErAs} \mid 1.5 \text{ nm C:InAlAs}]$ superlattice structure as previously published in Reference [214]. The photoconductor exhibits a resistivity of $3850 \Omega \text{ cm}$ and mobility of approximately $450 \text{ cm}^2/\text{Vs}$ [214]. For the detector structure, the C-doped InAlAs layer is excluded to facilitate a shorter carrier lifetime [215–217]. A total of 100 superlattice periods containing $[10 \text{ nm InGaAs} \mid \delta_C 0.8 \text{ ML ErAs}]$ are incorporated into the detector construction, which shows enhanced mobility of $775 \text{ cm}^2/\text{Vs}$ and a reduced resistivity of $240 \Omega \text{ cm}$ [214]. The carrier lifetime of the ErAs:InGaAs detector is $0.388 \pm 0.036 \text{ ps}$, whereas, for the emitter, it is $1.842 \pm 0.029 \text{ ps}$ [161]. The effective carrier lifetime of these photoconductors is reported to decrease almost linearly with increasing bias [76].

A $25 \mu\text{m}$ gap slotline antenna on the emitter material and a $5 \mu\text{m}$ gap H-dipole antenna on the detector are deposited to enable the THz radiation to be transmitted and received, respectively. The photoconductors are mounted on highly resistive, hemispherical silicon lenses with 10 mm diameter and 6.1 mm thickness to facilitate incoupling and outcoupling of the THz radiation [218]. Finally, the photoconductive devices are semi-packaged for device protection and robustness, i.e. integrated with a silicon lens and electrical BNC connectors but not with an optical fiber. Such packages necessitate the alignment of the laser spot with the active area but offer more flexibility for THz setup optimization.

With the Menlo C-fiber laser [213], the same as the one described in Section 3.1.1, this transmitter-receiver pair in a typical transmission THz-TDS setup achieves a 90 dB peak Dynamic Range (DNR) with more than 6.5 THz bandwidth (averaged over ~ 2000 scans with 6-8 min acquisition time). For this measurement, the transmitter and receiver are driven with

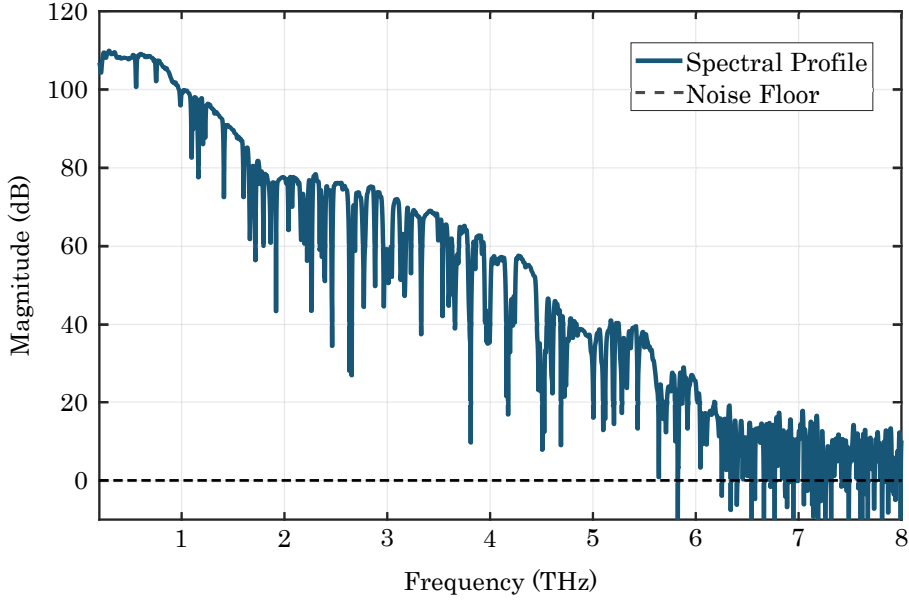


Figure 3.2: THz performance of the ErAs:In(Al)GaAs transmitter and ErAs:InGaAs receiver pair driven by a TeraFlash Pro laser system [212] for a transmission geometry THz-TDS setup. Adapted with permission from [76] ©2022 IEEE.

45 mW and 16 mW of optical power, respectively, and the transmitter is biased at 200 V [214]. In the latest publication regarding this transmitter-receiver pair, Nandi *et al.* reported a 110 dB peak DNR with more than 6 THz bandwidth (averaged over ~ 1000 scans with 1 min acquisition time), when operated in conjunction with the TeraFlash Pro [212] laser system (1550 nm operating wavelength, ~ 90 fs pulse width, 100 MHz repetition rate) driving the devices with 15 mW of power each [76] (Figure 3.2).

3.1.3 Test Set: Wire Grid Polarizer-based Directional Coupler

Measuring the reflection coefficients requires separating the incident and reflected waves traveling to and from the DUT. For broadband investigation, a frequency-independent directional element is required for this purpose.

A directional coupler based on a set of Wire Grid Polarizers (WGPs) is preferable over interference-based Directional Couplers (DCs) due to their inherent broadband feature, which is crucial for pulsed THz system. WGPs consist of metallic wires separated by a distance much smaller than the wavelength of the incident electromagnetic wave. When an incident electromagnetic wave encounters these metal stripes, the polarization component parallel to the stripes is reflected, while the component perpendicular to the stripes is transmitted.

To realize the DC, the utilized WGPs comprise free-standing Tungsten wires, with $w = 10 \mu\text{m}$ thickness and $p = 25 \mu\text{m}$ pitch (fill factor, $F = w/p = 0.4$), as depicted in Figure 3.3. Extinction Ratio (ER) and Insertion Loss (IL) are the parameters used to assess the overall quality of the WGP. The ER is determined by

$$ER = 20 \log_{10} \left(\frac{E_{\perp}}{E_{\parallel}} \right) \quad (3.1)$$

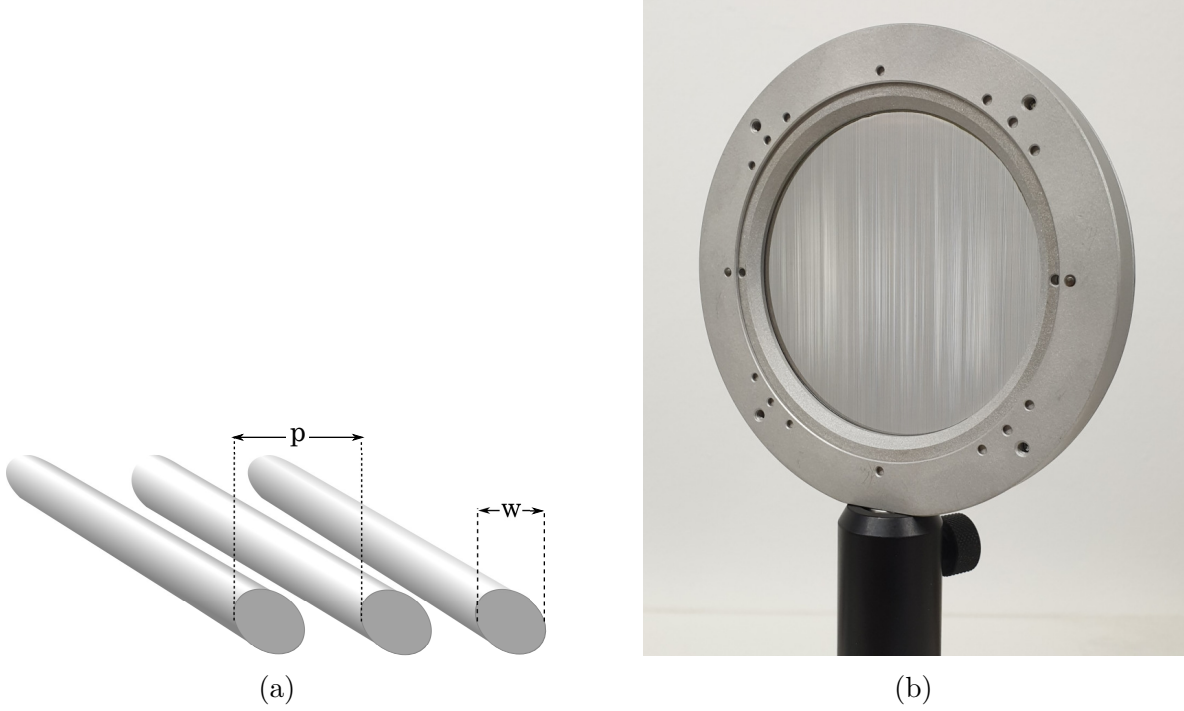


Figure 3.3: (a) Design parameters of the WGP, with diameter of the free-standing Tungsten wire $w = 10 \mu\text{m}$ and pitch $p = 25 \mu\text{m}$. (b) Photo of the WGP at 0° orientation.

where E_\perp is the transmitted E-field component perpendicular to the metal wires and E_\parallel is the unwanted signal or the transmitted E-field component parallel to the metal wires. The IL is expressed as

$$IL = 20 \log_{10} \left(\frac{E_\perp}{E_{ref}} \right) \quad (3.2)$$

where E_{ref} is the transmitted E-field in the absence of the WGP. The performance of the WGPs is evaluated using a commercial THz-TDS system, and the results are illustrated in Figure 3.4. The WGP shows a maximum ER of 40 dB at around 200 GHz, which reduces to 20 dB at around 2.5 THz. The IL increases with frequency and goes above 1 dB beyond 2 THz. From Figure 3.4, it is evident that the performance of the WGP degrades above 2 THz. However, conducting experiments up to 2.5 THz is still feasible.

In addition to separating the incident and reflected THz pulses, the DC guides the transmitted THz pulse toward the corresponding receiver for backward propagation. The arrangement of WGPs functioning as frequency-independent DCs is depicted in Figure 3.5.

WGP₁ and WGP₄ are tilted at $\theta = 45^\circ$ to the optical axis. To achieve a projection of $\alpha = 45^\circ$ orientation, the wires are inclined at $\beta = \arctan(\tan \alpha \cos \theta) \approx 35^\circ$. The projected orientation of 45° (α) allows maximum THz power to be propagated through the first encountered polarizer in respective paths as the transmitters radiate linearly polarized signal at -45° . In contrast, the $\theta = 45^\circ$ tilt with respect to the wavefront of the emitted THz beam guides the reflected signals from the DUT toward the corresponding receivers. To prompt reflection, the THz beam polarization is rotated by employing WGP₂ and WGP₃ oriented at 90° , and tilted slightly to deflect undesirable scattered signals off-axis.

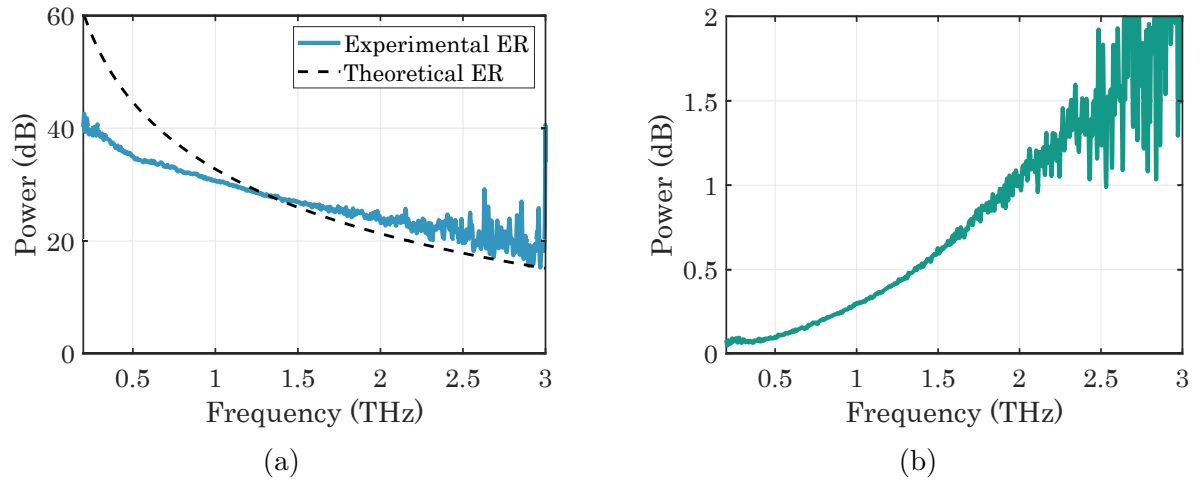


Figure 3.4: (a) Extinction ratio and (b) insertion loss of the WGP.

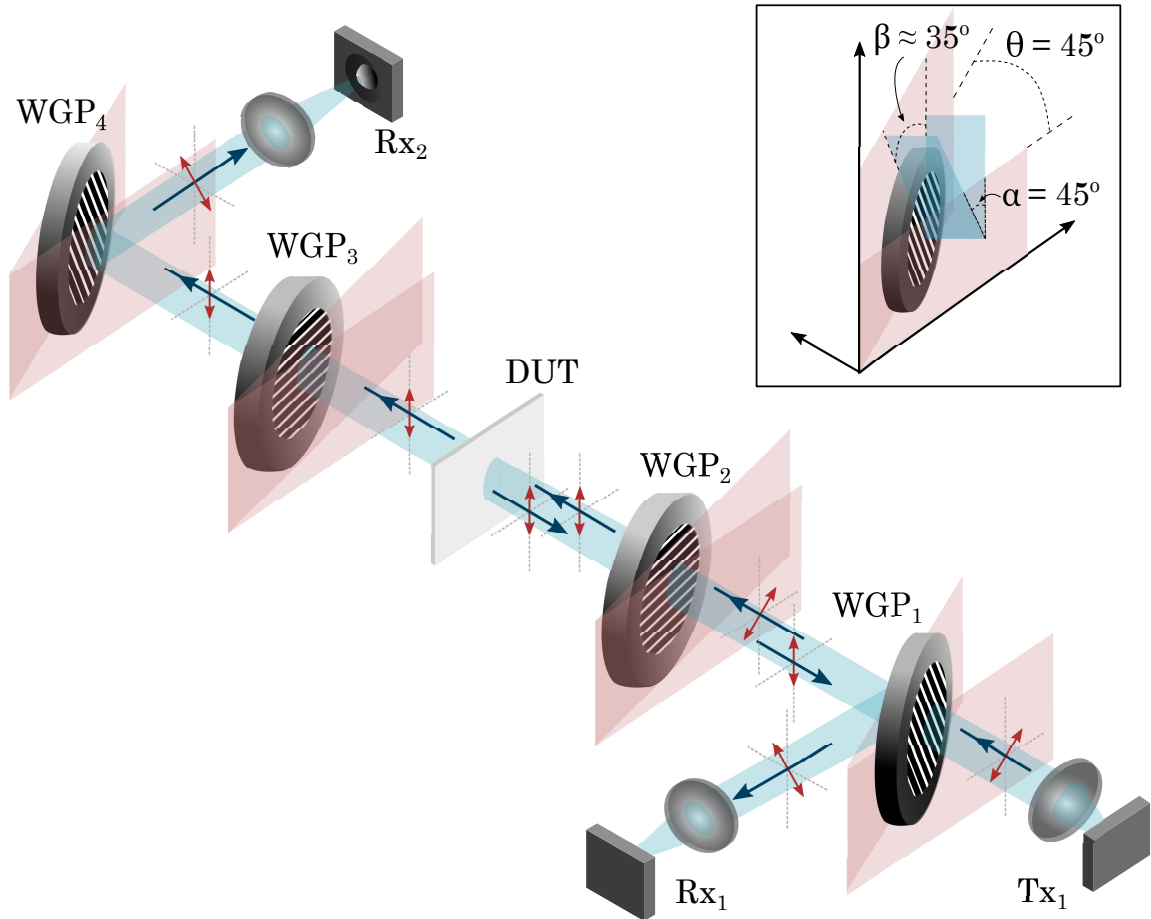


Figure 3.5: Operating principle of the WGP based DC for implementation in PVNA. Inset: Orientation of WGP_1 and WGP_4 .

For forward propagation, the diagonally polarized THz signal emitted from Tx₁ propagates through WGP₁ with an insertion loss of less than 1 dB and is subsequently converted to linear polarization by WGP₂. This conversion incurs a ~ 3 dB loss of signal power. Now the signal emerging after WGP₂ interacts with the DUT resulting in both transmission and reflection of the THz pulses. The reflected part propagates through WGP₂ unchanged in polarization, then gets reflected by WGP₁ with another ~ 3 dB loss towards Rx₁ at a diagonal polarization. The transmitted part similarly propagates through WGP₃ without changing polarization and is subsequently reflected by WGP₄, suffering a ~ 3 dB loss before getting detected by Rx₂ at diagonal polarization. For backward propagation, the THz signal emitted from Tx₂ also follows a similar path, and the transmitted and reflected signal from the DUT is detected by Rx₁ and Rx₂, respectively. Each signal path suffers ~ 6 dB loss due to polarization conversion and 1-2 dB more for insertion loss. However, this still yields a considerable signal due to the high available DNR of the system.

3.1.4 Post-Detection Electronics

The current generated in photoconductive detectors upon receiving THz pulses is generally between a few nA and a few pA. To amplify and transform current to voltage, a low noise Trans-Impedance Amplifier (TIA) from TEM Messtechnik (PDA-S) [219] is implemented. Subsequently, an Lock-In Amplifier (LIA) is utilized to extract the signal from the noisy background by demodulating the incoming signal at the reference frequency used for modulating the THz source. The demodulation process mainly involves multiplying the input signal with a sine wave at the reference frequency, followed by implementing a low pass filter with a predetermined time constant to obtain the DC component, which is the signal of interest. This is realized by employing LIAs from Zurich Instruments (MFLI-MD) [220], each consisting of two demodulators to simultaneously demodulate two differentially modulated incoming signals. Multiple LIAs can be synchronized so that their time stamps coincide. A graphic user interface designed in-house enables concurrent data reading and saving from the LIAs in sync with the delay stage movement (see Appendix A).

3.2 Calibration Standards and Calibration Process

Like EVNAs, the PVNA needs to be calibrated to eradicate systematic errors. However, this process is more straightforward for the PVNA, as the propagation occurs in the air with a well-known wave impedance of 376.7Ω . In contrast, for EVNA, the Smith chart has to be calibrated for the respective metal waveguides connected to the DUT. For the calibration of PVNA, we adapted a method that is similar to a combination of the ‘*Gated-Reflect-Line*’ (GRL) [149] and the ‘*Through-Through-Network*’ (TTN) self-calibration [151, 152] approach of EVNA (see Section 2.1.5). Mueh *et al.* also described a similar calibration technique for a 1.5-port system, which can be expanded to calibrate a complete two-port configuration [93].

A conventional EVNA calibration method implements a 12-term error model [126, 221, 222], with six terms each for forward and backward propagations. Although the complete set of S-parameters is retrieved concurrently in a PVNA, the signals emitted by various transmitters are effectively segregated from one another because their modulation frequencies are sufficiently spaced; therefore, there is almost no cross-talk. This indicates that the error terms determined for separate forward and reverse propagation models are valid for the two-port PVNA. Forward

and backward error models with six error components are depicted in Figure 3.6 and Table 3.1 describes the error sources. The error models and error-term calculations are partially based on the explanations found in References [93] and [222].

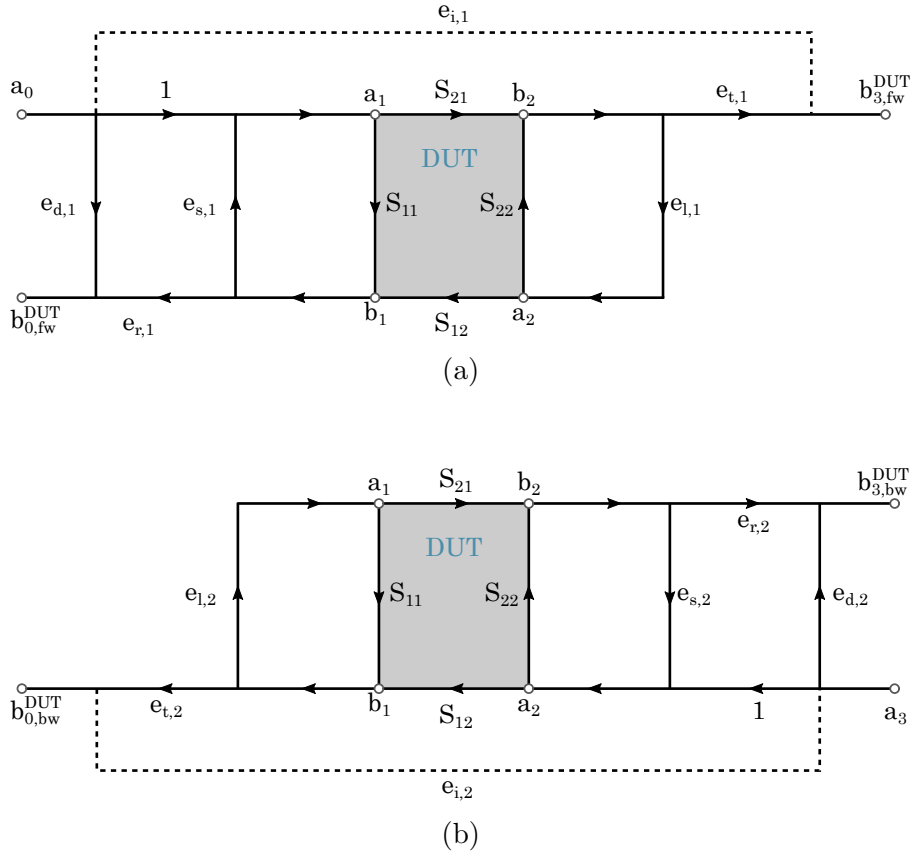


Figure 3.6: 6-term error model for (a) forward and (b) backward propagations.

Error term	Error Sources
$e_{d,1}, e_{d,2}$	Directivity
$e_{s,1}, e_{s,2}$	Source Match
$e_{r,1}, e_{r,2}$	Reflection Tracking
$e_{t,1}, e_{t,2}$	Transmission Tracking
$e_{l,1}, e_{l,2}$	Load Match
$e_{i,1}, e_{i,2}$	Leakage / Isolation

Table 3.1: Error sources.

As with the GRL method, time gating is implemented to calibrate the PVNA measurement for the elimination of source/load match error. As the measurement is already executed in the time-domain, it can be accomplished without requiring an inverse Fourier transformation of the measured data. Due to the finite delay length, the signal is already time gated; however, it may be further truncated to exclude signals interacting with the DUT multiple times, enabling perfect load/source matching. It is good practice to configure the system such that the unwanted reflections stemming from quasi-optical elements (such as beam splitters or lenses) arrive much later than the main pulse. We implement a modified Blackman window to realize the time gating to avoid any artifacts arising when the pulse is converted to the frequency-domain. For instance, if a rectangular window is utilized in the time-domain, it indicates a convolution between the THz spectrum and a sinc function in the frequency-domain, leading to enhanced side lobes [223]. Section 3.3.1 goes into further detail regarding the time-windowing procedure. By applying time gating, the error terms $e_{s,1}$ and $e_{l,1}$ for forward propagation and $e_{s,2}$ and $e_{l,2}$ for backward propagation can be eliminated.

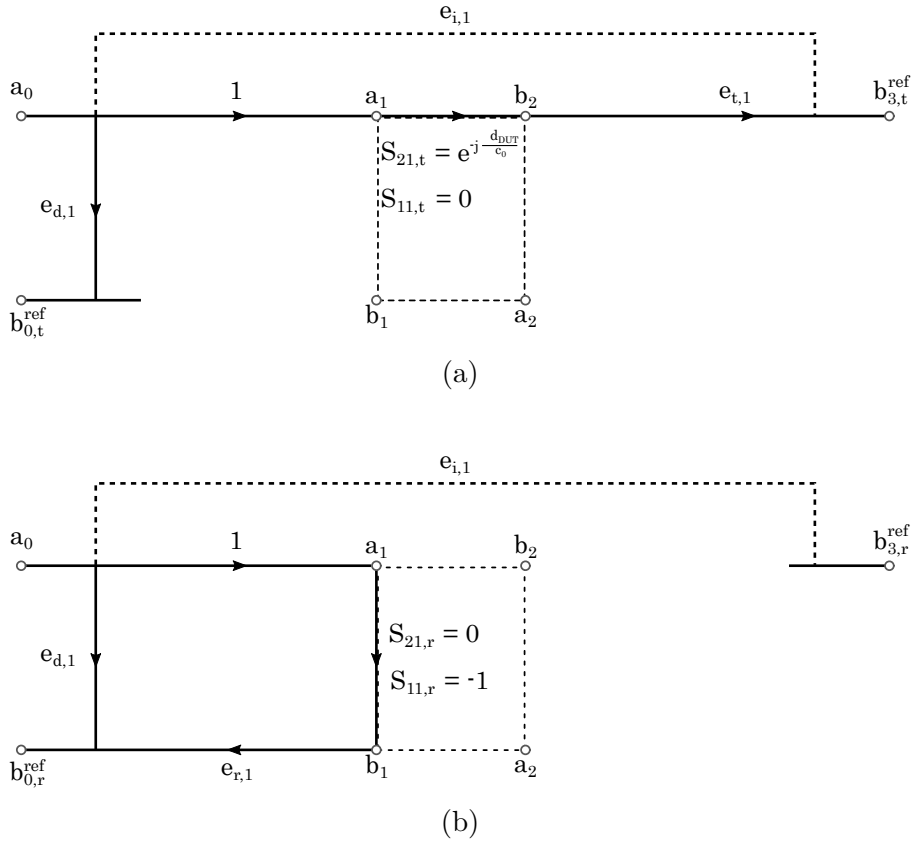


Figure 3.7: (a) *Through* and (b) *reflect* standard paths for forward measurement calibration.

For forward propagation with perfect source/load match ($e_{s,1} = e_{l,1} = 0$) the detected DUT/test signals are given by

$$b_{3,fw}^{DUT} = a_0(e_{t,1}S_{21} + e_{i,1}) \quad (3.3)$$

$$b_{0,fw}^{DUT} = a_0(e_{d,1} + e_{r,1}S_{11}) \quad (3.4)$$

To calculate the error terms, first the signals detected at both the receivers are recorded for an empty setup, similar to the reference measurement of a transmission THz-TDS. This corresponds to the *through* standard. From Figure 3.7(a), the detected reference signals can be expressed as

$$b_{3,t}^{ref} = a_0e_{i,1} + a_0e_{t,1} \exp(-j\phi_{DUT}) \quad (3.5)$$

$$b_{0,t}^{ref} = a_0e_{d,1} \quad (3.6)$$

where $\phi_{DUT} = \omega n_0 d_{DUT}/c_0$, with $n_0 \approx 1$ is the refractive index of air, d_{DUT} is the thickness of the DUT, and c_0 is the speed of light in vacuum. As the DUT is placed between the reference planes, the absence of it in the setup produces a phase difference that is dependent on the thickness of the DUT d_{DUT} . For performing the *through* calibration it is crucial to know the value of d_{DUT} . However, this phase difference between the DUT and reference measurements, which denotes the optical path length change introduced by placing the DUT in the setup, can also be used to extract material parameters such as refractive index and thickness as later explained in Section 3.3.2. Moreover, similar to the TTN technique, this broadband *through* measurement corresponds to several *line* measurements with 376.7Ω reference impedance. Since the electrical length varies with different frequencies, this corresponds to a change in the length of a mechanical line [152], eliminating the requirement for a separate *line* standard measurement.

Subsequently, a *reflect* standard is performed by placing a metal surface precisely at the position of the reference plane, similar to a reference measurement of the reflection THz-TDS. For this case, $S_{11} = -1$, and the detected reference signals are given by

$$b_{3,r}^{ref} = a_0e_{i,1} \quad (3.7)$$

$$b_{0,r}^{ref} = a_0(e_{d,1} - e_{r,1}) \quad (3.8)$$

From the above equations we can calculate the error terms as follows

$$e_{i,1} = \frac{b_{3,r}^{ref}}{a_0}, \quad e_{r,1} = \frac{b_{0,t}^{ref} - b_{0,r}^{ref}}{a_0} \quad (3.9)$$

$$e_{d,1} = \frac{b_{0,t}^{ref}}{a_0}, \quad e_{t,1} = \frac{b_{3,t}^{ref} - b_{3,r}^{ref}}{a_0} \exp(j\phi_{DUT}) \quad (3.10)$$

Now for a reference impedance $Z_0 = 376.7 \Omega$, the calibrated S -parameters can be expressed as

$$S_{21} = \frac{b_{3,fw}^{DUT} - b_{3,r}^{ref}}{b_{3,t}^{ref} - b_{3,r}^{ref}} \exp(-j\phi_{DUT}) \quad (3.11)$$

$$S_{11} = \frac{b_{0,fw}^{DUT} - b_{0,t}^{ref}}{-b_{0,r}^{ref} + b_{0,t}^{ref}} \quad (3.12)$$

From Equations 3.11 and 3.12, it is evident that both the reference and the DUT measurements are calibrated essentially by subtracting the corresponding error term or unwanted signal (transmitted signal when a mirror is placed and reflected signal when the setup is empty). The ratio of these calibrated test and reference signals yields the respective S -parameters. These calculations are repeated for backward propagation to obtain S_{12} and S_{22} parameters.

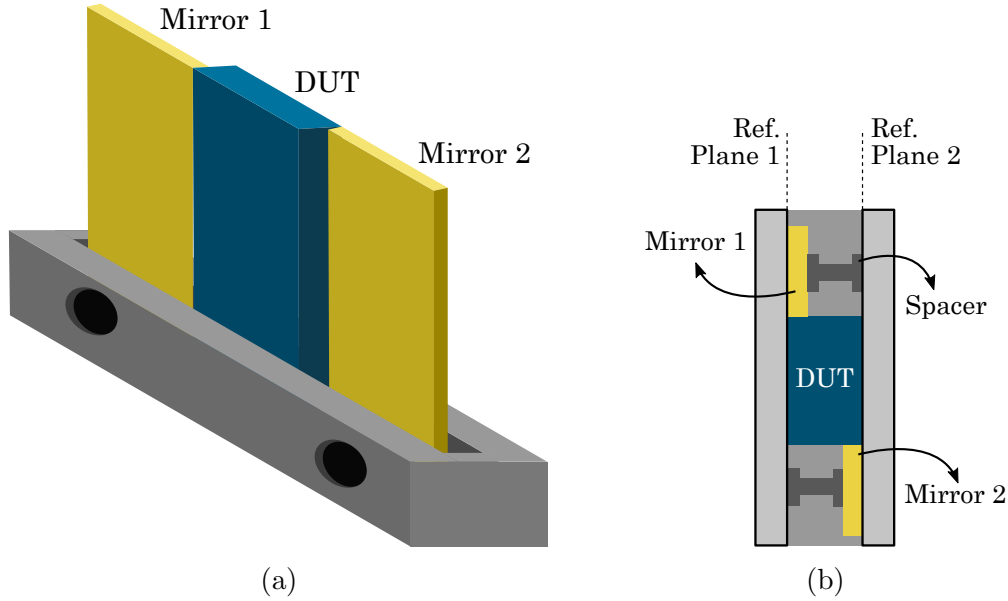


Figure 3.8: (a) Calibration tool. (b) Top view of the calibration tool.

To make the calibration process robust and repeatable, switching between DUT, reflector and empty configuration is the main challenge. Moreover, it is absolutely critical to ensure that the reference and the DUT planes are perfectly aligned. This is accomplished by implementing a calibration tool as depicted in Figure 3.8. One side of the tool is aligned with the DUT, while the other may be adjusted by a screw to match the reference plane established by the DUT. Two mirrors are positioned on two reference planes by implementing spacers to perform *reflect* calibrations for both ports. The calibration tool is mounted on a dovetail optical rail to facilitate switching between DUT and the mirrors. It can be moved out of the THz beam path to assume an empty setup configuration.

3.3 Data Evaluation

3.3.1 Time-Domain Data Processing

The time-domain signal is filtered and windowed to facilitate the extraction of DUT parameters (S -parameters and optical characteristics) and to eliminate spectral leakage and unwanted reflections within the setup. The raw data extracted from the lock-in amplifier contains oscillations, as depicted in Figure 3.9(a), due to resonances in the slot line antenna. Reflections of non-radiative frequencies within the antenna structure produce standing waves displaying

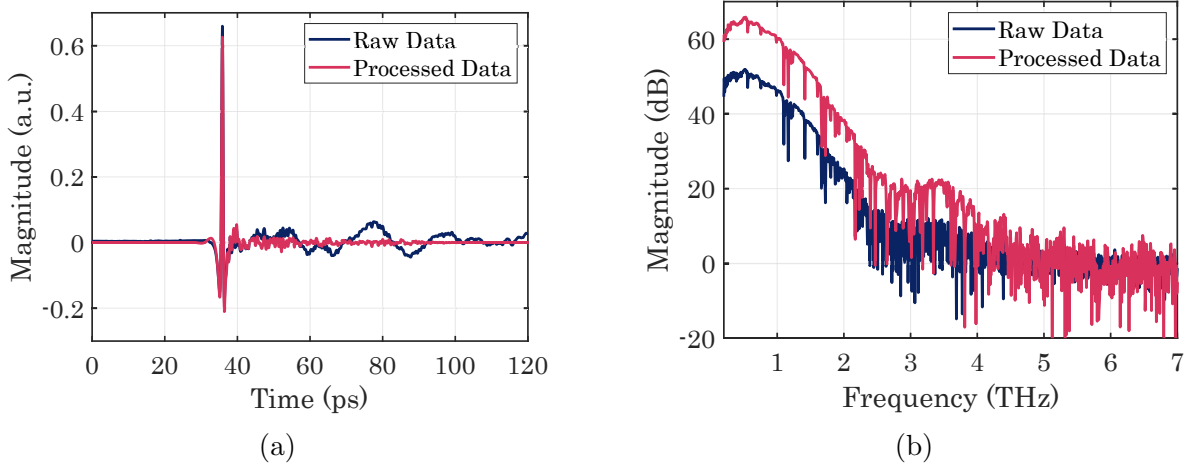


Figure 3.9: THz pulse before (blue) and after (red) processing. (a) Time-domain. (b) Frequency-domain.

strong resonance peaks separated by 50 GHz, with an effective wavelength equal to the strip's length [178]. These resonances exhibit different propagation constants compared to that of the leaky wave modes, resulting in dispersion of the emitted THz pulse and the manifestation of an unwanted time-harmonic oscillation following the primary pulse [178]. Due to these oscillations, it is challenging to distinguish the THz pulse, particularly for a highly absorptive DUT. To eliminate these oscillations, we implement a high-pass filter discarding any signal below 200 GHz. This also restricts the lower limit of the operational bandwidth to 200 GHz.

Applying apodization functions before performing a Fourier transform is a typical technique for reducing undesirable effects. Since the Fourier transform operates under the premise of infinite periodic signals, it is necessary to cope with the reality that experimentally obtained data is finite in the case of time-resolved measurements. Therefore, spectral leakage is an effect that must be considered [224]. Applying a suitable window to the time-domain signal is one way to eliminate this effect. In contrast, if no windowing was used, the finite length of the acquired signal acts as a rectangular window, which results in broadening and ringing in the spectrum [86]. The properties of the Fourier transform provide an explanation for this. Mathematically, the application of a rectangular window in the time-domain corresponds to multiplication with the Heaviside step function $\Pi(t)$, which goes from 1 to 0 at the point of truncation. This transforms into a convolution in the frequency-domain as

$$E_{THz}(t)\Pi(t) \xrightarrow{FT} E_{THz}(\omega) \otimes \mathcal{F}[\Pi(t)] \quad (3.13)$$

where $E_{THz}(t)$ is the unconstrained THz signal. The Fourier transform of the rectangular function $\Pi(t)$ with a finite measurement window of T is expressed as

$$\mathcal{F}[\Pi(t)] = \frac{T}{\sqrt{2\pi}} \left[\frac{\sin(\frac{\omega T}{2})}{\frac{\omega T}{2}} \right] \cdot \exp\left(\frac{-j\omega T}{2}\right) = \frac{T}{\sqrt{2\pi}} \left[\text{sinc}\left(\frac{\omega T}{2}\right) \right] \cdot \exp\left(\frac{-j\omega T}{2}\right) \quad (3.14)$$

The convolution of the THz spectrum with the sinc function produces a center maximum and several smaller side maxima, with the side maxima being responsible for spectral leakage [223]. The effect of spectral leakage is mitigated by employing a modified Blackman window, which

has been shown to enhance the DNR significantly [225]. In addition, this window enables the removal of undesired reflections caused by quasi-optical equipment, such as WGPs, lenses, etc., that arrive before and after the main pulse.

3.3.2 Algorithm for Material Characterization

A thorough understanding of the material's dielectric characteristics, such as its refractive index, absorption coefficient, or dielectric permittivity, is required before attempting to construct a THz component from it. For many years, free space EVNAs have been the system of choice for determining dielectric permittivity for frequencies lower than 300 GHz [59]. The use of commercially available frequency extenders has broadened the focus of the investigation to encompass signals up to 1.5 THz [60, 61]. Still, THz-TDS devices continue to be the preferred option for measuring the dielectric characteristics of materials beyond 3 GHz because of their extensive frequency coverage. However, THz-TDS systems are generally configured in either the transmission or reflection mode to characterize a material. With 1.5 port and two-port systems, the reflection and transmission coefficients are concurrently retrieved. This has proved to be useful not only because the availability of both measurements enhances accuracy (as demonstrated in our publication [226]) but also because the systems are adaptable since they enable the investigation of both transmissive and absorptive materials. To determine the complex refractive index or dielectric permittivity and thickness of the material under test we modified the algorithms reported by Taschin *et al.* [227] and Scheller [228] to incorporate both transmission and reflection data in conjunction. Since the Materials Under Test (MUTs) are plane-plane cut dielectrics, they are reciprocal in nature ($S_{21} = S_{12}$ and $S_{11} = S_{22}$); therefore, a measurement with only 1.5 ports is sufficient. Nevertheless, this technique may also be implemented on a two-port system. To a large extent, the algorithm described in this section is published in References [226] and [229].

The accuracy of the extracted parameters depends on the initial estimation of the thickness of the material. If the initial thickness is too far from the actual thickness, the algorithm optimizes for a local minima instead of a global one. Here, the time of flight technique is used to non-invasively estimate the thickness d_a from the peak locations in the time-domain data. The temporal delay Δt_1 between the reference pulse and the first transmitted pulse is derived from the transmission measurement shown in Figure 3.10 as

$$\Delta t_1 = (\bar{n} - n_0)d_a/c_0 \quad (3.15)$$

where \bar{n} is the mean refractive index of MUT, n_0 is the refractive index of air and c_0 is the speed of light. There are multiple peaks in both the transmission and reflection data due to round trips within the sample at intervals of

$$\Delta t_2 = 2\bar{n}d_a/c_0 \quad (3.16)$$

The values of \bar{n} and d_a can be derived from Equations 3.15 and 3.16. For materials with low absorption, d_a derived from time-domain data is fairly close to the actual value. In contrast, highly absorptive and dispersive materials suffer alteration in the form of the pulse relative to the reference pulse as a consequence of attenuation and a temporal shift of spectral components. In this case, the second peak for the first round trip or the first echo is sometimes indistinguishable in the transmission measurement (Figure 3.10 top). As shown in Figure 3.10 top inset, the THz

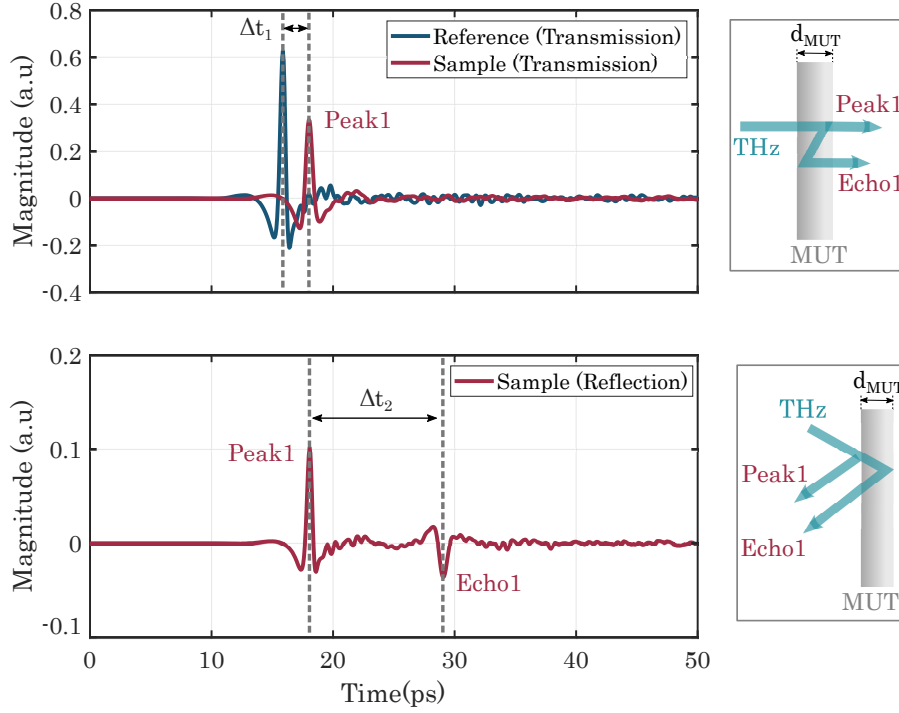


Figure 3.10: Measured transmitted (top) and reflected (bottom) time-domain THz pulse for absorptive materials. Inset: THz path of the main pulse (peak1) and first echo (echo1) transmitted through (top) or reflected from (bottom) the MUT. The echo of the transmitted pulse is too weak to distinguish from the noise floor. Adapted from [226] ©2018 IEEE.

pulses must travel $3d_{MUT}$ distance (where d_{MUT} is the thickness of the MUT) within the MUT and experience two transmissive and two reflective interactions at the MUT-to-air (or air-to-MUT) interface before the first echo can be recorded for transmission measurement. In reflection geometry (Figure 3.10 bottom inset), it travels a shorter $2d_{MUT}$ distance within the MUT and undergoes two interactions (one reflecting and one transmissive). Figure 3.10 depicts that for an absorptive MUT, the first echo is discernible only in reflection measurement for the above reasons. Therefore, the availability of data for both reflection and transmission is beneficial.

Now we convert the time-domain signal to the frequency-domain by fast Fourier transformation and calculate the field transmission and reflection coefficients (or S_{21} and S_{11} parameters) from the ratio of the DUT signal to the corresponding reference signal

$$S_{21}(\omega) = t(\omega) = \frac{E_T^{MUT}(\omega)}{E_T^{ref}(\omega)}, \quad S_{11}(\omega) = r(\omega) = \frac{E_R^{MUT}(\omega)}{E_R^{ref}(\omega)} \quad (3.17)$$

The phase for the transmission measurement is comparatively larger as it is prompted by the THz signal propagating through the whole thickness of the MUT and, unlike reflection measurement, is not prone to error due to misalignment of the DUT with the reference plane. For those reasons, the phase and amplitude recorded from transmission are utilized to determine the preliminary values of real ($n_a(\omega)$) and imaginary ($\kappa_a(\omega)$) part of the refractive index using

[206]

$$n_a(\omega) = n_0 - \frac{c_0}{\omega d_a} \angle t(\omega) \quad (3.18)$$

$$\kappa_a(\omega) = \frac{c_0}{\omega d_a} \left\{ \ln \frac{4n_0 n_a(\omega)}{(n_0 + n_a(\omega))^2} - \ln |t(\omega)| \right\} \quad (3.19)$$

where, $|t(\omega)|$ and $\angle t(\omega)$ are the magnitude and phase of the measured transmission coefficient. For the sake of calculation simplicity, the Fabry-Pérot (FP) component and the imaginary part of the refractive index in the Fresnel coefficients are disregarded in Equations 3.18 and 3.19. To prevent erroneous unwrapping, a modified phase unwrapping approach is employed [206].

The optimization procedure can then proceed from the preliminary values of d_a , $n_a(\omega)$ and $\kappa_a(\omega)$. An iterative technique numerically optimizes the frequency-dependent complex refractive index $\tilde{n}_a(\omega) = n_a(\omega, d_a) - j\kappa_a(\omega, d_a)$ by minimizing the global error function

$$err_g = \sum_{\omega} [(|t(\omega)| - |t_{th}(\omega)|)^2 + (|r(\omega)| - |r_{th}(\omega)|)^2] \quad (3.20)$$

and the local error function at each frequency step ω_x ,

$$err_l(\omega_x) = (|t(\omega_x)| - |t_{th}(\omega_x)|)^2 + (|r(\omega_x)| - |r_{th}(\omega_x)|)^2 \quad (3.21)$$

where $t_{th}(\omega)$ and $r_{th}(\omega)$ are the theoretical transmission and reflection transfer functions containing the fitted parameters. They are expressed as [206]

$$t_{th}(\omega) = \tau \tau' \exp \left[-j(\tilde{n}_a(\omega) - n_0) \frac{\omega d_a}{c_0} \right] FP(\omega) \quad (3.22)$$

$$r_{th}(\omega) = \rho + \tau \tau' \rho' \exp \left[-2j\tilde{n}_a(\omega) \frac{\omega d_a}{c_0} \right] FP(\omega) \quad (3.23)$$

where the FP term is given by

$$FP(\omega) = \left\{ 1 - \rho'^2 \exp \left[-2j\tilde{n}_a(\omega) \frac{\omega d_a}{c_0} \right] \right\}^{-1}, \quad (3.24)$$

and the field transmittance and reflectance are

$$\tau = \frac{2n_0}{n_0 + \tilde{n}_a(\omega)}; \quad \tau' = \frac{2\tilde{n}_a(\omega)}{n_0 + \tilde{n}_a(\omega)}; \quad \rho = \frac{\tilde{n}_a(\omega) - n_0}{n_0 + \tilde{n}_a(\omega)}; \quad \rho' = \frac{n_0 - \tilde{n}_a(\omega)}{n_0 + \tilde{n}_a(\omega)} \quad (3.25)$$

The numerical approach to determine the thickness and the complex refractive index of the MUT are outlined in a flow diagram in Figure 3.11. The initial thickness d_a is varied in arbitrarily selected increments of 0.001 mm, throughout a range of ± 0.1 mm. For each value of d_a , $n_a(\omega, d_a)$ and $\kappa_a(\omega, d_a)$ are calculated using Equations 3.18 and 3.19. However, $n_a(\omega, d_a)$ and $\kappa_a(\omega, d_a)$ are influenced by artificial oscillations as a result of the ignored FP term. In order to eliminate these FP oscillations and capture the actual physical frequency behavior, a polynomial fit of the optical parameters, with adjustable order and fitting range, is implemented.

A two variable Nelder-Mead (NM) simplex algorithm is used to optimize the fitted parameters for each value of d_a , with the goal of minimizing the global error function err_g . Through

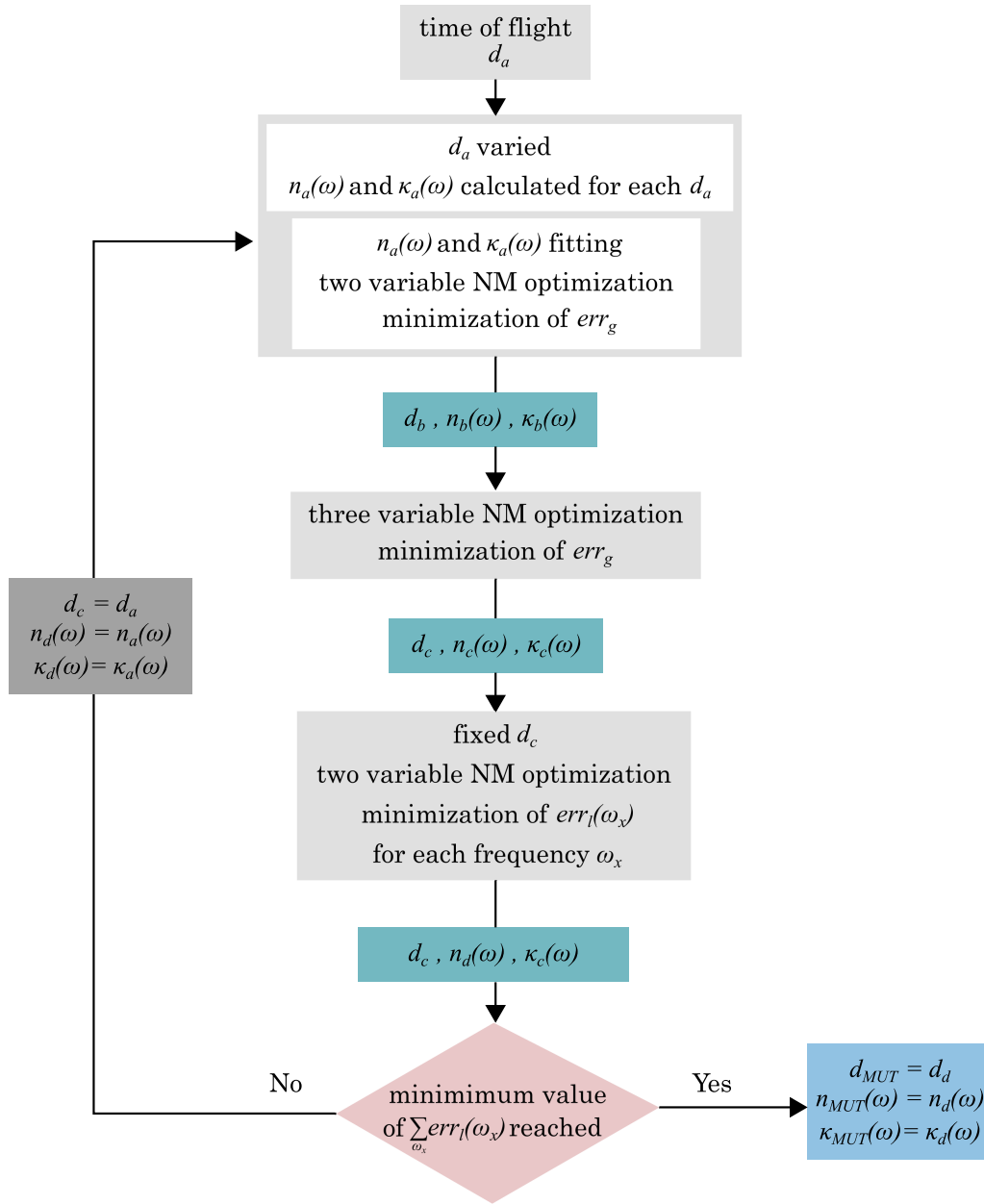


Figure 3.11: Schematic flowchart of the numerical approach for the determination of optical characteristics of a material. Adapted from [229] ©2021 Optical Society of America.

this optimization process, we obtain a thickness d_b along with $n_b(\omega, d_b)$ and $\kappa_b(\omega, d_b)$ such that err_g is minimized. Consequently, these parameters are fine-tuned using a three-variable NM process, yielding d_c , $n_c(\omega)$ and $\kappa_c(\omega)$. Finally, with the thickness held constant at d_c , the local error function $err_l(\omega_x)$ is minimized by optimizing $n_c(\omega)$ and $\kappa_c(\omega)$ for each frequency point ω_x . Any spectral details that were lost during the fitting procedure are now restored. The optimized values for d_c , $n_c(\omega)$ and $\kappa_c(\omega)$ are used as starting points for another round of optimization, and this procedure is repeated several times until a minimum value of $\sum_{\omega_x} err_l(\omega_x)$ is achieved.

From the determined extinction coefficient $\kappa_{MUT}(\omega)$ the absorption coefficient of the MUT can be calculated by

$$\alpha_{MUT} = \frac{2\omega\kappa_{MUT}(\omega)}{c_0} \quad (3.26)$$

The complex dielectric permittivity $\tilde{\epsilon}(\omega) = \epsilon'(\omega) - j\epsilon''(\omega)$ can be calculated from the extracted refractive index $n_{MUT}(\omega)$ and extinction coefficient $\kappa_{MUT}(\omega)$ using

$$\epsilon'(\omega) = n_{MUT}^2(\omega) - \kappa_{MUT}^2(\omega) \quad (3.27)$$

$$\epsilon''(\omega) = 2n_{MUT}(\omega)\kappa_{MUT}(\omega); \quad (3.28)$$

and the loss tangent by

$$\tan \delta(\omega) = \frac{\epsilon''(\omega)}{\epsilon'(\omega)} = \frac{2n_{MUT}(\omega)\kappa_{MUT}(\omega)}{n_{MUT}^2(\omega) - \kappa_{MUT}^2(\omega)} \quad (3.29)$$

The MATLAB code used to implement the algorithm is included in Appendix B. Based on a similar approach we also developed an application for the characterization of planer samples using commercial THz-TDS setup in transmission geometry (see Appendix C).

3.4 Conclusion

In this chapter, we covered the basics of the PVNA, including its components, how it is calibrated, and how data is analyzed. In the following chapters, we apply these techniques to construct THz-range characterization systems and execute practical applications designed to validate the effectiveness of such systems.

1.5 Port Pulsed Free Space Vector Spectrometer

With the purpose of developing efficient and affordable characterization systems in the THz range, a 1.5 port system is built, which is capable of conducting both transmission and reflection measurements simultaneously. The system can be utilized as a functional characterization instrument for component development as it is interesting for a variety of applications which requires concurrent measurement of S_{11} , S_{21} and S_{12} parameters.

Terahertz Time-Domain Spectroscopy (THz-TDS) is a popular non-contact, non-invasive and non-destructive technique for material property characterization in the THz range. The material studies with THz-TDS systems are conducted either in transmission [186, 230, 231] or reflection mode [191, 232–234]. Due to its higher accuracy and configuration convenience, the transmission geometry is typically selected; nevertheless, it is not appropriate for highly absorptive and opaque materials. The reflection geometry is applied in those circumstances. Reflection THz-TDS is very sensitive to the relative position of the reference mirror and the sample (misplacement error) [188] and the phase of the recorded reflected signal in this mode is significantly smaller [189]. As a result, the material parameters and the thickness extracted using the reflection geometry are prone to large errors. Moreover, for some components, such as metamaterials with a magnetic response (non-unity permeability) [235], or isolators that break Lorentz reciprocity [236], both transmission and reflection measurements are required to investigate their behavior.

The 1.5 port Vector Spectrometer (VSM) can simultaneously measure the transmittance and reflectance of a Device Under Test (DUT), since it integrates transmission and reflection geometries in a single setup. Compared to individual transmission or reflection mode configuration, the system is more versatile, accurate, and devoid of the inadequacies associated with transmission or reflection only measurement. Furthermore, for applications requiring both measurements, experimental errors due to sample positioning and transfer between two different setups are consequently prevented, resulting in shorter experimentation duration and decreased measurement uncertainty [237].

To date, several studies have reported systems that are capable of conducting both transmission and reflection measurements. In 2009, Brunner *et al.* [238] published an innovative system that simultaneously acquires reflection measurements at normal incidence and double

pass transmission measurements. This system is set up in a transceiver configuration in which the terahertz pulses are generated and detected in a single electro-optic crystal. This geometry allows reflection measurements at normal incidence without the drawback of a reduced terahertz signal caused by a beam splitter. The system is used to obtain the refractive index and absorption spectra of several materials as well as to measure phonon-polariton dispersion of salt crystals. However, this system requires a double pass through samples, adding complexities to the calculations, and is limited by the emitters or detectors that can be used in this configuration. Later, in 2013, Ung *et al.* [239] demonstrated a “dual-mode” spectrometer containing a large area inter-digitated array emitter with two photoconductive antennas as detector and a beam splitter acting as a directional coupler. The system has a usable reference bandwidth of approximately 3 THz and successfully characterized both float-zone (0.5-1 THz) and highly doped n-type silicon wafers (up to 2 THz) in terms of transmittance and reflectance. In 2018, we introduced our 1.5 port VSM and presented its capability in extracting the refractive index, absorption-coefficient and thickness of a highly absorptive material (Polyvinyl chloride) [226] and later in 2019, we showed its competence in characterizing a nonreciprocal device (THz Isolator) [240]. In 2021, Mueh *et al.* [93] published a paper about the error modelling and calibration scheme of such systems.

In this chapter, we discuss in detail about the 1.5 port VSM in terms of the experimental setup, system attributes and applications. The ability of this system is demonstrated in two main applications: characterization of a nonreciprocal device and extraction of optical parameters, i.e. refractive index, absorption coefficient and thickness of several materials.

4.1 Experimental Setup

Figure 4.1 illustrates a detailed diagram of a 1.5 port VSM containing one transmitter (Tx), and a pair of receivers Rx₁ and Rx₂, simultaneously recording the signals transmitted through and reflected from the DUT or Material Under Test (MUT), respectively. For this configuration, we use an ErAs:In(Al)GaAs-based photoconductive slotline antenna as transmitter and ErAs:InGaAs-based photoconductive H-dipole antennas as receivers. The photoconductors are driven using a mode-locked fiber laser from Menlo Systems [213] containing two fiber ports, which drive the receivers with 15 mW optical power each, and a free-space port that goes through a delay line and then drives the transmitter with 45 mW of optical power. A set of Wire Grid Polarizers (WGPs) (WGP₁ and WGP₂) functions as a broadband directional coupler and directs the reflected signal towards the receiver Rx₂, while WGP₃ functions only as a reflector, guiding the signal towards Rx₁. The transmitter and the receivers are polarization sensitive. Tx and Rx₂ are oriented at 45° to generate and detect THz wave with diagonal polarization, whereas Rx₁ is oriented at 0° to detect vertically polarized signal.

Generated THz pulses from Tx (with diagonal polarization) goes through WGP₁ and is converted to linear polarization at WGP₂ before interacting with the DUT. Depending on the properties of the DUT some part of the incident pulse is transmitted through and detected by Rx₁, and some part is reflected. The reflected signal goes back through WGP₂ without any change, followed by a 50% reflection to Rx₂ by WGP₁. Each polarization conversion from diagonal to linear and vice versa corresponds to a ~3 dB loss and a total of 6 dB loss for the reflected beam path. This means Rx₂ detects only 25% of the signal generated from Tx. However, this still yields a considerable signal due to the high available Dynamic Range (DNR) of the emitter. As opposed to interference-based directional couplers, the set of WGPs shows

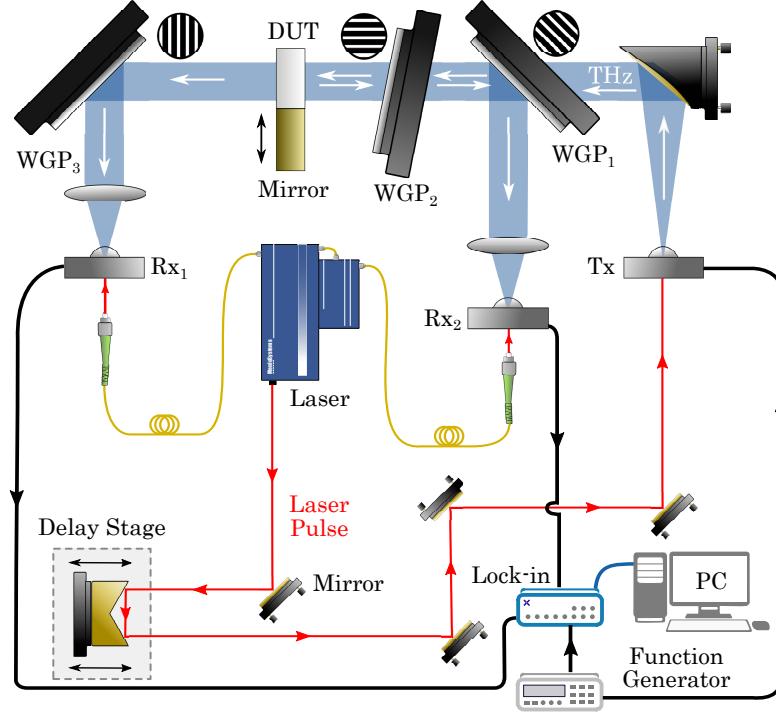


Figure 4.1: Schematic of 1.5 port VSM. WGP = Wire Grid Polarizer, DUT = Device under test, Tx = Transmitter, Rx = Receiver.

little frequency dependence up to several THz (~ 2.5 THz, see Section 3.1.3), which is a must for a pulsed THz system. The emitter is biased with a 90 V (peak) sinusoidal signal modulated at 11.17 kHz. Two lock-ins (Zurich Instruments MFLI-MD) [220] are used (one for each receiver output) with a synchronized time stamp to demodulate the received signals. Prior to the readout, a low noise transimpedance amplifier from TEM Messtechnik (PDA-S) [219] is used for both receivers. An in-house configured graphic user interface facilitates data reading and saving from the lock-ins concurrently in sync with the delay stage movement (A). A detailed description of the components used for this setup can be found in Section 3.1.

4.2 System Attributes

Like most of THz-TDS systems, the characterization process is done by calculating the transmittance ($T(\omega)$) and reflectance ($R(\omega)$) of the DUT, which is calculated by the ratio of the signal that is transmitted through or reflected from the DUT to the reference signal. In case of transmission geometry, the reference measurement is done by recording the signal transmitted through an empty setup ($E_{ref,t}(\omega)$). And for the reflection geometry reference measurement, a metal mirror is placed in the setup and the reflected signal ($E_{ref,r}(\omega)$) is recorded. Then the mirror is replaced by the DUT and both transmission ($E_{sam,t}(\omega)$) and reflection ($E_{sam,r}(\omega)$) measurements are recorded simultaneously and $t(\omega)$ and $r(\omega)$ are calculated as

$$t(\omega) = \frac{E_t^{DUT}(\omega)}{E_t^{ref}(\omega)}, \quad r(\omega) = \frac{E_r^{DUT}(\omega)}{E_r^{ref}(\omega)} \quad (4.1)$$

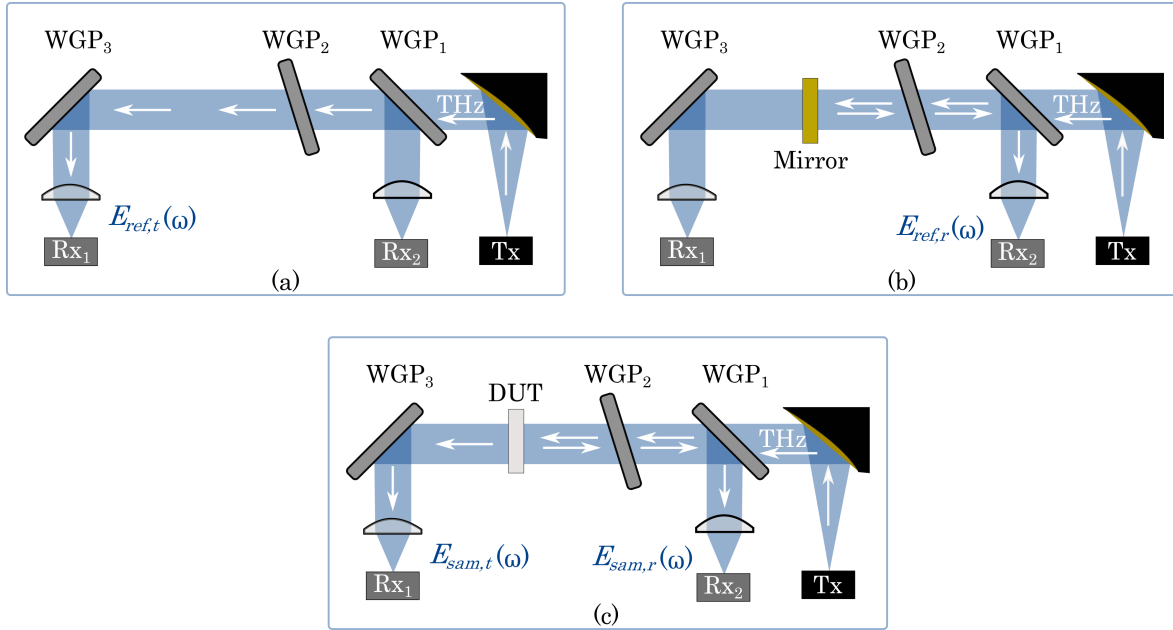


Figure 4.2: Reference measurement for the a) transmission (empty setup) and b) reflection (mirror) modes of the 1.5 port VSM. c) DUT measurement of the 1.5 port VSM.

For the reflection case it is absolutely important to put the mirror and the DUT exactly at the same place. Misplacement errors lead to erroneous phase determination, which in turn results in systematic errors in the determined DUT parameters, especially the refractive index.

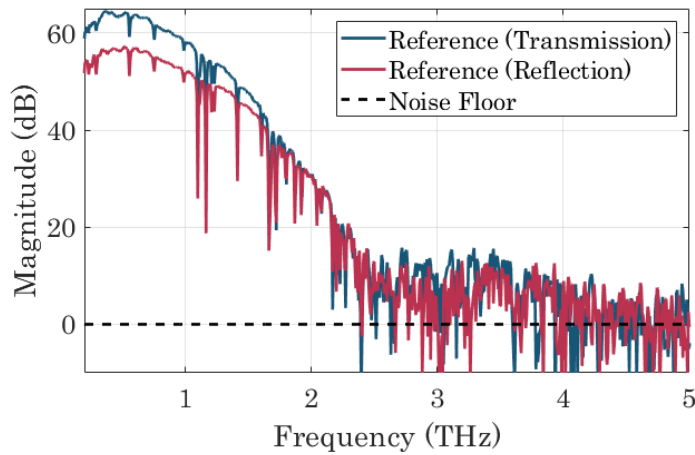


Figure 4.3: System attributes of the 1.5 port pulsed free space VSM. Available bandwidth 0.2-2.5 THz, with peak DNR of ~ 64 dB and ~ 57 dB (Equivalent Noise Bandwidth (ENBW) = 9.196 Hz) for transmission and reflection cases, respectively.

The reference measurements in this case provides a good knowledge about the available system attributes in terms of bandwidth and DNR. Figure 4.3 shows the reference spectra for transmission and reflection measurements. From the figure it is apparent that for both the transmission and reflection case the available bandwidth is around 0.2-2.5 THz, with the transmission geometry having a higher peak DNR of ~ 64 dB compared to ~ 57 dB peak DNR of the reflection case at around 0.5 THz (the transmitted beam path is shorter and only encounters one polarization conversion). However, at high frequencies (above 1.5 THz) both exhibits essentially the same DNR. The measurements reported in the figure are taken with a 3rd order low pass filter with an integration time of 10 ms (ENBW = 9.196 Hz) per time step and a wait time of 100 ms between subsequent points. The spectral resolution of the system is ~ 7 GHz.

4.3 Applications

4.3.1 Material Parameter Extraction

Accurate knowledge of the material properties is crucial for the design and development of THz system components such as waveguides [241–243], sensors, filters [244,245], lenses, metamaterials [246], metasurfaces [247,248] and absorbers [249]. THz-TDS has established itself as a very popular technique for material characterization in the THz range due to its wide bandwidth, which incorporates the spectral fingerprints of numerous materials, higher spatial resolution than microwaves, and ability to perform in-situ characterization through packaging materials (dry non-polar common packaging materials are transparent to THz) [250].

So far, significant efforts have been undertaken to optimize either transmission or reflection geometry THz-TDS. The 1.5 port VSM incorporates both systems in one and it is more adaptable and accurate. It is not limited by the type of material under investigation as the transmission THz-TDS is for highly absorptive and opaque materials and less prone to errors, unlike the reflection THz-TDS. In this section, we discuss about the determination of material properties performed using a 1.5 port VSM verifying its capability for such applications. The thickness of the sample is also concurrently extracted, which is very important for quality control applications [251,252].

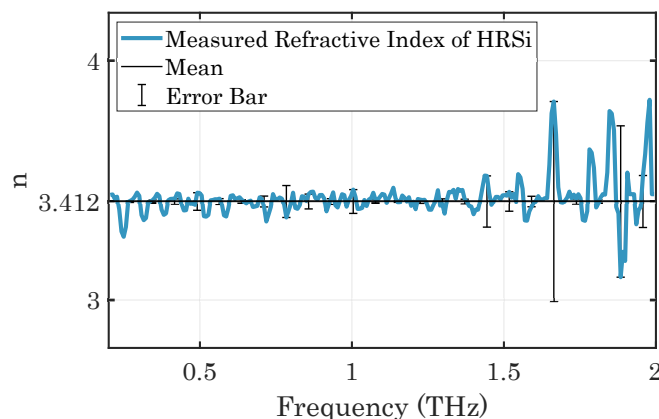


Figure 4.4: Refractive Index of Highly-resistive Silicon (HR-Si).

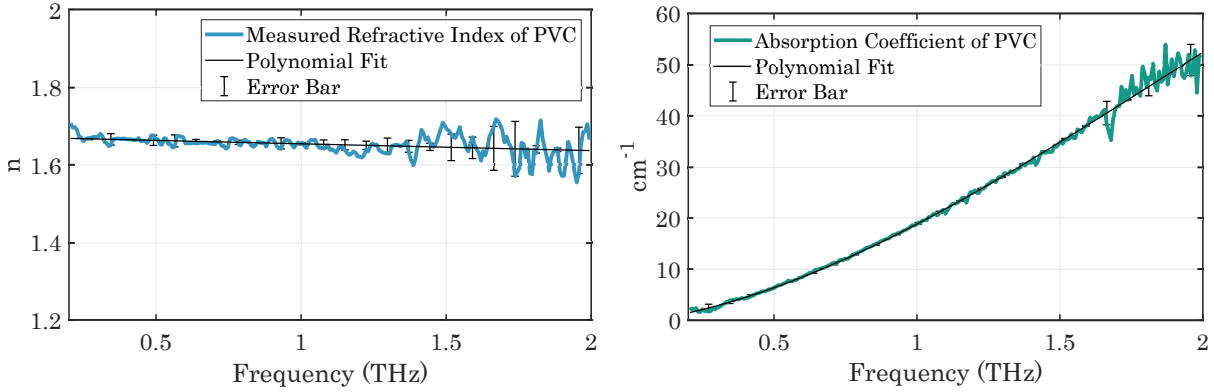


Figure 4.5: Refractive index (left) and absorption coefficient (right) of Polyvinyl chloride (PVC).

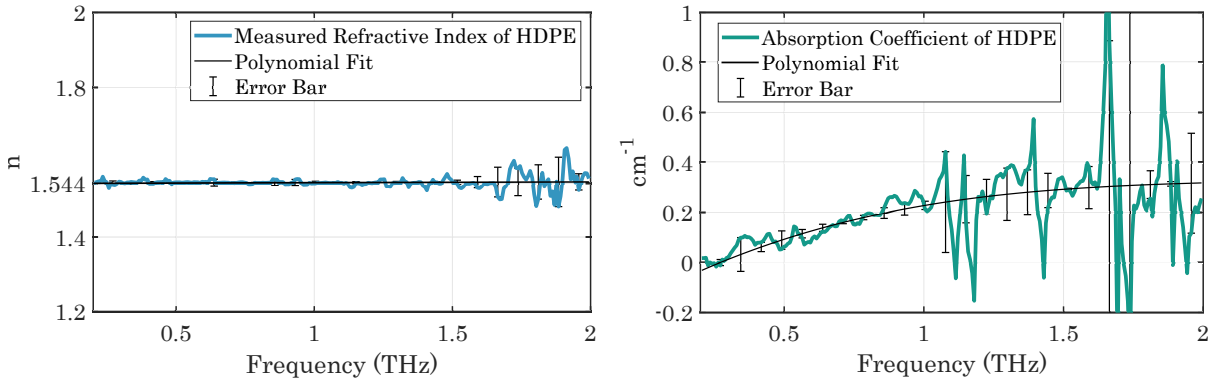


Figure 4.6: Refractive index (left) and absorption coefficient (right) of High-density polyethylene (HDPE).

First, the reference signals are recorded. For the transmission case, it is the THz signal transmitted through an empty setup (Figure 4.2(a)). For the reflection case, it is the THz signal reflected from a metal mirror (Figure 4.2(b)) exactly aligned to the first surface of the DUT using a custom holder. In the next step, the metal mirror is replaced with the MUT and both the signals transmitted through and reflected from the MUT are measured simultaneously (Figure 4.2(c)). These measured signals are then used to extract the refractive index, absorption coefficient as well as thickness of the material using the algorithm described in Section 3.3.2. Three different types of materials, namely, HR-Si ($>10000 \Omega\text{cm}$), PVC and HDPE are characterized and the results are reported in Figures 4.4, 4.5 and 4.6, respectively. The results are also summarized in Tables 4.1 and 4.2.

The extracted thickness using the 1.5 port VSM matches with the caliper measurements as shown in Table 4.1, however, with a factor of 20 higher precision. The error range of $\pm 0.005 \text{ mm}$ is observed by repeating the measurement several times for this specific measurement setup parameters. The extracted refractive indices and absorption coefficients are compared with the

Material	Extracted Thickness (mm)	Calliper Thickness (mm)
HR-Si	0.6518 ± 0.005	0.65 ± 0.01
PVC	1.0078 ± 0.005	1.01 ± 0.01
HDPE	2.9745 ± 0.005	2.98 ± 0.01

Table 4.1: Comparison between extracted and mechanically measured thickness by a Caliper.

Material	Extracted Refractive Index	Literature Refractive Index	Extracted Absorption Coefficient (at 1 THz)	Literature Absorption Coefficient (at 1 THz)
HR-Si	3.412 ± 0.06	3.42 ± 0.001 [253]	-	0.05 cm^{-1} [253]
PVC	1.668-1.637	1.64 - 1.59 [254] 1.675 - 1.645 [255]	18.85 cm^{-1}	21 cm^{-1} [255]
HDPE	1.544 ± 0.028	1.535 [247] 1.54 ± 0.01 [83]	0.22 cm^{-1}	0.22 cm^{-1} [247] 0.225 cm^{-1} [83]

Table 4.2: Comparison of extracted refractive index and absorption coefficient with literature data.

previously reported data in Table 4.2. For HR-Si the extracted refractive index is 3.412 ± 0.06 , in excellent agreement with the literature value of 3.42 [253]. The absorption coefficient for HR-Si is very small and below the detectable limit of the system with the available DNR. The refractive index of PVC shows a gradual decrease from 1.668 to 1.637 within 0.2 – 2 THz range. PVC is highly absorptive, exhibiting a power absorption coefficient $\alpha = 18.95 \text{ cm}^{-1}$ and 52.23 cm^{-1} at 1 THz and 2 THz, respectively. Compared to PVC, HDPE absorbs very little in the THz range, with $\alpha = 0.232 \text{ cm}^{-1}$ at 1 THz and $\alpha = 0.316 \text{ cm}^{-1}$ at 2 THz. The extracted refractive index of 1.544 ± 0.028 of HDPE also matches with previous reports. The error margins included in the refractive index measurements are the standard deviation from the mean or polynomial fit, excluding the artifacts resulting from the water absorption lines.

4.3.2 Device Characterization

As an example for device characterization, we analyze a Terahertz isolator. Isolators are nonreciprocal devices with the ability to disrupt time-reversal symmetry allowing only forward electromagnetic wave propagation with low losses and prevent backward propagation, prompting a substantial attenuation. It is crucial for the protection of source and detector, mitigating multipath interference, suppressing undesired signal routing, impedance matching, noise-cancelling, and decoupling [256–259]. THz isolators play a significant role in protecting highly sensitive detection systems [260, 261] and high-power terahertz sources [262–264] from the THz echoes caused by the reflection and scattering from the system components. These factors have led many research groups to develop THz isolators by implementing various strategies [265–269]. The characterization procedure for such components involves the measurement of both the

transmitted and the reflected signals, which necessitates switching between transmission and reflection geometries when classical THz-TDS setups are employed. In this section, we discuss the characterization of a THz isolator using the 1.5 port VSM that minimizes discrepancies that may arise while switching between setups.

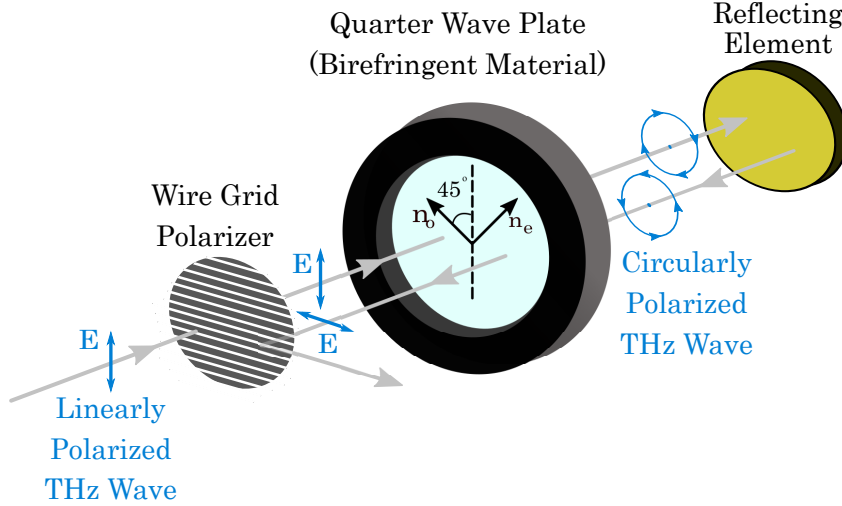


Figure 4.7: Operating principle of a THz Isolator. Reprinted with permission from [240] ©2019 IEEE.

A WGP and a birefringent material acting as a Quarter-Wave Plate (QWP) are combined to form the isolator under investigation, a design that is commonly employed in optics [270, 271] and later adapted in the THz range [272]. Figure 4.7 explains the basic principle of such an isolator. The fast axis of the QWP is oriented at a 45° angle with the incoming vertically polarized signal. Upon incidence, the electromagnetic wave is divided into two equal components that experience different refractive indices (n_e and n_o) and travel at different velocities within the material. After propagating through the thickness (d) of the birefringent material, the two orthogonal components obtain a phase difference of $\Delta\phi = k_0 d |n_o - n_e|$, where, $k_0 = \frac{2\pi f}{c_0}$ is the THz wave vector and c_0 is the speed of light in vacuum. At the design frequency, the phase difference becomes $\Delta\phi = (2m + 1)\frac{\pi}{2}$, converting the incident vertically polarized signal into a circularly polarized one. Any back-reflected signal propagates through the QWP again, resulting in a total phase difference of $\Delta\phi = (2m + 1)\pi$, between the orthogonal components. The polarization of the resultant beam becomes linearly polarized but rotated by 90° - making it orthogonal to the input signal polarization. Now this horizontally polarized signal is diverted by the WGP in the off-axis direction blocking it from backtracing the original path further than the WGP. Maximum isolation for this isolator configuration is achieved at frequencies $f_m = \frac{(2m+1)c_0}{4d|n_o-n_e|}$.

A Sapphire wafer, with 10-10 crystal orientation, is utilized as the QWP for the configuration of the isolator. The 10-10 cut sapphire crystal displays uniaxial birefringence due to its trigonal structure [273]. Figure 4.8 shows the extracted ordinary (n_o) and the extraordinary (n_e) refractive indices of the wafer that are determined using a data evaluation method similar to the one described in Section 3.3.2. A nitrogen purged commercial transmission geometry

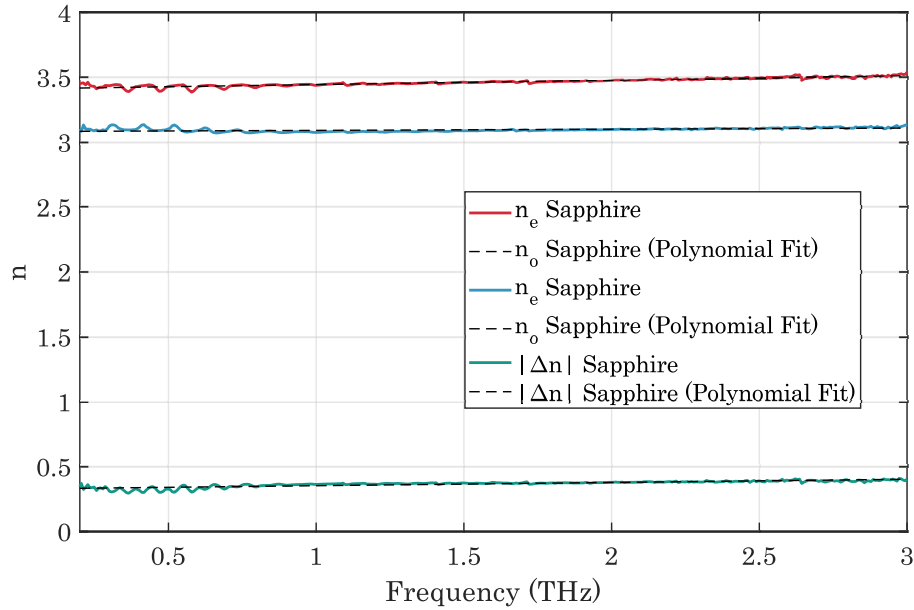


Figure 4.8: Ordinary (n_o) and extraordinary (n_e) refractive indices of 10-10 cut Sapphire and the difference between them (Δn), calculated from THz-TDS measurement data.

THz-TDS system (Menlo systems) is used to record the THz signals at two different polarization. The retrieved parameters ($n_o = 3.444$, $n_e = 3.091$ and $\Delta n = -0.353$ at 1 THz) are slightly higher compared with previously reported results for 10-10 crystal orientation of sapphire ($n_o = 3.39$, $n_e = 3.07$ and $\Delta n = -0.32$ at 1 THz) [273], but within the error limit. However, Δn shows a linear increase with increasing frequency, reaching -0.378 and -0.403 at 2 THz and 3 THz, respectively. The thickness extracted from the algorithm is 0.4181 ± 0.005 mm. Theoretical isolation level and insertion loss of the isolator are calculated by applying the data shown in Figure 4.8 to compare with the experimental results.

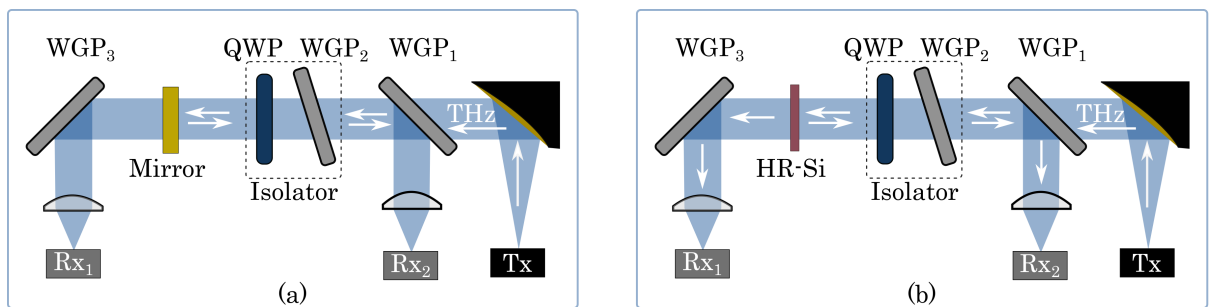


Figure 4.9: Experimental configurations for investigating the behavior of the isolator.

Figure 4.9 shows the experimental setup employed to determine the isolation level and the insertion loss of the isolator under investigation. In this case, the isolation level and the insertion loss are given as

$$\text{Isolation Level} = \frac{\text{Reflected THz signal without QWP in the setup}}{\text{Reflected THz signal with QWP present in the setup}}$$

$$\text{Insertion Loss} = \frac{\text{Transmitted THz signal without QWP in the setup}}{\text{Transmitted THz signal with QWP present in the setup}}$$

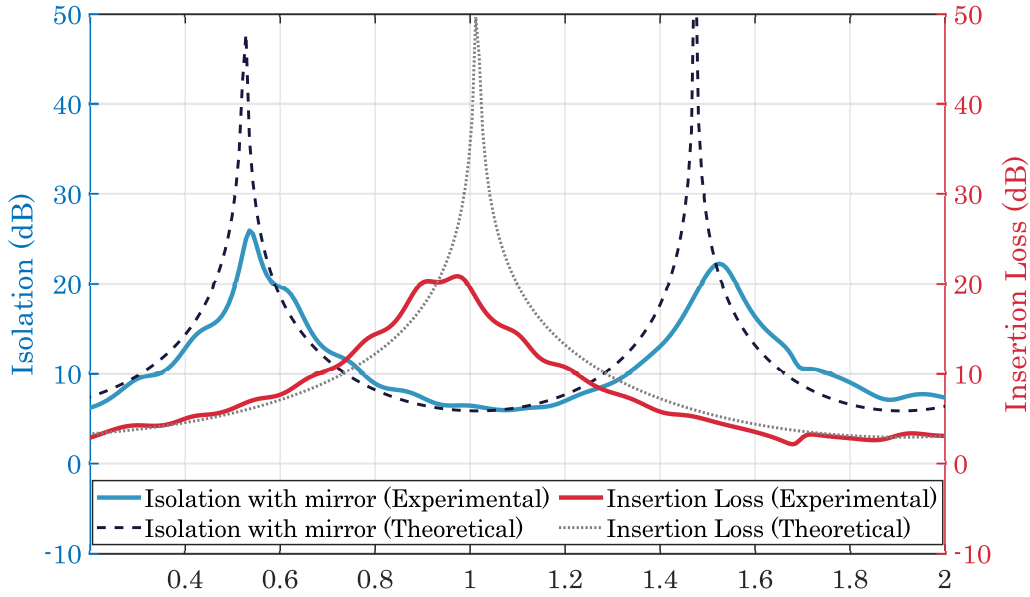


Figure 4.10: Measured isolation and insertion loss for the THz isolator with metal mirror as the reflecting element.

Two different cases are investigated. For the first case illustrated in Figure 4.9(a), the back reflection is prompted by a metal reflector after the QWP and then the reflected THz signals are recorded first with the QWP present and then after removing it from the system. For the insertion loss measurement, the mirror is removed and transmitted signals with and without QWP are recorded. For the second case (Figure 4.9(b)), the mirror is replaced by a HR-Si wafer and the measurements are repeated. However, in this case, the transmission and reflection measurements are recorded simultaneously. Figures 4.10 and 4.11 depict the extracted isolation level and insertion losses for the setups with metal mirror and the HR-Si wafer, respectively.

In the Figures 4.10 and 4.11, the isolation is prominent at 0.542 THz and 1.517 THz, within the range of 0.2-2 THz. For these cases the isolation levels are 26 dB and 22.23 dB, respectively, with insertion loss of 6.91 dB and 4.49 dB. This signifies that at $f_{iso,1} = 0.542$ THz only 0.2% signal can backtrace the original path, whereas 20% of the signal can transmit. For $f_{iso,2} = 1.517$ THz, 0.6% of the input signal returns back and 35% of the signal propagates in the forward direction.

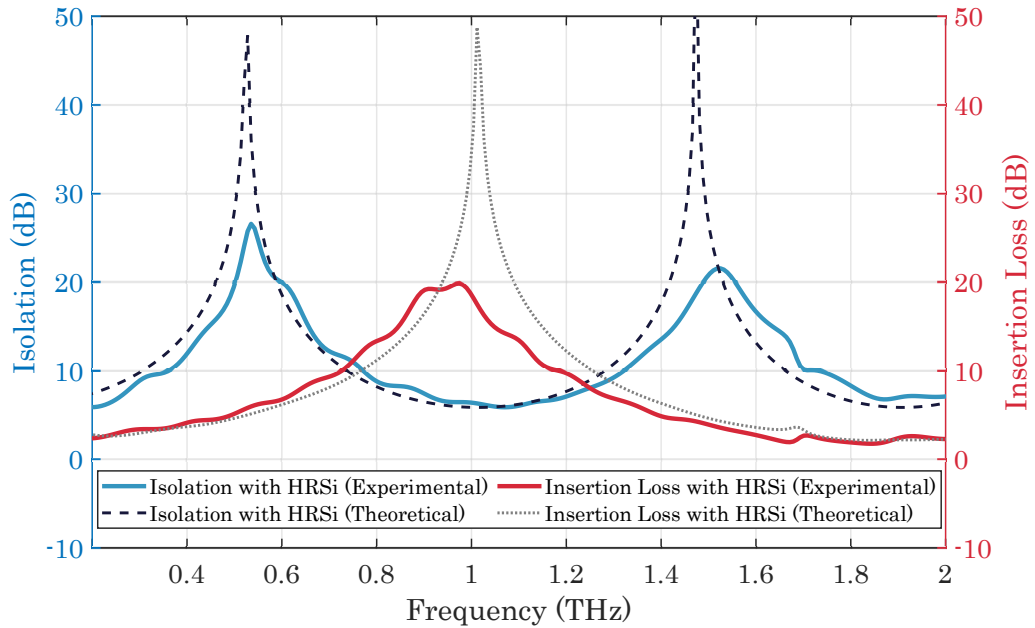


Figure 4.11: Measured isolation and insertion loss for the THz Isolator with HR-Si wafer as the reflecting element.

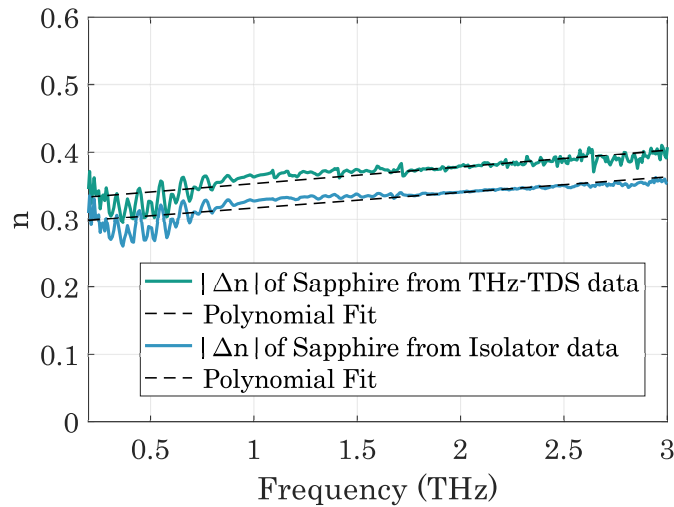


Figure 4.12: Extracted refractive index difference from THz-TDS measurements and isolator data.

The isolation level and insertion loss achieved by the isolator is not as good as predicted by the theory. The extinction ratio of the WGP, the positioning and the orientation of the QWP are contributing factors to this mismatch. The discrepancies between the theory and experimental data is most likely attributed to imprecise thickness and refractive index extraction. So the experimental data is fitted to find the thickness and refractive index difference of the Sapphire wafer and the results are depicted in Figures 4.13 and 4.14, respectively. The refractive index difference extracted from the fitting is compared with the THz-TDS measurement in

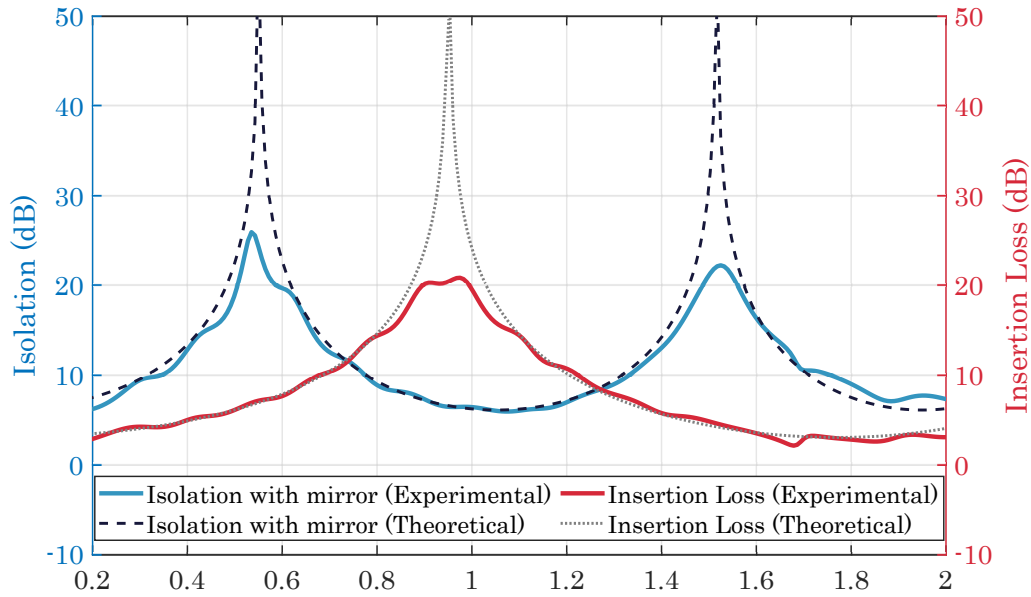


Figure 4.13: Measured isolation and insertion loss for the THz isolator (with metal mirror as the reflecting element) are compared with theoretical model evaluated from parameters extracted using isolator data.

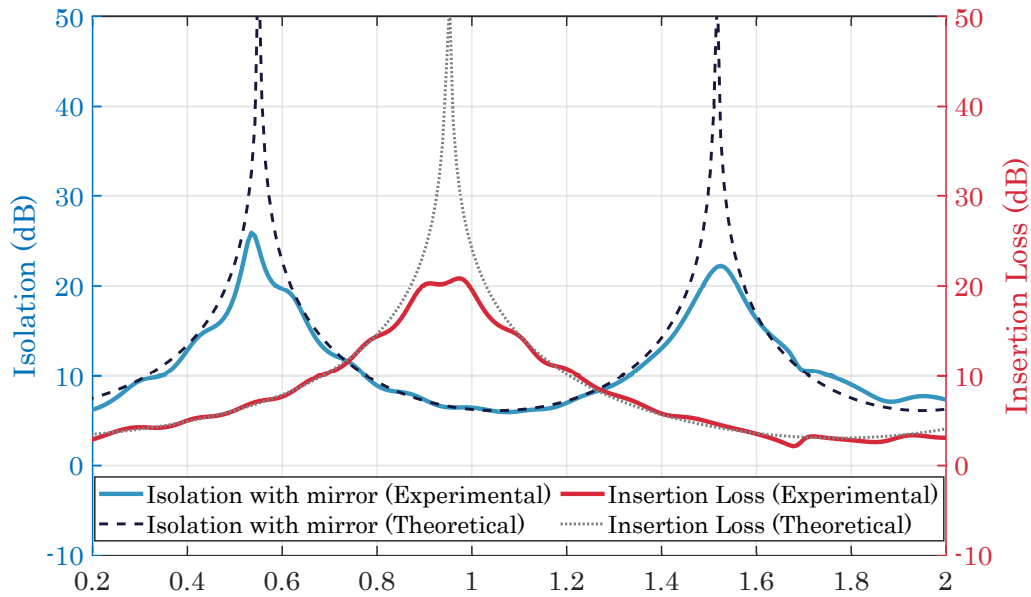


Figure 4.14: Measured isolation and insertion loss for the THz isolator (with HR-Si wafer as the reflecting element) are compared to the theoretical model evaluated from parameters extracted using isolator data.

Figure 4.12 and the new thickness is determined at 0.447 mm. The refractive index difference determined from the fitting also matches with the previously reported value of $\Delta n = -0.32$ at 1 THz [273–275]. It is also worth mentioning that the frequency resolution of the system is around 7 GHz, and for proper comparison, the theoretical data presented in the graphs are

averaged using a sliding average over 7 GHz.

An isolation is also noticeable at around 0.960 THz in the transmission data presented in Figures 4.10 and 4.11. This is due to the fact that at this frequency, the phase difference between the two orthogonal components becomes $\Delta\phi = (2m + 1)\pi$, signifying that the birefringent material functions as a Half-Wave Plate (HWP) at 0.960 THz. The HWP converts the polarization of the transmitted THz signal to horizontal (orthogonal to the initial signal polarization) and is reflected by WGP₃ to be detected by Rx₁ at vertical polarization.

4.4 Conclusion

The demonstrated 1.5 port VSM is an excellent characterization system with a bandwidth of 0.2- 2.5 THz and a peak DNR of 64 dB (57 dB) in transmission (reflection) geometry at an ENBW of 9.196 Hz, and is capable of extracting both transmission and reflection data simultaneously. This system successfully performed material characterization operation. We achieved an accuracy in the range of ± 0.05 for the extracted physical thickness of the material and the determined refractive indices and absorption coefficients are consistent with the literature values. The successful extraction of isolation level and insertion loss for the THz isolator verifies its ability to characterize non-reciprocal THz devices.

Although the 1.5 port VSM is versatile and provides crucial information about the behavior of the investigated component in the THz range, it is still inadequate to yield the complete characteristics of a full set of Scattering (S)-parameters in a single measurement. Especially in the case of non-symmetrical devices rotating the DUT is necessary, which again increases the experimental time and introduces uncertainties. To overcome this, a complete two-port system with two transmitters and receivers capable of measuring the complete set of S -parameters is essential.

Two-Port Pulsed Free Space Photonic Vector Network Analyzer

In this chapter, we discuss the system characteristics of the two-port Photonic Vector Network Analyzer (PVNA) and demonstrate its aptitude in several application examples, namely, the characterization of a Split-Ring Resonator (SRR) array, a Crossed-Dipole Resonator (CDR) array and a Distributed Bragg Reflector (DBR). The PVNA data is also used to extract material permittivity of Highly-resistive Silicon (HR-Si) and Polyvinyl chloride (PVC) wafers. Afterwards, the pulsed PVNA is compared with the Continuous Wave (CW) PVNA [276] and with a commercial Electronic Vector Network Analyzer (EVNA) in terms of system attributes and measured Scattering (S)-parameters. The work presented in this chapter is, to a large extent, published in References [229], [277] and [278].

5.1 Experimental Setup

Figure 5.1 shows the experimental setup of a two-port pulsed free space PVNA. It consists of two transmitters (Tx_1 , Tx_2), two detectors (Rx_1 , Rx_2) and two pairs of Wire Grid Polarizers (WGPs) functioning as directional couplers. A ~ 90 fs laser, containing two fiber ports and a free space port phase-locked with the fiber ports, optically modulate the conductance of the photoconductors. The fiber ports drive the detectors with 15 mW of power each, whereas the free space port activates the transmitters with 45 mW of optical power. The free space port laser path incorporates an optical delay unit followed by a beam splitter that splits the laser signal into two to facilitate the driving of both transmitters. The transmitters and receivers used for this setup are ErAs:In(Al)GaAs based photoconductive slotline antennas and ErAs:InGaAs based photoconductive H-dipole antennas, respectively, same as the ones used for the 1.5 port Vector Spectrometer (VSM). A detailed description of the components used for this configuration can be found in Chapter 3.

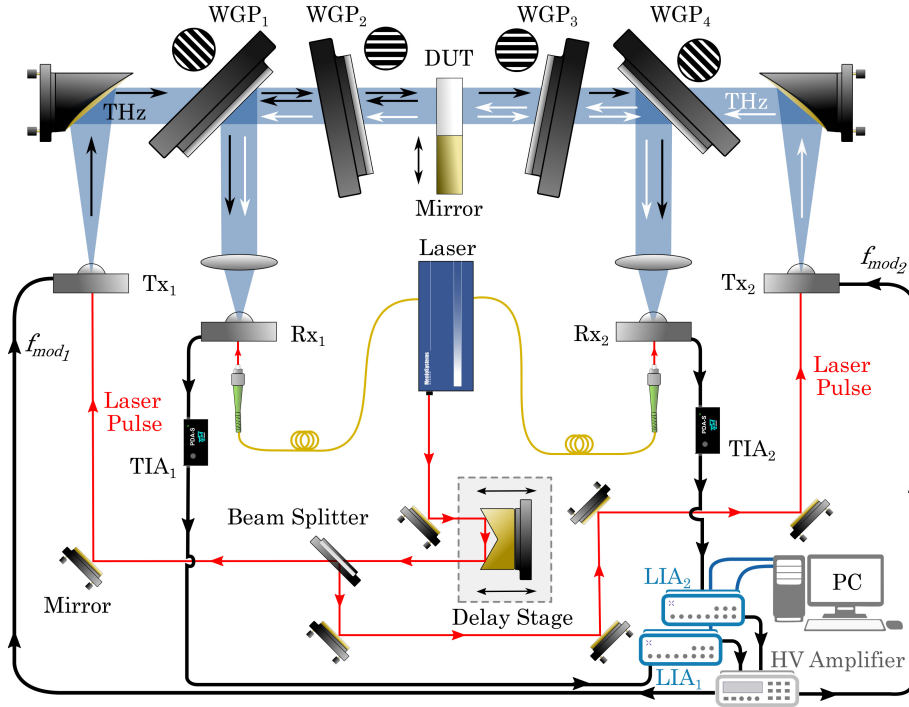


Figure 5.1: Detailed schematic of a two-port pulsed free space PVNA (adapted from [229]) ©2021 Optical Society of America.

As depicted in Figure 5.1, WGP₁ and WGP₄ have a 45° alignment to the optical axis and a 45° orientation projected on the axis, whereas WGP₂ and WGP₃ are oriented at 90° and aligned at a slight tilt to the optical axis. The orientation of WGP₂ and WGP₃ allows only the vertical component of the signal to pass through and the rest is reflected. The tilted alignment directs the reflected signal away from the system preventing it from being detected by the receivers. The operating principle of the WGP pair as frequency-independent directional coupler is detailed in Section 3.1.3.

The WGP pair, containing WGP₁ and WGP₂, directs the signal reflected from Device Under Test (DUT) (generated by Tx₁) and the signal transmitted through DUT (generated by Tx₂) towards Rx₁. Due to the symmetric nature of the system, Rx₂ also detects two signals originating from Tx₁ (transmission) and Tx₂ (reflection). In order to identify the signals coming from various sources, the biases of Tx₁ and Tx₂ are modulated at $f_{mod1} = 11.17$ kHz and $f_{mod2} = 19.71$ kHz, respectively, and demodulated at those frequencies using the lock-in technique. Two synchronized lock-in amplifiers containing two demodulators each (Zurich Instruments [220]) are utilized for this purpose, where the demodulation is achieved by using a 3rd order low pass filter with a Time Constant (TC) of 10 ms (Equivalent Noise Bandwidth (ENBW) = 9.196 Hz). The lock-ins' internal signal generators produce the biasing sinusoidal signals, and a high voltage amplifier amplifies them to 75 V (peak). For each receiver, the post-detection electronics also include a low noise Trans-Impedance Amplifier (TIA) from TEM Messtechnik (PDA-S) [219], which converts the photocurrent to voltage with a trans-impedance gain of 10^7 V/A. Data reading and storing concurrently from four demodulators, in conjunction with the delay stage movement, is facilitated by an in-house graphic user interface (Appendix A).

The delay stage scan is executed in a step-by-step manner, with 100 ms of waiting time per step, to ensure the settling of the lock-in filter. A 0.02 mm step size, corresponding to a sampling rate of $\Delta t = \frac{0.02\text{mm}}{3 \times 10^{11} \text{mms}^{-1}} \approx 0.067$ ps, indicates that it is possible to measure up to $(1/2\Delta t) \approx 7.46$ THz without aliasing (Shannon's theorem). The delay length used for the experiments presented in this chapter is 50 mm, equivalent to a time scale of $t_{dl} = 167$ ps, yielding a spectral resolution of $\Delta f \approx 1/2t_{dl} \approx 3$ GHz. By scanning a larger time window, this Δf can be improved. In terms of speed of the system, the step-by-step data acquisition is not ideal, as it takes approximately 17 minutes to complete a 50 mm scan with 0.02 mm increments and a 100 ms wait time per step. However, this scan time can be shortened at the expense of spectral resolution or measurement bandwidth. The spectral resolution and data acquisition speed are mainly limited by the mechanical stage used to achieve the time delay between the probe and the pump pulse. Utilizing systems such as Asynchronous Optical Sampling (ASOPS) [279] and Electronically Controlled Optical Sampling (ECOPS) [280, 281] based Terahertz Time-Domain Spectroscopy (THz-TDS), that do not require a mechanical translation stage, these limitations can be mitigated. These systems have demonstrated a spectral resolution of 50.5 MHz [193] and an acquisition rate of 2 kHz for a 100 ps scan window [282].

5.2 System Characteristics

5.2.1 Definition of Measurement Parameters

In a standard EVNA, the S -parameters are commonly used to characterize a DUT at high frequencies and are defined as the ratio of the scattered waves to the incident waves at its ports. For the case of a free space THz-TDS based PVNA, this is equivalent to the field transmission and reflection coefficients of the DUT, which are determined by the ratio of the transmitted or reflected field of the DUT to their corresponding reference signals.

The investigation of the behavior of a DUT using the two-port PVNA is done in four steps. In the first step, a measurement of an empty setup, as depicted in Figure 5.2 (a), is recorded. In this case, Rx₁ and Rx₂ detect the THz signals $E_{t_2}^{ref}(\omega)$ from Tx₂ and $E_{t_1}^{ref}(\omega)$ from Tx₁, respectively. $E_{t_1}^{ref}(\omega)$ and $E_{t_2}^{ref}(\omega)$ function as the references for S_{21} and S_{12} parameters. This corresponds to a *Through* calibration step in a classic EVNA.

In the second step, a metal mirror aligned with the DUT plane facing Tx₁ and Rx₁ is inserted as shown in Figure 5.2 (b), and the reflected signal $E_{r_1}^{ref}(\omega)$ is measured. Similarly, in third step the mirror is aligned with the DUT plane facing Tx₂ and Rx₂ (Figure 5.2 (c)) and the reflected signal $E_{r_2}^{ref}(\omega)$ is recorded. $E_{r_1}^{ref}(\omega)$ and $E_{r_2}^{ref}(\omega)$ corresponds to the reference for S_{11} and S_{22} , respectively, i.e. a *Reflect* calibration step in a EVNA. The second and third steps can be combined in one measurement step if the thickness of the sample and the mirror are exactly same or two mirrors can be aligned with both faces of the DUT simultaneously. Since the mirror serves as the physical reference plane, it is critical to precisely align the mirror at the same position as the DUT in order to eliminate errors in the measured S -parameter phase. EVNAs would require a third calibration step, e.g. a *Load* calibration. For a free space PVNA, however, the wave impedance of air, $Z_0=376.7 \Omega$ is very well known such that the *Load* calibration is not necessary. For the final step, the DUT is introduced in the collimated part of the setup (Figure 5.2 (d)) and all four signals are recorded simultaneously, where $E_{r_1}^{DUT}(\omega)$

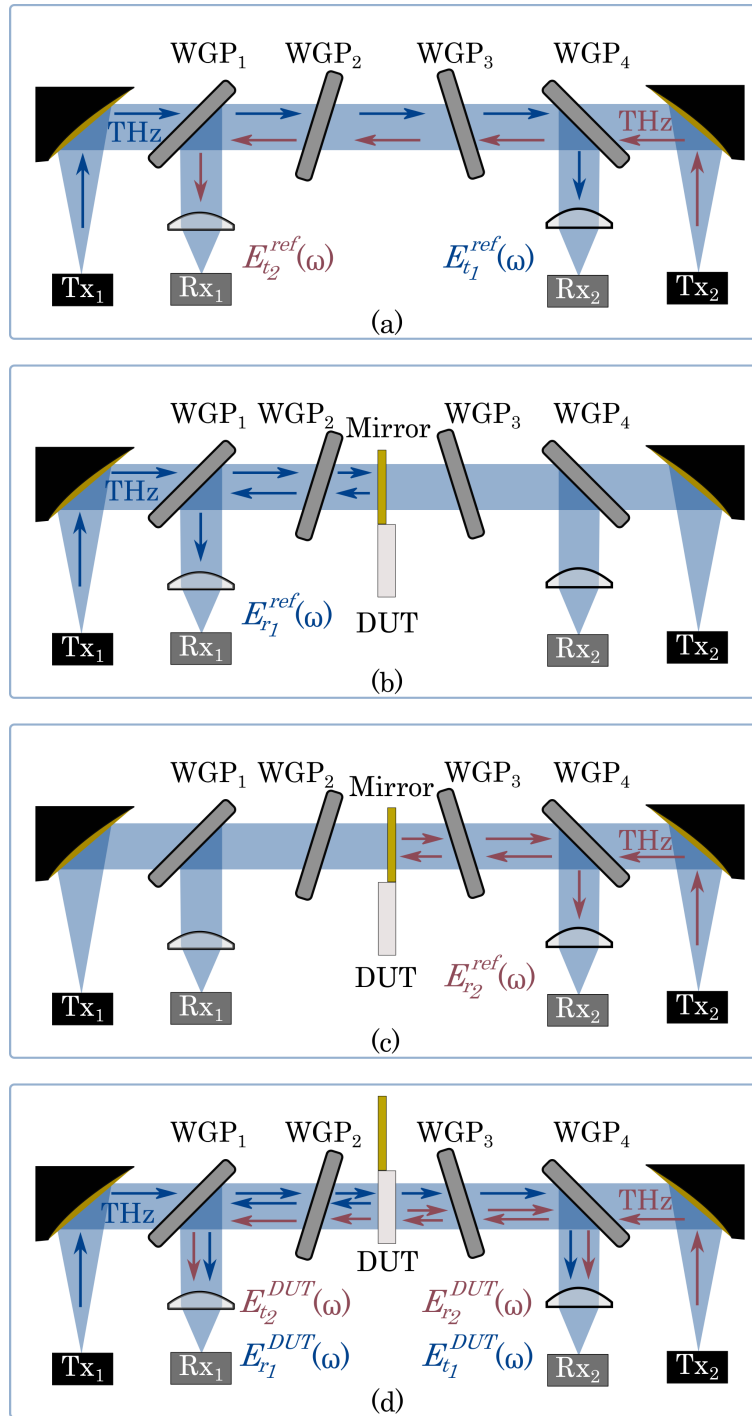


Figure 5.2: Setups for the calculation of S -parameters of a DUT. a) Reference measurement for S_{21} and S_{12} in an empty setup. b) Reference measurement for S_{11} with mirror aligned with one face of the DUT. c) Reference measurement for S_{11} with mirror aligned with the other face of the DUT. d) DUT characterization with DUT replacing the mirror.

and $E_{t_2}^{DUT}(\omega)$ are detected by Rx₁ and $E_{r_2}^{DUT}(\omega)$ and $E_{t_1}^{DUT}(\omega)$ and $E_{r_1}^{DUT}(\omega)$ are detected by Rx₂. These measurements are then applied to determine the S -parameters of the DUT

$$S_{21}(\omega) = t_1(\omega) = \frac{E_{t_1}^{DUT}(\omega)}{E_{t_1}^{ref}(\omega)} \quad (5.1)$$

$$S_{11}(\omega) = r_1(\omega) = \frac{E_{r_1}^{DUT}(\omega)}{E_{r_1}^{ref}(\omega)} \quad (5.2)$$

$$S_{12}(\omega) = t_2(\omega) = \frac{E_{t_2}^{DUT}(\omega)}{E_{t_2}^{ref}(\omega)} \quad (5.3)$$

$$S_{22}(\omega) = r_2(\omega) = \frac{E_{r_2}^{DUT}(\omega)}{E_{r_2}^{ref}(\omega)} \quad (5.4)$$

5.2.2 Cross-talk Measurement

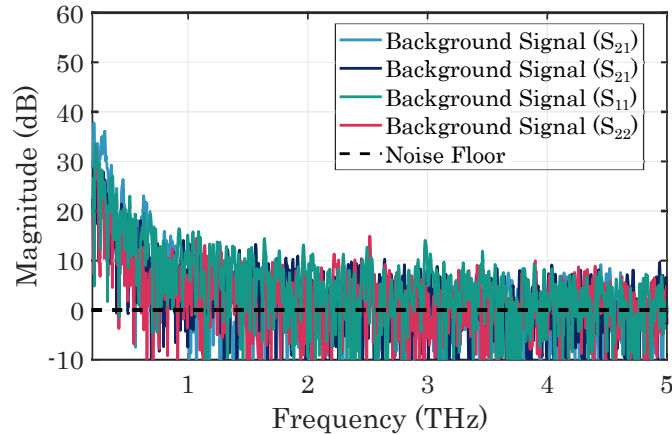


Figure 5.3: Measured cross-talk of the two-port pulsed free space PVNA.

The system is configured to minimize cross-talk across different paths. Firstly, the low pass filters employed in the lock-ins have an ENBW of only 9.196 Hz, which effectively suppresses the undesired frequency components, as the modulation frequencies $f_{mod_1} = 11.17$ kHz and $f_{mod_2} = 19.71$ kHz lie approximately 8 kHz apart. Secondly, the temporal separation between the transmitted and reflected signals arriving at the receivers ensure they can be further distinguished in the time domain. These procedures guarantee cross-talk-free measurement of the S -parameters because the receivers are operated considerably below their saturation regime. Moreover, there is no cross-talk within the emitter structures caused by receiving a reflected THz signal, as this reflected signal can only generate a bias that is, in the worst case, already 7 orders of magnitude smaller than the applied bias. The corresponding (power) isolation level is thus ~ 140 dB.

The background signal or cross-talk depicted in Figure 5.3 is recorded by blocking the THz path for S_{21} and S_{12} and removing the DUT and mirror from the setup for S_{11} and S_{22} . It is evident from Figure 5.3 that the system is not entirely free from cross-talk and background signals, as at lower frequencies, THz waves with a relative strength of about -20 dB at 500 GHz are detected. These are the result of minor scattering and reflections caused by four WGPs and a sample holder in the THz path, despite mounting the WGPs at an angle to ensure that the unwanted signal is directed off-axis. As these background reflections are mostly systematic, they are calibrated out using the techniques outlined in Section 3.2. Beyond 1.5 THz, the cross-talk is negligible.

5.2.3 System Bandwidth and Dynamic Range

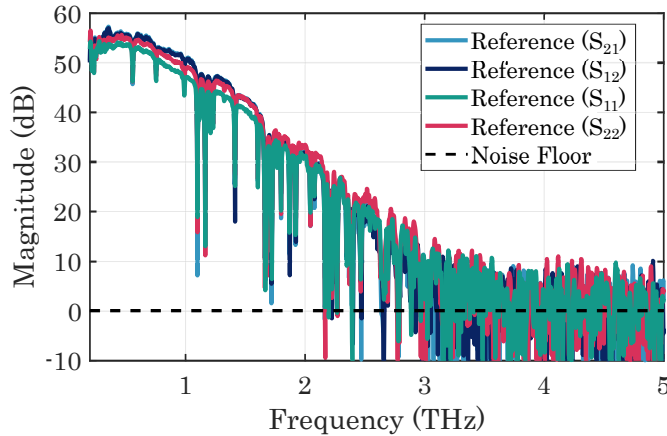


Figure 5.4: System attributes of the two-port pulsed free space PVNA. Available bandwidth 0.2-3 THz, with peak Dynamic Range (DNR) of 57 dB at 500 GHz for an ENBW=9.196 Hz. This figure is adapted from [229] ©2021 Optical Society of America.

The reference measurements discussed in Section 5.2.1 provide knowledge about the system attributes in terms of available DNR and bandwidth. Figure 5.4 illustrates the reference measurements of the S -parameters of the two-port PVNA. The PVNA exhibits a wide bandwidth ranging from 0.2 up to almost 3 THz with a peak DNR of 57 dB for S_{21} at around 500 GHz. For S_{22} the peak DNR is slightly lower at ~ 54 dB at 500 GHz. The available DNR at 1 THz is ~ 50 dB and at 2 THz close to 30 dB. These results are acquired by using a 3rd order low pass filter with ENBW = 9.196 Hz for the demodulation of the detected signals in the lock-in amplifier.

5.3 Applications

5.3.1 Metamaterial Characterization

Metamaterials are artificially engineered composite materials containing unique subwavelength metallic patterns or structures fabricated on a dielectric substrate. These novel class of functional materials derive their properties from the internal periodicity of identical unit cells, rather than the chemical composition of the base material. As a result, the effective electromagnetic properties of metamaterials can be designed to even show features not found in nature, such as negative refractive index.

Most bulk materials found in nature do not show strong magnetic or electric resonances between 1 to 3 THz. Metals exhibit resonances beyond the mid-infrared range due to phonon modes, whereas ordinary magnetic materials have resonances in the GHz range or lower [283]. As the properties of metamaterials can be customized, they possess immense potential in terms of developing devices and components operating in THz range. Experimental demonstrations include modified THz filters [284–286], absorbers [287,288], quarter-wave plates [289,290], modulators [291,292], sensors [293,294]. Their designable properties can significantly accelerate research and development in the field of THz radiation. This emphasizes the importance of developing systems that can accurately capture well established characteristics, such as S -parameters, of these components. In this section, we investigate two metamaterials exhibiting resonances in THz region, namely, a SRR array and a CDR array. Both of these metamaterials are mainly used in sensing applications [295–297].

In many cases, the response of a sample under test, to direct irradiation in a transmission or reflection setup, is too weak to be detected with sufficient sensitivity for the desired application. Even if the analyte does not show a THz resonance at all, its presence can be detected as shifts in the resonance frequency and the Quality (Q) factor of the resonance caused by the adsorption of that analyte [298]. From an optical perspective, the resonance shift is predominantly caused by the non-unity refractive index of the specimen under test present in the near field of a resonator. The Q factor is predominantly reduced by its absorption. Each of the unique patterns or unit cells of the metamaterial functions as a microscopic LC resonant circuit with a resonant frequency of $f_0 = \frac{1}{\sqrt{2\pi LC}}$, obtaining its inductance (L) from the magnetic field of flowing currents in the metal and its capacitance (C) from electric fields spanning parts of the structure. The changes in resonant frequency depend on the changes in the inductance and capacitance incurred by the investigated sample. From an electromagnetic perspective, the frequency shift and Q factor degradation provide a direct measure of the permittivity (ϵ) or the permeability (μ) of the substance. The high performance of metamaterial sensing systems relies on high- Q resonance and realization of higher sensitivity to the attributes of the investigated sample [295,299].

Split Ring Resonator Array

We characterize an SRR array with a design similar to the one presented in [296] by exploring its S -parameters. Figure 5.5 depicts a section of the SRR array and the dimensions of a unit cell. It is patterned with Gold ($d_g = 210$ nm) and Chromium ($d_c = 20$ nm), on a low-loss Quartz substrate of $d_q = 212$ μm thickness. Each ring has an inner radius (r_2) of 75 μm and an outer radius (r_1) of 100 μm with a periodicity (x) of the array of 300 μm . The ring asymmetry angle (θ) is set to 10° for a gap size (w) of 23 μm .

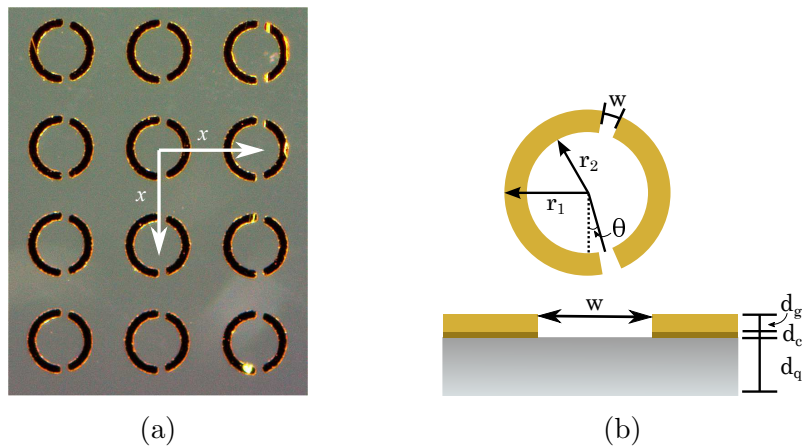


Figure 5.5: (a) Section of an SRR array (b) Design parameters of a SRR array unit cell. Reprinted from [229] ©2021 Optical Society of America.

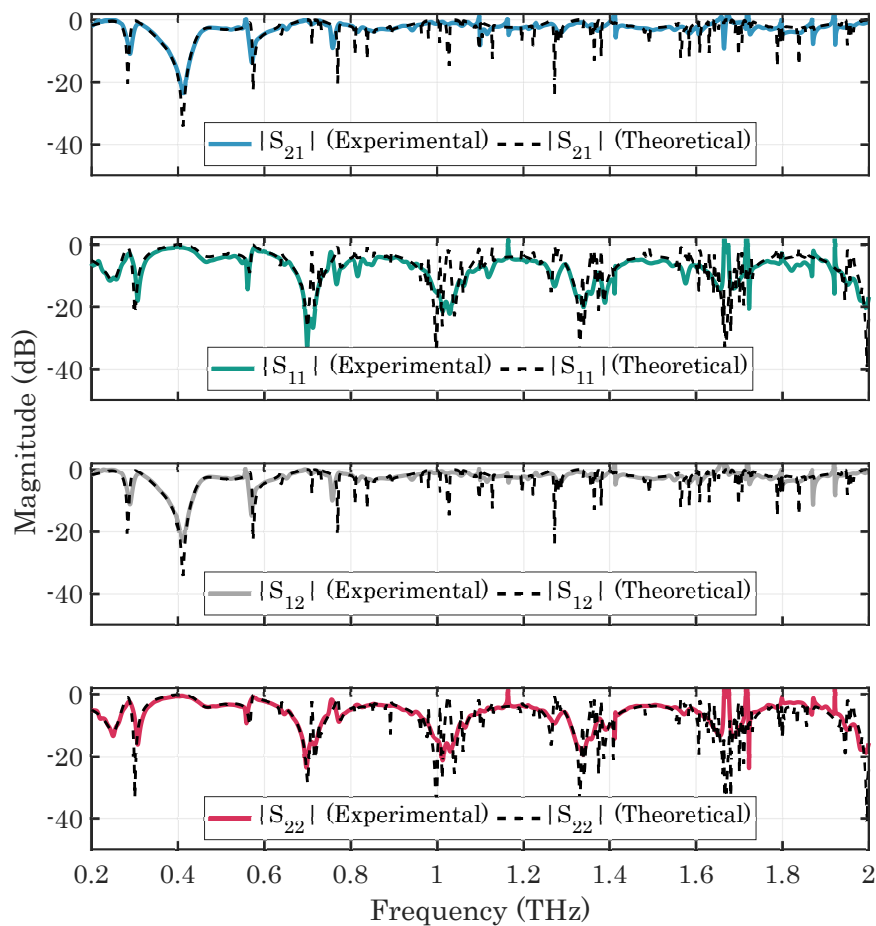


Figure 5.6: Magnitude of the S -parameters of an SRR array. Adapted from [229] ©2021 Optical Society of America.

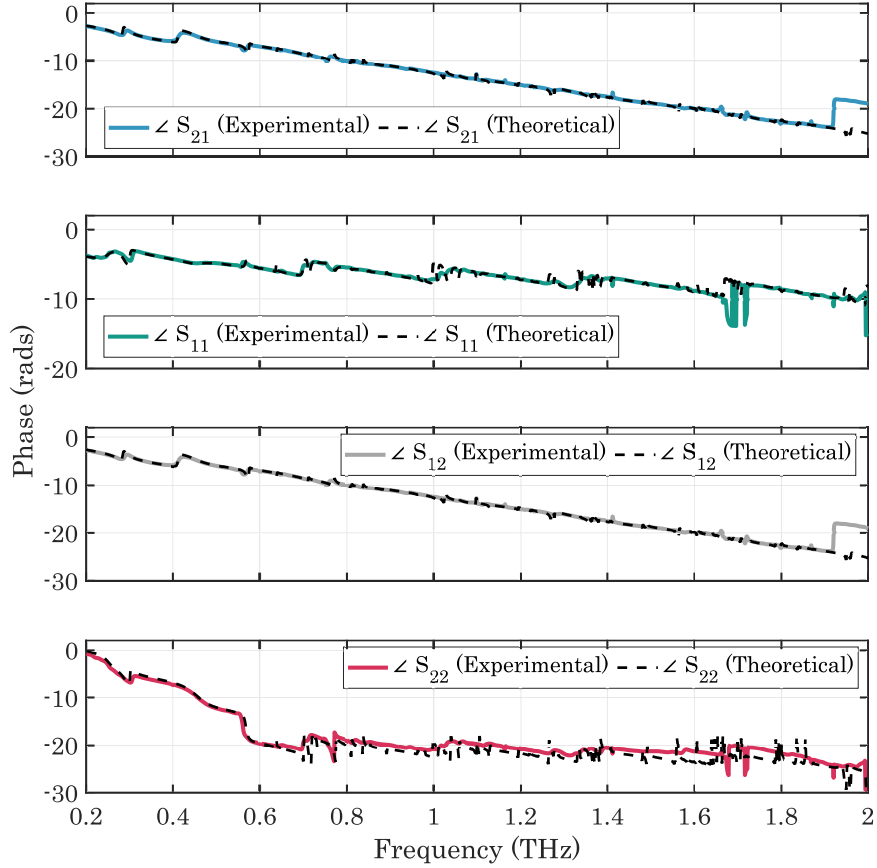


Figure 5.7: Phase of the S -parameters of the same SRR array.

Figures 5.6 and 5.7 compare the extracted magnitude and phase of the S -parameters with the simulations done using CST Microwave Studio for the investigated SRR array. The main resonances are well reproduced and match very well with the simulation. However, due to the low spectral resolution of the PVNA, the resonances have a comparatively lower Q -factor. Moreover, at higher frequencies, owing to decreasing DNR, the amplitude of the measured resonances also reduces. In spite of that, several double-peak structures are resolved in S_{11} and S_{22} parameters, and the extracted magnitude data shows good match with the simulated results. The phase of the S_{22} parameter shows a gradual phase difference between the simulation and the experimental data. This is due to the misalignment of the reference plane and the SRR array. Also, experimental S_{21} and S_{12} phase data exhibit a jump around 1.9 THz, which is caused by incorrect phase unwrapping and can be corrected by implementing a custom unwrapping algorithm. Beside these slight mismatches, the experimental phase data show good agreement with the simulated results.

Crossed Dipole Resonator Array

The design of the CDR array under investigation is illustrated in Figure 5.8. It is patterned with 50 nm thick Aluminium on a 95 μm thick High-density polyethylene (HDPE) substrate. The symmetric unit cells in this case are the Aluminum crosses consisting of 200 μm x 25 μm

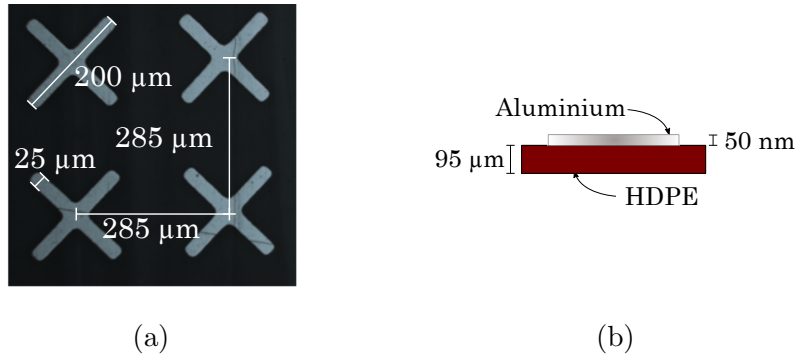


Figure 5.8: (a) Section of a CDR array (b) Thickness profile of the CDR array. Adapted from [229] ©2021 Optical Society of America.

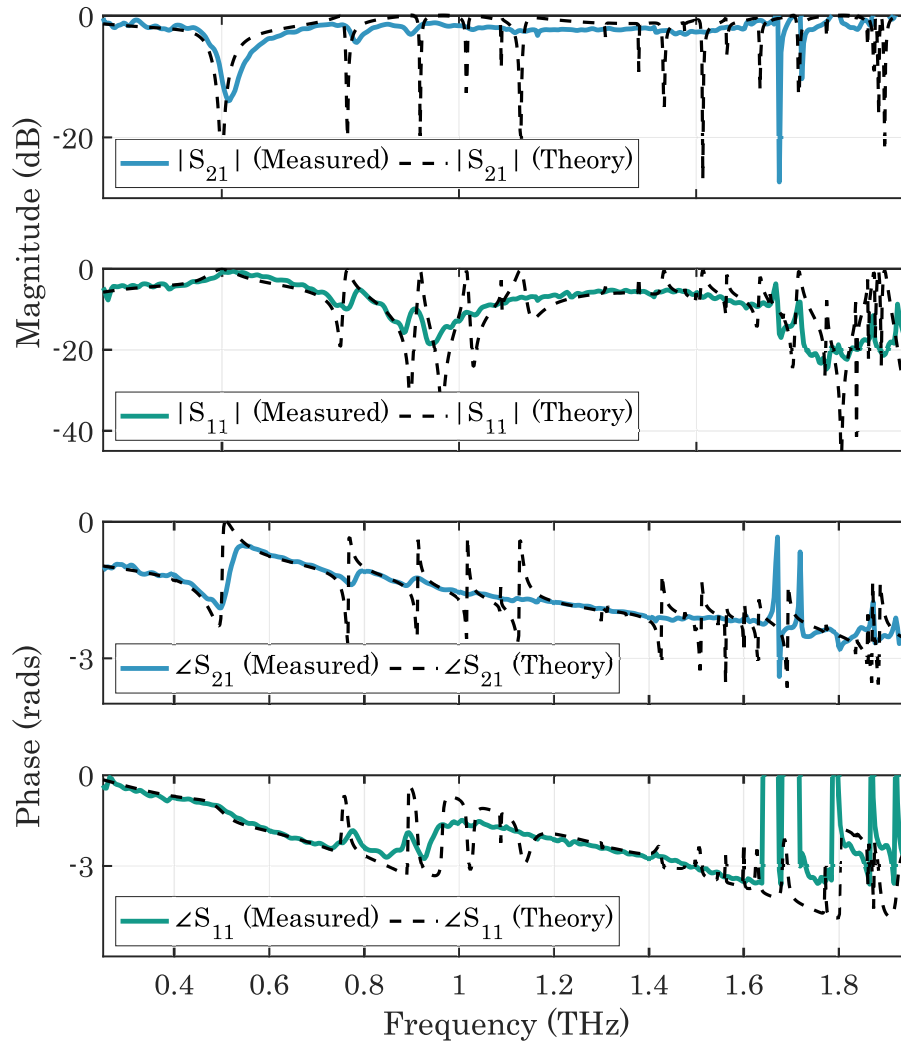


Figure 5.9: S -parameters of a CDR array. Adapted from [277] ©2021 IEEE.

dipole arms. The cells are separated by a distance of $285 \mu\text{m}$ in both directions. The data depicted here are published in [277].

Fig. 5.9 depicts the measured magnitude and phase of the S -parameters and compares it with the simulated (CST Microwave Studio) results. The primary design resonance in S_{21} at around 500 GHz is well reproduced, with reduced amplitude and slight shift. Although the error associated with the misalignment of the mirror and DUT (for reflection) and path length difference of measured and simulated data (for transmission) are corrected in post-processing, a slight mismatch is still evident. These discrepancies result from low spectral resolution, geometrical imperfections of the produced array, and the assumption of lossless material in the simulation, emphasising the significance of experimental characterization. Moreover, above 1.5 THz, the experimentally extracted S -parameters encounter low DNR and a relatively large number of water vapor resonances, which makes it challenging to distinguish the resonance features of the CDR array. Still, the measured S -parameters match the simulation fairly well.

5.3.2 Characterization of a Distributed Bragg-Reflector

DBRs are widely employed in optoelectronics for applications such as optical filters [300], surface-emitting lasers [301], photonic crystals [302], enhancing the efficiency of light-emitting diodes [303], and so on. A Bragg mirror consists of periodically alternating structures, each containing layers of two materials with different refractive indices and thicknesses. Fresnel reflections occur at each interface due to the difference in refractive index. The thickness of i^{th} layer d_{DBR}^i is chosen such that at the design wavelength, $d_{DBR}^i = \frac{(2m_i - 1)\lambda}{4n}$, where m_i is an integer, these reflections interfere constructively resulting in nearly 100% reflectance. In the transmitted part, destructive interference results in a pronounced stop band, and the DBR acts like a band block filter, blocking any signal from propagating within the design frequency band. Each of the high refractive index material layers of the DBR also functions as resonators that are weakly coupled by the low index material, implying that the system operates as coupled resonators with mode splitting [304]. Resonances will still occur even if the thickness of the low index material is significantly less than $\frac{\lambda}{4n}$.

The DBR under investigation comprises three HR-Si wafers of $520 \mu\text{m}$ thickness with $150 \mu\text{m}$ air in between, as illustrated in Figure 5.10(a). Within the error margin of the thickness measurement of about $\pm 10 \mu\text{m}$, the Bragg condition is fulfilled for the first time at around 510 GHz with $m_{air}=1$ and $m_{HRSi}=6$.

Figure 5.10(b) depicts the comparison between the extracted S -parameters and theoretical assessment. As the DBR is symmetric ($S_{21} = S_{12}$ and $S_{11} = S_{22}$), so S_{21} and S_{11} data are adequate for the comparison. The determined S -parameters show an excellent agreement with the theoretical model, within the resolution of the system, for both magnitude and phase, especially in the case of stopbands of S_{21} . The high- Q factor of the theoretical resonances of S_{11} is not precisely reproduced in the measurement, due to the experimental resolution limit of 3.66 GHz. In spite of that, the three-fold mode splitting caused by the three HR-Si wafers that act as cavities is distinguishable in the experimental data, as shown exemplarily for the peak centered at ~ 0.91 THz in the inset of Figure 5.10(b) with an excellent match to the simulation. Additionally, apparent disparities above 2 THz are primarily caused by declining DNR, which also magnifies absorption artifacts caused by water vapor resonances. We note that the phase of S_{11} is not unwrapped, as unwrapping would result in the removal of some of the comparatively sharp phase jumps induced by the resonances, rendering it unsuitable

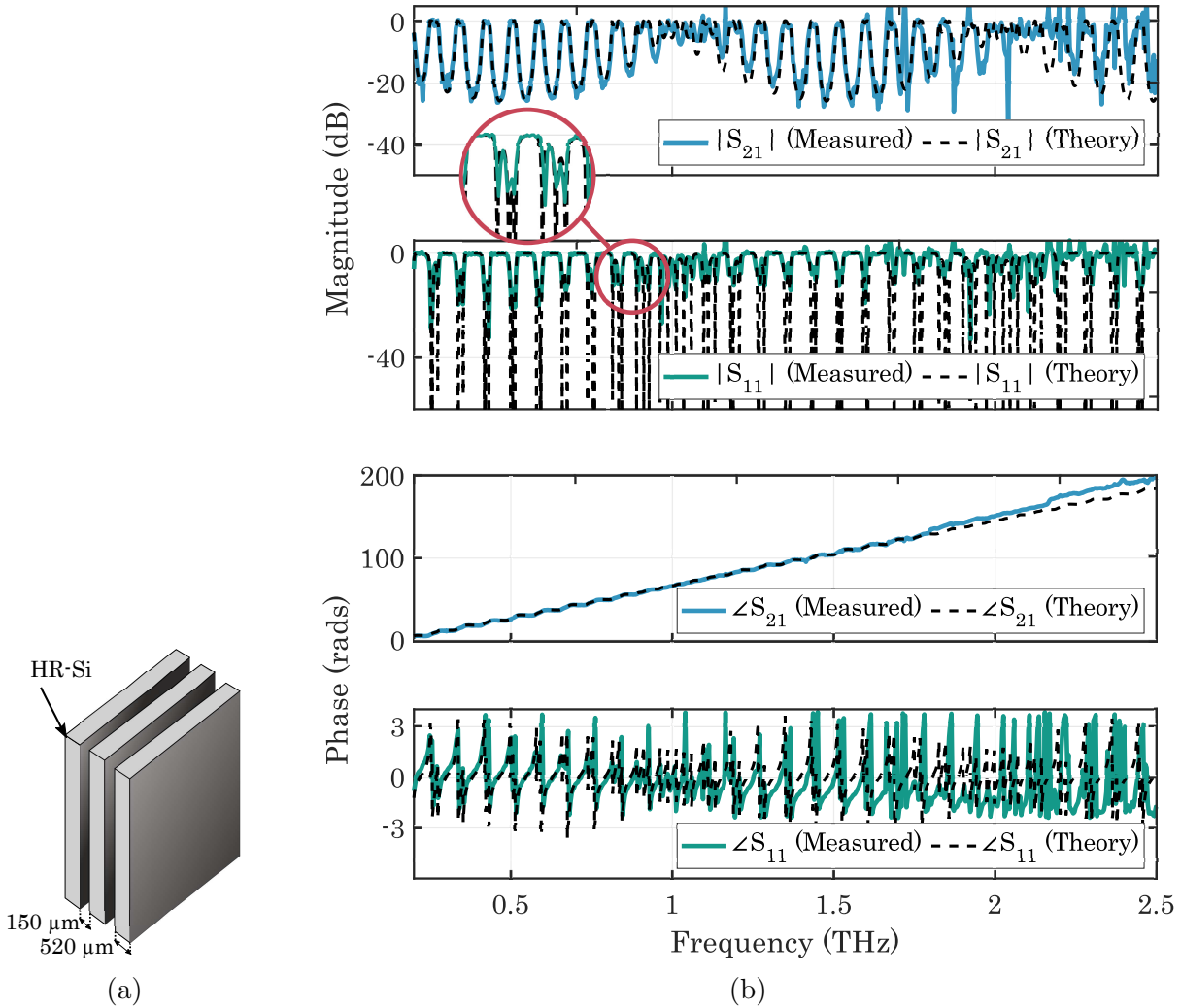


Figure 5.10: (a) Schematic of a DBR. Reprinted from [229] ©2021 Optical Society of America. (b) S -parameters of the DBR. Adapted from [229] ©2021 Optical Society of America.

for proper comparison. The reflection phase is susceptible to a slight mismatch between the reference and sample planes due to relative tilt and misalignment while switching between the mirror and the DBR. Although the switching has been done with caution by using a custom sample holder mounted on optical rail [276] it is very challenging to avoid this error. This could be another source for the slight mismatch apparent between the theoretical and measured S_{11} phase.

5.3.3 Material Permittivity and Thickness Extraction

Comprehensive knowledge of the dielectric characteristics of the material in terms of refractive index and absorption coefficient or dielectric permittivity is a prerequisite for designing a THz component. Traditionally, free space EVNAs have been employed to determine the permittivity

of materials below 300 GHz [59]. With the availability of frequency extenders, this investigation is now extended up to 1.5 THz [60,61]. Even though the DNR of EVNAs is high, it features two main disadvantages: 1) several waveguide bands must be employed and 2) the higher frequency bands are very expensive. Due to broad frequency coverage, THz-TDS systems still are the most popular choice for measuring dielectric properties of materials.

The PVNA data also enable material parameter extraction by recording the S -parameters from a plane-plane cut dielectric, in addition to S -parameter measurements of THz devices. To determine the complex dielectric permittivity (or, alternatively, the complex refractive index) and Material Under Test (MUT) thickness simultaneously, we implement an algorithm described in Section 3.3.2. The investigated materials, in this case, are HR-Si and PVC wafers as examples for an essentially lossless and a very lossy material, and since both are symmetric, $S_{12} = S_{21}$ and $S_{22} = S_{11}$.

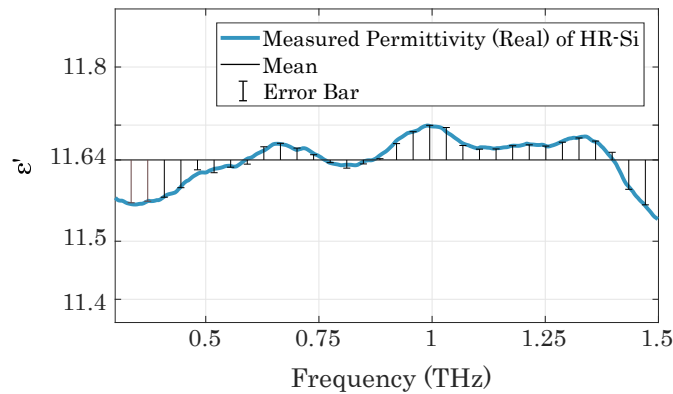


Figure 5.11: Permittivity (real) of HR-Si. Reprint from [229] ©2021 Optical Society of America.

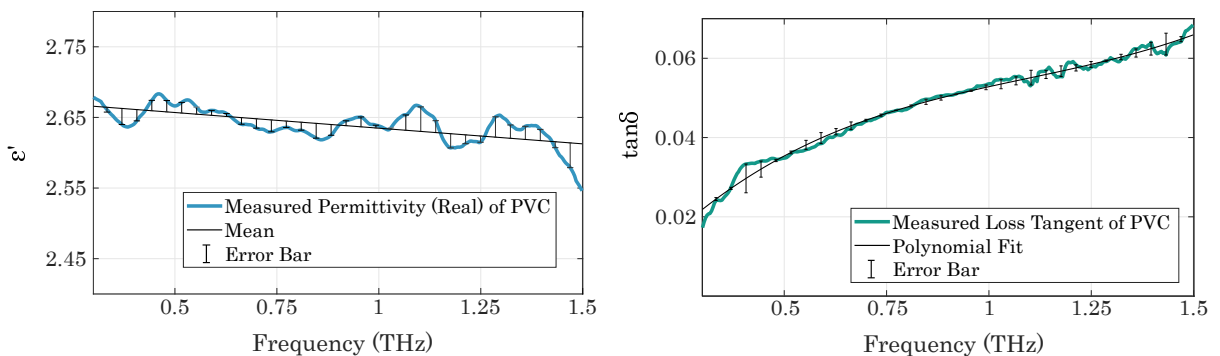


Figure 5.12: Permittivity (real) (left) and loss tangent (right) of PVC. Reprint from [229] ©2021 Optical Society of America.

Figure 5.11 shows the real part of a HR-Si ($> 10,000 \Omega\text{cm}$) wafer's dielectric permittivity. With a value of 11.6410 ± 0.0588 (averaged over the whole frequency range), the dielectric permittivity is constant within the measurement error and matches excellently with the published value of 11.67 at 1 THz [250]. Since the loss tangent is close to zero and below the lowest value that can be measured using the available DNR of the system, $\epsilon'' \approx 0$. The caliper measurement of 0.65 ± 0.01 mm is compliant with the determined HR-Si wafer thickness of 0.6544 ± 0.0050 mm.

The dielectric permittivity for PVC is depicted in Figure 5.12 as an example of a lossy dielectric. From the figure, we obtain, $\epsilon'' \approx 2.648$ and $\tan \delta = 0.053$ at 1 THz. The caliper reading of 1.01 ± 0.02 mm and the extracted thickness of 1.0179 ± 0.0100 mm are in excellent agreement (the surface of the used PVC sample is also uneven). We observe that in both instances, the measurement uncertainty limit of the PVNA is at least an order of magnitude less than that of the caliper.

5.4 Comparison with Continuous Wave PVNA

Historically the Vector Network Analyzers (VNAs) have been predominantly CW to exploit high spectral resolution. Single frequency sweep is also advantageous for analyzing non-linear THz components such as transistors, mixers or receiver diodes. However, CW systems have relatively narrow frequency coverage, and the measured data is often heavily affected due to the presence of standing waves.

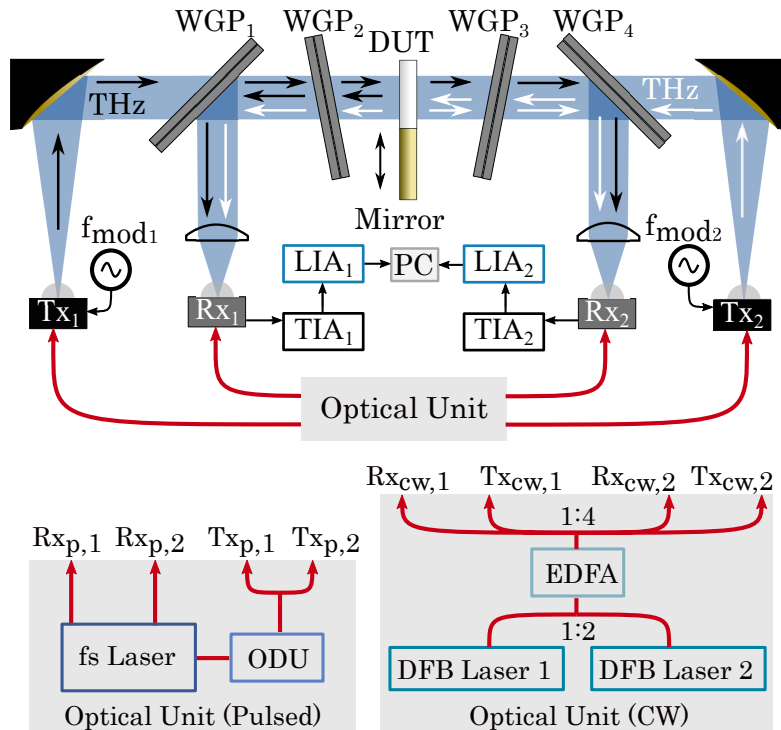


Figure 5.13: Comparison of experimental setup for two-port pulsed and CW PVNA. Reprinted with permission from [278] ©2022 IEEE.

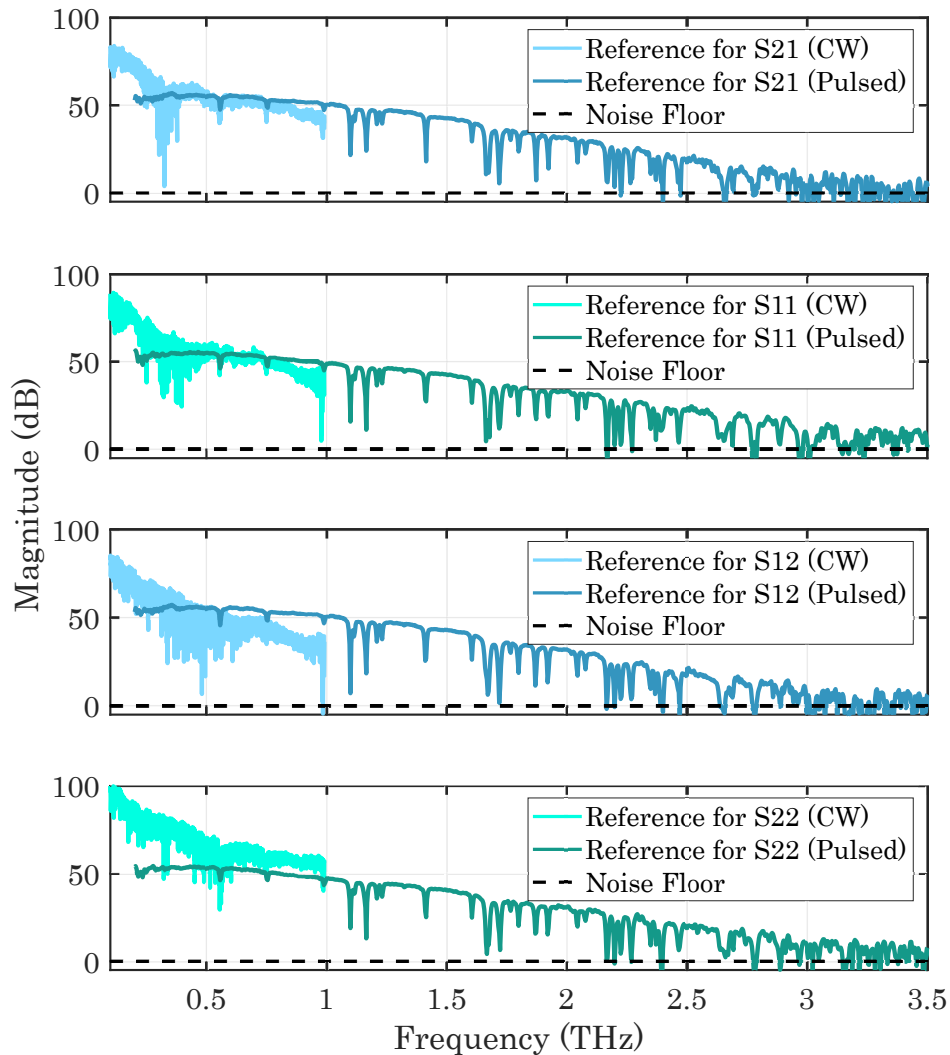


Figure 5.14: Bandwidth and DNR comparison between two-port pulsed and CW PVNA. Adapted from [278] ©2022 IEEE.

Recently, Fernandez Olvera *et al.* [276] reported a free space CW PVNA operating in the 0.1–1 THz range with a resolution of 20 MHz. As depicted in Figure 5.13, both the pulsed and the CW PVNAs have the same system architecture with the exception of the optical unit and the photomixers. The optical unit for the CW system contains a pair of telecom-wavelength DFB lasers from TOPTICA photonics [305] combined with a fiber coupler. The combined signal is then amplified by an Erbium-Doped Fiber Amplifier (EDFA), followed by a 1:4 splitter that distributes the optical signal to two photomixing transmitters and two photomixing detectors. The transmitters implemented in this case are commercial telecom-wavelength PIN photodiodes with an integrated bowtie antenna [305] ($\text{Tx}_{\text{cw},1}$ and $\text{Tx}_{\text{cw},2}$), whereas ErAs:InGaAs photoconductors ($\text{Rx}_{\text{cw},1}$ and $\text{Rx}_{\text{cw},2}$) operate as the detectors. Similar to the pulsed PVNA, two WGP pairs function as 3 dB directional couplers. The calibration process for the CW PVNA is identical to that of the pulsed PVNA and is carried out using a *Through* or *Line* standard (empty setup) and a *Reflect* standard (metal mirror replacing the DUT).

The reference measurements of the two systems for each of the four S -parameters are compared in Figure 5.14. The pulsed PVNA offers a bandwidth of 0.2-3 THz with a peak DNR of 57 dB at 0.5 THz (3rd order low pass filter, ENBW = 9.196 Hz). The CW PVNA only covers 0.1–1 THz of the frequency range but with a higher peak DNR of 90 dB at 0.1 THz (8th order low pass filter, ENBW = 0.5 Hz). However, the DNR of the CW and pulsed systems are comparable beyond 0.5 THz. Figure 5.14 further demonstrates that the CW PVNA data are severely influenced by the presence of unwanted reflections from the DUT, WGPss, and other quasi-optical components. The effects of these reflections can be minimized with appropriate filtering [276]. We would also like to point out that CW PVNA has a far superior frequency resolution of 20 MHz compared to 3.66 GHz of the aforementioned pulsed PVNA.

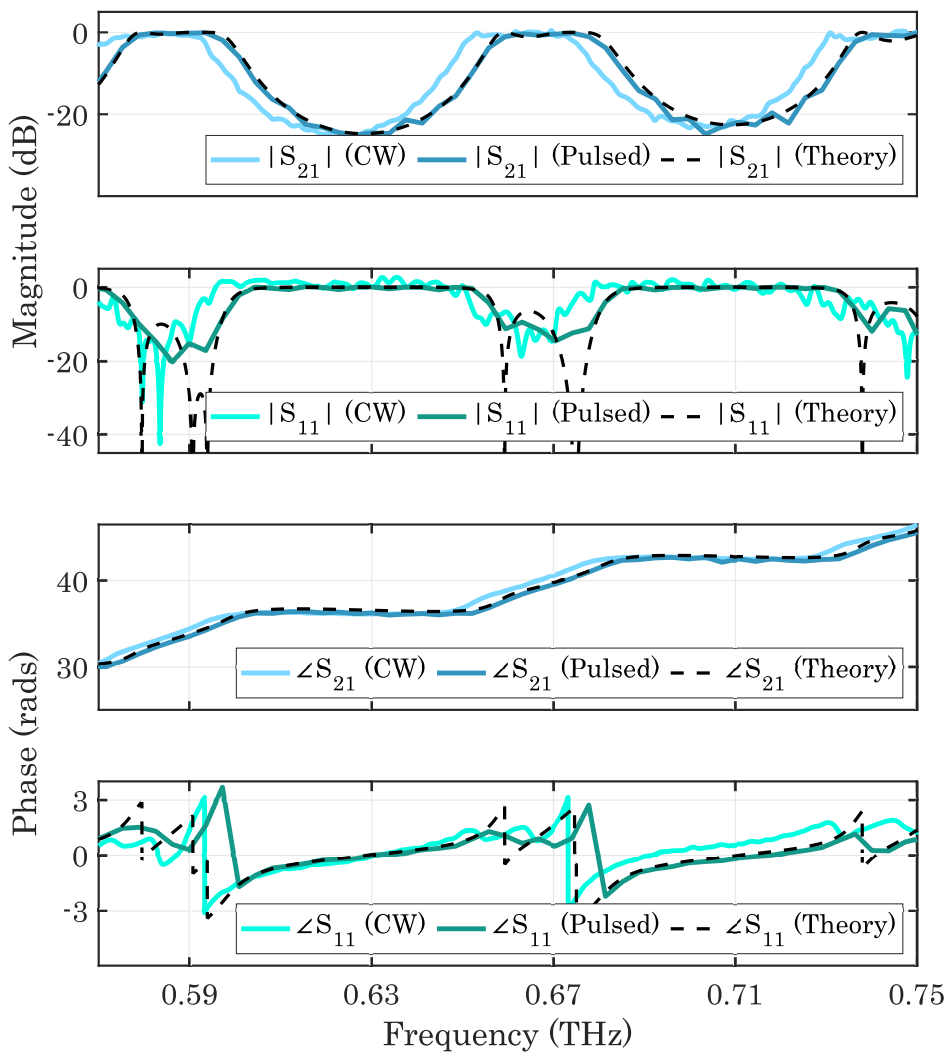


Figure 5.15: S -parameters of a DBR extracted using pulsed PVNA are compared with CW PVNA measurement and theoretical calculation. Adapted from [278] ©2022 IEEE.

We examine a DBR, similar to the one described in Section 5.3.2, and compare the characterization capabilities of the CW and pulsed PVNAs. The magnitude and phase of the S -parameters extracted using CW and pulsed PVNAs are depicted in figure 5.15, along with the theoretical data. Owing to its higher resolution, the CW PVNA reproduces the narrow resonances better with a relatively higher Q factor. However, the CW data shows a frequency shift compared to the pulsed and the theoretical data due to the thermal inertia and a miscalibration of the wavelength look-up table of the Distributed Feedback (DFB) diodes [305], which can, in principle, be recalibrated for a given tuning speed. The pulsed PVNA results show a rather good agreement with the theoretical data, especially for the S_{21} case. However, the resonance peaks for S_{11} parameter appear broadened due to low frequency resolution. A slight mismatch in the S_{21} phase data due to calibration plane misplacement error is also apparent.

Depending on the intended application, both versions of the PVNA show excellent capabilities as characterization systems in the THz range, where the pulsed PVNA is better suited for broadband investigation and CW PVNA for precise characterization of narrow spectral features.

5.5 Comparison with Electronic VNA

EVNAs are exceptionally sophisticated characterization systems that can perform fast measurements with excellent precision (frequency resolution in the Hz range) and high DNR (~ 120 dB). Commercially available EVNAs can now achieve frequency coverage of up to 1.5 THz with the help of frequency extenders [65]. However, these extending modules are narrowband, spanning a maximum bandwidth of just 50% of the center frequency. In order to cover the frequency range of 0.2-1.5 THz, five extenders or more must be employed (to ensure overlap), which makes broadband investigation using an EVNA a laborious and painstaking process because components need to be repeatedly exchanged, aligned and calibrated.

The bandwidth and DNR of the frequency extenders are detailed in Table 5.1. With a similar ENBW of ~ 10 Hz, the peak DNR of 57 dB for the two-port pulsed PVNA is relatively low compared to the typical DNR of 115 dB attained by the EVNA for WR3.4 band. However, within the 1.1-1.5 THz range, for a two-port configuration, the typical DNR for WR0.65 extender is ~ 45 dB¹ (minimum of 25 dB) [65]. The PVNA already shows a better DNR of 47-35 dB within this range. Moreover, to the knowledge of the author, there are no commercially available EVNA that can go beyond 1.5 THz, whereas the PVNA can reach up to 3 THz.

The S -parameters obtained using both the two-port pulsed PVNA and a commercial, electronic, frequency-extended VNA are compared to examine their characterization capabilities in the THz range. An Agilent Technologies PNA (N5222A) connected to a pair of Virginia Diodes, Inc. WR3.4 VNAX extenders [65], which operate in the frequency range of 220-330 GHz, is implemented for this investigation. Horn antennas couple the signals into the free space.

Figure 5.16(a) and 5.16(b) illustrate the retrieved S -parameters for the DBR and the SRR array, respectively. For better comparison, the PVNA data are zero-padded to realize 0.92 GHz resolution. For both DBR and SRR array, the S_{12} and S_{21} parameters of the PVNA and EVNA measurements match perfectly, with the main difference being the oscillations in the EVNA due to standing waves combined with its high spectral resolution (11 MHz).

¹WM164 (WR0.65) performance is specified for a TxRx-Rx configuration. Performance of a TxRx-TxRx configuration is estimated to have a ~ 15 dB degradation of dynamic range and may additionally require the use of a mmWave controller.

Waveguide Band	Frequency Coverage (GHz)	Dynamic Range (BW = 10 Hz, dB)	
		Typical	Minimum
WR3.4	220-330	115	105
WM-710 (WR2.8)	260-400	100	80
WM-570 (WR2.2)	330-500	110	100
WM-380 (WR1.5)	500-750	100	80
WM-380 (WR1.5) Mini	500-750	110	95
WM-250 (WR1.0)	750-1100	65	45
WM-250 (WR1.0) Mini	750-1100	95	75
WM-164 (WR0.65)*	1100-1500	60	40

Table 5.1: Specifications of EVNA extenders from Virginia Diodes, Inc. The DNR for WM-164 band mentioned here is for a 1.5 port setup. *The performance degrades by ~ 15 dB for a two-port system [65].

In contrast to the DBR, where the higher Q modes in S_{11} and S_{22} appear broadened due to the considerably lower spectral resolution, the measurements of S_{11} and S_{22} for SRR array show excellent matching. These data are situated at the lower edge of the spectrum, which means that windowing during the Fourier transformation may have an impact. Even so, the resonances are discernible in both measurements, including the double peak structure at 255 GHz for the DBR (5.16(a)). The extracted S -parameters are also compared with the theoretical calculations or simulations. In both the EVNA and PVNA measurements of the SRR array, high- Q resonances appear to have a slight frequency shift and exhibit reduced amplitude when compared with the simulations. This is due to geometrical imperfections in the produced array and consideration of lossless material in the simulation. The resonance modes of simulation and experiment, however, are reasonably well matched. The measured S -parameters and the theoretical calculations for DBR also show good agreement.

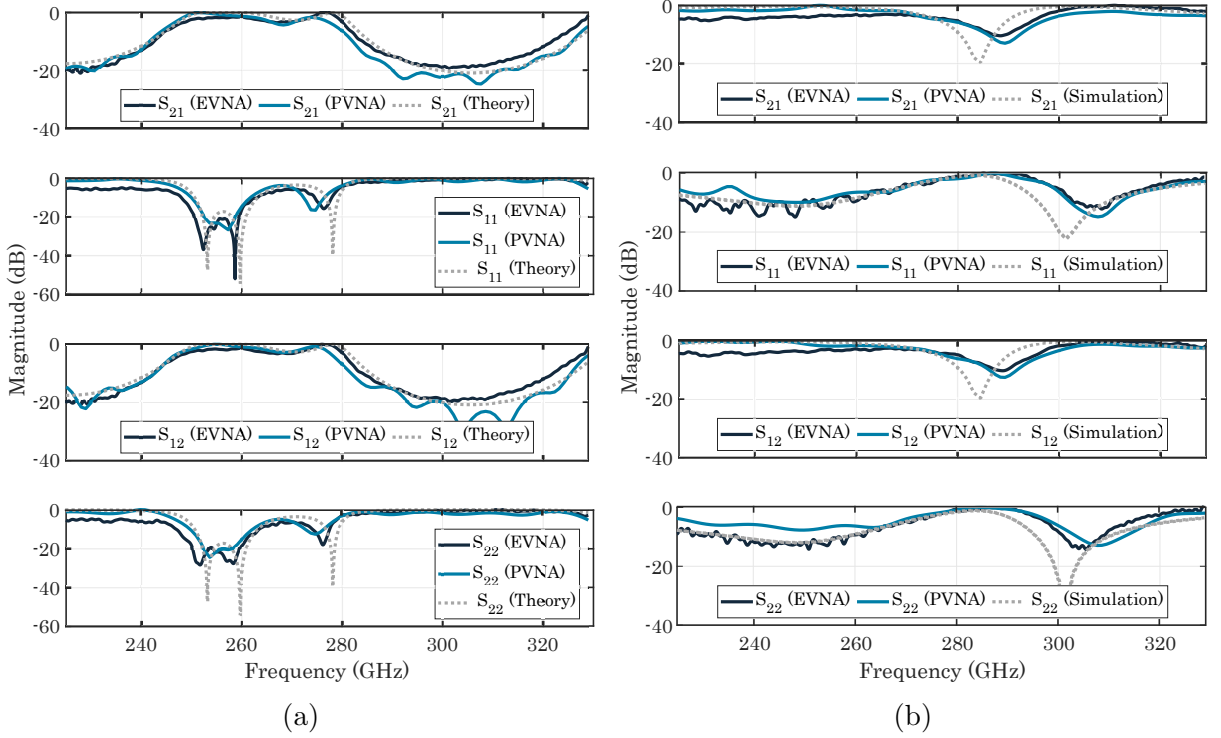


Figure 5.16: S -parameters extracted using PVNA is compared with commercial EVNA and theoretical calculation for (a) DBR and (b) SRR array. Reprinted from [229] ©2021 Optical Society of America.

5.6 Conclusion

In this chapter, we demonstrated a two-port pulsed free space PVNA with the ability to measure a complete set of S -parameters simultaneously. We achieve a bandwidth of 0.2-3 THz and a peak DNR of 57 dB with 10 ms integration time. The PVNA shows significant competence in extracting S -parameters for an SRR array, a CDR array and a DBR, by reproducing high- Q resonances up to about 273 at 1 THz. The PVNA also exhibits accuracy within the range of ± 0.005 for thickness extraction and ± 0.058 for frequency-dependent dielectric permittivity (real part).

The pulsed PVNA offers frequency coverage of up to 3 THz, which is beyond the available bandwidth of the CW PVNA (up to 1 THz) [276] and commercial EVNAs (up to 1.5 THz) [65]. In terms of DNR, the pulsed PVNA is comparable to the CW version within 0.5-1 THz with a peak DNR of 57 dB. The DNR obtained by the pulsed PVNA over the 1.1–1.5 THz range is approximately 47–35 dB, which is marginally higher than the 45 dB DNR of commercial EVNA for a two-port configuration. The frequency resolution of ~ 3 GHz is three orders of magnitude less than the CW PVNA (20 MHz) and EVNA (11 MHz) data used in this chapter. Still, the pulsed PVNA reproduces multiple adjacent resonant peaks successfully.

The two-port pulsed free space PVNA can potentially accelerate the development of THz components and devices by mitigating the lack of affordable and efficient characterization systems in the intermediate and higher THz range. The next step is to make the system compact and ready for on-chip integration. The current setup includes optical elements such as the

WGs, that make the system bulky and are also responsible for at least ~ 6 dB loss per detected signal. These elements can be eradicated from the system by replacing separate transmitter and receiver heads with a transceiver, which is the focus of the next chapter.

Terahertz Transceivers and Transceiver-based PVNA

In a conventional reflection-geometry Terahertz Time-Domain Spectroscopy (THz-TDS) setup with separate transmitter and receiver heads, the reflected THz signal from the Device Under Test (DUT) must be separated from the emitted signal beam path. This is accomplished either by implementing a beam splitter (for normal incidence) or by aligning the transmitter and detector heads at an angle relative to the surface normal of the DUT. The former suffers from a loss of at least 75% of the emitted signal due to the interactions with the broadband beam splitters, whereas the latter encounters complications in the alignment of the sensor heads due to the angled beam path. For the Photonic Vector Network Analyzer (PVNA) setups discussed in the last chapters, we implemented separate emitter and detector heads and a pair of Wire Grid Polarizers (WGPs) as frequency-independent directional couplers, similar to the beam splitter configuration. As previously indicated, this makes the systems cumbersome, inefficient, and costly. These issues can be mitigated by implementing THz transceivers that include both the source and the receiver integrated in one enclosure, hence enabling compact systems for measuring reflected THz signals under normal incidence. Moreover, the transceivers are ideally suited for industrial applications requiring compact devices for non-destructive, non-invasive, in-line process monitoring. It is also comparatively less expensive as only one head is needed instead of the two separate modules of classic THz-TDS configurations.

The THz transceiver concept was initially reported in 2000, which implemented a low-temperature-grown GaAs antenna with a shared photoconductive gap to generate and detect THz radiation under normal incidence [306]. Till now, two main design concepts for THz transceivers are reported in the literature: one that incorporates a common photoconductive gap for the generation and detection of THz radiation [306, 307] and the other that includes two spatially separated gaps on the same chip in close proximity [81, 308–310]. Since just one photoconductive gap needs to be illuminated for common gap transceivers, the optical coupling is simplified. However, the bias voltage of the emitter and the photocurrent produced by the optical excitation beams both contribute to the noise of the detector, limiting the bandwidth and Dynamic Range (DNR) of the system [306]. Hence, the bandwidth reported for this design is less than 2 THz with a peak DNR of 40 dB [306, 307]. The separate gap concept reduces the effect of the cross-talk but presents difficulties in terms of the optical coupling

of individual gaps. The distance between the antennas must also be carefully adjusted to prevent undesirable resonances [306] and distortion of the radiation pattern. Implementing this concept, Kohlhaas *et al.* have reported a Fe-doped InGaAs photoconductor-based transceiver with 6.5 THz bandwidth and a peak DNR of 75 dB (1000 scan average with 60 s measurement time) [310]. Prior to this, the same research group also reported a Be doped InGaAs-based transceiver with 4.5 THz bandwidth and 70 dB peak DNR [309]. Better electrical and dynamic characteristics of InGaAs:Fe photoconductive material are largely responsible for this drastic enhancement [310].

In this chapter, we present the design and fabrication process of an ErAs:In(Al)GaAs-based THz transceiver and evaluate the performance by implementing it in a one-port characterization system for Scattering (S)-parameter extraction applications.

6.1 Development of the Transceiver

6.1.1 Material Properties

For efficient generation and detection of THz radiation, the photoconductors must fulfill different requirements. High mobility and a large breakdown field strength are the most crucial properties for emitter materials in order to accelerate optically generated carriers in a large bias field in an efficient manner, whereas a short (sub-picosecond) carrier lifetime for detector materials allows for accurate time-domain sampling of the THz pulse [311]. These requirements are challenging to satisfy concurrently since they partially compete with one another. Hence, developing a photoconductor for THz transceivers that simultaneously meets the demands of the emitter and the receiver is difficult.

We utilize ErAs:In(Al)GaAs photoconductors, identical to the emitter material reported in Section 3.1.2, to fabricate the THz transceiver. It consists of 90 periods of a superlattice structure containing a 15 nm InGaAs layer, followed by 0.8 monolayers of C-delta-doped ErAs sandwiched between two 1.5 nm C-doped InAlAs layers [214]. The breakdown field strength of the material is 170 ± 40 kV/cm under dark conditions and above 130 ± 20 kV/cm when illuminated with 45 mW of optical power [214]. In addition to that, a resistivity of 3850 Ω cm and mobility of around 450 cm^2/Vs makes it an excellent choice for THz sources [214]. However, it exhibits a comparatively long carrier lifetime (1.842 ± 0.029 ps) [161], which is not ideal for a THz detector since it leads to a reduced signal-to-noise ratio (see Section 2.2.2). Systems based on these photoconductors have demonstrated more than 6 THz bandwidth and 110 dB peak DNR (averaged over ~ 1000 scans with 1 min acquisition time) [76]. Consequently, even with a lower DNR due to the longer carrier lifetime (>1 ps) of the material as a receiver, the detected THz radiation is expected to have sufficient strength for a variety of applications. Table 6.1 compares the material properties of ErAs:In(Al)GaAs and the state-of-the-art transceiver material Fe:InGaAs.

Material Type	Resistivity (Ωcm)	Mobility (cm^2/Vs)	Carrier Lifetime (ps)
ErAs:In(Al)GaAs	3850	450	1.842 ± 0.029
Fe:InGaAs	1570	710	0.25

Table 6.1: Typical material properties of ErAs:In(Al)GaAs and Fe:InGaAs [178,214,310].

6.1.2 Fabrication Process

The ErAs:In(Al)GaAs photoconductor grown on a 500 μm InP:Fe substrate wafer is cleaved to form a 7 mm \times 8 mm sample where the antenna and electrode structures will be patterned via contact Ultraviolet (UV) lithography. A thin layer of AZ[®] 5414 E photoresist is spin-coated at 6000 rpm on the sample, followed by the first lithography step that removes the outermost 1 mm wide stripe of photoresist from the edges of the sample using AZ[®] 726 MIF developer. This ensures good contact between the quartz mask and the active area (remaining 6 mm \times 7 mm area containing the photoresist) for the subsequent lithographic step, as spin-coating-induced irregularities in the edges of the sample are removed. Next, the antenna and the electrode structures are patterned by UV exposure, followed by the image reversal bake step, which entails heating the sample at 120 $^{\circ}\text{C}$ for one minute, and is conducted to transform the AZ[®] 5414 E from positive to negative. Afterwards, the sample is irradiated with UV light without any mask and subsequently developed exposing the sample surface featuring the desired layout. Figure 6.1 depicts these steps taken to prepare the sample for the subsequent metal antenna deposition stage.

The sample is immersed in a 1:1 solution of water and Hydrochloric acid (HCl) for 30 seconds to remove the native oxide of the InGaAs cap layer. This enhances the adhesion of the deposited metal resulting in better ohmic contact between the metal and the InGaAs layer. Subsequently, the thermal evaporation method is used to thermally deposit a 180 nm layer of Gold after depositing a 20 nm layer of Titanium using an electron beam evaporator. The sample is then submerged in acetone for 15 minutes to dissolve the photoresist along with the metal deposited on it from the untreated regions (Lift-off). A further annealing process, at 420 $^{\circ}\text{C}$ for 30 seconds in a Nitrogen purged chamber, is conducted to reduce the interface trap density to diffuse the metals into the semiconductor and establish an ohmic contact between the metal and the semiconductor. Figure 6.2 shows the metal deposition technique as detailed above.

In the mesa etching process, the ErAs:In(Al)GaAs layer is removed by wet etching from the sample, with the exception of the areas between the electrodes, beneath the antenna, and around the pads, as illustrated in Figure 6.3. A layer of AZ[®] 1518 is spin-coated on the sample at 4000 rpm, followed by patterning of the mesa structures using another photolithography step and subsequent development with the AZ[®] 726 MIF developer. Next, the photoresist is hard-baked for 15 minutes at 110 $^{\circ}\text{C}$, which causes any remaining solvent to evaporate, therefore strengthening the link between the resist and the structure and stabilizing it. In the regions not covered by the photoresist layer, the ErAs:In(Al)GaAs photoconductive material is etched away, exposing the semi-insulating, highly resistive InP:Fe substrate. The etching agent used in this case is a combination of Sulphuric acid (H_2SO_4), Hydrogen Peroxide (H_2O_2), and water ($\text{H}_2\text{SO}_4:\text{H}_2\text{O}_2:\text{H}_2\text{O} = 1:8:50$), which etches the photoconductive material at a rate of 14.5 nm/s.

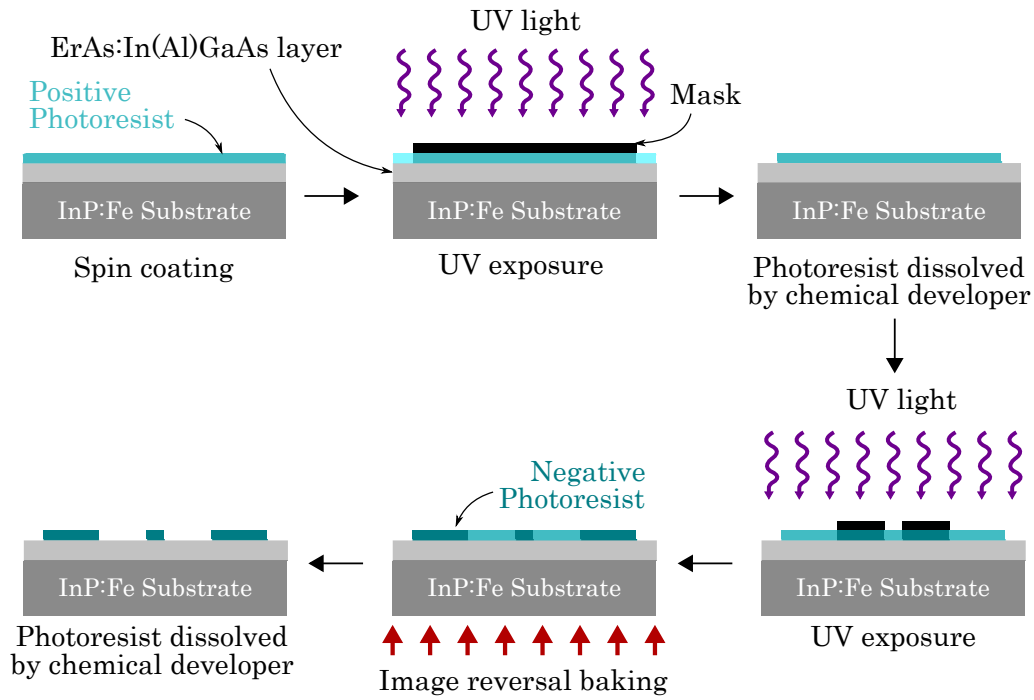


Figure 6.1: Preparation of sample before metal deposition.

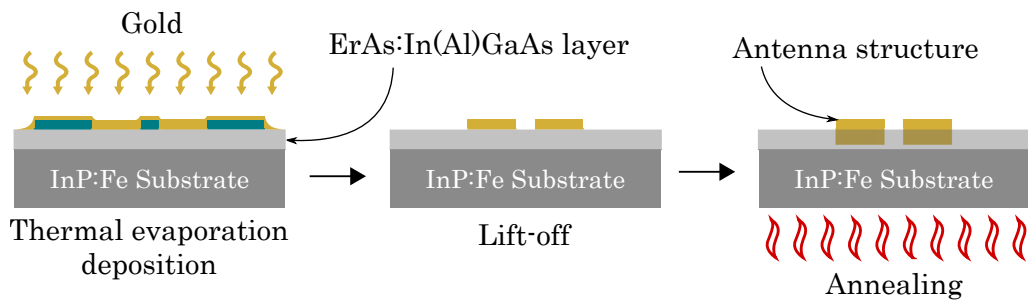


Figure 6.2: Metal deposition process.

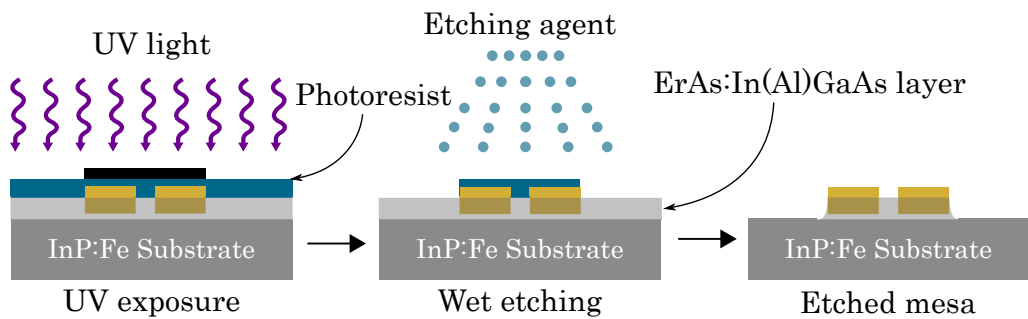


Figure 6.3: Mesa etching process.

The plasma-enhanced chemical vapor deposition process is used to structure a layer of Silicon Nitride (Si_3N_4) deposited on top of the sample (Figure 6.4). The layer thickness is optimized to reduce reflection for better coupling of the infrared laser into the active region. In addition, this layer protects the photoconductive material from oxidation and other types of contamination. AZ[®] 1518 photoresist is deposited on the sample by spin-coating at 4000 rpm. Using lithography and development, a protective photoresist coating covering only the electrode structure is subsequently patterned. Using Carbon Tetrafluoride (CF_4) as the etching agent, reactive ion etching process removes the Si_3N_4 layer from the exposed contact metal pads attached to the antenna. Using Carbon Tetrafluoride (CF_4) as the etching agent, reactive ion etching process removes the Si_3N_4 layer from the exposed contact metal pads attached to the antenna.

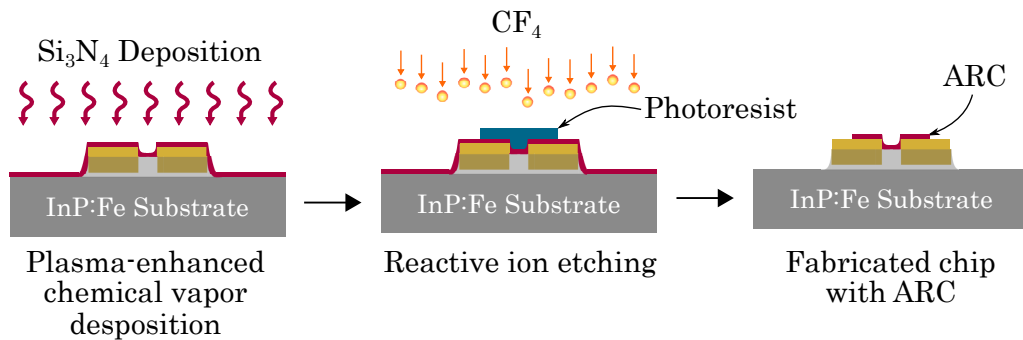


Figure 6.4: Anti-Reflection Coating (ARC) deposition process.

After the fabrication process, each transceiver chip is cleaved out for packaging. Figure 6.5 depicts the micrograph of a typical transceiver chip design. To emit the signal, a slotline antenna with a $25\ \mu\text{m}$ gap is implemented and to receive the THz radiation, an H-dipole antenna with a $10\ \mu\text{m}$ gap is employed. The transmitter and receiver modules are separated by a $20\ \mu\text{m}$ distance, ensuring a confocal THz beam path.

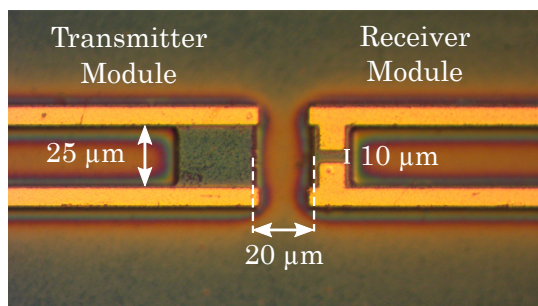


Figure 6.5: Micrograph of a ErAs:In(Al)GaAs photoconductor-based THz transceiver chip.

6.1.3 Packaging

The transceiver chip is semi-packaged in a 50 mm \times 40 mm housing containing a hyper hemispheric silicon lens with a diameter of 10 mm and thickness of 6.1 mm. UV curable glue is used to secure the chip once it has been positioned in the center of the silicon lens. The electrical contacts are realized via conductive epoxy bonding to the external circuits. The module also consists of separate coaxial cable connectors to facilitate the application of bias voltage and read-out of the detected THz signal. Free space coupling of the optical signals is achieved by an external lens that focuses both laser beams onto the individual gaps. A high-precision 3D stage with micrometer accuracy is used to align the focused laser spots onto the photoconductive gaps, which is necessary for free space coupling.

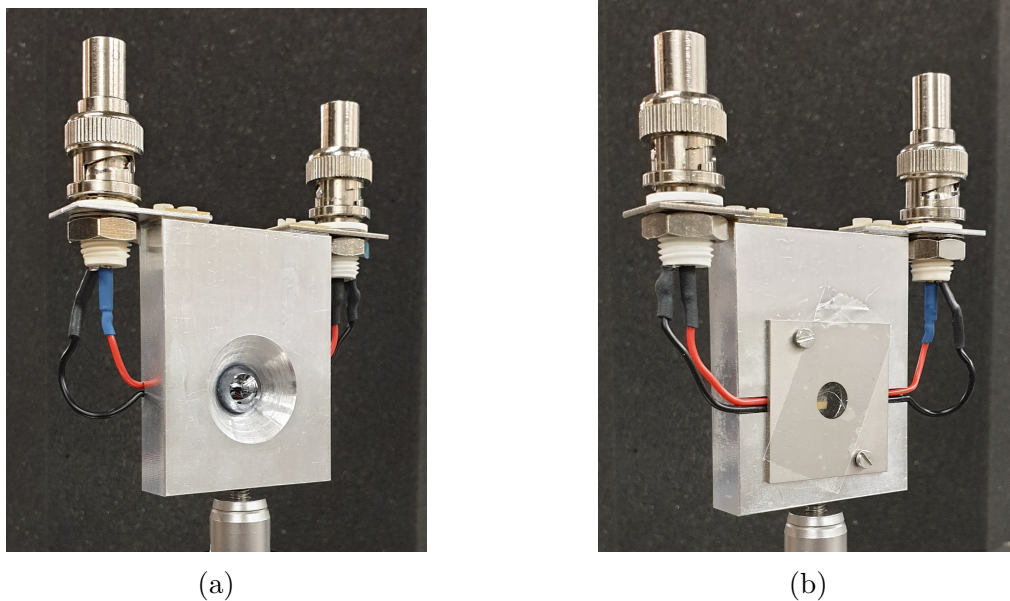


Figure 6.6: (a) Front and (b) rear view of the semi-packaged transceiver module.

6.2 Transceiver-based One-Port PVNA

To characterize the transceiver chip and verify its capability, a one-port PVNA containing the packaged transceiver is configured that can extract the S_{11} parameter of a DUT.

6.2.1 Experimental setup

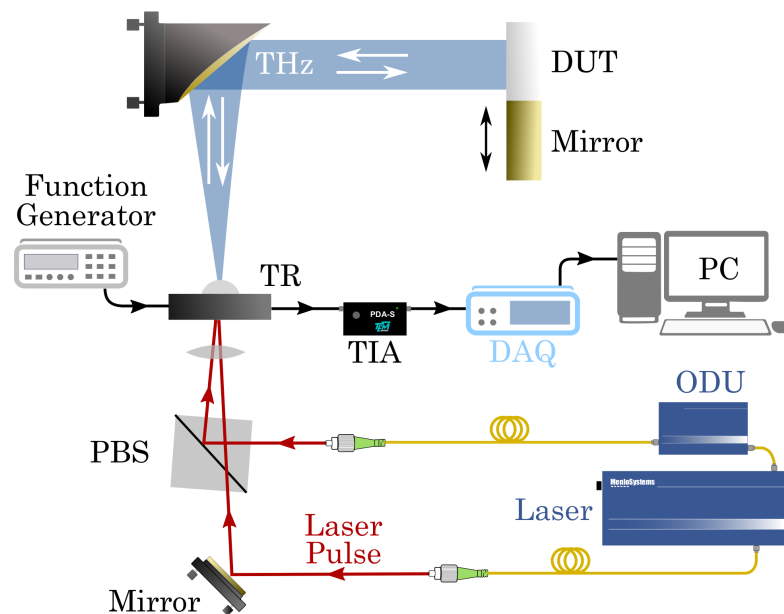


Figure 6.7: Experimental setup of a transceiver-based one-port PVNA. TR = Transceiver, PBS = Polarizing Beam Splitter, TIA = Transimpedance Amplifier, DAQ = Data Acquisition, ODU = Optical Delay Unit.

Figure 6.7 illustrates the experimental setup of a transceiver-based one-port pulsed free space PVNA. It consists of a monolithically integrated transceiver (TR) containing a transmitter and a detector module fabricated on the same chip that emits and receives the THz pulses. A commercially available Menlo Tera K15 time-domain system [312] containing a pulsed laser (1560 nm operation wavelength, 90 fs pulse duration, 100 MHz repetition rate) and an Optical Delay Unit (ODU) is used to realize the PVNA. Laser pulses emerging from the two fiber ports are launched into free space via beam collimators. A Polarizing Beam Splitter (PBS) is used to combine the pump and probe beams onto the electrode gaps of the transmitter and receiver module, respectively. The transmitter is driven with 28 mW of optical power, whereas the receiver is driven with 9 mW of optical power. A source measure unit (Keithley 2400 [313]) supplies the transmitter module with 40 V DC bias, and the read-out is performed by a Data Acquisition (DAQ) system. Prior to the read-out, the detected photocurrent is converted to voltage by implementing a low noise Trans-Impedance Amplifier (TIA) from TEM Messtechnik (PDA-S) [219] with a trans-impedance gain of 10^7 V/A. The DAQ and the data acquisition software are also contained within the commercial time-domain system. We point out that

the bias provided to the transmitter module is roughly half of that applied for 1.5 port Vector Spectrometer (VSM) and two-port PVNA (Chapters 4 and 5), to safeguard the transceiver for extended operation.

6.2.2 System Characteristics

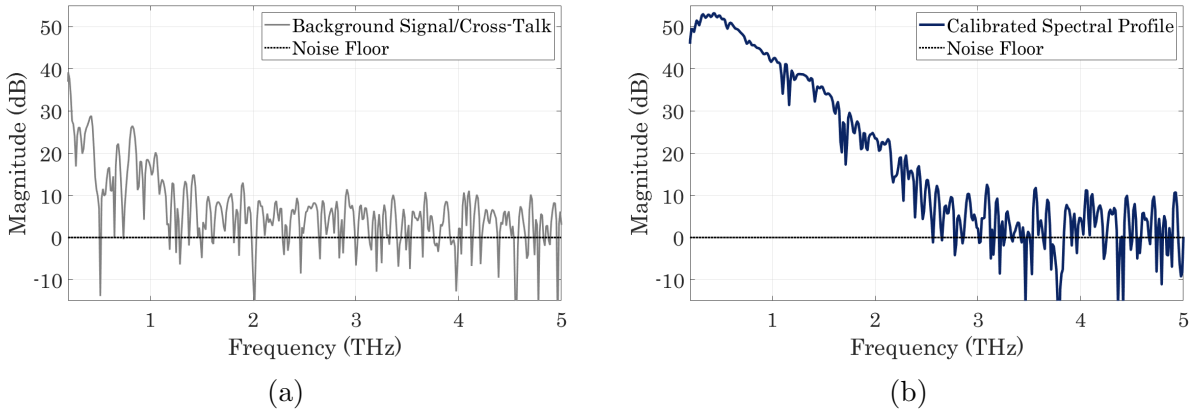


Figure 6.8: (a) Cross-talk and (b) calibrated spectral profile of the one-port PVNA.

Cross-talk may arise due to the close proximity of the transmitter and receiver modules on the same photoconductive chip. This is investigated by measuring the detected THz signal after removing all obstacles from the THz path that may prompt reflection of the emitted THz signal within the measurement window. Figure 6.7(a) depicts the spectral profile of this signal. It is evident from the figure that direct cross-talk between the transmitter and receiver through the substrate of the transceiver chip causes a noticeable amount of background in the received signal. This background signal or cross-talk is more prominent in the lower frequencies with a relative strength of about -28 dB at 0.4 THz and steadily decreases until it becomes negligible beyond 1.5 THz. Due to the static nature of this background, it can be calibrated out by subtracting it from the measured signals, similar to the approach discussed in Section 3.2.

For the determination of the S_{11} parameter with the one-port system, the reference measurement is recorded with a metal mirror placed at the reference plane and the test signal is recorded with the DUT replacing the mirror. The calibrated spectral profile of the reference signal is depicted in Figure 6.8(b), indicating that the system has a bandwidth of 0.2 to 2.5 THz with a peak DNR of ~ 53 dB. This measurement is recorded for an average of 1000 scans with a measurement duration of 100 seconds. The time domain measurements are performed using a time window of 80 ps, corresponding to a frequency resolution of around 7 GHz. This resolution can be improved by using a longer measurement window.

Compared to the two-port PVNA configured with isolated transmitter and receiver heads and WGP-formed directional couplers (Chapter 5), the bandwidth and DNR of the transceiver-based one-port PVNA are relatively lower. There are a number of factors that contribute to this. In comparison to the ErAs:InGaAs photoconductive receivers used for the isolated module PVNA, the transceiver's receiver module performs inferiorly due to its longer carrier lifetime, which has a direct impact on the system's signal-to-noise ratio. The DNR and operational band-

width of the system are also adversely affected by pronounced background and lower applied bias to the transmitter module. Despite this, the one-port PVNA can function at frequencies exceeding 2 THz, whereas a commercial Electronic Vector Network Analyzer (EVNA) frequency extender can only reach 1.5 THz [65].

6.2.3 Applications

To verify the principle of operation of the configured transceiver-based one-port PVNA, we investigate the S_{11} parameter of a Distributed Bragg Reflector (DBR) and a Split-Ring Resonator (SRR) array (same as the ones described in Sections 5.3.1 and 5.3.2) and compare the results with a theoretical model or simulation.

Characterization of a DBR

Figure 6.9 compares the retrieved S_{11} parameter of the DBR with the theoretically derived one in terms of magnitude and phase. The frequency resolution of the theoretical data is adapted to resemble to the measured data for a fair comparison. The extracted magnitude of the S_{11} parameter matches rather well with theoretical calculation. However, due to low DNR, the pass-bands exhibit reduced strength than estimated, yet their frequency positions fit the theoretical model perfectly. The phase of the S_{11} parameter also shows excellent agreement with the theory. Due to water vapor resonance-induced artifacts, there is a slight disparity above 1.6 THz in the phase of the extracted S_{11} parameter. Apart from that, the theoretical prediction and the observed value of the S_{11} parameter are well-matched.

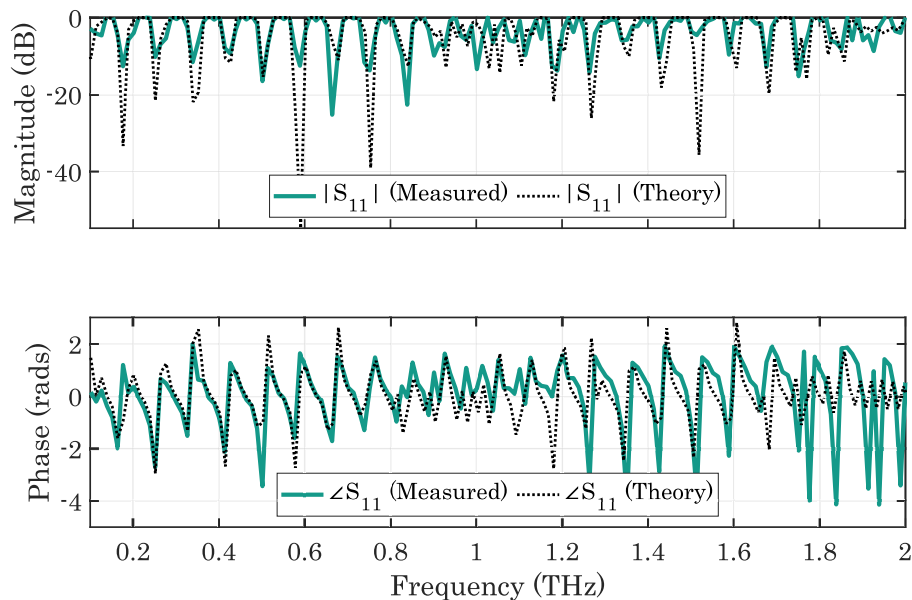


Figure 6.9: S_{11} parameter of a DBR extracted using a one-port transceiver-based PVNA and compared with the theoretical model.

Characterization of a SRR array

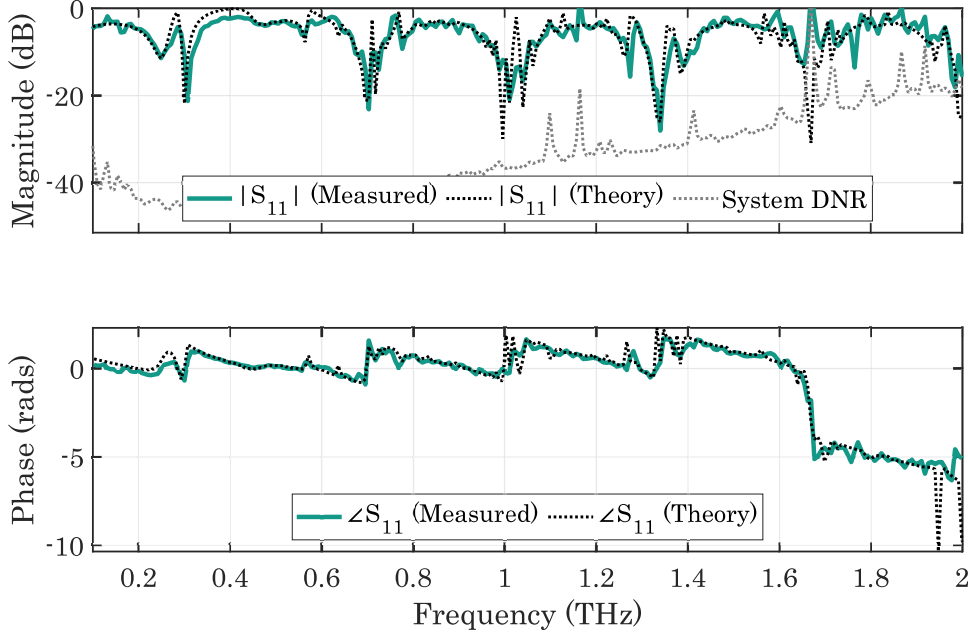


Figure 6.10: S_{11} parameter of a SRR extracted using a one-port transceiver-based PVNA and compared with the simulation.

Figure 6.10 depicts a comparison between the simulation (CST Microwave Studio) and the experimentally determined S_{11} parameter of the investigated SRR array in terms of magnitude and phase. The magnitude data demonstrate excellent agreement with simulated results. Each resonance peak is accurately resolved, having an almost identical Quality (Q)-factor. With a Q -factor of ~ 79 in the simulation and ~ 71 in the experimental data, the first resonance peak occurs at roughly 300 GHz. At around 1.7 THz, a high- Q resonance feature is absent in the extracted S_{11} parameter magnitude data. It is evident from the figure that the system lacks sufficient DNR to resolve the peak at this point. The SRR-induced resonance peak becomes harder to detect when the system DNR approaches the noise floor due to an overlapping water vapor resonance artifact. Besides that, a number of multi-peak features are reproduced, even with a frequency resolution of ~ 7 GHz. The phase data also closely resemble the simulated model. This demonstrates that the transceiver-based one-port PVNA can accurately determine the S_{11} parameter of a DUT with frequency coverage of 0.2-2 THz.

6.3 Conclusion

This chapter addressed the design and fabrication process of a THz transceiver based on ErAs:In(Al)GaAs photoconductor. We then assessed its performance by implementing it in a one-port PVNA configuration to measure the S_{11} parameter of several THz components. We showed that the bandwidth of the one-port system was between 0.2 and 2.5 THz, with a peak

DNR of 53 dB for a 1000 scan average during 100 s of measurement time (Time Constant (TC) ≈ 42 ms). By extracting the S_{11} parameter of a DBR and a SRR array, the transceiver-based PVNA demonstrates great aptitude, with magnitude and phase data showing excellent agreement with the theoretical model. The PVNA frequency coverage of up to 2.5 THz exceeds the maximum frequency that the commercial EVNA extenders can attain, which is 1.5 THz [65].

As demonstrated in Reference [310], if the photoconductive material could be engineered to have a shorter carrier lifetime while maintaining similar resistivity and mobility, the bandwidth and DNR of the transceiver would be significantly increased. Alterations to the antenna layout and substrate can also help to reduce the effect of cross-talk. The semi-packaged transceiver can be fully packaged by integrating the PBS and focusing lens into the head, further simplifying optical alignment and enabling plug-and-play configuration.

The transceiver-based one-port PVNA can be expanded to a complete two-port PVNA by adding a second transceiver enabling the extraction of a full set of S -parameters of a DUT. The most challenging aspect of this will be differentiating signals emanating from distinct transmitter modules. Activating one transmitter at a time and capturing both transmission and reflection data for that transmitter, as classic EVNAs do, is one approach to circumvent this issue. Incorporating a mechanical-delay-stage-free laser system, such as TeraFlash Pro [212], which has four fiber ports to facilitate the simultaneous driving of two transceivers, can further simplify the system's setup and data acquisition procedure, as well as increase the system's speed.

Summary and Outlook

Recent advancements in the generation and detection of THz radiation have resulted in room-temperature-operated tabletop photonic systems with enormous bandwidth and power. This has encouraged researchers to engineer THz devices and components for cross-disciplinary applications that greatly benefit from these attributes. However, the bottleneck for the development of such devices and components is the lack of efficient and cost-effective characterization systems capable of broadband and high frequency (>1.5 THz [65]) investigations. This thesis aims to provide a solution to this bottleneck and establish a solid foundation to mitigate the research gap that the present characterization systems are unable to address.

State-of-the-art electrical and photonic characterization systems for THz range investigation were discussed in Chapter 2. Electronic Vector Network Analyzers (EVNAs) are usually employed in the electronic domain to characterize THz devices and components, which require frequency extender modules to achieve a maximum frequency of 1.5 THz [65]. However, these modules are relatively narrowband, necessitating multiple units to cover a wide frequency range. In addition, upscaling these systems is difficult owing to manufacturing and alignment tolerances. At the same time, photonic Terahertz Time-Domain Spectroscopy (THz-TDS) systems based on photoconductive transmitters and receivers, driven by already well-established telecom-wavelength ultrafast pulsed lasers, can reach very high frequencies (~ 10 THz) [78] with considerable power (~ 110 dB peak Dynamic Range (DNR)) [76]. These systems enable the path for free space pulsed Photonic Vector Network Analyzers (PVNAs), which is the main focus of this thesis.

Since a pulsed PVNA uses a time-domain measurement approach rather than the frequency-domain measurement technique of an EVNA, the calibration and data evaluation processes are slightly different. The calibration of the PVNA is more straightforward than that of the EVNA, as the signal travels through the air with a well-known wave impedance of 376.6Ω . For the calibration of PVNA, we developed a method comparable to the combination of the 'Gated-Reflect-Line' (GRL) [149] and the '*Through-Through-Network*' (TTN) self-calibration [151,152] technique of EVNA. We also developed an algorithm to extract the complicated dielectric permittivity, alternatively, the refractive index and absorption coefficient, in addition to the thickness of a Material Under Test (MUT) from the retrieved Scattering (S)-parameters.

We configured a 1.5 port Vector Spectrometer (VSM) capable of simultaneously measuring both transmission and reflection coefficients, which are analogous to the S_{21} and S_{11} parameters, respectively. It is an upgrade of traditional THz-TDS systems that are configured either in transmission or reflection geometry and can measure either S_{21} or S_{11} parameters. With a demonstrated bandwidth of around 0.2–2.5 THz, the 1.5 port VSM provides coverage at frequencies that go beyond the range of currently available commercial Vector Network Analyzers (VNAs) [65]. Measurements were conducted in a single setup without the need to reconfigure the setup or move the Device Under Test (DUT) across systems. The aptitude of the VSM was verified by extracting optical parameters, including refractive index and absorption coefficient, and physical thickness of the MUT using the previously mentioned algorithm. The error margin of the determined refractive index is around ± 0.05 and less than $10 \mu\text{m}$ for thickness. The retrieved absorption coefficients are consistent with what has been reported in the literature. The VSM also successfully characterized an asymmetrical device, a THz isolator, in terms of insertion loss and isolation level, with an excellent match with the theoretical model.

The system is then extended to a two-port PVNA, which can concurrently extract a complete set of S -parameters with a demonstrated bandwidth of 0.2 to 3 THz and a peak DNR of 57 dB (Equivalent Noise Bandwidth (ENBW) ≈ 10 Hz). The frequency coverage of up to 3 THz for pulsed PVNA is significantly broader in comparison to their Continuous Wave (CW) (up to 1 THz) [276] and commercial electronic (up to 1.5 THz) [65] equivalent. In terms of DNR, the pulsed PVNA is comparable to the photonic CW version within the 0.5-1 THz range. The 47–35 dB DNR of the PVNA in the 1.1-1.5 THz band is better than the 45–25 dB DNR of the EVNA for a two-port configuration. Substantial proficiency in extracting S -parameters for a Split-Ring Resonator (SRR) array, a Crossed-Dipole Resonator (CDR) array, and a Distributed Bragg Reflector (DBR) was demonstrated by the PVNA, with both magnitude and phase data exhibiting excellent agreement with the simulations. In addition, the PVNA demonstrated high accuracy in thickness (± 0.005 mm) and frequency-dependent complex dielectric permittivity calculation.

Finally, a THz transceiver was manufactured with the aim of miniaturizing the PVNAs for on-chip integration and industrial application. The transceiver was then utilized to set up a one-port PVNA to assess its feasibility in configuring such characterization systems. We obtained a bandwidth of 0.2-2.5 THz and a peak DNR of 53 dB (Time Constant (TC) ≈ 42 ms) with this PVNA. This transceiver-based PVNA performs admirably by extracting the S_{11} parameter of a DBR and a SRR array, with magnitude and phase data exhibiting excellent agreement with the theoretical model.

Efficient pulsed free space PVNAs configured in this work incorporate a broad spectral range and are able to characterize a wide variety of THz components and materials in the THz range. The PVNA bandwidth exceeds six hollow metal waveguide bands in one system and unlike EVNAs, are not susceptible to measurement uncertainties originating from variances in the metal waveguide and flanges connections, unstable cables, standing waves. Broadband investigations can be carried out in a single setup, and the calibration process is greatly simplified. Compared to highly-priced EVNA extension modules, these systems are cost-effective. Therefore, the PVNAs pave the way for future THz-range characterization systems that are efficient and affordable, and creates a strong foundation for THz component development, enabling widespread adaptation of THz technologies in both research and industrial settings.

7.1 Limitations and Outlook

The configured PVNAs incorporate a few limitations in terms of measurement speed and frequency resolution. They are interrelated in the sense that the resolution of the system is dependent on the investigated time window, and both are linked with the mechanical delay stage. A ~ 160 ps window scan with 10 ms integration time (ENBW ≈ 10 Hz) takes approximately 15 minutes, corresponding to a ~ 3 GHz spectral resolution. The resolution is rather low compared to that of commercial EVNAs (a few Hz) [65] and CW PVNAs (a few MHz) [276]. By implementing Asynchronous Optical Sampling (ASOPS) [279] or Electronically Controlled Optical Sampling (ECOPS) [281] techniques, which do not require a mechanical delay stage, it is possible to circumvent this limitation to some extent. Systems based on these techniques have demonstrated a spectral resolution of 50.5 MHz [193] and an acquisition rate of 2 kHz for a 100 ps scan window [282].

Although we demonstrated the principle of operation for a PVNA built with transceivers, due to time constraints, we did not configure a transceiver-based two-port PVNA. Furthermore, the THz transceivers can still be improved in terms of cross-talk elimination, system bandwidth expansion, and DNR improvement. According to reference [310], this is accomplished by engineering photoconductive materials with a short carrier lifetime, high resistivity, and high mobility. Cross-talk can be minimized by modifying the antenna's architecture and the substrate. A two-port PVNA with improved transceivers may be investigated as part of a potential future extension of this work.

Due to free space configuration, the PVNA application examples discussed in this thesis were only confined to the characterization of planar THz components or materials. On-wafer THz component investigations utilizing EVNA are generally realized by implementing contact probes, which suffer from fragility and misalignment issues due to their minuscule dimensions required for THz frequency characterization. To test on-wafer transmission-line-coupled THz components, Caglayan *et al.* have devised a non-contact probing technique [314–316]. This technique can be studied further to determine its applicability in pulsed PVNA settings.

The next stage in the development process would be to integrate the system on chip, which would enable for widespread implementation of such systems in both academic and commercial settings. To realize on-chip pulsed PVNAs, broadband planar waveguide topology has to be developed. In addition, the development of broadband splitters with a well-defined splitting ratio and research into photoconductor-to-waveguide transitions, transitions to free space and coplanar waveguide design, etc., will be necessary. Our research group has already conducted some work regarding broadband THz photonic integrated circuits [317], and the results will guide future attempts to develop on-chip PVNAs.

THz technology is rapidly moving from the realm of basic science to widespread industrial use, thanks to the proliferation of multidisciplinary applications and the development of more effective generation and detection methods. However, characterization systems continue to lag behind, impeding the development of THz components and devices. With vast bandwidth and substantial power, pulsed free space PVNAs has the potential to become the characterization system that alleviates the demand constraint for THz components and expedites the development of THz technologies.

APPENDIX A

Data Acquisition GUI

Various components of the data acquisition Graphical User Interface (GUI) illustrated in Figure A.1 are outlined below.

Port denotes the port at which the mechanical delay stage controller is connected.

Initialize Delay Stage button initializes the mechanical delay stage.

Master Lock-in shows the connected primary lock-in amplifier.

Slave Lock-in shows the connected secondary lock-in amplifier.

Initialize Lockin(s) button initializes both the lock-in amplifiers and loads the preset parameters such as time constant, modulation frequency, filter order and data acquisition rate.

Synchronize button synchronizes both the lock-in amplifiers with a 10 MHz reference clock to have the same time stamp.

Move to button moves the mechanical stage to the input position.

Start displays the starting position of the stage.

End displays the ending position of the stage.

Step (for 'Scan' function) displays the step distance in mm.

Num. Scan (for 'Shake and Measure' function) displays the number of scans to be executed.

Speed shows the speed of the stage in mm/s.

The **Scan** button initializes the step-by-step scan and data fetching from the lock-in amplifier.

The **Shake and Measure** button initializes continuous scan and data fetching from the lock-in amplifier.

The **Shake** button prompts the stage to move between the start and end positions without taking any data. This technique is used mainly for alignment purposes.

The **Stop** button terminates the movement of the stage and data acquisition from the lock-in amplifier.

The **Save StepScan** button saves the data acquired for the step-by-step scan case.

The **Save ContinuousScan** button saves the data acquired for the continuous scan case.

The **FFT** button converts the acquired data from the time domain to the frequency domain and displays it.

The **Sample** is an editable text box, where the name of the investigated sample can be entered. This sample name is then included in the saved file.

TransmissionT2R1 displays the time-domain THz signal generated by Transmitter 2 and received by Receiver 1 after transmitting through the sample.

TransmissionT1R2 displays the time-domain THz signal generated by Transmitter 1 and received by Receiver 2 after transmitting through the sample.

ReflectionT1R1 displays the time-domain THz signal generated by Transmitter 1 and received by Receiver 1 after reflecting back from the sample.

ReflectionT2R2 displays the time-domain THz signal generated by Transmitter 2 and received by Receiver 2 after reflecting back from the sample.

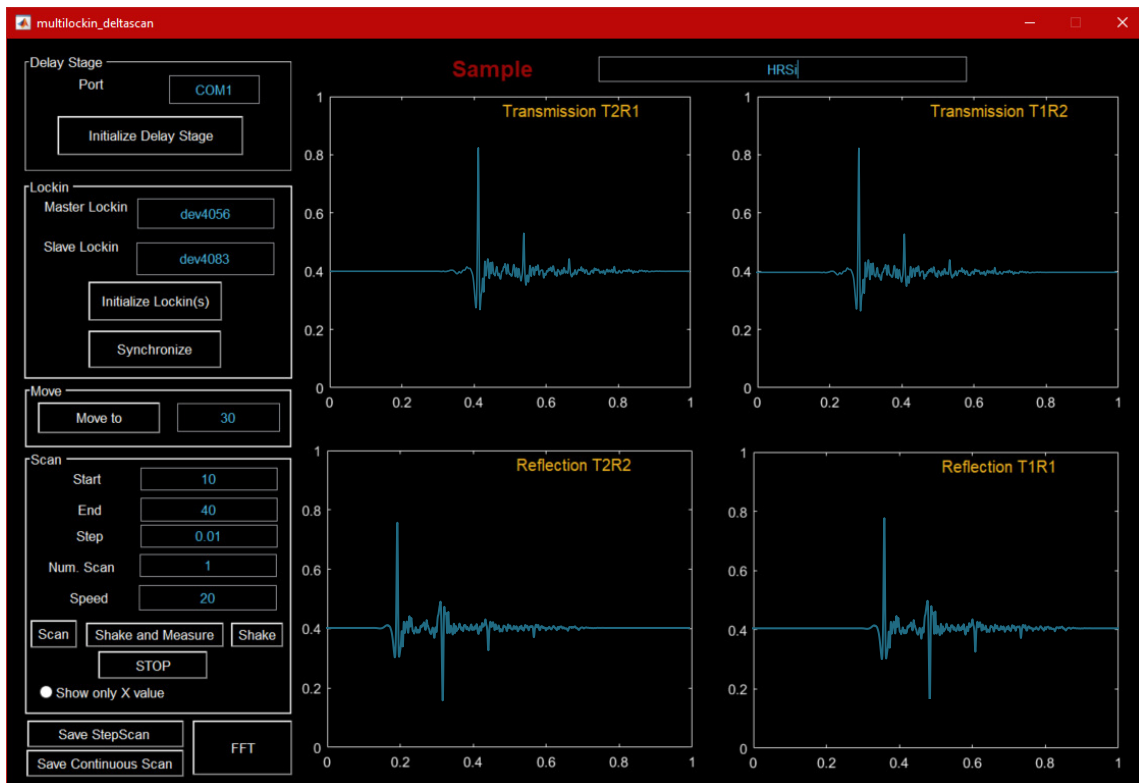


Figure A.1: Data acquisition GUI.

APPENDIX B

MATLAB Code for Material Characterization Algorithm

```
1 clear all;
2 close all;
3
4 % importing data file
5
6 % reference
7 ref_tr_t1r1 = importdata ('empty_t1r1.txt');
8 ref_tr_t2r2 = importdata ('empty_t2r2.txt');
9
10 ref_r_t1r1 = importdata ('mirror_t1r1.txt');
11 ref_r_t2r2 = importdata ('mirror_t2r2.txt');
12
13 % sample
14 sam_t2r1andt1r1 = importdata ('sample_transmissions_and_t1r1.txt');
15 sam_t1r2andt2r2 = importdata ('sample_transmissions_and_t2r2.txt');
16
17 %% getting data
18 % [t,x21,x11,x22,x12]
19
20 [ref_tr_time,ref_tr_21,no_ref_r_11,~,~] = func_2port_getdata (
    ref_tr_t1r1);
21 [ref_tr_time2,~,~,no_ref_r_22,ref_tr_12]= func_2port_getdata (
    ref_tr_t2r2);
22
23 [ref_r_time,no_ref_tr_21,ref_r_11,~,~] = func_2port_getdata (ref_r_t1r1
    );
24 [ref_r_time2,~,~,ref_r_22,no_ref_tr_12] = func_2port_getdata (
    ref_r_t2r2);
25
26 %port 1
27 [sam_time1,sam_tr_21,sam_r_11,~,~] = func_2port_getdata (
    sam_t2r1andt1r1);
```

```
28 %port 2
29 [sam_time2,~,~,sam_r_22,sam_tr_12] = func_2port_getdata (
    sam_t1r2andt2r2);
30
31 figure;
32 subplot (2,2,1);
33 plot (ref_tr_time, ref_tr_21);
34 hold on;
35 plot (sam_time1, sam_tr_21);
36 subplot (2,2,2);
37 plot (ref_tr_time2, ref_tr_12);
38 hold on;
39 plot (sam_time2, sam_tr_12);
40 subplot (2,2,3);
41 plot (ref_r_time, ref_r_11);
42 hold on;
43 plot (sam_time1, sam_r_11);
44 subplot (2,2,4);
45 plot (ref_r_time2, ref_r_22);
46 hold on;
47 plot (sam_time2, sam_r_22);
48
49 %% Windowing
50
51 % getting rid of data below 200 GHz
52
53
54 f_filter_min = 0.2;
55
56
57 ref_tr_21 = func_2port_hpfilter (t,f_filter_min,ref_tr_21);
58 ref_tr_12 = func_2port_hpfilter (t,f_filter_min,ref_tr_12);
59 ref_r_11 = func_2port_hpfilter (t,f_filter_min,ref_r_11);
60 ref_r_22 = func_2port_hpfilter (t,f_filter_min,ref_r_22);
61
62 sam_tr_21 = func_2port_hpfilter (t,f_filter_min,sam_tr_21);
63 sam_r_11 = func_2port_hpfilter (t,f_filter_min,sam_r_11);
64 sam_r_22 = func_2port_hpfilter (t,f_filter_min,sam_r_22);
65 sam_tr_12 = func_2port_hpfilter (t,f_filter_min,sam_tr_12);
66
67     %% Primary Thickness calculation
68
69 [d,n] = func_primarydn (tr,ts,ar,as)
70 % For Tx 1 and Rx1 and Rx2
71 [d_p1, n_p1, peakflag1] = func_2port_primarydn (t,ref_tr_12,sam_tr_12,
    sam_r_11);
72
73 % For Tx 2 and Rx1 and Rx2
74 [d_p2, n_p2, peakflag2] = func_2port_primarydn (t,ref_tr_21,sam_tr_21,
    sam_r_22);
75
76
```

```
77 %figure time domain
78
79     figure('Name','Transmission TD');
80     subplot (2,1,1);
81     plot (t*1e12,ref_tr_21, 'r');
82     hold on;
83     plot (t*1e12,sam_tr_21, 'k');
84     title('T2R1');
85     %axis([0 80 -0.1 0.15]);
86     grid on;
87     subplot (2,1,2);
88     plot (t*1e12,ref_tr_12, 'r');
89     hold on;
90     plot (t*1e12,sam_tr_12, 'k');
91     title('T1R2');
92     %axis([0 80 -0.1 0.15]);
93     grid on;
94
95     figure('Name','Reflection TD');
96     subplot (2,1,1);
97     plot (t*1e12,ref_r_11, 'r');
98     hold on;
99     plot (t*1e12,sam_r_11, 'k');
100    title('T1R1');
101    %axis([0 80 -0.1 0.15]);
102    grid on;
103    subplot (2,1,2);
104    plot (t*1e12,ref_r_22, 'r');
105    hold on;
106    plot (t*1e12,sam_r_22, 'k');
107    title('T2R2');
108    %axis([0 80 -0.1 0.15]);
109    grid on;
110
111
112 %% Frequency Domain conversion
113
114 %transmission
115 %ref
116 [f12,Aref_tr_12] = func_2port_time2freq (t,ref_tr_12);
117 [f21,Aref_tr_21] = func_2port_time2freq (t,ref_tr_21);
118 %sample
119 [f12,Asam_tr_12] = func_2port_time2freq (t,sam_tr_12);
120 [f21,Asam_tr_21] = func_2port_time2freq (t,sam_tr_21);
121
122 %reflection
123 %ref
124 [f11,Aref_r_11] = func_2port_time2freq (t,ref_r_11);
125 [f22,Aref_r_22] = func_2port_time2freq (t,ref_r_22);
126 %sample
127 [f11,Asam_r_11] = func_2port_time2freq (t,sam_r_11);
128 [f22,Asam_r_22] = func_2port_time2freq (t,sam_r_22);
```

```

129
130 f = f12;
131
132     figure('Name','Transmission FD');
133     subplot (2,1,1);
134     plot (f/1e12,20*log10(abs(Aref_tr_21)), 'r');
135     hold on;
136     plot (f/1e12,20*log10(abs(Asam_tr_21)), 'k');
137     title('T2R1');
138     axis([0.2 3 -70 inf]);
139     grid on;
140     subplot (2,1,2);
141     plot (f/1e12,20*log10(abs(Aref_tr_12)), 'r');
142     hold on;
143     plot (f/1e12,20*log10(abs(Asam_tr_12)), 'k');
144     title('T1R2');
145     axis([0.2 3 -70 inf]);
146     grid on;
147
148     figure('Name','Reflection FD');
149     subplot (2,1,1);
150     plot (f/1e12,20*log10(abs(Aref_r_11)), 'r');
151     hold on;
152     plot (f/1e12,20*log10(abs(Asam_r_11)), 'k');
153     title('T1R1');
154     axis([0.2 3 -70 inf]);
155     grid on;
156     subplot (2,1,2);
157     plot (f/1e12,20*log10(abs(Aref_r_22)), 'r');
158     hold on;
159     plot (f/1e12,20*log10(abs(Asam_r_22)), 'k');
160     title('T2R2');
161     axis([0.2 3 -70 inf]);
162     grid on;
163
164
165 %% Experimental Transfer Function
166
167 %port 1, transmitter 1, receiver 1(refl) and 2(trans)
168
169 T_p1 = Asam_tr_12./Aref_tr_12;
170
171     mag_T_p1      = abs (T_p1);
172     phase_T_p1    = unwrap(angle(T_p1));
173
174 R_p1 = Asam_r_11./Aref_r_11;
175
176     mag_R_p1      = abs (R_p1);
177     phase_R_p1    = unwrap(angle(R_p1));
178
179 %port 2, transmitter 2, receiver 2(refl) and 1(trans)
180 T_p2 = Asam_tr_21./Aref_tr_21;

```

```
181
182         mag_T_p2      = abs (T_p2);
183         phase_T_p2    = unwrap(angle(T_p2));
184
185 R_p2 = Asam_r_22 ./ Aref_r_22;
186
187         mag_R_p2      = abs (R_p2);
188         phase_R_p2    = unwrap(angle(R_p2));
189
190
191 figure('Name','Transfer Function');
192 subplot (2,1,1);
193 plot (f, abs(T_p1), 'r');
194 hold on;
195 plot (f, abs(T_p2), 'b');
196 xlim ([0.2e12 2e12]);
197 legend ('Port 1', 'Port 2');
198 title ('Transmission Coefficient');
199 subplot (2,1,2);
200 plot (f, abs(R_p1), 'r');
201 hold on;
202 plot (f, abs(R_p2), 'b');
203 xlim ([0.2e12 2e12]);
204 legend ('Port 1', 'Port 2');
205 title ('Reflection Coefficient');
206
207 %% Selecting Data with Usable Dynamic Range
208
209 fmin = 0.2; %in THz
210 fmax = 2.5; %in THz
211
212 range = find (f > fmin*1e12 & f < fmax*1e12 );
213 fr     = f(range);
214
215 range2 = find (f < fmax*1e12);
216 fr2    = f(range2);
217
218     %% adapt phase
219
220 phase_TF_exp_tr_12_adap = func_2port_adaptphase (fr,fr2,phase_T_p1 ,
221     range);
222 phase_TF_exp_tr_21_adap = func_2port_adaptphase (fr,fr2,phase_T_p2 ,
223     range);
224
225 %% selecting data within range
226 %Port1
227 Aref_tr_12      = Aref_tr_12(range);
228 Asam_tr_12      = Asam_tr_12(range);
229 T_p1            = T_p1(range);
230
```

```

231 mag_T_p1      = mag_T_p1(range);
232 phase_T_p1    = phase_T_p1(range);
233
234 Aref_r_11     = Aref_r_11(range);
235 Asam_r_11     = Asam_r_11(range);
236 R_p1         = R_p1(range);
237
238 %Port 2
239 Aref_tr_21    = Aref_tr_21(range);
240 Asam_tr_21    = Asam_tr_21(range);
241 T_p2         = T_p2(range);
242
243 mag_T_p2      = mag_T_p2(range);
244 phase_T_p2    = phase_T_p2(range);
245
246 Aref_r_22     = Aref_r_22(range);
247 Asam_r_22     = Asam_r_22(range);
248 R_p2         = R_p2(range);
249
250 %% Calculating initial n and k and alpha
251
252     c = 3e11;
253     n0 = 1;
254     wr = 2*pi.*fr;
255
256 % FP term is neglected and imaginary part of the refractive index in
257 % the Fresnel coefficients
258 % Also polyfit is used (which will be later put in the loop)
259 % for initial n and k calculation windowed data is used, but for
260 % optimization
261 % the error is calculated by comparing with not windowed transfer
262 % function
263
264 %using adapted phase to calculate the initial estimation of n and k
265
266 phase_T_p1 = phase_TF_exp_tr_12_adap;
267 phase_T_p2 = phase_TF_exp_tr_21_adap;
268
269 [n_es_tr_12,na_tr_12,k_es_tr_12,ka_tr_12,alp_es_tr_12,alpha_tr_12] =
270 func_2port_rawpoly (mag_T_p1,phase_T_p1,wr,d_p1);
271 [n_es_tr_21,na_tr_21,k_es_tr_21,ka_tr_21,alp_es_tr_21,alpha_tr_21] =
272 func_2port_rawpoly (mag_T_p2,phase_T_p2,wr,d_p2);
273
274 %% Calculate theoretical transfer function
275
276 % Port 1
277 n_com_1 = na_tr_12 - 1i*ka_tr_12;
278
279 T_p1_t = func_2port_transferfunction_transmission (n0,n_com_1, wr,c,

```

```

278     d_p1);
279     R_p1_t = func_2port_transferfunction_reflection (n0,n_com_1, wr,c,
280     d_p1);
281     err_T_p1_t = abs(T_p1)-abs (T_p1_t);
282     err_R_p1_t = abs(R_p1)-abs (R_p1_t);
283     % Port 2
284     n_com_2 = na_tr_21 - 1i*ka_tr_21;
285
286     T_p2_t = func_2port_transferfunction_transmission (n0,n_com_2, wr,c,
287     d_p2);
288     R_p2_t = func_2port_transferfunction_reflection (n0,n_com_2, wr,c,
289     d_p2);
290     err_T_p2_t = abs(T_p2)-abs (T_p2_t);
291     err_R_p2_t = abs(R_p2)-abs (R_p2_t);
292     % changing the name for the loop
293     n_raw_p1 = n_es_tr_12;
294     n_raw_p2 = n_es_tr_21;
295
296
297     k_raw_p1 = k_es_tr_12;
298     k_raw_p2 = k_es_tr_21;
299
300     for iteration1 = 1:10
301
302     %Tx1
303         [nn12,~,mn12] = polyfit (fr,n_raw_p1,2);
304         na_tr_12 = polyval (nn12,fr, [], mn12);
305
306         [kk12,~,mk12] = polyfit (fr,k_raw_p1, 2);
307         ka_tr_12 = polyval (kk12,fr, [], mk12);
308
309     %Tx2
310         [nn21,~,mn21] = polyfit (fr,n_raw_p2, 2);
311         na_tr_21 = polyval (nn21,fr, [], mn21);
312
313         [kk21,~,mk21] = polyfit (fr,k_raw_p2, 2);
314         ka_tr_21 = polyval (kk21,fr, [], mk21);
315
316         %% 2D optimization to find thickness
317
318         % vary the thickness and for each thickness minimize the error to
319         get n
320         % and k
321     %port 1
322     dr = 0.1; % range in mm.
323     di = 0.001; % increment in mm.
324

```

```

325
326 [d2d_p1, n2d_p1, k2d_p1, alp2d_p1] = func_2port_2dopti (c, n0, d_p1, dr
    , di, na_tr_12, ka_tr_12, wr, T_p1, R_p1);
327
328     R_p1_2d = func_2port_transferfunction_reflection (n0,n2d_p1 - 1
    i*k2d_p1, wr,c,d2d_p1);
329     T_p1_2d = func_2port_transferfunction_transmission (n0,n2d_p1 -
    1i*k2d_p1, wr,c,d2d_p1);
330
331     err_p1_2d (iteration1) = mean((abs(T_p1)-abs (T_p1_2d)).^2 + (abs(
    R_p1)-abs (R_p1_2d)).^2);
332
333 %port 2
334 [d2d_p2, n2d_p2, k2d_p2, alp2d_p2] = func_2port_2dopti (c, n0, d_p2, dr
    , di, n_es_tr_21, k_es_tr_21, wr, T_p2, R_p2);
335
336     R_p2_2d = func_2port_transferfunction_reflection (n0,n2d_p2 - 1
    i*k2d_p2, wr,c,d2d_p2);
337     T_p2_2d = func_2port_transferfunction_transmission (n0,n2d_p1 -
    1i*k2d_p2, wr,c,d2d_p2);
338
339     err_p2_2d (iteration1) = mean((abs(T_p2)-abs (T_p2_2d)).^2 + (
    abs(R_p2)-abs (R_p2_2d)).^2);
340
341 %% 3D optimization
342 %port 1
343 [d3d_p1, n3d_p1, k3d_p1, alp3d_p1] = func_2port_3dopti (c, n0, d2d_p1,
    n2d_p1, k2d_p1, wr, T_p1, R_p1);
344
345     R_p1_3d = func_2port_transferfunction_reflection (n0, n3d_p1 - 1i*
    k3d_p1, wr, c, d3d_p1);
346     T_p1_3d = func_2port_transferfunction_transmission (n0, n3d_p1 - 1i*
    k3d_p1, wr, c, d3d_p1);
347     err_p1_3d (iteration1) = mean((abs(T_p1)-abs (T_p1_3d)).^2 + (abs(
    R_p1)-abs (R_p1_3d)).^2);
348     d_p1_f (iteration1)= d3d_p1;
349
350
351 %port 2
352
353 [d3d_p2, n3d_p2, k3d_p2, alp3d_p2] = func_2port_3dopti (c, n0, d2d_p2,
    n2d_p2, k2d_p2, wr, T_p2, R_p2);
354
355     R_p2_3d = func_2port_transferfunction_reflection (n0, n3d_p2 - 1i*
    k3d_p2, wr, c, d3d_p2);
356     T_p2_3d = func_2port_transferfunction_transmission (n0, n3d_p2 - 1i*
    k3d_p2, wr, c, d3d_p2);
357     err_p2_3d (iteration1) = mean((abs(T_p2)-abs (T_p2_3d)).^2 + (abs(R_p2
    )-abs (R_p2_3d)).^2);
358     d_p2_f (iteration1)= d3d_p2;
359
360 %% each frequency optimization

```



```
361
362 [nf_p1,kf_p1,alpf_p1] = func_2port_fopti (c,n0,d3d_p1,n3d_p1,k3d_p1,wr,
      T_p1, R_p1);
363
364 [nf_p2,kf_p2,alpf_p2] = func_2port_fopti (c,n0,d3d_p2,n3d_p2,k3d_p2,wr,
      T_p2, R_p2);
365
366
367 R_p1_f = func_2port_transferfunction_reflection (n0,nf_p1 - 1i*kf_p1,
      wr,c,d3d_p1);
368 T_p1_f = func_2port_transferfunction_transmission (n0,nf_p1 - 1i*kf_p1
      , wr,c,d3d_p1);
369
370 err_p1_f(iteration1) = mean((abs(T_p1)-abs (T_p1_f)).^2 + (abs(R_p1)-
      abs (R_p1_f)).^2);;
371
372 R_p2_f = func_2port_transferfunction_reflection (n0,nf_p2 - 1i*kf_p2,
      wr,c,d3d_p2);
373 T_p2_f = func_2port_transferfunction_transmission (n0,nf_p2 - 1i*kf_p2
      , wr,c,d3d_p2);
374
375 err_p2_f(iteration1) = mean((abs(T_p2)-abs (T_p2_f)).^2 + (abs(R_p2)-
      abs (R_p2_f)).^2);;
376
377 n_raw_p1 = nf_p1;
378 k_raw_p1 = kf_p1;
379
380 n_raw_p2 = nf_p2;
381 k_raw_p2 = kf_p2;
382
383 n_best_p1 (:,iteration1) = nf_p1;
384 k_best_p1 (:,iteration1) = kf_p1;
385
386
387 n_best_p2 (:,iteration1) = nf_p2;
388 k_best_p2 (:,iteration1) = kf_p2;
389
390 end
391
392 % minimum error
393
394 [err_minp1, emindexp1] = min (err_p1_f);
395 [err_minp2, emindexp2] = min (err_p2_f);
396
397 % parameters for minimum error
398
399 nf_p1 = n_best_p1(:,emindexp1);
400 nf_p2 = n_best_p2(:,emindexp2);
401
402 kf_p1 = k_best_p1(:,emindexp1);
403 kf_p2 = k_best_p2(:,emindexp2);
404
```

```
405 alp_p1 = 2 * wr .* kf_p1 ./ (c*0.1) ;
406 alp_p2 = 2 * wr .* kf_p2 ./ (c*0.1) ;
407
408 d3d_p1 = d_p1_f (emindexp1);
409 d3d_p2 = d_p2_f (emindexp2);
410
411 figure('Name', 'Final Characteristics');
412 subplot (1,2,1);
413 plot (fr, nf_p1, 'r');
414 hold on;
415 plot (fr, nf_p2, 'k');
416 title ('Refractive Index');
417 legend ('Port 1', 'Port 2');
418 subplot (1,2,2);
419 plot (fr, alp_p1, 'r');
420 hold on;
421 plot (fr, alp_p2, 'k');
422 title ('Absorption Coefficient');
423 legend ('Port 1', 'Port 2');
```

Material Characterization Software

Detailed instructions for using the program to characterize materials are provided in this appendix. The application interface is depicted in Figure C.1. This program is only applicable for transmission mode Terahertz Time-Domain Spectroscopy (THz-TDS) measurements.

The **Get Reference** and **Get Sample** buttons open a modal dialog box for selecting the corresponding reference data and test data files, respectively. After selecting the files, the data is loaded in the form of time-domain signals in the top left graph. The signals are then transformed into the frequency domain by Fourier transform and displayed in the top right figure.

Clicking the **Calculate** button will calculate the primary thickness of the Material Under Test (MUT) using the time-of-flight method. In cases where the Fabry-Pérot (FP) peaks overlap or at least two peaks in the test signal are not detectable due to absorption, the prompt will ask for mechanically measured thickness.

In the **Characterization Range** editable text box, the user can enter the frequency range in which the parameters will be extracted. It is recommended to use a frequency range with sufficient Dynamic Range (DNR) (at least 20 dB).

When **Characterize** button is clicked, the application will calculate the refractive index, absorption coefficient and thickness of the MUT and display them. The prompt below will show '**Characterizing DONE**' after the characterization process is complete. The **Save Data** button can then be used to save the determined optical parameters in a file.

The **Reset** button clears all the data and prepares the application for the next operation.

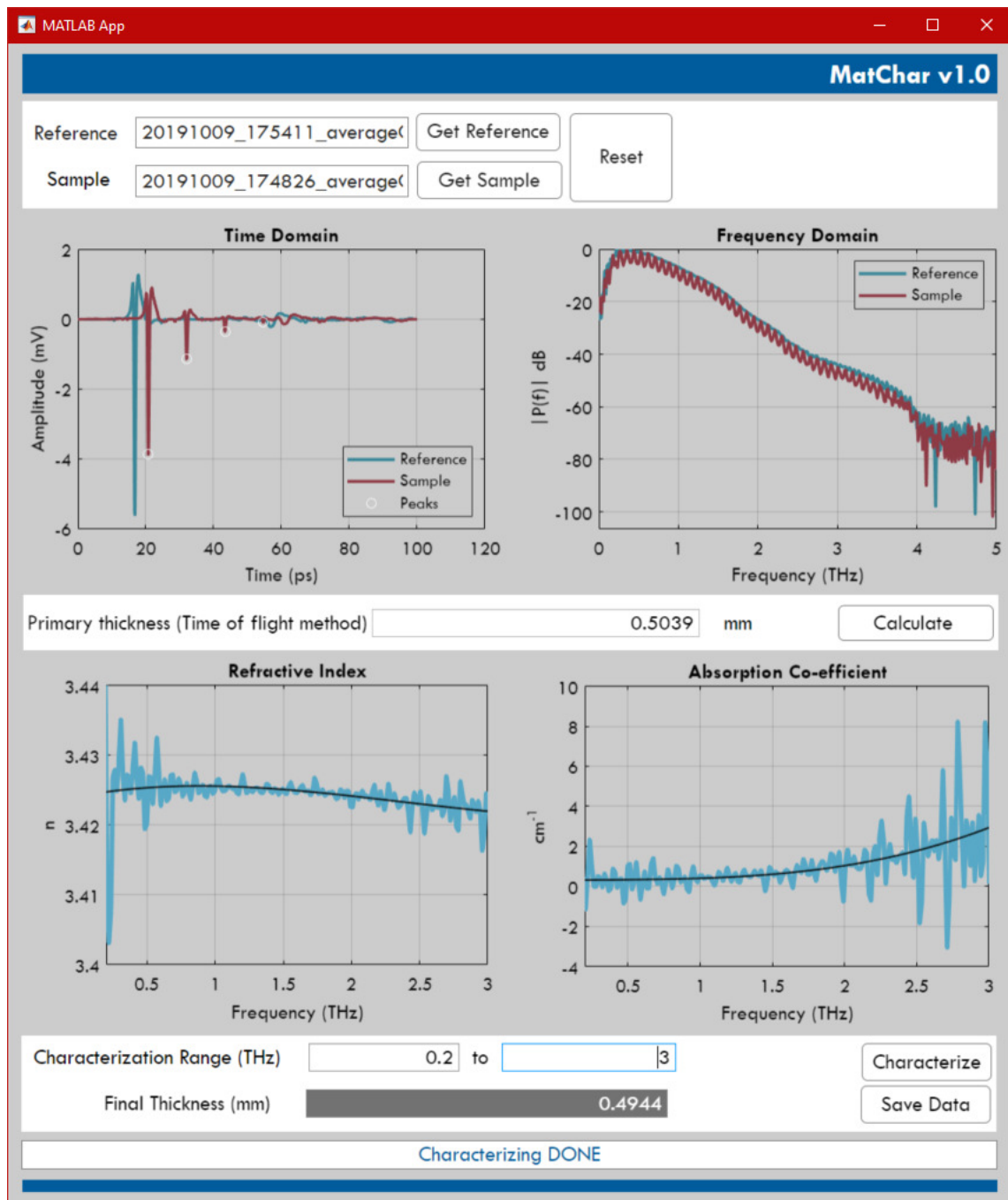


Figure C.1: MatChar (version 1.0) software interface for the determination of refractive index, absorption coefficient and thickness of a MUT. The parameters are extracted from the THz-TDS measurement in transmission mode.

REFERENCES

- [1] D. H. Auston, "Picosecond optoelectronic switching and gating in silicon," *Applied Physics Letters*, vol. 26, pp. 101–103, Sep 1975.
- [2] G. Mourou, C. V. Stancampiano, and D. Blumenthal, "Picosecond microwave pulse generation," *Applied Physics Letters*, vol. 38, pp. 470–472, Aug 1981.
- [3] R. Sprik, I. N. Duling, C. C. Chi, and D. Grischkowsky, "Far infrared spectroscopy with subpicosecond electrical pulses on transmission lines," *Applied Physics Letters*, vol. 51, pp. 548–550, Aug 1987.
- [4] C. Fattinger and D. Grischkowsky, "Point source terahertz optics," *Applied Physics Letters*, vol. 53, pp. 1480–1482, Nov 1988.
- [5] H. Elayan, O. Amin, B. Shihada, R. M. Shubair, and M.-S. Alouini, "Terahertz Band: The Last Piece of RF Spectrum Puzzle for Communication Systems," *IEEE Open Journal of the Communications Society*, vol. 1, pp. 1–32, 2020.
- [6] C. E. Shannon, "Communication in the Presence of Noise," *Proceedings of the IRE*, vol. 37, no. 1, pp. 10–21, 1949.
- [7] A. Shafie, G. N. Yang, C. Han, J. M. Jornet, M. Juntti, and T. Kurner, "Terahertz Communications for 6G and Beyond Wireless Networks: Challenges, Key Advancements, and Opportunities," *IEEE Network*, pp. 1–8, Sep 2022.
- [8] Y. Zhang, C. Wang, B. Huai, S. Wang, Y. Zhang, D. Wang, L. Rong, and Y. Zheng, "Continuous-Wave THz Imaging for Biomedical Samples," *Applied Sciences*, vol. 11, p. 71, Dec 2020.
- [9] J. A. Zeitler and Y.-C. Shen, *Industrial Applications of Terahertz Imaging*, pp. 451–489. Berlin, Heidelberg: Springer Berlin Heidelberg, 2013.
- [10] J.-H. Son, S. J. Oh, and H. Cheon, "Potential clinical applications of terahertz radiation," *Journal of Applied Physics*, vol. 125, p. 190901, May 2019.
- [11] M. Heyden, J. Sun, S. Funkner, G. Mathias, H. Forbert, M. Havenith, and D. Marx, "Dissecting the THz spectrum of liquid water from first principles via correlations in time and space," *Proceedings of the National Academy of Sciences*, vol. 107, pp. 12068–12073, Jul 2010.
- [12] J.-H. Son, *Terahertz biomedical science and technology*. CRC Press, 2014.

- [13] E. R. Brown, E. A. Mendoza, Y. Kuznetsova, A. Neumann, and S. R. J. Brueck, "THz signatures of DNA in nanochannels under electrophoretic control," in *2013 IEEE SENSORS*, pp. 1–3, IEEE, Nov 2013.
- [14] W. Zhang, E. R. Brown, M. Rahman, and M. L. Norton, "Observation of terahertz absorption signatures in microliter DNA solutions," *Applied Physics Letters*, vol. 102, p. 023701, Jan 2013.
- [15] W. Yi, J. Yu, Y. Xu, F. Wang, Q. Yu, H. Sun, L. Xu, Y. Liu, and L. Jiang, "Broadband terahertz spectroscopy of amino acids," *Instrumentation Science & Technology*, vol. 45, pp. 423–439, Jul 2017.
- [16] D.-K. Lee, J.-H. Kang, J.-S. Lee, H.-S. Kim, C. Kim, J. Hun Kim, T. Lee, J.-H. Son, Q.-H. Park, and M. Seo, "Highly sensitive and selective sugar detection by terahertz nano-antennas," *Scientific Reports*, vol. 5, p. 15459, Dec 2015.
- [17] P. Kaurav, S. K. Koul, and A. Basu, "Non-Invasive Glucose Measurement Using Sub-Terahertz Sensor, Time Domain Processing, and Neural Network," *IEEE Sensors Journal*, vol. 21, pp. 20002–20009, Sep 2021.
- [18] Y. Ogawa, S. Hayashi, M. Oikawa, C. Otani, and K. Kawase, "Interference terahertz label-free imaging for protein detection on a membrane," *Optics Express*, vol. 16, p. 22083, Dec 2008.
- [19] H. Cheon, H.-J. Yang, and J.-H. Son, "Toward Clinical Cancer Imaging Using Terahertz Spectroscopy," *IEEE Journal of Selected Topics in Quantum Electronics*, vol. 23, pp. 1–9, Jul 2017.
- [20] H. Lindley-Hatcher, R. I. Stantchev, X. Chen, A. I. Hernandez-Serrano, J. Hardwicke, and E. Pickwell-MacPherson, "Real time THz imaging—opportunities and challenges for skin cancer detection," *Applied Physics Letters*, vol. 118, p. 230501, Jun 2021.
- [21] Y. C. Sim, J. Y. Park, K.-M. Ahn, C. Park, and J.-H. Son, "Terahertz imaging of excised oral cancer at frozen temperature," *Biomedical Optics Express*, vol. 4, p. 1413, Aug 2013.
- [22] F. Wahaia, I. Kašalynas, L. Minkevičius, C. Carvalho Silva, A. Urbanowicz, and G. Valušis, "Terahertz spectroscopy and imaging for gastric cancer diagnosis," *Journal of Spectral Imaging*, vol. 9, Jan 2020.
- [23] Y. Peng, C. Shi, X. Wu, Y. Zhu, and S. Zhuang, "Terahertz Imaging and Spectroscopy in Cancer Diagnostics: A Technical Review," *BME Frontiers*, vol. 2020, pp. 1–11, Sep 2020.
- [24] H. Cheon, H.-j. Yang, S.-H. Lee, Y. A. Kim, and J.-H. Son, "Terahertz molecular resonance of cancer DNA," *Scientific Reports*, vol. 6, p. 37103, Dec 2016.
- [25] T. Nakaoka, Y. Saito, and H. Saito, "Aberrant DNA Methylation as a Biomarker and a Therapeutic Target of Cholangiocarcinoma," *International Journal of Molecular Sciences*, vol. 18, p. 1111, May 2017.
- [26] H. Cheon, J. H. Paik, M. Choi, H.-J. Yang, and J.-H. Son, "Detection and manipulation of methylation in blood cancer DNA using terahertz radiation," *Scientific Reports*, vol. 9, p. 6413, Dec 2019.

- [27] L. Ho, M. Pepper, and P. Taday, "Signatures and fingerprints," *Nature Photonics*, vol. 2, pp. 541–543, Sep 2008.
- [28] A. G. Davies, A. D. Burnett, W. Fan, E. H. Linfield, and J. E. Cunningham, "Terahertz spectroscopy of explosives and drugs," *Materials Today*, vol. 11, pp. 18–26, Mar 2008.
- [29] S. Gui, Y. Yang, J. Li, F. Zuo, and Y. Pi, "THz Radar Security Screening Method for Walking Human Torso with Multi-Angle Synthetic Aperture," *IEEE Sensors Journal*, vol. 21, pp. 17962–17972, Aug 2021.
- [30] D. Sheen, D. McMakin, and T. Hall, "Near-field three-dimensional radar imaging techniques and applications," *Applied Optics*, vol. 49, pp. E83–E93, Jul 2010.
- [31] D. M. Sheen, T. E. Hall, R. H. Severtsen, D. L. McMakin, B. K. Hatchell, and P. L. J. Valdez, "Standoff concealed weapon detection using a 350-GHz radar imaging system," in *Passive Millimeter-Wave Imaging Technology XIII*, vol. 7670, p. 767008, SPIE, Apr 2010.
- [32] K. B. Cooper, R. J. Dengler, N. Llombart, A. Talukder, A. V. Panangadan, C. S. Peay, I. Mehdi, and P. H. Siegel, "Fast high-resolution terahertz radar imaging at 25 meters," in *Terahertz Physics, Devices, and Systems IV: Advanced Applications in Industry and Defense*, vol. 7671, p. 76710Y, SPIE, Apr 2010.
- [33] Y. Jiang, B. Deng, H. Wang, Z. Zhuang, and Z. Wang, "Raw Signal Simulation for Multi-Circular Synthetic Aperture Imaging at Terahertz Frequencies," *IEEE Geoscience and Remote Sensing Letters*, vol. 17, pp. 377–380, Mar 2020.
- [34] F. Gumbmann and S. S. Ahmed, "Walk through screening with multistatic mmW technology," in *Millimetre Wave and Terahertz Sensors and Technology IX* (N. A. Salmon and S. S. Ahmed, eds.), vol. 9993, p. 999306, SPIE, Oct 2016.
- [35] Y. H. Tao, A. J. Fitzgerald, and V. P. Wallace, "Non-contact, non-destructive testing in various industrial sectors with terahertz technology," Jan 2020.
- [36] M. Naftaly, N. Vieweg, and A. Deninger, "Industrial applications of terahertz sensing: State of play," Sep 2019.
- [37] K. Ahi, S. Shahbazmohamadi, and N. Asadizanjani, "Quality control and authentication of packaged integrated circuits using enhanced-spatial-resolution terahertz time-domain spectroscopy and imaging," *Optics and Lasers in Engineering*, vol. 104, pp. 274–284, May 2018.
- [38] A. Abina, U. Puc, A. Jeglič, and A. Zidanšek, "Applications of terahertz spectroscopy in the field of construction and building materials," Apr 2015.
- [39] S. Wietzke, C. Jördens, N. Krumbholz, B. Baudrit, M. Bastian, and M. Koch, "Terahertz imaging: A new non-destructive technique for the quality control of plastic weld joints," *Journal of the European Optical Society*, vol. 2, p. 7013, Apr 2007.
- [40] T. Tanabe and Y. Oyama, "Terahertz non-destructive monitoring for infrastructure components," in *Asia-Pacific Microwave Conference Proceedings, APMC*, vol. 2018-Novem, pp. 1471–1473, Institute of Electrical and Electronics Engineers Inc., Jan 2019.

- [41] N. Hasegawa, T. Löffler, M. Thomson, and H. G. Roskos, "Remote identification of protrusions and dents on surfaces by terahertz reflectometry with spatial beam filtering and out-of-focus detection," *Applied Physics Letters*, vol. 83, pp. 3996–3998, Nov 2003.
- [42] U. Kaatzke and C. Hübner, "Electromagnetic techniques for moisture content determination of materials," *Measurement Science and Technology*, vol. 21, p. 082001, aug 2010.
- [43] S. Fan, K. Jeong, V. P. Wallace, and Z. Aman, "Use of Terahertz Waves to Monitor Moisture Content in High-Pressure Natural Gas Pipelines," *Energy and Fuels*, pp. 8026–8031, Apr 2019.
- [44] I. S. Gregory, R. K. May, P. F. Taday, and P. Mounaix, "Extending terahertz paint thickness measurements to advanced industry-standard automotive paint structures," in *International Conference on Infrared, Millimeter, and Terahertz Waves, IRMMW-THz*, vol. 2016-Novem, IEEE Computer Society, Nov 2016.
- [45] S. Krimi, J. Klier, J. Jonuscheit, G. Von Freymann, R. Urbansky, and R. Beigang, "Highly accurate thickness measurement of multi-layered automotive paints using terahertz technology," *Applied Physics Letters*, vol. 109, p. 021105, Jul 2016.
- [46] P. De Maagt, P. H. Bolivar, and C. Mann, "Terahertz Science, Engineering and Systems—from Space to Earth Applications," in *Encyclopedia of RF and Microwave Engineering*, John Wiley & Sons, Ltd, Apr 2005.
- [47] P. De Maagt, "Terahertz technology for space and EARTH applications," in *Conference Proceedings - 2007 IEEE International Workshop on Antenna Technology: Small and Smart Antennas Metamaterials and Applications, iWAT 2007*, pp. 111–115, 2007.
- [48] P. H. Siegel, "THz Instruments for Space," *IEEE Transactions on Antennas and Propagation*, vol. 55, pp. 2957–2965, Nov 2007.
- [49] K. Ikushima, Y. Yoshimura, T. Hasegawa, S. Komiyama, T. Ueda, and K. Hirakawa, "Photon-counting microscopy of terahertz radiation," *Applied Physics Letters*, vol. 88, p. 152110, Apr 2006.
- [50] W. J. Padilla, A. J. Taylor, C. Highstrete, M. Lee, and R. D. Averitt, "Dynamical electric and magnetic metamaterial response at terahertz frequencies," *Physical Review Letters*, vol. 96, p. 107401, Mar 2006.
- [51] R. Huber, C. Kübler, S. Tübel, A. Leitenstorfer, Q. T. Vu, H. Haug, F. Köhler, and M. C. Amann, "Femtosecond formation of coupled phonon-plasmon modes in InP: Ultrabroadband THz experiment and quantum kinetic theory," *Physical Review Letters*, vol. 94, p. 027401, Jan 2005.
- [52] E. Beaurepaire, G. M. Turner, S. M. Harrel, M. C. Beard, J. Y. Bigot, and C. A. Schmuttenmaer, "Coherent terahertz emission from ferromagnetic films excited by femtosecond laser pulses," *Applied Physics Letters*, vol. 84, pp. 3465–3467, Apr 2004.
- [53] S. K. Mathanker, P. R. Weckler, and N. Wang, "Terahertz (THZ) applications in food and agriculture: A review," *Transactions of the ASABE*, vol. 56, no. 3, pp. 1213–1226, 2013.

- [54] A. Samad, W. D. Hu, W. Shahzad, H. Raza, and L. P. Ligthart, "Design of highly sensitive complementary metamaterial-based microwave sensor for characterisation of dielectric materials," *IET Microwaves, Antennas & Propagation*, vol. 14, no. 15, pp. 2064–2073, 2020.
- [55] A. Mason, O. Korostynska, M. Ortoneda-Pedrola, A. Shaw, and A. Al-Shamma'a, "A resonant co-planar sensor at microwave frequencies for biomedical applications," *Sensors and Actuators A: Physical*, vol. 202, pp. 170–175, Nov 2013.
- [56] A. Basir, M. Zada, Y. Cho, and H. Yoo, "A Dual-Circular-Polarized Endoscopic Antenna With Wideband Characteristics and Wireless Biotelemetric Link Characterization," *IEEE Transactions on Antennas and Propagation*, vol. 68, pp. 6953–6963, Oct 2020.
- [57] L. Zheng Tung, G. Amouzed Mahdiraji, and L. Chia Ping, "Comparative Study between Planar and Bent Antenna Characterization," *MATEC Web of Conferences*, vol. 152, p. 03002, Feb 2018.
- [58] J. Akkermans, R. van Dijk, and M. Herben, "Millimeter-wave antenna measurement," in *2007 European Microwave Conference*, pp. 83–86, IEEE, 2007.
- [59] T. Tosaka, K. Fujii, K. Fukunaga, and A. Kasamatsu, "Development of complex relative permittivity measurement system based on free-space in 220-330-GHz range," *IEEE Transactions on Terahertz Science and Technology*, vol. 5, pp. 102–109, Jan 2015.
- [60] A. Kazemipour, M. Hudlička, M. Salhi, T. Kleine-Ostmann, and T. Schrader, "Free-space quasi-optical spectrometer for material characterization in the 50-500 GHz frequency range," *European Microwave Week 2014: Connecting the Future, EuMW 2014 - Conference Proceedings; EuMC 2014: 44th European Microwave Conference*, pp. 636–639, Dec 2014.
- [61] J. Hammler, A. J. Gallant, and C. Balocco, "Free-Space Permittivity Measurement at Terahertz Frequencies with a Vector Network Analyzer," *IEEE Transactions on Terahertz Science and Technology*, vol. 6, pp. 817–823, Nov 2016.
- [62] Rohde & Schwarz GmbH & Co KG, "R&S[®]ZVA vector network analyzer — rohde-schwarz.com." https://www.rohde-schwarz.com/us/products/test-and-measurement/network-analyzers/rs-zva-vector-network-analyzer_63493-9660.html. [Accessed 02-Nov-2022].
- [63] Keysight Technologies, "Netzwerkanalysatoren — keysight.com." <https://www.keysight.com/de/de/products/network-analyzers.html>. [Accessed 01-Oct-2022].
- [64] Rohde & Schwarz GmbH & Co KG, "Netzwerkanalysatoren — rohde-schwarz.com." https://www.rohde-schwarz.com/de/produkte/messtechnik/netzwerkanalysatoren_64043.html. [Accessed 01-Oct-2022].
- [65] Virginia Diodes Inc., "Vector Network Analyzer Extension Modules (VNAX) — vadiodes.com." <https://www.vadiodes.com/en/products/vector-network-analyzer-extension-modules>. [Accessed 01-Oct-2022].

- [66] J. Digby, C. McIntosh, G. Parkhurst, B. Towlson, S. Hadjiloucas, J. Bowen, J. Chamberlain, R. Pollard, R. Miles, D. Steenson, L. Karatzas, N. Cronin, and S. Davies, "Fabrication and characterization of micromachined rectangular waveguide components for use at millimeter-wave and terahertz frequencies," *IEEE Transactions on Microwave Theory and Techniques*, vol. 48, pp. 1293–1302, Aug 2000.
- [67] M. Horibe and R. Kishikawa, "Performance of new design of waveguide flange for measurements at frequencies from 800 GHz to 1.05 THz," in *79th ARFTG Microwave Measurement Conference*, pp. 1–6, IEEE, Jun 2012.
- [68] M. Horibe, "Measurement Uncertainty in Terahertz VNAs: Using Terahertz Vector Network Analyzers for Stable, Accurate Measurement and to Evaluate Uncertainty," *IEEE Microwave Magazine*, vol. 19, pp. 24–34, Mar 2018.
- [69] M. Horibe, "Measurement Uncertainty Model for Vector Network Analyzers With Frequency Extension Modules at Terahertz Frequencies," *IEEE Transactions on Instrumentation and Measurement*, vol. 66, pp. 1605–1612, Jun 2017.
- [70] C. Oleson and A. Denning, "Millimeter Wave Vector Analysis Calibration and Measurement Problems Caused by Common Waveguide Irregularities," in *56th ARFTG Conference Digest*, pp. 1–9, IEEE, Nov 2000.
- [71] N. M. Ridler and R. G. Clarke, "Establishing Traceability to the International System of Units for Scattering Parameter Measurements From 750 GHz to 1.1 THz," *IEEE Transactions on Terahertz Science and Technology*, vol. 6, pp. 2–11, Jan 2016.
- [72] J. Champion and J. Oberhammer, "Silicon Micromachined Waveguide Calibration Standards for Terahertz Metrology," *IEEE Transactions on Microwave Theory and Techniques*, vol. 69, pp. 3927–3942, Aug 2021.
- [73] H. Lu, D. G. Ouellette, S. Preu, J. D. Watts, B. Zaks, P. G. Burke, M. S. Sherwin, and A. C. Gossard, "Self-Assembled ErSb Nanostructures with Optical Applications in Infrared and Terahertz," *Nano Letters*, vol. 14, pp. 1107–1112, Mar 2014.
- [74] A. J. Alazemi and G. M. Rebeiz, "A 100–300-GHz Free-Space Scalar Network Analyzer Using Compact Tx and Rx Modules," *IEEE Transactions on Microwave Theory and Techniques*, vol. 64, pp. 4021–4029, Nov 2016.
- [75] D. Bourreau, A. Peden, and S. Le Maguer, "A Quasi-Optical Free-Space Measurement Setup Without Time-Domain Gating for Material Characterization in the W-Band," *IEEE Transactions on Instrumentation and Measurement*, vol. 55, pp. 2022–2028, Dec 2006.
- [76] U. Nandi, M. Scheer, H. Lu, J. C. Norman, A. C. Gossard, and S. Preu, "Bias-Dependent Carrier Dynamics and Terahertz Performance of ErAs:In(Al)GaAs Photoconductors," *IEEE Transactions on Terahertz Science and Technology*, vol. 12, pp. 353–362, Jul 2022.
- [77] R. B. Kohlhaas, S. Breuer, L. Liebermeister, S. Nellen, M. Deumer, M. Schell, M. P. Semtsiv, W. T. Masselink, and B. Globisch, "637 μ W emitted terahertz power from photoconductive antennas based on rhodium doped InGaAs," *Applied Physics Letters*, vol. 117, p. 131105, Sep 2020.

-
- [78] R. B. Kohlhaas, S. Breuer, S. Mutschall, M. Kehrt, S. Nellen, L. Liebermeister, M. Schell, and B. Globisch, "Ultrabroadband terahertz time-domain spectroscopy using III-V photoconductive membranes on silicon," *Optics Express*, vol. 30, p. 23896, Jun 2022.
- [79] S. Preu, "A Unified Derivation of the Terahertz Spectra Generated by Photoconductors and Diodes," *Journal of Infrared, Millimeter, and Terahertz Waves*, vol. 35, pp. 998–1010, Dec 2014.
- [80] D. R. Bacon, J. Madéo, and K. M. Dani, "Photoconductive emitters for pulsed terahertz generation," *Journal of Optics*, vol. 23, p. 064001, Jun 2021.
- [81] M. Tani, M. Watanabe, and K. Sakai, "Photoconductive twin dipole antennas for THz transceiver," *Electronics Letters*, vol. 38, no. 1, p. 5, 2002.
- [82] D. Mittleman, M. Gupta, R. Neelamani, R. Baraniuk, J. Rudd, and M. Koch, "Recent advances in terahertz imaging," *Applied Physics B: Lasers and Optics*, vol. 68, pp. 1085–1094, Jun 1999.
- [83] M. Naftaly and R. E. Miles, "Terahertz time-domain spectroscopy for material characterization," *Proceedings of the IEEE*, vol. 95, no. 8, pp. 1658–1665, 2007.
- [84] C.-Y. Jen and C. Richter, "Sample Thickness Measurement with THz-TDS: Resolution and Implications," *Journal of Infrared, Millimeter, and Terahertz Waves*, vol. 35, pp. 840–859, Oct 2014.
- [85] Y. Yang, M. Mandehgar, and D. Grischkowsky, "THz-TDS Characterization of the Digital Communication Channels of the Atmosphere and the Enabled Applications," *Journal of Infrared, Millimeter, and Terahertz Waves*, vol. 36, pp. 97–129, Feb 2015.
- [86] J. Neu and C. A. Schmuttenmaer, "Tutorial: An introduction to terahertz time domain spectroscopy (THz-TDS)," *Journal of Applied Physics*, vol. 124, p. 231101, Dec 2018.
- [87] Q. Wang, L. Xie, and Y. Ying, "Overview of imaging methods based on terahertz time-domain spectroscopy," *Applied Spectroscopy Reviews*, vol. 57, pp. 249–264, Mar 2022.
- [88] J.-M. Rämmer and G. von Freymann, "Terahertz waveform generation for S_{21} -parameter measurements using a fiber-coupled optical pulse shaper," *Optics Express*, vol. 23, p. 30872, Nov 2015.
- [89] J.-M. Ramer and G. von Freymann, "A Terahertz Time-Domain Spectroscopy-Based Network Analyzer," *Journal of Lightwave Technology*, vol. 33, pp. 403–407, Jan 2015.
- [90] M. Bieler, H. Fuser, and K. Pierz, "Time-Domain Optoelectronic Vector Network Analysis on Coplanar Waveguides," *IEEE Transactions on Microwave Theory and Techniques*, vol. 63, pp. 3775–3784, Nov 2015.
- [91] M. Y. Frankel, "Optoelectronic techniques for ultrafast device network analysis to 700 GHz," *Optical and Quantum Electronics*, vol. 28, pp. 783–800, Jul 1996.

- [92] Y. Cui and G. C. Trichopoulos, "Toward a terahertz quasi-optical vector network analyzer," in *2017 IEEE International Symposium on Antennas and Propagation & US-NC/URSI National Radio Science Meeting*, vol. 2017-Janua, pp. 1511–1512, IEEE, Jul 2017.
- [93] M. Mueh, S. Brandl, P. Hinz, C. Waldschmidt, and C. Damm, "Calibration Technique for THz Time-Domain Spectrometers Enabling Vectorial Scattering Parameter Measurements," *IEEE Microwave and Wireless Components Letters*, vol. 31, pp. 805–807, Jun 2021.
- [94] D. Etayo, J. C. Iriarte, I. Palacios, I. Maestrojuan, J. Teniente, I. Ederra, and R. Gonzalo, "THz imaging system for industrial quality control," in *2011 IEEE MTT-S International Microwave Workshop Series on Millimeter Wave Integration Technologies*, pp. 172–175, IEEE, Sep 2011.
- [95] A. Keil, J. Peuser, T. Loeffler, V. Krozer, J. Dall, A. Kusk, V. Zhurbenko, T. Jensen, and P. de Maagt, "300 GHz imaging system with 8 meter stand-off distance and one-dimensional synthetic image reconstruction for remote detection of material defects," in *33rd ESA Antenna Workshop on Challenges for Space Antenna Systems*, pp. 1–5, 2011.
- [96] J. Burki, T. Ali, and S. Arshad, "Vector network analyzer (VNA) based synthetic aperture radar (SAR) imaging," in *INMIC*, pp. 207–212, IEEE, Dec 2013.
- [97] K.-S. Lim and V. C. Koo, "Design and Construction of Wideband VNA Ground-Based Radar System with Real and Synthetic Aperture Measurement Capabilities," *Progress In Electromagnetics Research*, vol. 86, pp. 259–275, 2008.
- [98] Y. Wang, X. Shang, N. M. Ridler, M. Naftaly, A. I. Dimitriadis, T. Huang, and W. Wu, "Material Measurements Using VNA-Based Material Characterization Kits Subject to Thru-Reflect-Line Calibration," *IEEE Transactions on Terahertz Science and Technology*, vol. 10, pp. 466–473, Sep 2020.
- [99] Hewlett-Packard Company, "Applying Error Correction to Network Analyzer Measurements (Application Note 1287-3)," tech. rep., 1997.
- [100] M. Hiebel, *Fundamentals of vector network analysis*. Rohde & Schwarz, 2007.
- [101] Hewlett-Packard Company, "Understanding the Fundamental Principles of Vector Network Analysis (Application Note 1287-1)," tech. rep., 1997.
- [102] N. Hiromoto, S. R. Tripathi, M. Takeda, and M. Aoki, "Study on random errors in THz signal and optical constants observed with THz time-domain spectroscopy," in *35th International Conference on Infrared, Millimeter, and Terahertz Waves*, pp. 1–2, IEEE, Sep 2010.
- [103] F. Caspers, "RF engineering basic concepts: S-parameters," *CAS 2010 - CERN Accelerator School: RF for Accelerators, Proceedings*, pp. 67–93, Jan 2012.
- [104] S. R. Pennock and O. Abdul-Latif, "Enhanced vector network analyzer time domain measurement using normalized superimposition," in *2017 IEEE MTT-S International Microwave Symposium (IMS)*, pp. 1255–1258, IEEE, Jun 2017.

- [105] R. Hui and M. O'Sullivan, "Basic Instrumentation for Optical Measurement," in *Fiber Optic Measurement Techniques*, pp. 129–258, Elsevier, Jan 2009.
- [106] S. K. Koul and P. Kaurav, "Electronic Sub-Terahertz VNA Measurement Techniques," pp. 31–56, Springer, Singapore, 2022.
- [107] J. Dunsmore, "Novel method for vector mixer characterization and mixer test system vector error correction," in *2002 IEEE MTT-S International Microwave Symposium Digest (Cat. No.02CH37278)*, vol. 3, pp. 1833–1836, IEEE, 2002.
- [108] J. Zhang, W. Li, H.-L. Cui, C. Shi, X. Han, Y. Ma, J. Chen, T. Chang, D. Wei, Y. Zhang, and Y. Zhou, "Nondestructive Evaluation of Carbon Fiber Reinforced Polymer Composites Using Reflective Terahertz Imaging," *Sensors*, vol. 16, p. 875, Jun 2016.
- [109] A. Maestrini, B. Thomas, H. Wang, C. Jung, J. Treuttel, Y. Jin, G. Chattopadhyay, I. Mehdi, and G. Beaudin, "Schottky diode-based terahertz frequency multipliers and mixers," *Comptes Rendus Physique*, vol. 11, pp. 480–495, Aug 2010.
- [110] "IEEE Standard for Rectangular Metallic Waveguides and Their Interfaces for Frequencies of 110 GHz and Above—Part 1: Frequency Bands and Waveguide Dimensions," *IEEE Std 1785.1-2012*, pp. 1–22, 2013.
- [111] R. M. Weikle, H. Li, A. Arsenovic, S. Nadri, L. Xie, M. Bauwens, N. Alijabbari, N. S. Barker, and A. Lichtenberger, "Micromachined Interfaces for Metrology and Packaging Applications in the Submillimeter-Wave Band," *Additional Conferences (Device Packaging, HiTEC, HiTEN, and CICMT)*, vol. 2017, pp. 1–36, Jan 2017.
- [112] J. Champion, U. Shah, and J. Oberhammer, "Silicon-Micromachined Waveguide Calibration Shims for Terahertz Frequencies," in *2019 IEEE MTT-S International Microwave Symposium (IMS)*, vol. 2019-June, pp. 1265–1268, IEEE, Jun 2019.
- [113] S. Kim, D. Novotny, J. A. Gordon, and J. R. Guerrieri, "A Free-Space Measurement Method for the Low-Loss Dielectric Characterization Without Prior Need for Sample Thickness Data," *IEEE Transactions on Antennas and Propagation*, vol. 64, pp. 3869–3879, Sep 2016.
- [114] A. Kazemipour, M. Hudlicka, See-Khee Yee, M. A. Salhi, D. Allal, T. Kleine-Ostmann, and T. Schrader, "Design and Calibration of a Compact Quasi-Optical System for Material Characterization in Millimeter/Submillimeter Wave Domain," *IEEE Transactions on Instrumentation and Measurement*, vol. 64, pp. 1438–1445, Jun 2015.
- [115] E. Hajisaeid, A. F. Dericoglu, and A. Akyurtlu, "All 3-D Printed Free-Space Setup for Microwave Dielectric Characterization of Materials," *IEEE Transactions on Instrumentation and Measurement*, vol. 67, pp. 1877–1886, Aug 2018.
- [116] J. L. Hesler, Y. Duan, B. Foley, T. W. Crowe, J. L. Hesler, Y. Duan, B. Foley, and T. W. Crowe, "THz vector network analyzer measurements and calibration," in *21st International Symposium on Space Terahertz Technology 2010, ISSTT 2010*, pp. 273–275, 2010.

- [117] M. Naftaly, R. G. Clarke, D. A. Humphreys, and N. M. Ridler, “Metrology State-of-the-Art and Challenges in Broadband Phase-Sensitive Terahertz Measurements,” *Proceedings of the IEEE*, vol. 105, pp. 1151–1165, Jun 2017.
- [118] H.-W. Hubers, M. F. Kimmitt, N. Hiromoto, and E. Brundermann, “Terahertz Spectroscopy: System and Sensitivity Considerations,” *IEEE Transactions on Terahertz Science and Technology*, vol. 1, pp. 321–331, Sep 2011.
- [119] Y.-J. Lin and M. Jarrahi, “Heterodyne terahertz detection through electronic and optoelectronic mixers,” *Reports on Progress in Physics*, vol. 83, p. 066101, Jun 2020.
- [120] F. C. De Lucia, “Noise, detectors, and submillimeter–terahertz system performance in nonambient environments,” *Journal of the Optical Society of America B*, vol. 21, p. 1273, Jul 2004.
- [121] N. Ridler, R. Clarke, M. Salter, and A. Wilson, “The Trace Is on Measurements: Developing Traceability for S-Parameter Measurements at Millimeter and Submillimeter Wavelengths,” *IEEE Microwave Magazine*, vol. 14, pp. 67–74, Nov 2013.
- [122] R. G. Clarke and N. M. Ridler, “Metrology for Vector Network Analyzers,” in *Terahertz Metrology* (M. Naftaly, ed.), ch. 9, pp. 185–249, Artech House, 2015.
- [123] R. J. Collier and A. D. Skinner, *Microwave measurements*, vol. 12. IET, 2007.
- [124] Agilent Technologies, “Advanced calibration techniques for vector network analyzers — agilent.com.” http://anlage.umd.edu/Agilent_Advanced_VNA_calibration.pdf, 2006. [Accessed 01-Oct-2022].
- [125] Anritsu, “Understanding VNA Calibration — anritsu.com.” http://anlage.umd.edu/Anritsu_understanding-vna-calibration.pdf, 2012. [Accessed 01-Oct-2022].
- [126] S. Rehnmark, “On the Calibration Process of Automatic Network Analyzer Systems (Short Papers),” *IEEE Transactions on Microwave Theory and Techniques*, vol. 22, pp. 457–458, Apr 1974.
- [127] A. Rumiantsev and N. Ridler, “VNA calibration,” *IEEE Microwave magazine*, vol. 9, no. 3, pp. 86–99, 2008.
- [128] N. Shoaib, “General Introduction,” in *PoliTO Springer Series*, pp. 1–21, Springer, 2017.
- [129] W. Kruppa and K. Sodomsy, “An Explicit Solution for the Scattering Parameters of a Linear Two-Port Measured with an Imperfect Test Set (Correspondence),” *IEEE Transactions on Microwave Theory and Techniques*, vol. 19, pp. 122–123, Jan 1971.
- [130] S. Padmanabhan, P. Kirby, J. Daniel, and L. Dunleavy, “Accurate broadband on-wafer SOLT calibrations with complex load and thru models,” in *61st ARFTG Conference Digest, Spring 2003.*, pp. 5–10, IEEE, 2003.
- [131] D. Blackham and K. Wong, “Latest advances in VNA accuracy enhancements,” *Microwave Journal*, vol. 48, no. 7, pp. 78–87, 2005.

- [132] N. M. Ridler and N. Nazoa, "Using simple calibration load models to improve accuracy of Vector Network Analyzer measurements," in *2006 67th ARFTG Conference*, pp. 104–110, IEEE, Jun 2006.
- [133] G. Engen and C. Hoer, "Thru-Reflect-Line: An Improved Technique for Calibrating the Dual Six-Port Automatic Network Analyzer," *IEEE Transactions on Microwave Theory and Techniques*, vol. 27, pp. 987–993, Dec 1979.
- [134] N. M. Ridler, "Choosing line lengths for calibrating waveguide vector network analysers at millimetre and sub-millimetre wavelengths.," NPL Report TQE 5, National Physical Laboratory, Teddington, UK, March 2009.
- [135] C. A. Hoer and G. F. Engen, "On-line accuracy assessment for the dual six-port ANA: Extension to nonmating connectors," *IEEE Transactions on Instrumentation and Measurement*, vol. IM-36, pp. 524–529, Jun 1987.
- [136] K.-F. Fuh, "Formulation for Propagation Factor Extractions in Thru-Reflect-Line/Line-Reflect-Line Calibrations and Related Applications," *IEEE Transactions on Microwave Theory and Techniques*, vol. 64, pp. 1594–1606, May 2016.
- [137] R. Marks, "A multiline method of network analyzer calibration," *IEEE Transactions on Microwave Theory and Techniques*, vol. 39, pp. 1205–1215, Jul 1991.
- [138] D. Williams, J. Wang, and U. Arz, "An optimal vector-network-analyzer calibration algorithm," *IEEE Transactions on Microwave Theory and Techniques*, vol. 51, pp. 2391–2401, Dec 2003.
- [139] D. F. Williams, "500 GHz–750 GHz Rectangular-Waveguide Vector-Network-Analyzer Calibrations," *IEEE Transactions on Terahertz Science and Technology*, vol. 1, pp. 364–377, Nov 2011.
- [140] D. F. Williams, "Comparison of Sub-Millimeter-Wave Scattering-Parameter Calibrations With Imperfect Electrical Ports," *IEEE Transactions on Terahertz Science and Technology*, vol. 2, pp. 144–152, Jan 2012.
- [141] N. M. Ridler and R. G. Clarke, "Evaluating the effect of using precision alignment dowels on connection repeatability of waveguide devices at frequencies from 750 GHz to 1.1 THz," in *84th ARFTG Microwave Measurement Conference*, pp. 1–10, IEEE, Dec 2014.
- [142] N. M. Ridler and R. G. Clarke, "Further investigations into connection repeatability of waveguide devices at frequencies from 750 GHz to 1.1 THz," in *83rd ARFTG Microwave Measurement Conference*, pp. 1–7, IEEE, Jun 2014.
- [143] N. M. Ridler and R. G. Clarke, "Investigating connection repeatability of waveguide devices at frequencies from 750 GHz to 1.1 THz," in *82nd ARFTG Microwave Measurement Conference*, pp. 1–13, IEEE, Nov 2013.
- [144] I. Rolfes and B. Schiek, "Calibration methods for microwave free space measurements," *Advances in Radio Science*, vol. 2, pp. 19–25, May 2005.

- [145] D. Ghodgaonkar, V. Varadan, and V. Varadan, "Free-space measurement of complex permittivity and complex permeability of magnetic materials at microwave frequencies," *IEEE Transactions on Instrumentation and Measurement*, vol. 39, pp. 387–394, Apr 1990.
- [146] D. Blackham, "Free space characterization of materials," in *Antenna Measurement Techniques Association Symposium*, vol. 15, pp. 58–60, 1993.
- [147] H. Henermann and B. Schiek, "Line network network (LNN): an alternative in-fixture calibration procedure," *IEEE Transactions on Microwave Theory and Techniques*, vol. 45, pp. 408–413, Mar 1997.
- [148] I. Rolfes and B. Schiek, "Calibration Methods for Free Space Dielectric Microwave Measurements with a 4-Channel-Network-Analyzer," in *32nd European Microwave Conference, 2002*, pp. 1–4, IEEE, Oct 2002.
- [149] P. Bartley and S. Begley, "Improved Free-Space S-Parameter Calibration," in *2005 IEEE Instrumentation and Measurement Technology Conference Proceedings*, vol. 1, pp. 372–375, IEEE, 2005.
- [150] H.-J. Eul and B. Schiek, "A generalized theory and new calibration procedures for network analyzer self-calibration," *IEEE Transactions on Microwave Theory and Techniques*, vol. 39, pp. 724–731, Apr 1991.
- [151] B. Will and I. Rolfes, "The TTN-method - a phase shift calibration technique for vector network analyzers," in *Asia-Pacific Microwave Conference 2011*, pp. 697–700, 2011.
- [152] B. Will and I. Rolfes, "A new approach on broadband calibration methods for free space applications," in *2012 IEEE/MTT-S International Microwave Symposium Digest*, pp. 1–3, IEEE, Jun 2012.
- [153] J.-S. Kang, "SOLR calibration using planar offset short in free-space material measurement," in *2020 Antenna Measurement Techniques Association Symposium (AMTA)*, pp. 1–4, 2020.
- [154] A. Kazemipour, J. Hoffmann, M. Wollensack, M. Hudlicka, J. Rufenacht, D. Stalder, D. Allal, G. Gaumann, and M. Zeier, "Standard Load Method: A New Calibration Technique for Material Characterization at Terahertz Frequencies," *IEEE Transactions on Instrumentation and Measurement*, vol. 70, pp. 1–10, 2021.
- [155] P. Goy, "8-1000 GHz vector network analyzer," in *15th International Conference on Infrared and Millimeter Waves*, vol. 1514, p. 32, SPIE, Dec 1990.
- [156] P. Goy and M. Gross, "Vector Measurements from 8 Ghz to the THz Range, Obtained in a Real Life Experiment," in *New Directions in Terahertz Technology*, pp. 323–340, Dordrecht: Springer Netherlands, 1997.
- [157] OML (Oleson Microwave Labs), "Frequency extension source modules to extend signal capability from 50 to 325 GHz," *Microw. J.*, vol. 47, no. 3, pp. 124–134, 2004.

- [158] D. Koller, S. Durant, C. Rowland, E. Bryerton, and J. Hesler, "Initial measurements with WM164 (1.1–1.5THz) VNA extenders," in *2016 41st International Conference on Infrared, Millimeter, and Terahertz waves (IRMMW-THz)*, vol. 2016-Novem, pp. 1–2, IEEE, Sep 2016.
- [159] A. Maestrini, J. Ward, J. Gill, H. Javadi, E. Schlecht, G. Chattopadhyay, F. Maiwald, N. Erickson, and I. Mehdi, "A 1.7-1.9 THz local oscillator source," *IEEE Microwave and Wireless Components Letters*, vol. 14, pp. 253–255, Jun 2004.
- [160] M. Deumer, S. Breuer, R. Kohlhaas, S. Nellen, L. Liebermeister, S. Lauck, M. Schell, and B. Globisch, "Continuous wave terahertz receivers with 4.5 THz bandwidth and 112 dB dynamic range," *Optics Express*, vol. 29, p. 41819, Dec 2021.
- [161] U. Nandi, K. Dutzi, A. Deninger, H. Lu, J. Norman, A. C. Gossard, N. Vieweg, and S. Preu, "ErAs:In(Al)GaAs photoconductor-based time domain system with 45 THz single shot bandwidth and emitted terahertz power of 164 μ W," *Optics Letters*, vol. 45, p. 2812, May 2020.
- [162] K. L. Vodopyanov, "Optical generation of narrow-band terahertz packets in periodically-inverted electro-optic crystals: conversion efficiency and optimal laser pulse format," *Optics Express*, vol. 14, p. 2263, Mar 2006.
- [163] F. Meyer, N. Hekmat, T. Vogel, A. Omar, S. Mansourzadeh, F. Fobbe, M. Hoffmann, Y. Wang, and C. J. Saraceno, "Milliwatt-class broadband THz source driven by a 112 W, sub-100 fs thin-disk laser," *Optics Express*, vol. 27, p. 30340, Oct 2019.
- [164] Y. Liu, K. Zhong, A. Wang, M. Zhou, S. Li, L. Gao, and Z. Zhang, "Optical Terahertz Sources Based on Difference Frequency Generation in Nonlinear Crystals," *Crystals*, vol. 12, p. 936, Jul 2022.
- [165] S. Preu, G. H. Döhler, S. Malzer, L. J. Wang, and A. C. Gossard, "Tunable, continuous-wave Terahertz photomixer sources and applications," *Journal of Applied Physics*, vol. 109, p. 061301, Mar 2011.
- [166] R. Safian, G. Ghazi, and N. Mohammadian, "Review of photomixing continuous-wave terahertz systems and current application trends in terahertz domain," *Optical Engineering*, vol. 58, p. 1, Nov 2019.
- [167] T. Seifert, S. Jaiswal, U. Martens, J. Hannegan, L. Braun, P. Maldonado, F. Freimuth, A. Kronenberg, J. Henrizi, I. Radu, E. Beaurepaire, Y. Mokrousov, P. M. Oppeneer, M. Jourdan, G. Jakob, D. Turchinovich, L. M. Hayden, M. Wolf, M. Münzenberg, M. Kläui, and T. Kampfrath, "Efficient metallic spintronic emitters of ultrabroadband terahertz radiation," *Nature Photonics*, vol. 10, pp. 483–488, Jul 2016.
- [168] U. Nandi, M. S. Abdelaziz, S. Jaiswal, G. Jakob, O. Gueckstock, S. M. Rouzegar, T. S. Seifert, M. Kläui, T. Kampfrath, and S. Preu, "Antenna-coupled spintronic terahertz emitters driven by a 1550 nm femtosecond laser oscillator," *Applied Physics Letters*, vol. 115, p. 022405, Jul 2019.
- [169] E. T. Papaioannou and R. Beigang, "THz spintronic emitters: a review on achievements and future challenges," *Nanophotonics*, vol. 10, pp. 1243–1257, Feb 2021.

- [170] Z. Feng, H. Qiu, D. Wang, C. Zhang, S. Sun, B. Jin, and W. Tan, “Spintronic terahertz emitter,” *Journal of Applied Physics*, vol. 129, p. 010901, Jan 2021.
- [171] Y. C. Shen, P. C. Upadhyaya, H. E. Beere, E. H. Linfield, A. G. Davies, I. S. Gregory, C. Baker, W. R. Tribe, and M. J. Evans, “Generation and detection of ultrabroadband terahertz radiation using photoconductive emitters and receivers,” *Applied Physics Letters*, vol. 85, pp. 164–166, Jul 2004.
- [172] F. Peter, S. Winnerl, S. Nitsche, A. Dreyhaupt, H. Schneider, and M. Helm, “Coherent terahertz detection with a large-area photoconductive antenna,” *Applied Physics Letters*, vol. 91, p. 081109, Aug 2007.
- [173] N. M. Burford and M. O. El-Shenawee, “Review of terahertz photoconductive antenna technology,” *Optical Engineering*, vol. 56, p. 010901, Jan 2017.
- [174] Q. Wu and X. Zhang, “Free-space electro-optic sampling of terahertz beams,” *Applied Physics Letters*, vol. 67, pp. 3523–3525, Dec 1995.
- [175] A. Nahata, A. S. Weling, and T. F. Heinz, “A wideband coherent terahertz spectroscopy system using optical rectification and electro-optic sampling,” *Applied Physics Letters*, vol. 69, pp. 2321–2323, Oct 1996.
- [176] A. I. Shugurov, S. B. Bodrov, E. A. Mashkovich, H. Kitahara, N. A. Abramovsky, M. Tani, and M. I. Bakunov, “Noncollinear electro-optic sampling detection of terahertz pulses in a LiNbO₃ crystal while avoiding the effect of intrinsic birefringence,” *Optics Express*, vol. 30, p. 3741, Jan 2022.
- [177] S. Preu, G. H. Döhler, S. Malzer, A. Stöhr, V. Rymanov, T. Göbel, E. R. Brown, M. Feiginov, R. Gonzalo, M. Beruete, and M. Navarro-Cía, *Principles of THz Generation*, ch. 2, pp. 3–68. Wiley, Aug 2015.
- [178] U. Nandi, *ErAs:In(Al)GaAs photoconductors for 1550 nm-based Terahertz time domain spectroscopy systems*. PhD thesis, Technische Universität Darmstadt, 2021.
- [179] E. Castro-Camus, L. Fu, J. Lloyd-Hughes, H. H. Tan, C. Jagadish, and M. B. Johnston, “Photoconductive response correction for detectors of terahertz radiation,” *Journal of Applied Physics*, vol. 104, p. 053113, Sep 2008.
- [180] E. Castro-Camus and M. Alfaro, “Photoconductive devices for terahertz pulsed spectroscopy: a review [Invited],” *Photonics Research*, vol. 4, p. A36, Jun 2016.
- [181] M. Ashida, “Ultra-Broadband Terahertz Wave Detection Using Photoconductive Antenna,” *Japanese Journal of Applied Physics*, vol. 47, pp. 8221–8225, Oct 2008.
- [182] S. Kono, M. Tani, and K. Sakai, “Ultrabroadband photoconductive detection: Comparison with free-space electro-optic sampling,” *Applied Physics Letters*, vol. 79, pp. 898–900, Aug 2001.
- [183] L. Liebermeister, S. Nellen, R. Kohlhaas, S. Breuer, M. Schell, and B. Globisch, “Ultrafast, High-Bandwidth Coherent CW THz Spectrometer for Non-destructive Testing,” *Journal of Infrared, Millimeter, and Terahertz Waves*, vol. 40, pp. 288–296, Mar 2019.

- [184] D. Stanze, B. Globisch, R. J. B. Dietz, H. Roehle, T. Gobel, and M. Schell, "Multilayer Thickness Determination Using Continuous Wave THz Spectroscopy," *IEEE Transactions on Terahertz Science and Technology*, vol. 4, pp. 696–701, Nov 2014.
- [185] M. S. Islam, J. Sultana, C. M. B. Cordeiro, A. L. S. Cruz, A. Dinovitser, B. W. Ng, and D. Abbott, "Broadband Characterization of Glass and Polymer Materials Using THz-TDS," in *2019 44th International Conference on Infrared, Millimeter, and Terahertz Waves (IRMMW-THz)*, vol. 2019-Septe, pp. 1–2, IEEE, Sep 2019.
- [186] S. Nashima, O. Morikawa, K. Takata, and M. Hangyo, "Temperature dependence of optical and electronic properties of moderately doped silicon at terahertz frequencies," *Journal of Applied Physics*, vol. 90, p. 837, Jun 2001.
- [187] L.-H. Kang and D.-H. Han, "Robotic-based terahertz imaging for nondestructive testing of a PVC pipe cap," *NDT & E International*, vol. 123, p. 102500, Oct 2021.
- [188] M. Bernier, F. Garet, and J. L. Coutaz, "Precise determination of the refractive index of samples showing low transmission bands by THz time-domain spectroscopy," *IEEE Transactions on Terahertz Science and Technology*, vol. 3, no. 3, pp. 295–301, 2013.
- [189] A. Pashkin, M. Kempa, H. Němec, F. Kadlec, and P. Kužel, "Phase-sensitive time-domain terahertz reflection spectroscopy," *Review of Scientific Instruments*, vol. 74, pp. 4711–4717, Nov 2003.
- [190] R. Burger, J. Frisch, M. Hübner, M. Goldammer, O. Peters, E. Rönneberg, and D. Wu, "THz-TDS Reflection Measurement of Coating Thicknesses at Non-Perpendicular Incidence: Experiment and Simulation," *Sensors*, vol. 21, p. 3473, May 2021.
- [191] S. D. Siv Sachin, V. Vijayan, and R. N. Kini, "Non-destructive evaluation of coatings using terahertz reflection spectroscopy," *Journal of Optics*, vol. 24, p. 044014, Mar 2022.
- [192] J. Xu, T. Yuan, S. Mickan, and X. C. Zhang, "Limit of Spectral Resolution in Terahertz Time-Domain Spectroscopy," *Chinese Physics Letters*, vol. 20, pp. 1266–1268, Aug 2003.
- [193] T. Yasui, K. Kawamoto, Y.-D. Hsieh, Y. Sakaguchi, M. Jewariya, H. Inaba, K. Minoshima, F. Hindle, and T. Araki, "Enhancement of spectral resolution and accuracy in asynchronous-optical-sampling terahertz time-domain spectroscopy for low-pressure gas-phase analysis," *Opt. Express*, vol. 20, pp. 15071–15078, Jul 2012.
- [194] M. Takeda, S. R. Tripathi, M. Aoki, and N. Hiromoto, "Exploration of the origin of random error in spectrum intensity measured with THz-TDS," in *35th International Conference on Infrared, Millimeter, and Terahertz Waves*, pp. 1–2, IEEE, Sep 2010.
- [195] J. Son, J. V. Rudd, and J. F. Whitaker, "Noise characterization of a self-mode-locked Ti:sapphire laser," *Optics Letters*, vol. 17, p. 733, May 1992.
- [196] H. Haus and A. Mecozzi, "Noise of mode-locked lasers," *IEEE Journal of Quantum Electronics*, vol. 29, pp. 983–996, Mar 1993.
- [197] A. Poppe, L. Xu, F. Krausz, and C. Spielmann, "Noise characterization of sub-10-fs Ti:sapphire oscillators," *IEEE Journal of Selected Topics in Quantum Electronics*, vol. 4, pp. 179–184, Mar 1998.

- [198] M. van Exter and D. Grischkowsky, "Characterization of an optoelectronic terahertz beam system," *IEEE Transactions on Microwave Theory and Techniques*, vol. 38, no. 11, pp. 1684–1691, 1990.
- [199] L. Duvillaret, F. Garet, and J.-L. Coutaz, "Influence of noise on the characterization of materials by terahertz time-domain spectroscopy," *Journal of the Optical Society of America B*, vol. 17, p. 452, Mar 2000.
- [200] J. Letosa, M. Garcia-Gracia, J. Fornies-Marquina, and J. Artacho, "Performance limits in TDR technique by Monte Carlo simulation," *IEEE Transactions on Magnetics*, vol. 32, pp. 958–961, May 1996.
- [201] N. Cohen, J. W. Handley, R. D. Boyle, S. L. Braunstein, and E. Berry, "Experimental signature of registration noise in pulsed terahertz systems," *Fluctuation and Noise Letters*, vol. 06, pp. L77–L84, Mar 2006.
- [202] M. Grabe, "Estimation of measurement uncertainties - an alternative to the ISO Guide," *Metrologia*, vol. 38, pp. 97–106, Apr 2001.
- [203] W. Withayachumnankul, B. M. Fischer, H. Lin, and D. Abbott, "Uncertainty in terahertz time-domain spectroscopy measurement," *Journal of the Optical Society of America B*, vol. 25, p. 1059, Jun 2008.
- [204] D. Mittleman, R. Jacobsen, R. Neelamani, R. Baraniuk, and M. Nuss, "Gas sensing using terahertz time-domain spectroscopy," *Applied Physics B: Lasers and Optics*, vol. 67, pp. 379–390, Sep 1998.
- [205] R. Allman and R. Foltynowicz, "Terahertz time-domain spectroscopy of atmospheric water vapor from 0.4 to 2.7 THz.," tech. rep., Sandia National Laboratories (SNL), Albuquerque, NM, and Livermore, CA (United States), Oct 2005.
- [206] W. Withayachumnankul and M. Naftaly, "Fundamentals of Measurement in Terahertz Time-Domain Spectroscopy," *Journal of Infrared, Millimeter, and Terahertz Waves*, vol. 35, pp. 610–637, Aug 2014.
- [207] X. Xin, H. Altan, A. Saint, D. Matten, and R. R. Alfano, "Terahertz absorption spectrum of para and ortho water vapors at different humidities at room temperature," *Journal of Applied Physics*, vol. 100, p. 094905, Nov 2006.
- [208] Y. Shimada, H. Iida, and M. Kinoshita, "Recent Research Trends of Terahertz Measurement Standards," *IEEE Transactions on Terahertz Science and Technology*, vol. 5, no. 6, pp. 1166–1172, 2015.
- [209] M. Kinoshita, H. Iida, and Y. Shimada, "Frequency Calibration of Terahertz Time-Domain Spectrometer Using Air-Gap Etalon," *IEEE Transactions on Terahertz Science and Technology*, vol. 4, pp. 756–759, Nov 2014.
- [210] M. Naftaly, "Metrology Issues and Solutions in THz Time-Domain Spectroscopy: Noise, Errors, Calibration," *IEEE Sensors Journal*, vol. 13, pp. 8–17, Jan 2013.

- [211] Y. Deng, Q. Sun, and J. Yu, “On-line calibration for linear time-base error correction of terahertz spectrometers with echo pulses,” *Metrologia*, vol. 51, pp. 18–24, Feb 2014.
- [212] TOPTICA Photonics AG, “TeraFlash pro — TOPTICA Photonics AG — toptica.com.” <https://www.toptica.com/products/terahertz-systems/time-domain/teraflash-pro>. [Accessed 17-Oct-2022].
- [213] Menlo Systems GmbH, “Femtosecond Erbium Laser — Menlo Systems — menlosystems.com.” <https://www.menlosystems.com/products/femtosecond-lasers-and-amplifiers/c-fiber/>. [Accessed 26-Nov-2022].
- [214] U. Nandi, J. C. Norman, A. C. Gossard, H. Lu, and S. Preu, “1550-nm Driven ErAs:In(Al)GaAs Photoconductor-Based Terahertz Time Domain System with 6.5 THz Bandwidth,” *Journal of Infrared, Millimeter, and Terahertz Waves*, vol. 39, pp. 340–348, Apr 2018.
- [215] J. Y. Suen, P. R. Krogen, S. Preu, H. Lu, A. C. Gossard, D. C. Driscoll, and P. M. Lubin, “Measurement and modeling of ErAs:In 0.53 Ga 0.47 As nanocomposite photoconductivity for THz generation at 1.55 μ m pump wavelength,” *Journal of Applied Physics*, vol. 116, p. 013703, Jul 2014.
- [216] B. Globisch, R. J. B. Dietz, D. Stanze, T. Göbel, and M. Schell, “Carrier dynamics in Beryllium doped low-temperature-grown InGaAs/InAlAs,” *Applied Physics Letters*, vol. 104, p. 172103, Apr 2014.
- [217] K. K. Williams, Z. D. Taylor, J. Y. Suen, H. Lu, R. S. Singh, A. C. Gossard, and E. R. Brown, “Toward a 1550 nm InGaAs photoconductive switch for terahertz generation,” *Optics Letters*, vol. 34, p. 3068, Oct 2009.
- [218] D. Filipovic, S. Gearhart, and G. Rebeiz, “Double-slot antennas on extended hemispherical and elliptical silicon dielectric lenses,” *IEEE Transactions on Microwave Theory and Techniques*, vol. 41, no. 10, pp. 1738–1749, 1993.
- [219] TEM Messtechnik GmbH, “PDA Photo Diode Amplifier - TEM-Messtechnik — tem-messtechnik.de.” <https://tem-messtechnik.de/en/products/photo-diode-amplifier/#overview>. [Accessed 13-Oct-2022].
- [220] Zurich Instruments AG, “MFLI 500 kHz / 5 MHz Lock-in Amplifier — zhinst.com.” <https://www.zhinst.com/europe/en/products/mfli-lock-amplifier>. [Accessed 13-Oct-2022].
- [221] R. B. Marks, “Formulations of the Basic Vector Network Analyzer Error Model including Switch-Terms,” in *50th ARFTG Conference Digest*, pp. 115–126, IEEE, Dec 1997.
- [222] D. K. Rytting, “Network Analyzer Accuracy Overview,” in *58th ARFTG Conference Digest*, pp. 1–13, IEEE, Nov 2001.
- [223] S. E. Tavares, “A Comparison of Integration and Low-Pass Filtering,” *IEEE Transactions on Instrumentation and Measurement*, vol. 15, pp. 33–38, Mar 1966.

- [224] H. Stephani, M. Herrmann, K. Wiesauer, S. Katletz, and B. Heise, “Enhancing the interpretability of terahertz data through unsupervised classification,” in *19th IMEKO World Congress 2009*, vol. 1, 2009.
- [225] J. Vázquez-Cabo, P. Chamorro-Posada, F. J. Fraile-Peláez, Ó. Rubiños-López, J. M. López-Santos, and P. Martín-Ramos, “Windowing of THz time-domain spectroscopy signals: A study based on lactose,” *Optics Communications*, vol. 366, pp. 386–396, May 2016.
- [226] F. R. Faridi, U. Nandi, and S. Preu, “1.5 Port Vector Spectrometer for Terahertz Time Domain Spectroscopy,” in *2018 43rd International Conference on Infrared, Millimeter, and Terahertz Waves (IRMMW-THz)*, pp. 1–2, IEEE, Sep 2018.
- [227] A. Taschin, P. Bartolini, J. Tasseva, and R. Torre, “THz time-domain spectroscopic investigations of thin films,” *Measurement*, vol. 118, pp. 282–288, Mar 2018.
- [228] M. Scheller, “Real-time terahertz material characterization by numerical three-dimensional optimization,” *Optics Express*, vol. 19, pp. 10647–10655, May 2011.
- [229] F. R. Faridi and S. Preu, “Pulsed free space two-port photonic vector network analyzer with up to 2 THz bandwidth,” *Optics Express*, vol. 29, pp. 12278–12291, Apr 2021.
- [230] C. Fattinger, D. Grischkowsky, and M. van Exter, “Terahertz time-domain spectroscopy of water vapor,” *Optics Letters*, vol. 14, pp. 1128–1130, Oct 1989.
- [231] H. Cheng, H.-c. Huang, M.-f. Yang, M.-h. Yang, H. Yan, S. Panezai, Z.-Y. Zheng, Z. Zhang, and Z.-l. Zhang, “Characterization of the remediation of chromium ion contamination with bentonite by terahertz time-domain spectroscopy,” *Scientific Reports 2022 12:1*, vol. 12, pp. 1–16, Jul 2022.
- [232] T. I. Jeon and D. Grischkowsky, “Characterization of optically dense, doped semiconductors by reflection THz time domain spectroscopy,” *Applied Physics Letters*, vol. 72, p. 3032, Jun 1998.
- [233] H. Merbold, P. U. Jepsen, and U. Møller, “Investigation of aqueous alcohol and sugar solutions with reflection terahertz time-domain spectroscopy,” *Optics Express*, vol. 15, pp. 14717–14737, Oct 2007.
- [234] W. Fuscaldo, S. D. Simone, D. Dimitrov, V. Marinova, V. Mussi, R. Beccherelli, and D. C. Zografopoulos, “Terahertz characterization of graphene conductivity via time-domain reflection spectroscopy on metal-backed dielectric substrates,” *Journal of Physics D: Applied Physics*, vol. 55, p. 365101, Jun 2022.
- [235] A. F. Starr, P. M. Rye, D. R. Smith, and S. Nemat-Nasser, “Fabrication and characterization of a negative-refractive-index composite metamaterial,” *Physical Review B - Condensed Matter and Materials Physics*, vol. 70, p. 113102, Sep 2004.
- [236] A. N. Grebenchukov, V. I. Ivanova, A. V. Suslov, G. I. Kropotov, and M. K. Khodzitsky, “Broadband Terahertz Isolator,” *IEEE Transactions on Terahertz Science and Technology*, vol. 12, pp. 81–86, Jan 2022.

- [237] B. M. Fischer, D. Abbott, H. Lin, and W. Withayachumnankul, "Uncertainty in terahertz time-domain spectroscopy measurement," *JOSA B*, Vol. 25, Issue 6, pp. 1059-1072, vol. 25, pp. 1059–1072, Jun 2008.
- [238] F. D. J. Brunner, A. Schneider, and P. Günter, "A terahertz time-domain spectrometer for simultaneous transmission and reflection measurements at normal incidence," *Optics Express*, vol. 17, p. 20684, Nov 2009.
- [239] B. S. Ung, J. Li, H. Lin, B. M. Fischer, W. Withayachumnankul, and D. Abbott, "Dual-Mode Terahertz Time-Domain Spectroscopy System," *IEEE Transactions on Terahertz Science and Technology*, vol. 3, pp. 216–220, Mar 2013.
- [240] F. R. Faridi and S. Preu, "Characterization of a Terahertz Isolator using a 1.5 Port Vector Spectrometer," in *2019 44th International Conference on Infrared, Millimeter, and Terahertz Waves (IRMMW-THz)*, pp. 1–2, IEEE, Sep 2019.
- [241] M. S. Islam, J. Sultana, S. Rana, M. R. Islam, M. Faisal, S. F. Kaijage, and D. Abbott, "Extremely low material loss and dispersion flattened TOPAS based circular porous fiber for long distance terahertz wave transmission," *Optical Fiber Technology*, vol. 34, pp. 6–11, Mar 2017.
- [242] M. S. Islam, S. Rana, M. R. Islam, M. Faisal, H. Rahman, and J. Sultana, "Porous core photonic crystal fibre for ultra-low material loss in THz regime," *IET Communications*, vol. 10, pp. 2179–2183, Nov 2016.
- [243] A. k. Mukherjee, M. Xiang, and S. Preu, "Broadband Dielectric Waveguides for 0.5–1.1 THz Operation," in *2020 45th International Conference on Infrared, Millimeter, and Terahertz Waves (IRMMW-THz)*, pp. 1–2, IEEE, Nov 2020.
- [244] B. Wu, H. Li, H. Xiao, J. Yuan, S. Atakaramians, W. Wang, Y. Li, and Z. Han, "Terahertz polarization-maintaining subwavelength filters," *Optics Express*, vol. 26, pp. 25617–25629, Oct 2018.
- [245] F. Pavanello, F. Garet, M. B. Kuppam, E. Peytavit, M. Vanwollegem, F. Vaurette, J. L. Coutaz, and J. F. Lampin, "Broadband ultra-low-loss mesh filters on flexible cyclic olefin copolymer films for terahertz applications," *Applied Physics Letters*, vol. 102, p. 111114, Mar 2013.
- [246] X. He, "Tunable terahertz graphene metamaterials," *Carbon*, vol. 82, pp. 229–237, Feb 2015.
- [247] M. S. Islam, J. Sultana, M. Biabanifard, Z. Vafapour, M. J. Nine, A. Dinovitser, C. M. Cordeiro, B. W. Ng, and D. Abbott, "Tunable localized surface plasmon graphene metasurface for multiband superabsorption and terahertz sensing," *Carbon*, vol. 158, pp. 559–567, Mar 2020.
- [248] R. Tanyi Ako, A. Upadhyay, W. Withayachumnankul, M. Bhaskaran, S. Sriram, R. T. Ako, A. Upadhyay, M. Bhaskaran, S. Sriram, and W. Withayachumnankul, "Dielectrics for Terahertz Metasurfaces: Material Selection and Fabrication Techniques," *Advanced Optical Materials*, vol. 8, p. 1900750, Feb 2020.

- [249] Z. Shi, L. Song, and T. Zhang, “Optical and Electrical Characterization of Pure PMMA for Terahertz Wide-band Metamaterial Absorbers,” *Journal of Infrared, Millimeter, and Terahertz Waves*, vol. 40, pp. 80–91, Jan 2019.
- [250] P. H. Bolivar, M. Brucherseifer, J. G. Rivas, R. Gonzalo, I. Ederra, A. L. Reynolds, M. Holker, and P. De Maagt, “Measurement of the dielectric constant and loss tangent of high dielectric-constant materials at terahertz frequencies,” *IEEE Transactions on Microwave Theory and Techniques*, vol. 51, pp. 1062–1066, Apr 2003.
- [251] F. Ellrich, M. Bauer, N. Schreiner, A. Keil, T. Pfeiffer, J. Klier, S. Weber, J. Jonuscheit, F. Friederich, and D. Molter, “Terahertz Quality Inspection for Automotive and Aviation Industries,” *Journal of Infrared, Millimeter, and Terahertz Waves*, vol. 41, pp. 470–489, Apr 2020.
- [252] C. Li, J. Cao, Z. Zhang, J. Li, L. Wang, Q. He, and C. Zhang, “Measurement of thermal barrier coating thickness of turbine blade based on THz-TDS,” in *Infrared, Millimeter-Wave, and Terahertz Technologies VIII* (X.-C. Zhang, M. Tani, and C. Zhang, eds.), vol. 11906, p. 56, SPIE, Oct 2021.
- [253] C. Fattinger, D. Grischkowsky, M. van Exter, and S. Keiding, “Far-infrared time-domain spectroscopy with terahertz beams of dielectrics and semiconductors,” *JOSA B*, vol. 7, pp. 2006–2015, Oct 1990.
- [254] S. Sommer, M. Koch, and A. Adams, “Terahertz Time-Domain Spectroscopy of Plasticized Poly(vinyl chloride),” *Analytical Chemistry*, vol. 90, pp. 2409–2413, Feb 2018.
- [255] N. Farman, M. Mumtaz, M. A. Mahmood, S. D. Khan, M. A. Zia, M. Raffi, M. Ahmed, and I. Ahmad, “Investigation of optical and dielectric properties of polyvinyl chloride and polystyrene blends in terahertz regime,” *Optical Materials*, vol. 99, p. 109534, Jan 2020.
- [256] H. S. Skulason, D. L. Sounas, F. Mahvash, S. Francoeur, M. Siaj, C. Caloz, and T. Szkopek, “Field effect tuning of microwave Faraday rotation and isolation with large-area graphene,” *Applied Physics Letters*, vol. 107, p. 093106, Sep 2015.
- [257] C. A. Ross, C. Wang, D. Huang, J. Bowers, J. Hu, L. Bi, L. Deng, P. Pintus, Q. Du, S. Liu, T. Fakhrol, and Y. Zhang, “Monolithic integration of broadband optical isolators for polarization-diverse silicon photonics,” *Optica*, vol. 6, pp. 473–478, Apr 2019.
- [258] D. Jalas, A. Petrov, M. Eich, W. Freude, S. Fan, Z. Yu, R. Baets, M. Popović, A. Melloni, J. D. Joannopoulos, M. Vanwolleghem, C. R. Doerr, and H. Renner, “What is — and what is not — an optical isolator,” *Nature Photonics 2013 7:8*, vol. 7, pp. 579–582, Jul 2013.
- [259] F. Fan, S. Chen, and S. J. Chang, “A review of magneto-optical microstructure devices at terahertz frequencies,” *IEEE Journal on Selected Topics in Quantum Electronics*, vol. 23, Jul 2017.
- [260] H. Zhao, X. Chen, C. Ouyang, H. Wang, D. Kong, P. Yang, B. Zhang, C. Wang, G. Wei, T. Nie, W. Zhao, J. Miao, Y. Li, L. Wang, and X. Wu, “Generation and manipulation of chiral terahertz waves in the three-dimensional topological insulator Bi_2Te_3 ,” *Advanced Photonics*, vol. 2, p. 066003, Oct 2020.

- [261] O. Mitrofanov, I. Brener, T. S. Luk, and J. L. Reno, "Photoconductive Terahertz Near-Field Detector with a Hybrid Nanoantenna Array Cavity," *ACS Photonics*, vol. 2, pp. 1763–1768, Dec 2015.
- [262] Y. Jin, Y. Jin, J. L. Reno, and S. Kumar, "Phase-locked terahertz plasmonic laser array with 2 W output power in a single spectral mode," *Optica*, vol. 7, pp. 708–715, Jun 2020.
- [263] M. Tong, Y. Hu, X. Xie, X. Zhu, Z. Wang, X. Cheng, T. Jiang, M. Tong, Y. Hu, X. Xie, X. Zhu, Z. Wang, X. Cheng, and T. Jiang, "Helicity-dependent THz emission induced by ultrafast spin photocurrent in nodal-line semimetal candidate Mg_3Bi_2 ," *Opto-Electronic Advances*, vol. 3, no. 12, pp. 200023–1, 2020.
- [264] M. Tong, Y. Hu, Z. Wang, T. Zhou, X. Xie, X. Cheng, and T. Jiang, "Enhanced Terahertz Radiation by Efficient Spin-to-Charge Conversion in Rashba-Mediated Dirac Surface States," *Nano Letters*, vol. 21, pp. 60–67, Jan 2021.
- [265] S. Yuan, L. Chen, Z. Wang, W. Deng, Z. Hou, C. Zhang, Y. Yu, X. Wu, and X. Zhang, "On-chip terahertz isolator with ultrahigh isolation ratios," *Nature Communications 2021 12:1*, vol. 12, pp. 1–8, Sep 2021.
- [266] M. Shalaby, M. Peccianti, Y. Ozturk, and R. Morandotti, "A magnetic non-reciprocal isolator for broadband terahertz operation," *Nature Communications*, vol. 4, pp. 1557–1558, 2013.
- [267] Z. Tan, F. Fan, D. Zhao, S. Li, X. Wang, and S. Chang, "Linear-polarized terahertz isolator by breaking the gyro-mirror symmetry in cascaded magneto-optical metagrating," *Nanophotonics*, vol. 10, pp. 4141–4148, Nov 2021.
- [268] M. Tamagnone, C. Moldovan, J. M. Poumirol, A. B. Kuzmenko, A. M. Ionescu, J. R. Mosig, and J. Perruisseau-Carrier, "Near optimal graphene terahertz non-reciprocal isolator," *Nature Communications 2016 7:1*, vol. 7, pp. 1–6, Apr 2016.
- [269] S. Lin, S. Silva, J. Zhou, D. Talbayev, S. Lin, D. Talbayev, S. Silva, and J. Zhou, "A One-Way Mirror: High-Performance Terahertz Optical Isolator Based on Magnetoplasmonics," *Advanced Optical Materials*, vol. 6, p. 1800572, Oct 2018.
- [270] E. D. Black, "An introduction to Pound–Drever–Hall laser frequency stabilization," *American Journal of Physics*, vol. 69, p. 79, Dec 2000.
- [271] E.-B. Kley, H.-J. Fuchs, H. Bartelt, S. Schröter, and T. Glaser, "Diffractive optical isolator made of high-efficiency dielectric gratings only," *Applied Optics*, vol. 41, pp. 3558–3566, Jun 2002.
- [272] R. Mendis, M. Nagai, W. Zhang, and D. M. Mittleman, "Artificial dielectric polarizing-beamsplitter and isolator for the terahertz region," *Scientific Reports*, vol. 1, pp. 1–8, 2017.
- [273] Y. Kim, M. Yi, B. G. Kim, and J. Ahn, "Investigation of THz birefringence measurement and calculation in Al_2O_3 and LiNbO_3 ," *Applied Optics*, vol. 50, no. 18, p. 2906, 2011.
- [274] E. D. Palik, *Handbook of optical constants of solids*, vol. 1. Academic press, 1985.

- [275] E. D. Palik, *Handbook of optical constants of solids*, vol. 2. Academic press, 1985.
- [276] A. D. J. F. Olvera, A. K. Mukherjee, and S. Preu, "A Fully Optoelectronic Continuous-Wave 2-Port Vector Network Analyzer Operating From 0.1 THz to 1 THz," *IEEE Journal of Microwaves*, vol. 1, pp. 1015–1022, Sep 2021.
- [277] F. R. Faridi and S. Preu, "Characterization of a Crossed Dipole Resonator Array using a Pulsed Free Space Two-Port Photonic VNA," in *2021 46th International Conference on Infrared, Millimeter and Terahertz Waves (IRMMW-THz)*, vol. 2021-Augus, pp. 1–2, IEEE, Aug 2021.
- [278] F. R. Faridi, A. D. J. Fernandez Olvera, A. k. Mukherjee, and S. Preu, "A Comparison of Continuous-Wave and Pulsed Free Space 2-Port Photonic Vector Network Analyzers for Terahertz Characterization," in *2022 47th International Conference on Infrared, Millimeter and Terahertz Waves (IRMMW-THz)*, pp. 1–2, IEEE, Aug 2022.
- [279] T. Yasui, E. Saneyoshi, and T. Araki, "Asynchronous optical sampling terahertz time-domain spectroscopy for ultrahigh spectral resolution and rapid data acquisition," *Applied Physics Letters*, vol. 87, p. 061101, Aug 2005.
- [280] M. Yahyapour, K. Dutzi, B. Schmauss, P. Leisching, N. Vieweg, and A. Deninger, "Extremely Fast Thickness Measurements with an ECOPS-Based TD-THz System," in *2018 43rd International Conference on Infrared, Millimeter, and Terahertz Waves (IRMMW-THz)*, vol. 2018-Septe, pp. 1–2, IEEE, Sep 2018.
- [281] Y. Kim and D.-S. Yee, "High-speed terahertz time-domain spectroscopy based on electronically controlled optical sampling," *Optics Letters*, vol. 35, p. 3715, Nov 2010.
- [282] Z. B. Harris and M. H. Arbab, "Terahertz PHASR Scanner with 2 kHz, 100 picosecond Time-Domain Trace Acquisition Rate and an Extended Field-of-View Based on a Helio-stat Design," *IEEE Transactions on Terahertz Science and Technology*, pp. 1–15, Aug 2022.
- [283] D. R. Smith, J. B. Pendry, and M. C. Wiltshire, "Metamaterials and negative refractive index," *Science*, vol. 305, pp. 788–792, Aug 2004.
- [284] J. F. Ruan, F. Lan, Z. Tao, Z. F. Meng, and S. W. Ji, "Tunable terahertz metamaterial filter based on applying distributed load," *Physics Letters A*, vol. 421, p. 127705, Jan 2022.
- [285] B. Zhang, C. Pan, C. Lou, F. Yang, J. Xu, Q. Wu, R. Feng, and X. Wang, "THz band-stop filter using metamaterials surfaced on LiNbO₃ sub-wavelength slab waveguide," *Optics Express*, vol. 23, pp. 16042–16051, Jun 2015.
- [286] E. R. Brown, M. Lu, and W. Li, "Second-order bandpass terahertz filter achieved by multilayer complementary metamaterial structures," *Optics Letters*, vol. 36, pp. 1071–1073, Apr 2011.
- [287] C. M. Bingham, H. Tao, N. I. Landy, R. D. Averitt, W. J. Padilla, and X. Zhang, "A metamaterial absorber for the terahertz regime: Design, fabrication and characterization," *Optics Express*, vol. 16, pp. 7181–7188, May 2008.

- [288] J. Liu, W. Chen, W. Z. Ma, Y. S. Chen, X. C. Deng, P. P. Zhuang, and Q. Ye, “Biaxial hyperbolic metamaterial THz broadband absorber utilizing anisotropic two-dimensional materials,” *Results in Physics*, vol. 22, p. 103818, Mar 2021.
- [289] Z. Han, S. Ohno, Y. U. Tokizane, K. Nawata, T. Notake, Y. Takida, and H. Minamide, “Off-resonance and in-resonance metamaterial design for a high-transmission terahertz-wave quarter-wave plate,” *Optics Letters*, vol. 43, pp. 2977–2980, Jun 2018.
- [290] J. Luo, J. Luo, X. Shi, X. Shi, X. Luo, F. Hu, F. Hu, G. Li, G. Li, and G. Li, “Broadband switchable terahertz half-/quarter-wave plate based on metal-VO₂ metamaterials,” *Optics Express*, vol. 28, pp. 30861–30870, Oct 2020.
- [291] A. J. Taylor, A. C. Gossard, H.-T. Chen, J. M. O. Zide, R. D. Averitt, S. R. Bank, and W. J. Padilla, “Ultrafast optical switching of terahertz metamaterials fabricated on ErAs/GaAs nanoisland superlattices,” *Optics Letters*, vol. 32, pp. 1620–1622, Jun 2007.
- [292] A. Grebenchukov, M. Masyukov, A. Zaitsev, and M. Khodzitsky, “Asymmetric graphene metamaterial for narrowband terahertz modulation,” *Optics Communications*, vol. 476, p. 126299, Dec 2020.
- [293] S. Shen, X. Liu, Y. Shen, J. Qu, E. Pickwell-Macpherson, X. Wei, Y. Sun, S. Shen, X. Liu, Y. Sun, J. Qu, Y. Shen, E. Pickwell-Macpherson, and X. Wei, “Recent Advances in the Development of Materials for Terahertz Metamaterial Sensing,” *Advanced Optical Materials*, vol. 10, p. 2101008, Jan 2022.
- [294] A. S. Saadeldin, M. F. O. Hameed, E. M. Elkaramany, and S. S. Obayya, “Highly Sensitive Terahertz Metamaterial Sensor,” *IEEE Sensors Journal*, vol. 19, pp. 7993–7999, Sep 2019.
- [295] F. Yan, H. Zhou, S. Tan, W. Wang, and Y. Hou, “Ultrasensitive terahertz metamaterial sensor based on vertical split ring resonators,” *Photonics Research*, vol. 5, pp. 571–577, Dec 2017.
- [296] M. Mueh, M. Maasch, R. A. Knieb, H. U. Goringe, and C. Damm, “Detection of African trypanosomes using asymmetric double-split ring based THz sensors,” *IEEE Journal of Electromagnetics, RF and Microwaves in Medicine and Biology*, vol. 1, pp. 66–73, Dec 2017.
- [297] P. Rodríguez-Ulibarri, S. A. Kuznetsov, and M. Beruete, “Wide angle terahertz sensing with a cross-dipole frequency selective surface,” *Applied Physics Letters*, vol. 108, p. 111104, Mar 2016.
- [298] T. Chen, S. Li, and H. Sun, “Metamaterials Application in Sensing,” *Sensors 2012*, vol. 12, pp. 2742–2765, Feb 2012.
- [299] L. Cong, S. Tan, R. Yahiaoui, F. Yan, W. Zhang, and R. Singh, “Experimental demonstration of ultrasensitive sensing with terahertz metamaterial absorbers: A comparison with the metasurfaces,” *Applied Physics Letters*, vol. 106, p. 031107, Jan 2015.
- [300] J. Dai, W. Gao, B. Liu, X. Cao, T. Tao, Z. Xie, H. Zhao, D. Chen, H. Ping, and R. Zhang, “Design and fabrication of UV band-pass filters based on SiO₂/Si₃N₄ dielectric distributed bragg reflectors,” *Applied Surface Science*, vol. 364, pp. 886–891, 2016.

- [301] B. Kogel, P. Debernardi, P. Westbergh, J. S. Gustavsson, A. Haglund, E. Haglund, J. Bengtsson, and A. Larsson, “Integrated MEMS-Tunable VCSELs Using a Self-Aligned Reflow Process,” *IEEE Journal of Quantum Electronics*, vol. 48, pp. 144–152, Feb 2012.
- [302] G. Ma, J. Shen, Z. Zhang, Z. Hua, and S. H. Tang, “Ultrafast all-optical switching in one-dimensional photonic crystal with two defects,” *Optics Express*, vol. 14, p. 858, Jan 2006.
- [303] H.-Y. Lin, K.-J. Chen, S.-W. Wang, C.-C. Lin, K.-Y. Wang, J.-R. Li, P.-T. Lee, M.-H. Shih, X. Li, H.-M. Chen, and H.-C. Kuo, “Improvement of light quality by DBR structure in white LED,” *Opt. Express*, vol. 23, pp. A27–A33, Feb 2015.
- [304] S. Preu, H. G. L. Schwefel, S. Malzer, G. H. Döhler, L. J. Wang, M. Hanson, J. D. Zimmerman, and A. C. Gossard, “Coupled whispering gallery mode resonators in the Terahertz frequency range,” *Opt. Express*, vol. 16, pp. 7336–7343, May 2008.
- [305] A. J. Deninger, A. Roggenbuck, S. Schindler, and S. Preu, “2.75 THz tuning with a triple-DFB laser system at 1550 nm and InGaAs photomixers,” *Journal of Infrared, Millimeter, and Terahertz Waves*, vol. 36, pp. 269–277, Mar 2015.
- [306] M. Tani, Z. Jiang, and X.-C. Zhang, “Photoconductive terahertz transceiver,” *Electronics Letters*, vol. 36, no. 9, p. 804, 2000.
- [307] C. Jördens, N. Krumbholz, T. Hasek, N. Vieweg, B. Scherger, L. Bähr, M. Mikulics, and M. Koch, “Fibre-coupled terahertz transceiver head,” *Electronics Letters*, vol. 44, no. 25, p. 1473, 2008.
- [308] S. Busch, T. Probst, M. Schwerdtfeger, R. Dietz, J. Palací, and M. Koch, “Terahertz transceiver concept,” *Optics Express*, vol. 22, p. 16841, Jul 2014.
- [309] B. Globisch, R. J. B. Dietz, R. B. Kohlhaas, S. Nellen, M. Kleinert, T. Göbel, and M. Schell, “Fiber-coupled transceiver for terahertz reflection measurements with a 4.5 THz bandwidth,” *Optics Letters*, vol. 41, p. 5262, Nov 2016.
- [310] R. B. Kohlhaas, L. Liebermeister, S. Breuer, M. Amberg, D. de Felipe, S. Nellen, M. Schell, and B. Globisch, “Fiber Coupled Transceiver with 6.5 THz Bandwidth for Terahertz Time-Domain Spectroscopy in Reflection Geometry,” *Sensors*, vol. 20, p. 2616, May 2020.
- [311] P. U. Jepsen, R. H. Jacobsen, and S. R. Keiding, “Generation and detection of terahertz pulses from biased semiconductor antennas,” *Journal of the Optical Society of America B*, vol. 13, p. 2424, Nov 1996.
- [312] Menlo Systems GmbH, “All fiber-coupled Terahertz Spectrometer — Menlo Systems — menlosystems.com.” <https://www.menlosystems.com/de/products/thz-time-domain-solutions/terak15-terahertz-spectrometer/>. [Accessed 25-Oct-2022].
- [313] Datatec AG, “Keithley 2400 SMU— datatec.eu.” <https://www.datatec.eu/tektronix-keithley-smu-2400>. [Accessed 25-Oct-2022].

-
- [314] C. Caglayan, G. C. Trichopoulos, and K. Sertel, “Non-Contact Probes for On-Wafer Characterization of Sub-Millimeter-Wave Devices and Integrated Circuits,” *IEEE Transactions on Microwave Theory and Techniques*, vol. 62, pp. 2791–2801, Nov 2014.
- [315] Y. Karisan, C. Caglayan, G. C. Trichopoulos, and K. Sertel, “Lumped-Element Equivalent-Circuit Modeling of Millimeter-Wave HEMT Parasitics Through Full-Wave Electromagnetic Analysis,” *IEEE Transactions on Microwave Theory and Techniques*, vol. 64, pp. 1419–1430, May 2016.
- [316] Y. Cui and G. C. Trichopoulos, “A Quasi-Optical Testbed for Wideband THz On-Wafer Measurements,” *IEEE Transactions on Terahertz Science and Technology*, vol. 9, pp. 126–135, Mar 2019.
- [317] A. k. Mukherjee, M. Xiang, and S. Preu, “Broadband Terahertz Photonic Integrated Circuit with Integrated Active Photonic Devices,” *Photonics*, vol. 8, p. 492, Nov 2021.

LIST OF FIGURES

2.1	(a) A one-port network with incident and reflected wave. (b) A two-port network with all S -parameters.	10
2.2	S -parameter measurement for (a) forward and (b) backward propagations. . . .	11
2.3	Block diagram of a typical Vector Network Analyzer (VNA) architecture. Recreated and adapted from [106].	12
2.4	Frequency extender configuration to perform THz measurements with Radio Frequency (RF) VNA. Adapted from [116].	14
2.5	Block diagram of THz measurement setup of THz VNA demonstrating the connection of Electronic Vector Network Analyzer (EVNA) with frequency extenders [65].	14
2.6	Systematic measurement errors. Reflection tracking is calculated by A/R and transmission tracking by B/R . Adapted from [124].	15
2.7	Calibration standards. Adapted from [106].	16
2.8	Calibration standards for free space VNA configuration. Antenna 1 (Ant1) is connected to port 1 and Antenna 2 (Ant2) is connected to port 2 of the VNA.	18
2.9	Photomixing process. (a) Heterodyne mixing of two lasers, (b) resulting electric field and (c) resulting power modulation with a beat node at the difference frequency.	21
2.10	(a) Temporal profile, (b) spectral profile and (c) time-domain intensity of a femtosecond laser pulse. Reproduced and adapted from [178].	23
2.11	Current response for a transient overlap between THz and laser pulses. Top: For a short carrier lifetime ($\tau_c \ll 1$ ps) material. Bottom: For a long carrier lifetime ($\tau_c \gg 1$ ps) material. Reproduced and adapted from [179].	25
2.12	System architecture of a typical THz-TDS setup. LIA = Lock-in Amplifier, TIA = Transimpedance Amplifier.	27
2.13	(a) Temporal and (b) spectral profile of a THz pulse.	28
2.14	Transmission geometry THz-TDS setup for (a) reference and (b) test measurements.	29
2.15	(a) Reference and (b) test measurement setup for perpendicular incidence reflection THz-TDS. (c) Reference and (d) test measurement setup for oblique incidence reflection THz-TDS. Tx = Transmitter, Rx = Receiver, BS = Beam Splitter.	29

2.16	Error sources of THz-TDS measurement and error types (grey). Blue rectangles denote the parameter extraction procedure steps. Adapted from [203].	32
2.17	Frequency calibration using water vapor absorption lines	32
2.18	State-of-the-art commercial THz-TDS measurement (Toptica Photonics /Fraunhofer HHI, Berlin). (a) THz spectrum (b) Peak DNR versus number of averaged time traces and total acquisition time [212].	33
2.19	DNR of VNA extenders from Virginia Diodes Inc. [65] and state-of-the-art THz-TDS measurement [161]. *For two-port configuration.	34
3.1	Simple block diagrams of (a) a 1.5 port Vector Spectrometer (VSM) and (b) a two-port Photonic Vector Network Analyzer (PVNA). Tx = Transmitter, Rx = Receiver, DC = Directional coupler, ODU = Optical delay unit, PD = Post-detection.	38
3.2	THz performance of the ErAs:In(Al)GaAs transmitter and ErAs:InGaAs receiver pair driven by a TeraFlash Pro laser system [212] for a transmission geometry THz-TDS setup. Adapted with permission from [76] ©2022 IEEE.	39
3.3	(a) Design parameters of the Wire Grid Polarizer (WGP), with diameter of the free-standing Tungsten wire $w = 10 \mu\text{m}$ and pitch $p = 25 \mu\text{m}$. (b) Photo of the WGP at 0° orientation.	40
3.4	(a) Extinction ratio and (b) insertion loss of the WGP.	41
3.5	Operating principle of the WGP based Directional Coupler (DC) for implementation in PVNA. Inset: Orientation of WGP ₁ and WGP ₄	41
3.6	6-term error model for (a) forward and (b) backward propagations.	43
3.7	(a) <i>Through</i> and (b) <i>reflect</i> standard paths for forward measurement calibration.	44
3.8	(a) Calibration tool. (b) Top view of the calibration tool.	46
3.9	THz pulse before (blue) and after (red) processing. (a) Time-domain. (b) Frequency-domain.	47
3.10	Measured transmitted (top) and reflected (bottom) time-domain THz pulse for absorptive materials. Inset: THz path of the main pulse (peak1) and first echo (echo1) transmitted through (top) or reflected from (bottom) the MUT. The echo of the transmitted pulse is too weak to distinguish from the noise floor. Adapted from [226] ©2018 IEEE.	49
3.11	Schematic flowchart of the numerical approach for the determination of optical characteristics of a material. Adapted from [229] ©2021 Optical Society of America.	51
4.1	Schematic of 1.5 port VSM. WGP = Wire Grid Polarizer, DUT = Device under test, Tx = Transmitter, Rx = Receiver.	55
4.2	Reference measurement for the a) transmission (empty setup) and b) reflection (mirror) modes of the 1.5 port VSM. c) Device Under Test (DUT) measurement of the 1.5 port VSM.	56
4.3	System attributes of the 1.5 port pulsed free space VSM. Available bandwidth 0.2-2.5 THz, with peak DNR of ~ 64 dB and ~ 57 dB (Equivalent Noise Bandwidth (ENBW) = 9.196 Hz) for transmission and reflection cases, respectively.	56
4.4	Refractive Index of Highly-resistive Silicon (HR-Si).	57
4.5	Refractive index (left) and absorption coefficient (right) of Polyvinyl chloride (PVC).	58

4.6	Refractive index (left) and absorption coefficient (right) of High-density polyethylene (HDPE).	58
4.7	Operating principle of a THz Isolator. Reprinted with permission from [240] ©2019 IEEE.	60
4.8	Ordinary (n_o) and extraordinary (n_e) refractive indices of 10-10 cut Sapphire and the difference between them (Δn), calculated from THz-TDS measurement data.	61
4.9	Experimental configurations for investigating the behavior of the isolator.	61
4.10	Measured isolation and insertion loss for the THz isolator with metal mirror as the reflecting element.	62
4.11	Measured isolation and insertion loss for the THz Isolator with HR-Si wafer as the reflecting element.	63
4.12	Extracted refractive index difference from THz-TDS measurements and isolator data.	63
4.13	Measured isolation and insertion loss for the THz isolator (with metal mirror as the reflecting element) are compared with theoretical model evaluated from parameters extracted using isolator data.	64
4.14	Measured isolation and insertion loss for the THz isolator (with HR-Si wafer as the reflecting element) are compared to the theoretical model evaluated from parameters extracted using isolator data.	64
5.1	Detailed schematic of a two-port pulsed free space PVNA (adapted from [229]) ©2021 Optical Society of America.	68
5.2	Setups for the calculation of Scattering (S)-parameters of a DUT. a) Reference measurement for S_{21} and S_{12} in an empty setup. b) Reference measurement for S_{11} with mirror aligned with one face of the DUT. c) Reference measurement for S_{11} with mirror aligned with the other face of the DUT. d) DUT characterization with DUT replacing the mirror.	70
5.3	Measured cross-talk of the two-port pulsed free space PVNA.	71
5.4	System attributes of the two-port pulsed free space PVNA. Available bandwidth 0.2-3 THz, with peak DNR of 57 dB at 500 GHz for an ENBW=9.196 Hz. This figure is adapted from [229] ©2021 Optical Society of America.	72
5.5	(a) Section of an Split-Ring Resonator (SRR) array (b) Design parameters of a SRR array unit cell. Reprinted from [229] ©2021 Optical Society of America.	74
5.6	Magnitude of the S -parameters of an SRR array. Adapted from [229] ©2021 Optical Society of America.	74
5.7	Phase of the S -parameters of the same SRR array.	75
5.8	(a) Section of a Crossed-Dipole Resonator (CDR) array (b) Thickness profile of the CDR array. Adapted from [229] ©2021 Optical Society of America.	76
5.9	S -parameters of a CDR array. Adapted from [277] ©2021 IEEE.	76
5.10	(a) Schematic of a Distributed Bragg Reflector (DBR). Reprinted from [229] ©2021 Optical Society of America. (b) S -parameters of the DBR. Adapted from [229] ©2021 Optical Society of America.	78
5.11	Permittivity (real) of HR-Si. Reprint from [229] ©2021 Optical Society of America.	79
5.12	Permittivity (real) (left) and loss tangent (right) of PVC. Reprint from [229] ©2021 Optical Society of America.	79

5.13	Comparison of experimental setup for two-port pulsed and CW PVNA. Reprinted with permission from [278] ©2022 IEEE.	80
5.14	Bandwidth and DNR comparison between two-port pulsed and CW PVNA. Adapted from [278] ©2022 IEEE.	81
5.15	S -parameters of a DBR extracted using pulsed PVNA are compared with Continuous Wave (CW) PVNA measurement and theoretical calculation. Adapted from [278] ©2022 IEEE.	82
5.16	S -parameters extracted using PVNA is compared with commercial EVNA and theoretical calculation for (a) DBR and (b)SRR array. Reprinted from [229] ©2021 Optical Society of America.	85
6.1	Preparation of sample before metal deposition.	90
6.2	Metal deposition process.	90
6.3	Mesa etching process.	90
6.4	Anti-Reflection Coating (ARC) deposition process.	91
6.5	Micrograph of a ErAs:In(Al)GaAs photoconductor-based THz transceiver chip.	91
6.6	(a) Front and (b) rear view of the semi-packaged transceiver module.	92
6.7	Experimental setup of a transceiver-based one-port PVNA. TR = Transceiver, PBS = Polarizing Beam Splitter, TIA = Transimpedance Amplifier, DAQ = Data Acquisition, ODU = Optical Delay Unit.	93
6.8	(a) Cross-talk and (b) calibrated spectral profile of the one-port PVNA.	94
6.9	S_{11} parameter of a DBR extracted using a one-port transceiver-based PVNA and compared with the theoretical model.	95
6.10	S_{11} parameter of a SRR extracted using a one-port transceiver-based PVNA and compared with the simulation.	96
A.1	Data acquisition Graphical User Interface (GUI).	104
C.1	MatChar (version 1.0) software interface for the determination of refractive index, absorption coefficient and thickness of a MUT. The parameters are extracted from the THz-TDS measurement in transmission mode.	116

LIST OF PUBLICATIONS

Journal Publications

- **F. R. Faridi** and S. Preu, “Pulsed free space two-port photonic vector network analyzer with up to 2 THz bandwidth,” *Opt. Express*, vol. 29, no. 8, pp. 12278-12291, Apr 2021.
- K.-H. Tybussek, K. Kolpatzeck, **F. R. Faridi**, S. Preu, and J. C. Balzer, “Terahertz Time-Domain Spectroscopy Based on Commercially Available 1550 nm Fabry–Perot Laser Diode and ErAs:In(Al)GaAs Photoconductors,” *Applied Sciences*, vol. 9, no. 13, p. 2704, Jul. 2019.

Conference Publications

- **F. R. Faridi**, U. Nandi and S. Preu, “1.5 Port Vector Spectrometer for Terahertz Time Domain Spectroscopy,” *2018 43rd International Conference on Infrared, Millimeter, and Terahertz Waves (IRMMW-THz)*, Nagoya, Japan, 2018, pp. 1-2, Sep. 2018.
- **F. R. Faridi** and S. Preu, “Characterization of a Terahertz Isolator using a 1.5 Port Vector Spectrometer,” *2019 44th International Conference on Infrared, Millimeter, and Terahertz Waves (IRMMW-THz)*, Paris, France, 2019, pp. 1-2, Oct. 2019.
- **F. R. Faridi** and S. Preu, “Characterization of a Crossed Dipole Resonator Array using a Pulsed Free Space Two-Port Photonic VNA,” *2021 46th International Conference on Infrared, Millimeter and Terahertz Waves (IRMMW-THz)*, Chengdu, China, 2021, pp. 1-2, Oct. 2021.
- **F. R. Faridi**, A. D. J. Fernandez Olvera, A. k. Mukherjee and S. Preu, “A Comparison of Continuous-Wave and Pulsed Free Space 2-Port Photonic Vector Network Analyzers for Terahertz Characterization,” *2022 47th International Conference on Infrared, Millimeter and Terahertz Waves (IRMMW-THz)*, Delft, Netherlands, 2022, Sep. 2022.

Other Conference Contribution

- **F. R. Faridi** and S. Preu, “An ErAs:In(Al)GaAs Based Transceiver for S_{11} parameter measurements up to 2.5 THz,” *2022 French-German TeraHertz Conference*, La Grande Motte, France, May 2022.

Workshop Contribution

- U. Nandi, **F. R. Faridi**, A. D. J. F. Olvera, J. Norman, H. Lu, A. C. Gossard and S. Preu, “High Dynamic Range THz Systems using ErAs:In(Al)GaAs Photoconductors,” *2019 IEEE MTT-S International Microwave Workshop Series on Advanced Materials and Processes for RF and THz Applications (IMWS-AMP)*, Bochum, Germany, pp. 115-117, Oct. 2019.

ACRONYMS

<i>Q</i>	Quality.
<i>S</i>	Scattering.
ADC	Analogue to Digital Converter.
ARC	Anti-Reflection Coating.
ASOPS	Asynchronous Optical Sampling.
CAE	Computer-Aided Engineering.
CDR	Crossed-Dipole Resonator.
CW	Continuous Wave.
DAQ	Data Acquisition.
DBR	Distributed Bragg Reflector.
DC	Directional Coupler.
DFB	Distributed Feedback.
DNR	Dynamic Range.
DUT	Device Under Test.
ECOPS	Electronically Controlled Optical Sampling.
EDFA	Erbium-Doped Fiber Amplifier.
ENBW	Equivalent Noise Bandwidth.
ER	Extinction Ratio.
EVNA	Electronic Vector Network Analyzer.
FP	Fabry-Pérot.
FWHM	Full Width at Half Maximum.
GSG	Ground-Source-Ground.
GUI	Graphical User Interface.
HDPE	High-density polyethylene.
HR-Si	Highly-resistive Silicon.
HWP	Half-Wave Plate.
IL	Insertion Loss.

LIA	Lock-In Amplifier.
LO	Local Oscillator.
MUT	Material Under Test.
NA	Network Analyzer.
NM	Nelder-Mead.
ODU	Optical Delay Unit.
PBS	Polarizing Beam Splitter.
PVC	Polyvinyl chloride.
PVNA	Photonic Vector Network Analyzer.
QWP	Quarter-Wave Plate.
RF	Radio Frequency.
SA	Spectrum Analyzer.
SI	International System of Units.
SRR	Split-Ring Resonator.
TC	Time Constant.
THz	Terahertz.
THz-TDS	Terahertz Time-Domain Spectroscopy.
TIA	Trans-Impedance Amplifier.
UV	Ultraviolet.
VNA	Vector Network Analyzer.
VSM	Vector Spectrometer.
WGP	Wire Grid Polarizer.

ACKNOWLEDGMENTS

What a fantastic journey it has been! When I first joined as a PhD student, I knew very little about terahertz, and today I am (almost) done with writing a 100-page thesis. Through the ups and downs, pain and gain, agony and bliss, the last 5 years or so have taught me a lot about science, life and most of all, about myself. I will always treasure this period and remember it as the most significant time of my life. However, this endeavor would not have been possible without the people around me, who have given their invaluable support and assistance to help me reach here.

I would like to start by expressing my deepest gratitude to Prof. Dr. Sascha Preu for providing me the opportunity to work in this top-notch research team. I have been fortunate to have a great leader and mentor as my supervisor. In addition to science, you have taught me a lot about patience, time and people management. I appreciate you giving us the “my door is (almost) always open” and “let’s walk and talk” policies, even if you have a ton on your plate. I am extremely grateful to you for your valuable time in the Terahertz lab and for helping me to prepare for my talks at conferences.

I consider myself exceedingly lucky to be a member of the Tera-fighters, also known as the Terahertz Systems and Devices group. This allowed me the chance to work with some brilliant individuals and get to know some amazing human beings who I am fortunate enough to call friends. You are the sole reason that living in Darmstadt has been bearable.

I owe a debt of gratitude to Uttam, who taught me a great deal about packaging and alignment during my first few months in the lab and provided me with the devices that I used to produce the majority of the findings in my thesis. You have also been a fantastic friend, a passable cook, and a tolerable travel companion. The workplace really misses having you here. I want to express my gratitude to Anuar for his invaluable contributions and assistance with my research work. You have taught me a lot about commitment to one’s work. This has to be said that without you, the lunch debates would not be as provocative. I would also like to thank my awesome officemate Amlan. During the time that we spent in the office not planning trips or where to eat next, you have always been there, ready to discuss work-related problems, which really helped me, and I hope, helped you too. I am also grateful to you for pushing me to finish writing the thesis and providing me post-processing ideas.

Thanks should also go to Romina for showing me how to be extraordinarily organized and introducing me to some good restaurants in Darmstadt. I would like to thank Benedikt for assisting me with the abstract translation, asking me ‘Do you have food?’ and ‘Where do you want to go?’ almost like clockwork and baking amazing brownies for us. Speaking of desserts, how can I forget Yasameen’s unparalleled Baklava. Also, the unforgettable train ride from Rotterdam to Darmstadt with you and Amlan was, for me, the highlight of IRMMW 2022. Special thanks to Rahul for driving me to Frankfurt following ‘The five night shifts at FELBE’ experience and organizing bowling evenings. Many thanks to Irene for after lunch ‘coffee breaks’

and ‘with that attitude’ talks which helped me a lot, and to Mojdeh for considering me worthy of being ‘a friend from work’ and for your contagious positivity.

I would be remiss in not mentioning Ahid, my football strike partner. Hope to see you soon in the field. I would like to extend my sincere thanks to Mario for his preliminary work on the material characterization and scanning program, which helped me immensely. I am also thankful to Stefan for introducing me to good coffee and after-work beer. Julijan deserves special mention for being a kind and helpful friend to me.

I would like to acknowledge Peter Kießlich and Andreas Semrad for their prompt help with manufacturing sample holders, and Alejandro for his assistance with the VNA measurements.

I would like to express my deepest gratitude to my parents. Without their continuous support, I would never be where I am now. I would also like to thank my siblings Priyanka, Promy and Pritul for being my pillars of encouragement. Special thanks to my parents-in-law for their love and blessings.

I would like to take this opportunity to express my appreciation to my wife, Rubaiya, now known as Dr. Hussain; without you, this PhD would not have been possible. You have been a continuous source of motivation not only as my partner and friend but also as a peer. Thanks for always inspiring me to be a better person. I often wonder why or how you put up with me, but I am very glad that you do!

Special thanks to the instruments, devices and components that worked endlessly, sometimes on weekends and sometimes overnight, to provide me with great results. To the two devices that were killed in action, your contributions will not be forgotten; may you rest in pieces (Thank you for donating your parts for the packaging of other devices). I would also like to thank my nemesis, still undefeated, the mechanical delay stage, who has provided me with many challenges and hurdles during the last year.

CURRICULUM VITAE

Fahd Rushd Faridi

Merckstraße 25, Room S3|06 524, 64283 Darmstadt
+49615116-28479
fahd.faridi@tu-darmstadt.de

Employment History

- | | |
|---------------------|--|
| Jul 2017 – Present | Research Scientist
Technical University of Darmstadt
Darmstadt |
| Mar 2015 – Mar 2016 | Student Research Assistant
Fraunhofer IZM
Berlin |
| Jan 2012- Sept 2012 | Lecturer
University of Information, Technology and Sciences
Bangladesh |

Education

- | | |
|---------------------|---|
| Oct 2012 – Nov 2015 | Master of Science in Optics and Photonics
Karlsruhe Institute of Technology, KSOP
Karlsruhe
Specialization : Optical Systems |
| Jan 2007 – Nov 2010 | Bachelor of Science in Electrical and Electronic Engineering
Islamic University of Technology
Bangladesh |

ERKLÄRUNGEN LAUT PROMOTIONSORDNUNG

§8 Abs. 1 lit. c PromO

Ich versichere hiermit, dass die elektronische Version meiner Dissertation mit der schriftlichen Version übereinstimmt.

§8 Abs. 1 lit. d PromO

Ich versichere hiermit, dass zu einem vorherigen Zeitpunkt noch keine Promotion versucht wurde. In diesem Fall sind nähere Angaben über Zeitpunkt, Hochschule, Dissertationsthema und Ergebnis dieses Versuchs mitzuteilen.

§9 Abs. 1 PromO

Ich versichere hiermit, dass die vorliegende Dissertation selbstständig und nur unter Verwendung der angegebenen Quellen verfasst wurde.

§9 Abs. 2 PromO

Die Arbeit hat bisher noch nicht zu Prüfungszwecken gedient.

Ort, Datum

FR Faridi

